DEPARTMENT OF MATERIALS

TRINITY COLLEGE

UNIVERSITY OF OXFORD

Synthesis and Characterisation of Large Area Monolayer Tungsten Disulphide

Youmin Rong

Supervised by Prof. Jamie H. Warner & Prof. G. Andrew D. Briggs

January 2016

Submitted in Conformity with the Requirements for the Degree of DPhil in Materials Science

Declaration

The material contained within this thesis has not previously been submitted for a degree at the University of Oxford or any other university. The research reported within this thesis has been conducted by the author unless indicated otherwise.

Copyright Notice

Abstract

Two-dimensional (2D) transition metal dichalcogenides (TMDs), equipped with direct bandgaps in the visible range of electromagnetic spectrum have extended the promise of 2D materials (graphene) to optoelectronics. Towards facilitating the future industrialization of 2D TMDs, this project focused on developing chemical vapour deposition (CVD) techniques for the growth of large area monolayer tungsten disulphide (WS_2), which was followed by characterisations of their structural and semiconducting properties.

It was demonstrated that controlling the introduction time and the amount of sulphur (S) vapour relative to the tungsten trioxide (WO_3) precursor during the CVD growth of WS_2 was critical to achieving large crystal domains on the surface of silicon wafers with a 300 nm oxide layer. This improvement for CVD techniques enabled the formation of single crystalline WS_2 monolayers with edges up to 370 μm which were visible to the naked eye.

Synthetic 2D materials grown by CVD are typically polycrystalline, and determining grain size within domains and continuous films is crucial for determining their structure. The thesis showed that grain boundaries (GBs) in monolayer WS_2, grown by CVD, could be preferentially oxidized by controlled heating in air. Under apposite conditions, the degradation of GBs led to their clear and rapid identification using a standard optical microscope.

Subsequent studies showed that how these monolayer WS_2 GBs influenced the electroluminescence (EL) behaviour in lateral source-drain devices under bias. Real time imaging of the WS_2 EL detected arcing between the electrodes when probing across a GB, which then localized at the GB region as it eroded under high bias conditions. Analysis of the eroded GB region showed the formation of micro- and nanoribbons across the monolayer WS_2 domains. These results provide important insights into future EL devices that utilize CVD grown monolayer TMDs when GBs are present in the active device region.

Acknowledgements

The research demonstrated in this thesis would not have been accomplished without the support, understanding and advice of my supervisors, colleagues, families and friends. Therefore, I would like to take this opportunity to thank Prof. Jamie H. Warner for providing me the kindest guidance and the most genuine mentorship during the course of my three-year-DPhil at Oxford. Being able to complete this DPhil degree successfully in terms of academic achievement is indebted tremendously to Prof. Warner's exceptional and meticulous supervision. What is more, the encouragement and vision I gained from my senior supervisor, Prof. Andrew Briggs, in exploring my research interest was also invaluable, for which I would like to express my sincere appreciation.

Besides, this project involves several individuals who had been most helpful in providing their expertise and knowledge when using material characterisation facilities. Dr. Mercè Pacios in Prof. Harish Bhaskaran's group was constantly genial and supportive to assist with experiments relating to atomic force microscopy. Dr. Alex W. Robertson was zealous and helpful when the Oxford's JEOL-2200 transmission electron microscopy (TEM) was in need. Two of my colleagues, Mr. Kuang He and Mr. Ye Fan provided generous support and performed adroitly on the use of the JEOL-2100 TEM and the Begbroke's AFM, respectively.

Lastly, I would like to proffer my deepest gratitude to my parents without whom I would never be able to reach this far, completing the degree. Their unconditional financial support, as well as their love I have been always imbued with, have made me persevere and fearless in pursuing academic greatness. My heartfelt thanks also needs to go to my benevolent girlfriend, Miss. Xiaoyang Li, who is in Stanford University and has always been there to support and invigorate me regardless of her own hectic schedule.

Publications

Here presents a list of published first-/co-author research accomplished during the course of this project. First-author publications are enumerated individually corresponding to the result chapters in the thesis.

Chapter 4

Youmin Rong, Ye Fan, Ai Leen Koh, Alex W. Robertson, Kuang He, Shanshan Wang, Haijie Tan, Robert Sinclair, and Jamie H. Warner. *"Controlling Sulphur Precursor Addition for Large Single Crystal Domains of WS_2".* **Nanoscale**, 2014, 6, 12096-12103.

Chapter 5

Youmin Rong, Kuang He, Merce Pacios, Alex W. Robertson, Harish Bhaskaran, and Jamie H. Warner. *"Controlled Preferential Oxidation of Grain Boundaries in Monolayer Tungsten Disulphide for Direct Optical Imaging".* **ACS Nano**, 2015, 9(4), 3696-3703, published as ACS AuthorChoice.

Chapter 6

Youmin Rong, Yuewen Sheng, Merce Pacios, Xiaochen Wang, Zhengyu He, Harish Bhaskaran, and Jamie H. Warner. *"Electroluminescence Dynamics across Grain Boundary Regions of Monolayer Tungsten Disulphide".* **ACS Nano**, 2016, 10(1), 1093-1100.

First-Author

Youmin Rong, and Jamie H. Warner. *"Wired Up: Interconnecting Two-Dimensional Materials with One-Dimensional Atomic Chains"*. **ACS Nano**, 2014, 8(12), 11907-11912.

Co-Author

1. Haijie Tan, Ye Fan, **Youmin Rong**, Ben Porter, Chit Siong Lau, Yingqiu Zhou, Zhengyu He, Shanshan Wang, Harish Bhaskaran, Jamie H. Warner. *"Doping Graphene Transistors Using Vertical Stacked Monolayer WS_2 Heterostructures Grown by Chemical Vapour Deposition"*. **ACS Applied Materials & Interfaces**, 2016, 8(3), 1644-1652.

2. Yuewen Sheng, Wenshuo Xu, Xiaochen Wang, Zhengyu He, **Youmin Rong**, and Jamie H. Warner. *"Mixed Multilayered Vertical Heterostructures Utilizing Strained Monolayer WS_2"*. **Nanoscale**, 2016, 8, 2639-2647.

3. Zhengyu He, Wenshuo Xu, Yingqiu Zhou, Xiaochen Wang, Yuewen Sheng, **Youmin Rong**, Shaoqiang Guo, Junying Zhang, Jason M. Smith, and Jamie H. Warner. *"Biexciton Formation in Bilayer Tungsten Disulphide".* **ACS Nano**, 2016, 10(2), 2176-2183.

4. Zhengyu He, Yuewen Sheng, **Youmin Rong**, Gun-Do Lee, Ju Li, and Jamie H. Warner. *"Layer-Dependent Modulation of Tungsten Disulphide Photoluminescence by Lateral Electric Fields"*. **ACS Nano**, 2015, 9(3), 2740-2748.

5. Yuewen Sheng, **Youmin Rong**, Zhengyu He, Ye Fe, and Jamie H. Warner. *"Uniformity of Large-Area Bilayer Graphene Grown by Chemical Vapour Deposition"*. **Nanotechnology**, 2015, 26, 395601.

6. Shanshan Wang, **Youmin Rong**, Ye Fan, Merce Pacios, Harish Bhaskaran, Kuang He, and Jamie H. Warner. *"Shape Evolution of Monolayer MoS_2 Crystals Grown by Chemical Vapour Deposition"*. **Chemistry of Materials**, 2014, 26(22), 6371-6379.

Contents

Chapter 1

Introduction

1.1 Project Aims

The doctorate project was dedicated to establishment and development of the facilities and methods for the chemical vapour deposition (CVD) synthesis of large area monolayer WS_2, and subsequently investigation of the structural and semiconducting properties of the product *via* a selection of characterisation techniques.

1.2 The Scope of this Thesis

The thesis embodies the research executed over the time span of three years of UK PhD degree at the Materials Department, University of Oxford. It unfolds by enclosing a literature review chapter that epitomizes monolayer WS_2's properties, its synthetic approaches and digital electronic applications, as well as apposite characterisation techniques.

The first task, as the prerequisite of all results, was to establish a functional CVD system for the synthesis of monolayer WS_2. In the process of validating the CVD for monolayer production, the first novel result was obtained, corresponding to *Chapter 4*. The as-developed CVD parameters were later used by other members of the group, leading to development of new research projects in areas such as transmission electron microscopy (TEM) characterisation and photo-detector/-transistor applications.

Subsequent to improving the CVD technique for growth of monolayer continuous films, the project moved onto the study of grain boundaries (GBs) in monolayer WS_2 *via* optical microscopy (OM). To observe a GB in 2D materials under OM, one will require additional pre-treatments. As a result, *Chapter 5* on optical imaging of monolayer WS_2 GBs revealed using a controlled oxidation procedure was established. Characterisation such as atomic force microscopy (AFM) was done by Mr. Fan while TEM was supported by Mr. He and Dr. Robertson.

By taking advantage of large WS_2 domain size synthesized in our CVD system, it was then possible to use ultrafine metallic probes for directly generating bias across individual GBs. At high bias, monolayer WS_2 GB degraded but localized electroluminescence (EL). *Chapter 6* therefore was accomplished by analysing EL dynamics across monolayer WS_2 GB regions subject to applied biasing.

The final chapter was delivered to recapitulate and conclude the above-demonstrated studies, and as a consequence, to envision potential problems and further research projects that could be apprehended for improvements.

Chapter 2

Literature Review

2.1 Introduction

In the ever-expanding field of two-dimensional (2D) materials, this chapter aims to encapsulate recent endeavours in the nascent development of 2D transition-metal-dichalcogenides (TMDs), where tungsten disulphide (WS_2) will be given a dedicated focus. Molybdenum disulphide (MoS_2) was the first 2D TMD realized and now it remains the closest kin to WS_2 among all other 2D TMDs. Therefore, experiments on 2D MoS_2 should also have a place in this review on 2D WS_2. Considering the thesis subject, the review will cover the synthesis and characterisation of 2D WS_2, although work on 2D MoS_2 will be also introduced when needed. I begin by first introducing a summary of the structure, properties and applications of 2D WS_2 (MoS_2). The review then encompasses a scrupulous discussion of currently available techniques for the synthesis of 2D WS_2 (MoS_2) and their respective practicality for various demands, and lastly introduces characterisation tools and techniques that have been critical to the development of 2D TMDs. As a result, some key issues that have prevented 2D TMDs from industrialization and the role of 2D WS_2 in the 2D industry shall be comprehended.

2.1.1 2D Materials beyond Graphene

The concept of 2D materials was brought to universal attention when graphene, a single layer of hexagonally packed carbon atoms from graphite, was successfully isolated by

Novoselov et al. in 2004. Figure 1 vividly depicts the configuration of a single-atom-thick graphene in relation to other dimensions of carbon materials. The discovery of graphene's incomparable properties, such as high Young's modulus, low white-light adsorption, high electron mobility *etc.*, has completely revolutionized the course of nanotechnology development. It is believed that graphene might substitute silicon in 21st century's semiconducting industry. Significant progress has already been made in areas such as transport devices, optoelectronics, energy generation and storage devices, chemical sensors as well as DNA sequencing. Despite these promising applications, graphene however is a semimetal with no band gap in between valence and conduction bands. In modern semiconducting industry, band gaps are crucial to all logical circuits where field-effect transistors (FETs) are fabricated to have high current on/off ratio in order to reduce its standby power dissipation. Therefore, the practicability of miniaturizing silicon-based electronics to 2D will remain ambitious, unless alternative 2D materials are found.

The persistent search for 2D semiconductors has shed light on a new arena of 2D materials beyond graphene. In recent years, emergent classes of non-graphene-layered compounds include boron nitride, TMDs, hydroxides, and oxychlorides. Nonetheless, only a handful of these layered materials can be referred to as semiconductors, among which a very limited few have been successfully isolated as air-stable and high-quality 2D crystals. The most prominent class of layered materials that can be repeatedly fabricated into atomic layer structures and also proven to have excellent semiconducting capability are the TMDs. In the post-graphene 2D development, TMDs have been the most extensively investigated layered materials in the pursuit of 2D electronic and optoelectronic applications.

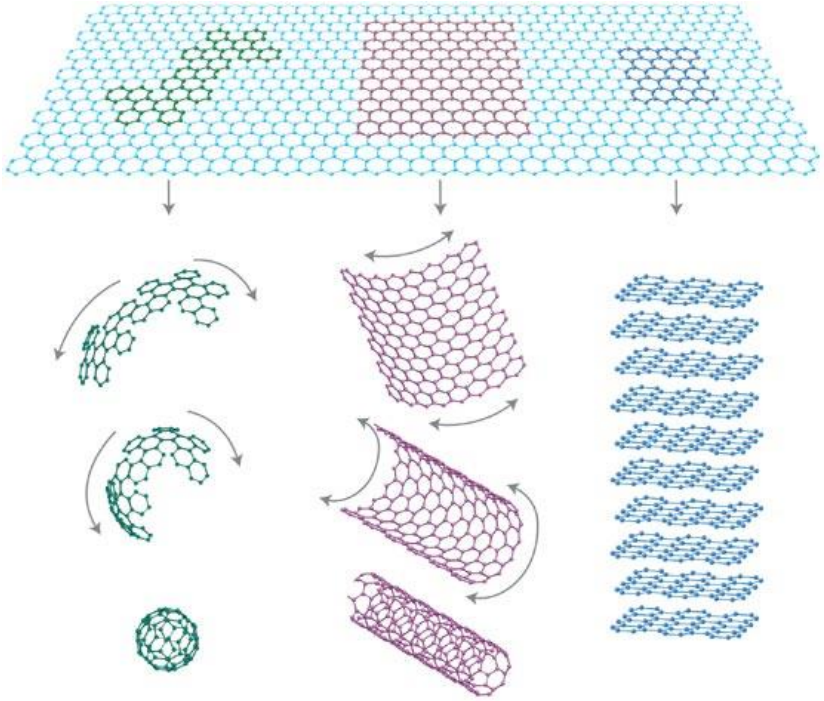

Figure 1. 2D graphene is the building block for carbon materials in all dimensions such as 0D buckyballs, 1D nanotubes and 3D graphite. Reprinted (adapted) with permission from ref.*(1)*, © 2007 Nature Publishing Group.

2.1.2 What are 2D TMDs?

TMD bulk crystals are composed of hexagonal layers of transition metal atoms (M) sandwiched between two layers of chalcogen atoms (X), which renders a stoichiometry of MX_2. Figure 2a shows that changing the combination of these elements can generate more than 40 different TMD compounds, albeit not all provide layered crystalline structures. For example, NiS_2 is demonstrated to have a pyrite structure while $NiTe_2$ is still a layered compound. Group 4-7 TMDs are primarily layered, but group 8-10 TMDs are generally non-layered structures. The majority of layered TMDs are as naturally abundant as graphite. Also, the layered structure of TMDs very much resembles that of graphite but with one exception: a single layer of TMD is of three-atom-thick (X-M-X). These 2D single layers, often referred as monolayers, have a reported thickness of 0.6 to 0.7 nm. They

have strong in-plane covalent bonding while also have a week van der Waals force in between the sandwich layers (figure 2b). Therefore cleavage of such TMD monolayers is easily accomplished by mechanical or chemical exfoliation. Figure 2d shows a typical monolayer TMD (MoS_2) after being successfully separated from its bulk form (figure 2c) *via* mechanical exfoliation and subsequently transferred onto a supporting substrate.

The properties of bulk TMDs are versatile, and so it follows that not all layered TMDs are semiconductors. Non-semiconducting TMDs include insulators such as HfS_2, semi-metals such as WTe_2 and $TiSe_2$, and pure metals such as NbS_2 and VSe_2. At low temperatures, a few bulk TMDs such as $NbSe_2$ and TaS_2 show superconductivity, charge density wave (a periodic distortion of the crystal lattice) and Mott transition (metal to non-metal transition).*(2)* The potent industrial prospect of 2D semiconductors however have brought five particular TMD semiconductors (with band gaps varying from the visible to the near-infrared) under the spotlight; namely MoS_2, WS_2, $MoSe_2$, WSe_2 and $MoTe_2$.*(3)* Notably, chalcogenides of Ti, Sn and Zr have also been reported to be semiconducting but there is no experimental evidence suggesting their suitability reveals for monolayer isolation and device fabrication. On the contrary, the Mo- and W-based chalcogenides have been investigated rigorously in recent years and proven to have convincingly potential in applications of digital electronic devices, energy storage, optoelectronics and chemical sensors.

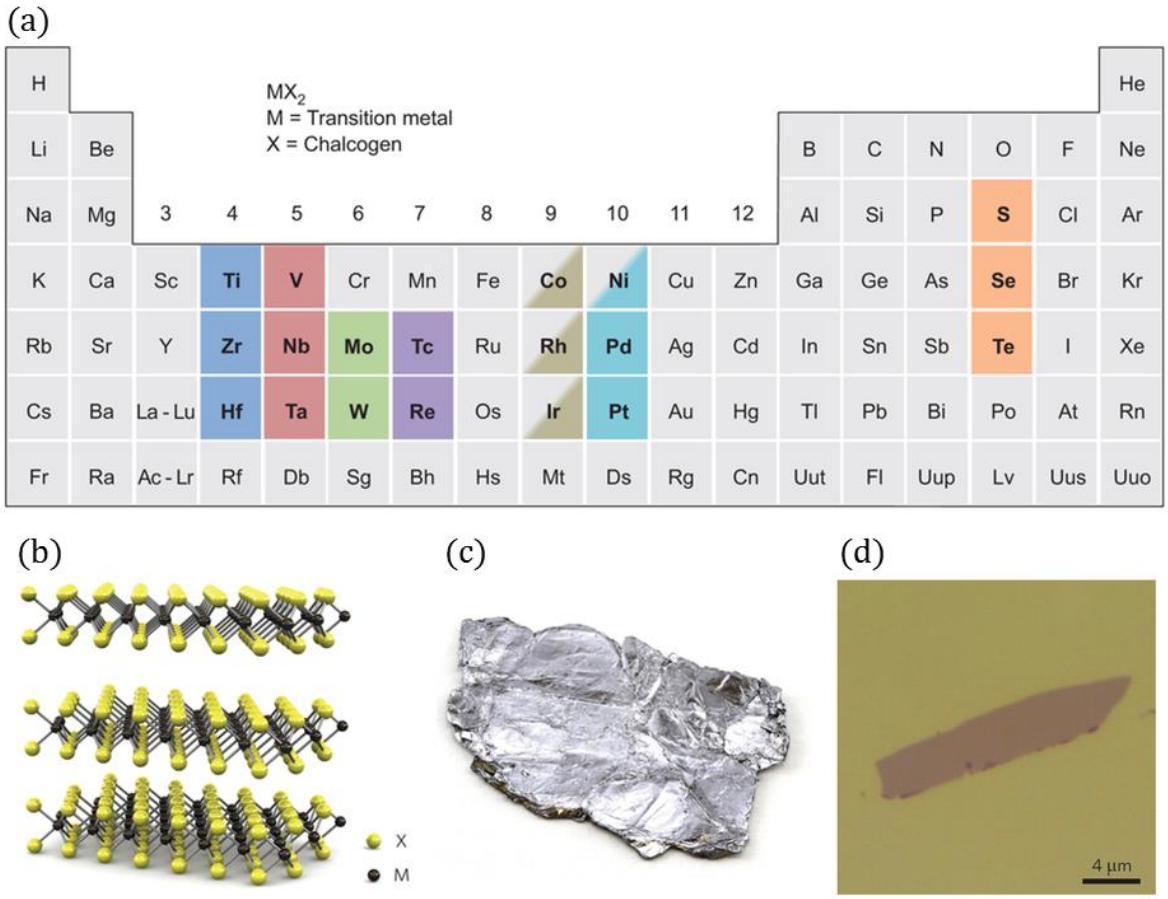

Figure 2. Layered TMDs. (a) Periodic table of colour-highlighted transition metal and chalcogen elements, where full-coloured transition metals can form layered structures with chalcogens while partial-coloured metals (Co, Rh, Ir and Ni) generate some non-layered TMD structures. (b) 3D Schematic of a typical layered TMD structure; the chalcogen (X) and transition metal (M) atoms are shown in yellow and black, respectively. (c) Photograph of a bulk MoS_2 crystal (1 cm long). (d) Optical image of a monolayer MoS_2 flake mechanically exfoliated from the bulk crystal in (c). Figures reprinted (adapted) with permission from: (a), ref.*(2)*, © 2013 Macmillan Publishers Limited; (b), ref.*(4)*, © 2011 Macmillan Publishers Limited; (c), ref.*(5)*, © 2012 Macmillan Publishers Limited; (d), ref.*(6)*, © 2011 IOP Publishing Ltd.

2.1.3 Why is Monolayer WS_2 Important?

The idea of exfoliating TMD crystals for functional purposes did not result from today's zeal for 2D materials, but instead has been sought-after since the 1960s.*(2,7)* Nevertheless, it is because of graphene's discovery that led to a re-initiation of TMD exfoliation with a particular twist towards fabricating higher-quality and monolayer structures.*(7)* Transforming bulk TMDs into monolayers incurs significant changes to the electronic structure of their bulk counterparts, mostly due to altered interlayer coupling, degree of quantum confinement, and symmetry elements in 2D platform.*(2)* Surprisingly, it is found that the effect becomes even more predominant in 2D semiconducting TMDs (*i.e.,* Group 6 chalcogenides, except WTe_2); a transition of band structure from an indirect bandgap in the bulk to a direct bandgap in the monolayer. A direct-bandgap structure allows electrons in semiconducting TMD monolayers to instantly emit photons at corresponding bandgaps, resulting in a conspicuous enhancement of photo- or electroluminescence in comparison with that in indirect-bandgap multilayers. By knowing that 2D materials are atomically thin and mechanically processable, this characteristic enables the application of 2D semiconducting TMDs in areas that were never viable with graphene, such as flexible and transparent optoelectronics.

Sulphur-based MoS_2 and WS_2 are the two most widely recognized 2D direct-bandgap TMDs, owing to their more straightforward and larger-scale synthetic approaches. Selenium- and tellurium-based 2D TMDs are more challenging to produce in large quantities because of the inferior reactivity of Se and Te elements during chemical fabrication.*(8,9)* MoS_2 was the first semiconducting TMD isolated in the monolayer form and immediately gained global attention by demonstrating a high on/off current ratio and ultralow off-state energy dissipation in integrated circuits.*(10)* High-performance transport devices also demonstrated monolayer MoS_2 has carrier motilities of >60 $cm^2V^{-1}s^{-1}$ at room temperature.*(11)* The inherent direct bandgap of monolayer MoS_2 was explored

extensively in its application to ultrasensitive photodetectors,*(12)* phototransistors,*(13)* light-emitting devices.*(14)*

In lieu of MoS_2, monolayer WS_2 has gained its popularity as a result of many promising predictions: i) theoretical models predict that monolayer WS_2 should have the highest mobility amidst the semiconducting 2D TMDs because of its reduced effective mass.*(15)* ii) the spin orbit splitting at the valence band of WS_2 monolayers is considered three times larger than that for MoS_2,*(16)* implicating the formation of explicit spin-valley coupling leading to easier observation of the valley Hall effect.*(17)* iii) monolayer WS_2 was observed to have 20 times higher yield than MoS_2 (exfoliated from natural crystals) in photoluminescence,*(18,19)* which potentially indicates WS_2 optoelectronics are viable to attain higher quantum efficiency. iv) bulk WS_2 is of higher melting point than MoS_2 whereby monolayer WS_2 should be more prone to withstand high-temperature working conditions. On the other hand, the higher melting point has made synthesis of monolayer WS_2 harder to achieve for large-area continuous films,*(20-22)* provided that MoS_2 could have easily over-grown into multi-layered films.*(23-25)* To devise a large-scale synthesis method that produces high-quality monolayer WS_2 films is certainly one of the major hurdles that stop 2D WS_2 from extensive research and future industrial applications. However, it is the result of this that makes this particular area of 2D semiconducting TMDs worthy of a dedicated focus.

2.2 The Properties of Monolayer WS_2 (MoS_2)

None of the characterisation techniques and industrial applications are meaningful unless we first address what physical properties have made monolayer WS_2 so unique in 2D materials. More-than-a-decade of devotion to graphene development has already laid a solid foundation for understanding 2D TMD characteristics. In this section, new 2D semiconducting behaviour deserves a particular focus through the lens of monolayer WS_2

research. As of carrying out this project, the amount of research carried on WS_2 was still primitive compared to MoS_2. In discussion, monolayer MoS_2 will be occasionally employed for demonstration and prediction purposes as the result of their high similarity in crystal configuration. Theoretical models and experimental findings, reported in published articles, will be introduced to help demonstrate crystalline, electronic as well as optical features of monolayer WS_2 that are germane to latter chapters.

2.2.1 Crystal Structure

In terms of crystal structure, monolayer WS_2 (MoS_2) is more complex than graphene due to its additional atomic layers and element. However, it is this complexity that made 2D TMDs transcend the limits of graphene and paved the path towards 2D semiconducting applications. The versatility of the S-W-S bond structuring has been the origin of many important properties and effects that will interweave the remaining body of this thesis.

2.2.1.1 Crystal Phases

Unlike graphite, bulky WS_2 embodies a wide variety of polymorphs and stacking polytypes, owing to the constitution of monolayer WS_2 – a W atomic layer sandwiched in between two S layers (S-W-S) providing an experimental thickness of 0.8~1 nm.*(19,21,26)* Figures 3a and b demonstrate monolayer WS_2 itself can either be trigonal prismatic (AbA stacking, the capital and lower case letters symbolize sulphur and tungsten atoms, respectively) or octahedral (AbC stacking) W-coordinated. Preference on either one of the two coordination modes is totally dependent on the thermodynamic combination of W and S elements.*(2)* In bulk TMDs, polymorphous phases are commonly found in 1T, 2H and 3R, where each number represents the number of X-M-X units in one unit cell, and the letters account for trigonal, hexagonal and rhombohedral symmetry, respectively (figure 3c). A

2H polymorph can provide another three different polytypes as the result of different X-M-X stacking sequences (*i.e.,* AbA-AbA, AbC-AbC and AbA-AbC). Predicting these structural symmetries or stacking orders for a bulk WS_2 is extremely complicated, which fortunately is beyond the scope of this thesis. In a 2D platform, the monolayer WS_2 will only exhibit two polymorphs (excluding any polytypes): trigonal prismatic (1H) and octahedral phases (1T).

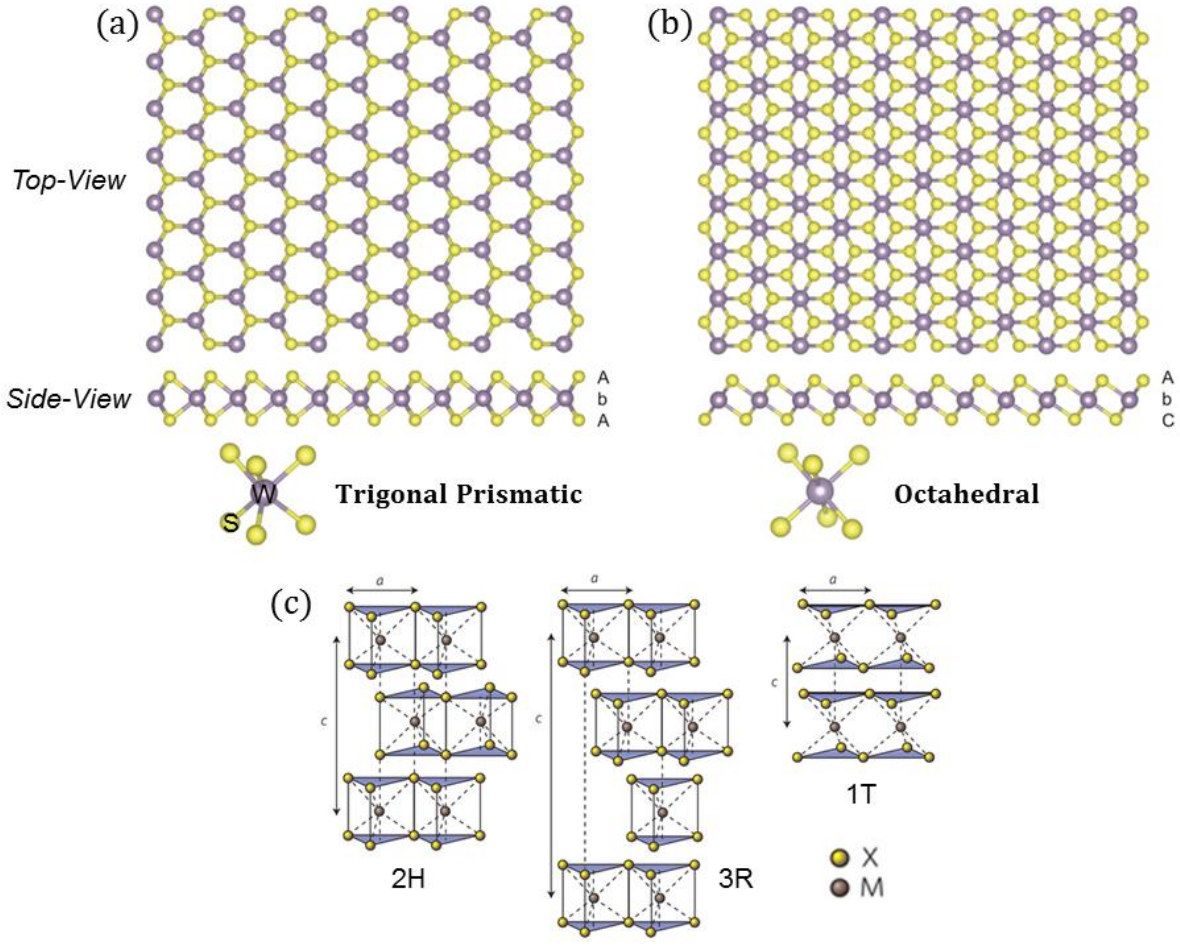

Figure 3. Crystalline structure of 2D layered TMDs (WS_2). (a) and (b) Top- and side-view of monolayer WS_2 (or other layered TMDs) atomic models for trigonal prismatic (a) and octahedral (b) W-coordination in lattice. Tungsten (W) and sulphur (S) are colour-coded in purple and yellow, respectively. The labelling of AbA and AbC indicates the stacking sequence where the upper- and lower-case letters denote S and W elements, respectively. (c) Atomic models for the structural polytypes: 2H, 3R and 1T; the number represents layer number repeating unit while the letter means hexagonal, rhombohedral, and tetragonal symmetry, respectively. In each layer, 2H, 3R and

1T are, respectively, trigonal prismatic, trigonal prismatic and octahedral W-coordinated. M and X symbolize transition metals and chalcogens, respectively. The lattice constant and the stacking index (number of layers in each stacking order) are labelled in 'a' and 'c', respectively. Figures reprinted (adapted) with permission from: (a) and (b), ref.*(2)*, © 2013 Macmillan Publishers Limited; (c), ref.*(5)*, © 2012 Macmillan Publishers Limited.

2.2.1.2 Grain Boundaries (GBs)

A GB in 2D materials is the interface formed in between two 2D single crystals with distinct crystal orientations. It is hence prevalent in polycrystalline materials and considered as crystalline defects that are inclined to diminish electrical and thermal conductivity in 2D transport devices. For graphene, chemical vapour deposition (CVD) was developed to facilitate its large-scale synthesis, though as-produced polycrystalline films have been troublesome for many electrical *(27,28)* and mechanical applications.*(29)* In the synthesis of such polycrystalline graphene, graphene single crystals or domains simultaneously nucleate at random locations and orientations, whereby GBs are produced as domains continue to grow interconnected. To avoid GBs in industrial application is already renowned in the field of Si-based electronics, where large single-crystal Si wafers are obtained in high-quality.*(30)* In order to compete with Si in device applications, controllable synthesis of large-scale single crystalline graphene or techniques of eluding GBs in device fabrication has been desired,*(31-34)* as well as beneficial to new emergent 2D TMDs.

Crystalline structures in monolayer semiconducting TMDs are of high resemblance.*(35-37)* Hence GB structure of monolayer MoS_2 can well serve as an analogy to that of monolayer WS_2. With the help of scanning transmission electron microscopy (STEM), the atomic configuration of a long-range MoS_2 GB is unveiled in figure 4a. GBs are easily characterized at atomic scale when a line of distorted crystalline structures is observed. A

pristine 1H-phase TMD monolayer should consist of repeating 6-membered rings from the top-view (figure 3a). However, it was proposed by van der Zande *et al.* that the misorientation of two monolayer MoS_2 crystals at GB interface incurred formation of repeating defected structures such as 8-4-4 membered rings (Figure 4b and c).*(36)* In contrast to graphene, electron transport ability (conductance) measured across these MoS_2 GBs has shown no significant variation from those done in pristine (single crystalline) regions. In this work, the variation of conductance from any measured GBs was only marginally higher than the device-to-device variation.*(36)*

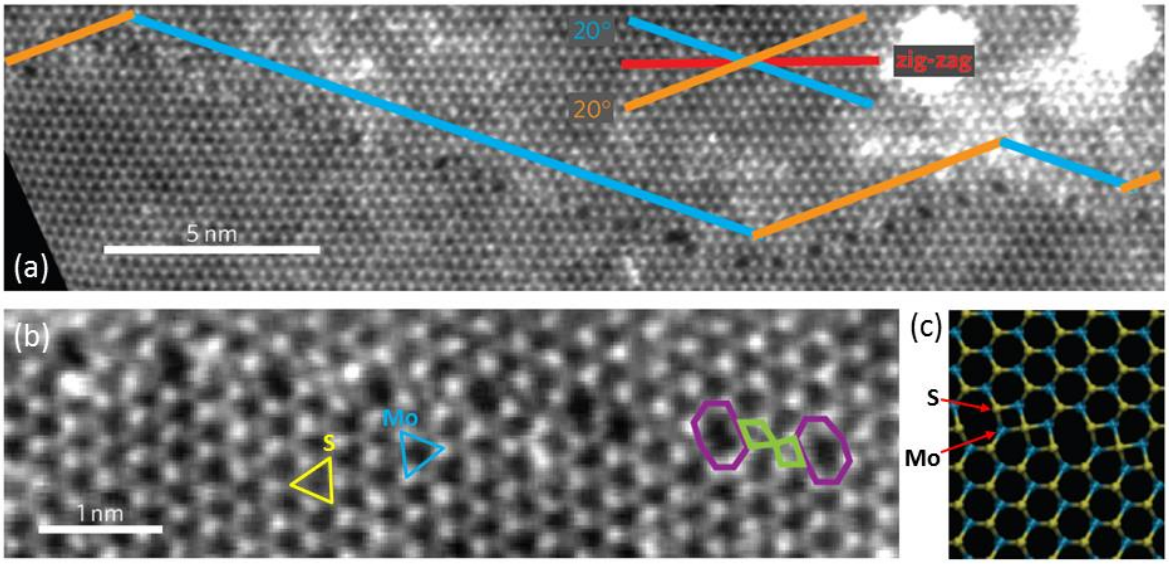

Figure 4. Atomic structure of monolayer MoS_2 GBs. (a) High-resolution (angular dark field) ADF-STEM image of a typical GB at ±20º to the zigzag lattice direction. (b) Selected grain-boundary area of (a) exhibiting a repeating unit of 8-4-4-membered ring along the GB. Sulphur and molybdenum atoms are highlighted in yellow and blue, respectively. (c) Atomic model of the GB structure visualized in (b). Figures reprinted (adapted) with permission from: (a)-(c), ref.*(36)*, © 2013 Macmillan Publishers Limited.

Although STEM can clearly unveil the atomic structure of GBs in 2D materials, it remains challenging to gain insight into the distribution of GBs in a particular crystal domain or a

film, due to confined nanoscale size of the imaging window. In figure 5, Zhang *et al.* successfully imaged overall GB distribution in different configurations of as-grown WS_2 monolayer domain using scanning electron microscopy (SEM).*(26)* In this study, monolayer WS_2 domains were synthesized by CVD and then were mildly oxidized in air to allow the GB imaging. Revealing the WS_2 GBs at this complete domain-scale is an advantage for the understanding of CVD-grown domain configuration and material quality (GB defects), and is useful for screening for further device fabrication.

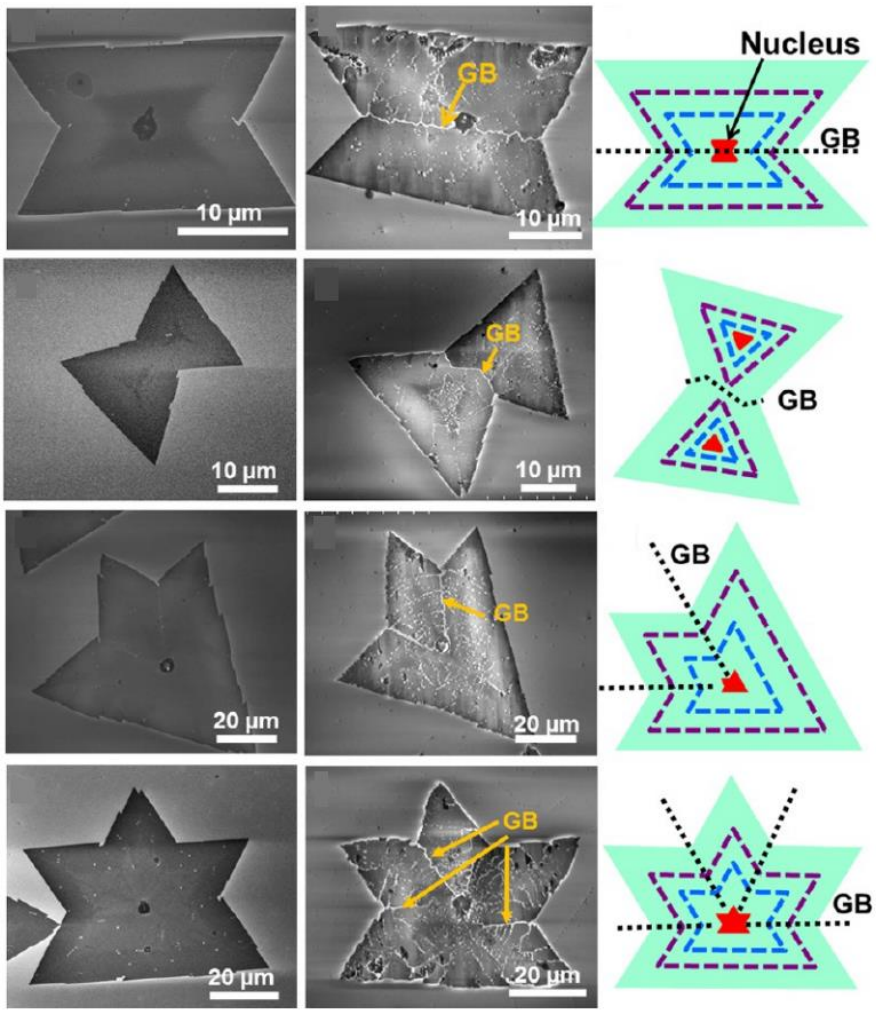

Figure 5. GBs of monolayer WS_2 domains introduced by CVD are revealed under SEM due to mild (atmospheric) oxidation. Left to right columns are, respectively, SEM images of as-grown monolayer WS_2 domains, SEM images of mildly oxidized monolayer WS_2 domains, and schematics of monolayer WS_2 domain configurations derived from the revealed GB locations. Reprinted (adapted) with permission from ref.*(26)*, © 2013 American Chemical Society.

2.2.2 Electronic Properties

It is already widely known that graphene provides an extraordinary high carrier mobility exceeding 10^6 $cm^2V^{-1}s^{-1}$ at 2K,*(38)* while at room temperature surpassing 10^5 $cm^2V^{-1}s^{-1}$ when between BN dielectric layers.*(39)* However, as previously mentioned, graphene is not suitable for modern electronics unless it attains a bandgap. Effort has been paid to bandgap engineering of graphene using nanostructuring,*(40,41)* chemical functionalization *(42)* and application of a high electric field to bilayer graphene,*(43)* all which compromise graphene's mobility and complicate the device fabrication process. Herein, monolayer WS_2 plays an essential role because it naturally provides a tunable direct bandgap, reopening opportunities for 2D logic circuits and bringing new possibilities to optoelectronic devices.

2.2.2.1 Band Structure

The band structure physics in monolayers is basically the same for semiconducting MoS_2, WS_2, $MoSe_2$ and WSe_2.*(17)* Here, we first take the extensively researched MoS_2 as an example. Band structures are calculated from first principles density functional theory (DFT) to gain insight into the influence of low-dimension quantum confinement. Figure 6 provides an evolution of band structures from bulk to monolayer MoS_2, calculated using DFT/PBE functional.*(44)* A fundamental indirect bandgap (arrows in figure 6b) derives from the energy required for transition of electrons from the top of valence band at the Γ point of the Brillouin zone to the bottom of conduction band halfway between Γ and K at the T symmetry point (figure 6a). The optical direct bandgap is located at K point in bulk MoS_2. In figure 6b, the indirect bandgap increases with reduction of MoS_2 layers, starting from 1.2 eV in bulk to the point (1.9 eV) that the conduction band at the T point is no longer the lowest in monolayers. As the conduction band at K almost remains independent of the MoS_2 thickness variation, the bottom of the conduction band in

monolayers inherently becomes situated at the point that is the optical direct bandgap from bulk MoS_2. Thus the value of direct bandgap in monolayer MoS_2 will be in close proximity to the optical direct bandgap observed in bulk MoS_2.

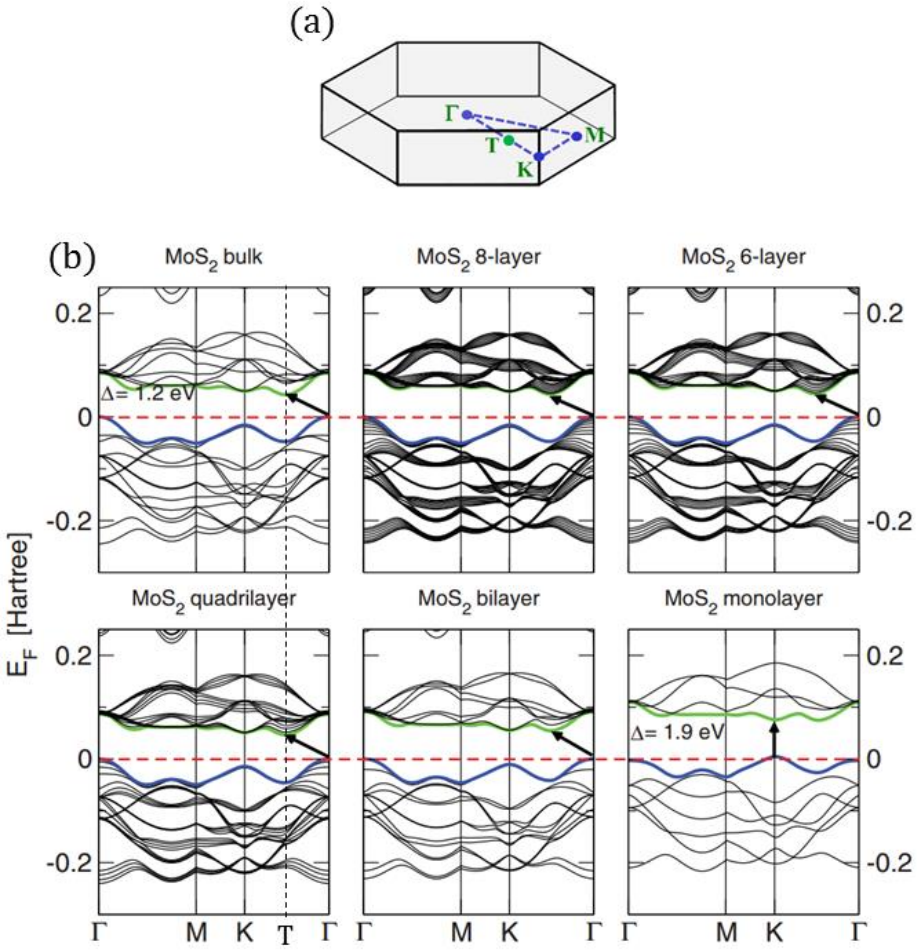

Figure 6. Electronic structure of MoS_2. (a) 2D hexagonal Brillouin zone for monolayer MoS_2 (or WS_2). (b) Band structures of MoS_2 from bulk to its monolayer, calculated at the DFT/PBE level (*i.e.,* general gradient approximation (GGA) used in the scheme of PBE (Perdew-Burke-Ernzerhof) *(44)*). The horizontal red dashed lines are the Fermi level. The arrows highlight the direct or indirect transitions. The valence band maxima and conduction band minima are coloured in blue and green, respectively. Figures reprinted (adapted) with permission from: (a), ref.*(19)*, © 2013 American Chemical Society; (b), ref.*(45)*, © 2011 American Physical Society.

The indirect- to direct-bandgap transition due to the quantum size effect is also a salient feature in WS_2, as presented in figure 7. To a first-order approximation, the band structure of WS_2 consists of partially filled W d-orbitals sandwiched between W-S s-p bonding and antibonding orbitals.*(46)* For a trigonal prismatic W-coordination, the d-orbital can split into three groups: A_1(d_{z^2}), E($d_{xy}, d_{x^2}-d_{y^2}$) and E'(d_{xz}, d_{yz}).*(17)* Nonetheless, in the monolayer confinement, only A_1 and E hybridization are viable due to the reflection symmetry in the $\bar{z}$ direction.

It is theoretically calculated that bulk WS_2 has an indirect bandgap of 1.3 eV, whereas monolayer WS_2 renders an optical direct bandgap of 2.05 to 2.1eV in visible (red) frequency range.*(19,45)* In bulk WS_2, conduction-band states at the T point result from linear hybridization of tungsten d-orbitals and antibonding sulphur p_z-orbitals, which have interlayer-coupling and hence are susceptible to the number of WS_2 layers. However, conduction-band states at the K point are solely due to localized d-orbitals on the tungsten atoms, located in the middle of S-W-S sandwich structure, and are relatively unaffected by interlayer coupling (insensitive to layer number).*(19)* Therefore, a direct bandgap from monolayer WS_2 is accomplished when the electronics states between indirect transition becomes so apart that the transition becomes preferable through the invariant states at K.

Additionally, it is worth mentioning that there is a small difference in valence band between bulk and monolayer WS_2 at the K point. Figure 7a clearly exhibits the splitting of the valence band in bulk WS_2 that leads to two distinct direct electronic transitions (A and B) at the K point. They have been experimentally observed by absorption spectroscopy, and widely known as excitons A at 1.95 eV and B at 2.36 eV.*(47-49)* On the other hand, monolayer WS_2 does not yield the splitting, allowing only one direct electronic transition that is observable through optical spectroscopy.*(19)* The valence-band splitting at K points in bulk WS_2 is the consequence of interlayer coupling that is absent in monolayers.*(46)*

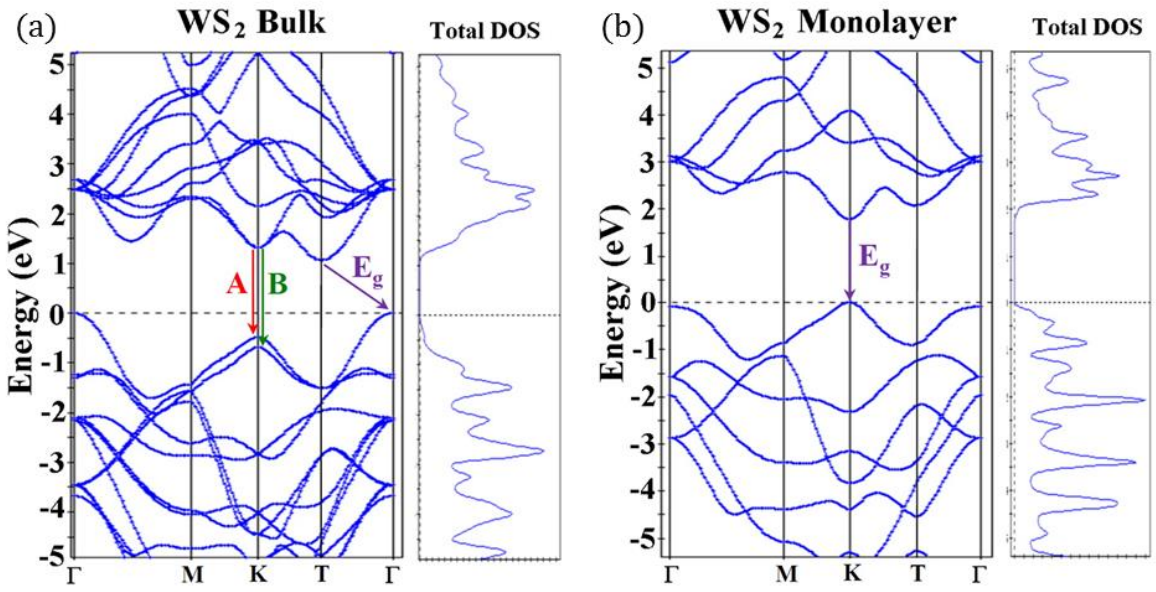

Figure 7. Band Structure of WS_2. (a) and (b) Electronic band structure (left) and total density of states (right) for, respectively, the bulk and monolayer WS_2. Figures reprinted (adapted) with permission from: (a) and (b), ref.*(19)*, © 2013 American Chemical Society.

2.2.2.2 The Spin-Valley Coupling

According to figures 6 and 7, the edges of conduction and valence bands in monolayer MoS_2 or WS_2 are situated at the K point of the 2D hexagonal Brillouin zone. The creation of these two distinct and distant valley systems gives possible access to the implementation of valley index as a potential information carrier in valleytronics. The valley index represents the confinement of electrons or holes in distinct conduction-band minima or valence-band maxima at the same energies (K point) but different positions in momentum space.*(5)* In an effort to controllably manipulate the valley index, graphene, with its inherent K (-K) valleys, have been considered theoretically for the application of valleytronics.*(50,51)* Graphene valleytronics require the breaking of its inversion symmetry, the feasibility of which is yet to be confirmed experimentally. Monolayer TMD semiconductors (MoS_2, $MoSe_2$, WS_2 and WSe_2), on the other hand, could be more

suitable for the task, due to their direct-bandgaps and graphene-like structures.*(17)* Inversion symmetry is clearly broken in above TMD monolayers, which has led to observation of the valley Hall effect *(50)* and creation of a spin-dependent optical selection rule for interband transitions.*(51)* Moreover, semiconducting TMDs such as MoS_2 consist of heavy metal atoms at d-orbital, giving rise to giant spin-orbit splitting *(16)* deemed unrealistic in graphene.*(52)* Recently, it has been experimentally proposed that monolayer semiconducting TMDs are suitable candidates for valleytronics. *(53-56)*

In contrast to the valence-band splitting in bulk WS_2 (figure 7a), the valence-band spin splitting at K points is however the cause of spin-orbit coupling and inversion symmetry breaking in monolayer WS_2, though they are in comparable splitting sizes. The inversion symmetry and time-reversal symmetry prevent bulk or multilayers from adapting spin splitting at K points. Figure 8a schematically depicts the spin splitting between valence-band valleys at K and –K points of a monolayer Brillouin zone; meanwhile it highlights the spin splitting at different valleys must be in opposite direction. The wave functions that extrapolate the K-point valley edges are *(17)*

$$|\emptyset_c\rangle = |d_{z^2}\rangle, \qquad |\emptyset_v^{\tau}\rangle = \frac{1}{\sqrt{2}}\left(\left|d_{x^2-y^2}\right\rangle + i\tau\left|d_{xy}\right\rangle\right), \qquad Equation\ 2.1$$

where the subscript c, v indicates conduction and valence band, respectively; τ is the valley index equivalent to spin-up (+1) or spin-down (-1); $|\emptyset_v^{\tau}\rangle$ is the valence-band wave functions at the two valleys (figure 8a), $|\emptyset_v^{+}\rangle$ and $|\emptyset_v^{-}\rangle$ are related in time-reversal symmetry.

The valence-band spins and valleys are inherently coupled in monolayer semiconducting TMDs with opposite intravalley or intervalley spin momenta, as shown in figure 8b. Between the valence-band maxima the splitting of contrasting valley spins is quantified to be 148, 183, 426, and 456 meV for monolayer MoS_2, $MoSe_2$, WS_2, and WSe_2, respectively.*(16)* This abrupt change in spin splitting size of W-based monolayers results

from that fact that the spin-orbit coupling is stronger for heavier metals. The massive spin separation, as in WS_2, can better avert spin degeneracy (disable valley-spin flipping) and hence leads to long valley-spin lifetime. What is more, figure 8b also denotes two band-edge excitonic transition frequencies (ω_d and ω_u) coupled with spin momenta, which implies the possibility of addressing different valleys by controlling the photon angular momentum, in other words, by the helicity (circular polarization sate) of light.*(53)* The giant spin-valley coupling of monolayer WS_2 offers a more promising strategy to control carrier spin and promotes the development of high-performance valley-based electronics and optoelectronics.

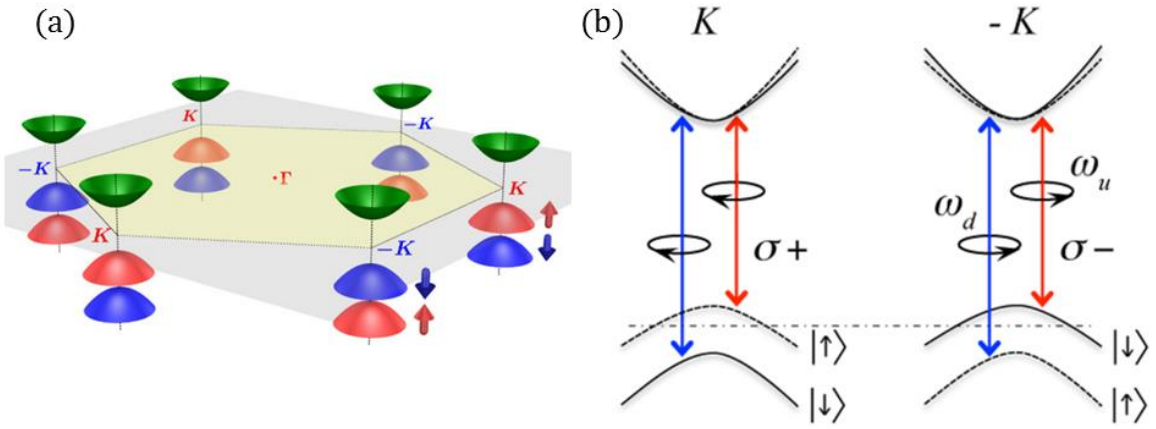

Figure 8. Spin-valley interaction in 2D TMD semiconductors. (a) Schematic of the 2D-TMD band structure at the K-point band edges. (b) Valley/spin optical transition selection rules, where solid and dashed curves are bands accredited, respectively, with spin-down and spin-up at the out-of-plane direction; ω_d and ω_u are, respectively, the transition frequencies from the two split valence-band maxima to the conduction-band minimum. Figures reprinted (adapted) with permission from: (a) and (b), ref.*(17)*, © 2012 American Physical Society.

2.2.2.3 Carrier Mobility

Conductivity is proportional to the product of carrier mobility and density. Both carrier mobility and carrier density will therefore determine the conductivity of a semiconducting

material. Upon applied voltage, a low conductivity semiconductor (low carrier mobility or density) increases the power dissipation of its corresponding electronic device, hence endangering the electronic device performance. In monolayer TMDs, transport and scattering of electron/hole carriers are confined to the 2D plane of the material. The mobility of carriers is commonly subjected to the following intrinsic mechanisms: i) Coulomb scattering at charged impurities; ii) acoustic and optical phonon scattering; iii) roughness scattering; iv) surface interface phonon scattering.*(57,58)* The majority of these mechanisms are also encountered in graphene devices.*(59)* To what extent these mechanisms affect the carrier mobility is totally dependent on carrier density, temperature, layer thickness, effective carrier mass, electronic band structure and phonon band structure.*(5)*

Coulomb scattering is the dominant scattering effect for graphene *(60)* as well as 2D TMDs at low temperatures. The scattering originates from randomly charged impurities located within or on a monolayer, which are commonly introduced by synthetic processing or impurity doping for tuning carrier concentration and bandgap. Hence the degree of doping level sometimes has to be compromised in order to fulfil high-mobility device performance at low temperatures. Figure 9a denotes the correlation between carrier density and carrier mobility in monolayer MoS_2 at decreasing temperatures. Despite increasing device carrier density by impurity doping the carrier mobility does not decrease significantly, but it does become more prominent when temperature is reduced down to 100K, as result of Coulomb scattering.

At higher temperatures, phonon scattering becomes the governing factor that influences carrier mobility in 2D TMDs.*(61)* High temperatures can lead to deformation of 2D TMDs where metal and chalcogen atoms are partially ionic bonded. The deformation incurs polarized fields within ionic bonding that can interact with and scatter electrons.*(5)* By first-principle calculations, the temperature dependence of electron mobility in monolayer MoS_2 was predicted in figure 9b. In the plots, the mobility variation as a function of temperature

splits into three causes: acoustic phonon scattering, total effect of acoustic and optical phonon scattering and the effect of quenching out-of-plane homopolar mode. In reference to the acoustic plot, it is apparent that the acoustic element dictates the mobility at low temperatures (T < 100K), whereas at higher temperatures the optical element becomes dominant. The quenching element, usually owing to top-gated device design, will play only a minor effect to the increasing mobility. As a result of figure 9a and b, the carrier mobility of 2D-TMD field-effect transistors (FETs) will be significantly undermined under room-temperature conditions. Overall, the joint effect of phonons and charged impurities on the mobility of monolayer MoS_2 can be further ascertained by a similar trend attained from multilayer MoS_2, shown in figure 9c.*(5)*

Additionally, surface phonon scattering and roughness scattering are also worth noting in such ultra-thin 2D materials. Graphene devices fabricated on dielectric SiO_2 experience surface polar phonon scattering;*(59)* meanwhile the ruling scattering in suspended graphene results from out-of-plane flexural phonons.*(62)* Interfacial roughness scattering was found to be dominant in GaAs based quantum wells.*(63)* However, in graphene, Coulomb scattering overwhelms short-range (defects or dislocations) and surface roughness scattering (ripples).*(64)* Similar ripples were also discovered in free standing MoS_2,*(65)* implying that either of these scattering mechanisms may have a minor contribution towards 2D-semiconducting-TMD FETs fabricated on SiO_2.

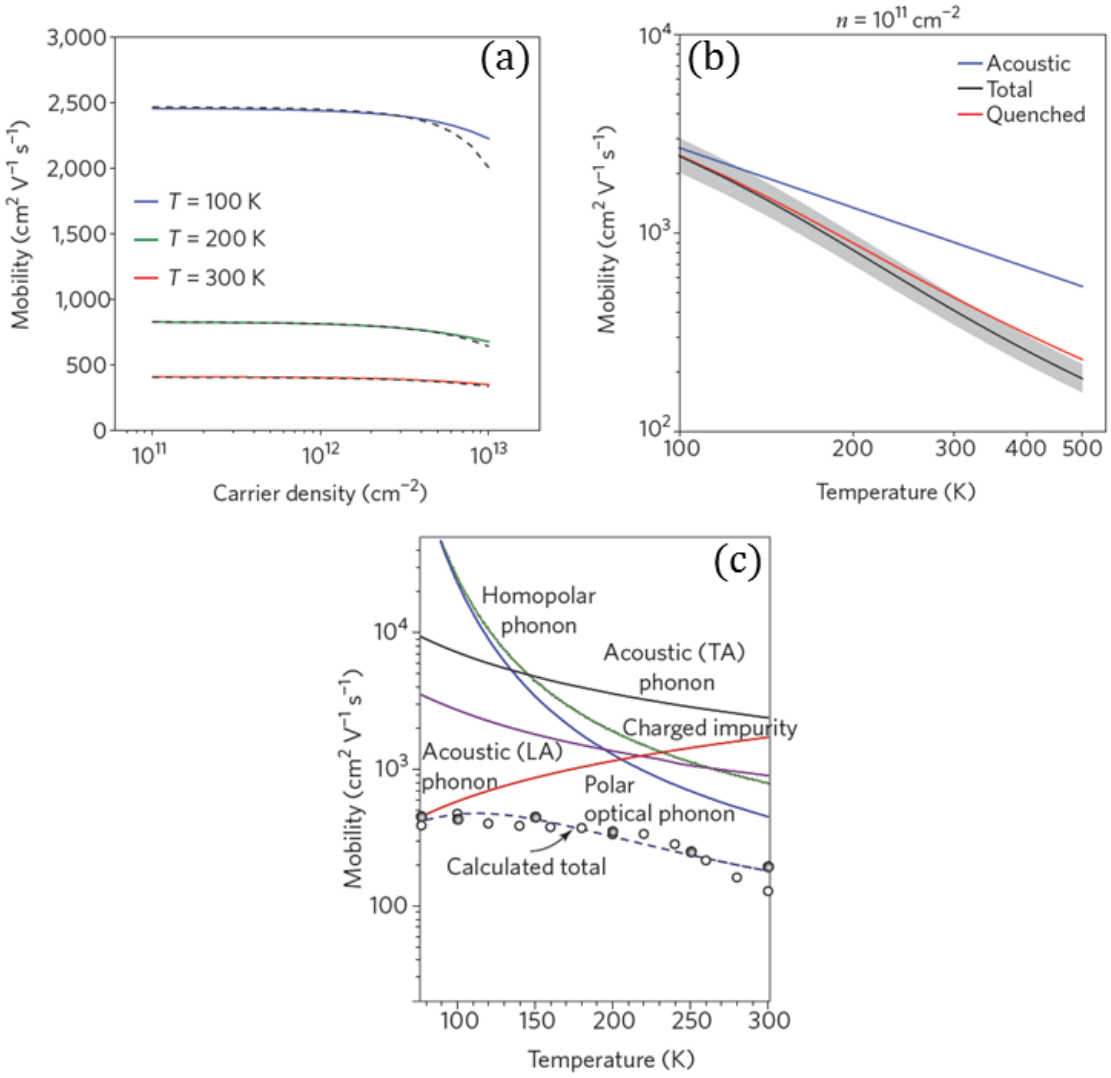

Figure 9. Intrinsic properties of carrier transport in semiconducting 2D TMDs. (a) and (b) The influence of carrier density (a) and temperature (b) on the carrier mobility of monolayer MoS_2, as a result of the first-principle DFT calculations for the electronic band structure, phonon dispersion and electron-phonon interactions. Grey band in (b) emphasizes the uncertainty in calculated mobility values. (c) Carrier mobility in multilayer MoS_2 as a function of temperature, explicitly demonstrating the scattering contributions from charged impurities (red), homopolar phonons (green) and polar-optical phonons (blue), all of which combined to provide the total mobility (dashed line). Figures reprinted (adapted) with permission from: (a) and (b), ref.*(61)* , © 2012 American Physical Society; (c), ref.*(66)*, © 2012 Macmillan Publishers Limited.

In an as-prepared FET, the carrier mobility can be calculated using the equation below,

$$\mu = \left[\frac{dI_{ds}}{dV_{bg}}\right] \times \left[\frac{L}{WC_iV_{ds}}\right], \qquad C_i = \frac{\varepsilon_0\varepsilon_r}{d}, \qquad Equation\ 2.2$$

where μ is the carrier mobility, I_{ds} is source-drain current, V_{bg} is back-gate voltage, L is the channel length, W is the channel width, C_i is the capacitance between the channel and the back gate per unit area, V_{ds} is source-drain voltage, ε_0 is the electric constant, ε_r is the dielectric constant, and d is thickness of dielectric layer.

Figure 10a and b recapitulate the carrier mobility values of monolayer/multilayer MoS_2 and WS_2 determined in 2D TMD electronic devices. The majority of values presented here are electron mobilities owing to the fact that exfoliation and chemical synthesis of these materials preferably render n-type semiconductors. In figure 10a, the electron mobility values of monolayer MoS_2 are widely scattered over the span of 3 orders of magnitude (1-1000 $cm^2V^{-1}s^{-1}$), and are categorized by substrates, measurement temperatures, synthetic approaches and other measurement conditions. The wide-ranging variation of mobility values indicates that device performance of monolayer MoS_2 is considerably susceptible to as-synthesized material quality, measurement conditions, developing process and device configuration. It is not difficult to realize that low-temperature devices are prone to providing slightly higher electron mobility than those carried at higher temperatures. These experimental results agree well with the aforementioned theoretical predictions, where phonon scattering is the dominating effect on mobility reduction at high temperatures (figure 9b). Furthermore, there is no clear mobility discrepancy between devices based on CVD-grown MoS_2 and those employing exfoliated MoS_2 at room-temperature (*i.e.,* an exceptional few of exfoliated ones are about an order of magnitude higher than those CVD-grown), however, note that electron mobilities above >100 $cm^2V^{-1}s^{-1}$ are mostly obtained from exfoliated monolayer MoS_2 at low temperatures. In the case of graphene, carrier mobilities in mechanically exfoliated or single crystalline graphene have shown significantly superior to that in CVD-grown graphene, largely due to polycrystalline

effects.*(27,28,32,67)* It may be reasonable to postulate that the presence of GBs can have a minor effect on charge transport devices based on CVD-grown TMD monolayers.

Monolayer WS_2 was only realized after the success in exploiting monolayer MoS_2. Due to more critical conditions required by CVD synthesis of monolayer WS_2, mechanical exfoliation still remains as a more preferable method for device fabrication of WS_2 mono- to multi-layers. Figure 10b shows electron mobilities of exfoliated monolayer WS_2 ranging from <1 to 140 $cm^2V^{-1}s^{-1}$,*(68-70)* where the application of hexagonal boron nitride (h-BN) substrate (instead of SiO_2) has successfully enhanced electron mobility at room-temperature.*(69)* Figure 10c unveils the correlation between carrier mobilities and the bandgaps of semiconducting TMDs accompanied by conventional semiconductors and 2D materials including graphene and black phosphorous. At similar bandgap sizes, semiconducting TMDs are of lower carrier mobilities as against conventional semiconductors such as bulk InP and bulk GaAs. Among monolayer TMDs, WS_2 shares similar carrier mobilities with MoS_2 and $MoSe_2$, where all three rank the lowest in the contest of semiconducting materials.

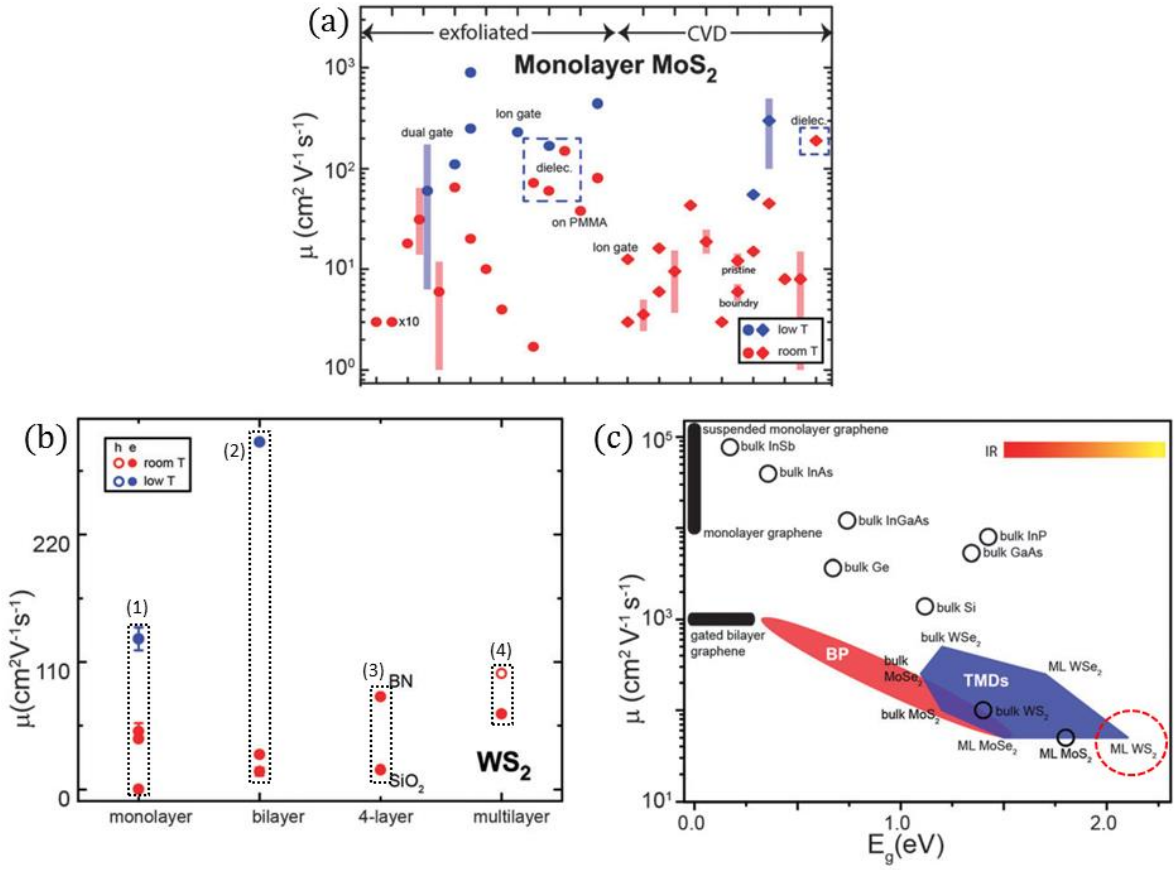

Figure 10. Carrier mobility values reported thus far for MoS_2 and WS_2. (a) Room-/low-temperature carrier mobility values reported for monolayer MoS_2 synthesized using exfoliation and CVD methods. (b) Carrier mobility values reported for mono-layer to few-layer WS_2 at room-/low-temperatures, where (1)-(4) is from ref.*(68-70)*, ref.*(68, 70)*, ref.*(69)* and ref.*(71)*, respectively. (b) Demonstration of mobility vs. band gap in various 2D semiconductors (BP = black phosphorus; ML = monolayer). The colour scale (top right) represents the infrared (IR)-visible light range corresponding to the bandgap energy. Figures reprinted (adapted) with permission from: (a)-(c), ref.*(72)*, © The Royal Society of Chemistry 2015.

2.2.3 Electron-Hole Recombination

The electronic band structures described earlier implies excellent accessibility of exploring optical properties of 2D TMD semiconductors with the help of external energies.

Photoluminescence (PL) is an excellent example in this category and is deemed the foundation for understanding 2D TMD's applications such as photodetectors, light-emitting devices, photovoltaics or opto-valleytronics. It is therefore of great necessity to reveal the mechanism of electron-hole interactions in monolayer WS_2 before picturing its optical applications or characterisations in the following sections.

In 2D semiconducting TMDs, the spatial confinement of carriers and the reduction of dielectric screening have enhanced Coulomb interactions between holes and electrons, giving rise to giant electron-hole binding energy at room temperature.*(73-77)* Upon apposite photonic excitation, excitons (*i.e.,* a bound state of one electron and one hole) in the direct-bandgap monolayer are tightly bound, recombining to provide robust PL at corresponding optical bandgap (figure 11a). On the other hand, PL intensity in bilayer is greatly compromised due to the direct-to-indirect transition of the band structure, as shown in figure 11a (right). In monolayer MoS_2, the exciton binding energy is calculated to be 0.897 eV.*(73)* Hence PL quantum yield of monolayer MoS_2 was found to be 10^4 times higher than that of bulk MoS_2.*(78)* In fact, the overall quantum yield obtained so far in monolayer MoS_2 is only 0.4%,*(78)* manifesting a significant underperformance compared to common direct-bandgap semiconductors with near-unity values. Although the quantum yield can be moderately improved in suspended samples *(78)* or samples left on h-BN substrates,*(53)* understanding the PL quenching mechanisms in monolayer MoS_2 is desired for its future optoelectronic applications.

Figure 11b elucidates that, in general, the production of PL from monolayer TMD semiconductors is accredited to three possible optical transitions: A exciton, B exciton and A-/A+ trion (*i.e.,* a bound state of either two electrons and one hole or two holes and one electron). In monolayer WS_2, the room-temperature A-excitonic recombination generates light-emission at photon energies ranging from 1.94 eV~2.02 eV,*(18-20,26,79-82)* depending on photonic excitation energy, used synthesis approach as well as point of interest in the sample. It is reasonable that the experimental PL emitting bandgap is

always found slightly lower than the calculated optical bandgap (~2.05 eV), given the fact that direct optical transition essentially occurs at lower density states than conduction-band minima owing to the excitonic relaxation (dashed line in figure 11b).*(19)* Moreover, the B-exciton component, which is found notably next to A-exciton in monolayer MoS_2, has not been identified likewise in the PL of monolayer WS_2, *(80,83,84)* largely due to the greater valence-band-spin splitting in monolayer WS_2 (section 2.2.2.2). As specified in figure 11b, a negatively charged trion is formed at lower density states of the direct bandgap compared to A/B exciton, so its contribution to PL in 2D semiconductors will manifest at photon energies smaller than the A-exciton gap.*(9,80,85,86)* The giant spin splitting in the valence band also enabled frequent observation of negatively charged A^- trions instead of A^+ in monolayer MoS_2, which is also the case in monolayer WS_2 with A^- trion binding energy from 40 to 62 meV.*(87-89)* In an effective system of excitonic recombination, trionic recombination only plays a minor or sometimes indistinguishable contribution to the PL in monolayer WS_2. To observe prominent effect of A^- trions in PL, monolayer WS_2 will have to undergo one of the following: impurity doping *(80,82)*, mechanical strain *(90)* and low-temperature treatment.*(91)*

In monolayer WS_2, the exciton binding energy of the band-edge excitons around the K valley in the Brillouin zone was discovered to be as high as 0.71 ± 0.01 eV, which accounts for a third of its direct optical bandgap.*(92)* Due to this WS_2 monolayers ought to render strong PL intensity, attributed to the efficient direct recombination of A-excitons at the K-point (figure 7). Figure 11c shows the PL intensity of monolayer WS_2 can be ~200 times higher than that of bilayer WS_2. The B-exciton feature would only gain its negligible influence on PL as layer thickness gradually increases (figure 11d).*(18, 19)* Furthermore, monolayer WS_2 is capable of ~ 6% PL quantum yield, considerably higher than the rest of 2D semiconducting TMDs.*(93)*

Many-body interaction is especially prominent in 2D materials. Hence, the high density of excitons produced by optical excitation can easily incur a many-body scattering process,

engendering non-radiative relaxation of excitons. For example, non-radiative exciton-exciton annihilation is found in 2D semiconducting TMDs, portrayed in figure 11a.*(94-98)* In WS_2, monolayers are of higher exciton-exciton annihilation rate than few-layers by two orders of magnitude, largely owing to enhanced electron-hole interaction in 2D as well as the non-phonon assisted (direct-bandgap-induced) electron-electron annihilation.*(93)* The PL quantum yield can therefore be derived as follows:*(93)*

$$\emptyset_{PL} = \frac{\tau_{ob}}{\tau_r}, \qquad \frac{1}{\tau_{ob}} = \frac{1}{\tau_r} + \frac{1}{\tau_{nr}}, \qquad Equation\ 2.3$$

where $\emptyset_{PL}$ represents the quantum yield, τ_{ob} the observed PL lifetime, τ_r radiative lifetime and τ_{nr} non-radiative lifetime.

In order to increase the PL quantum yield in 2D TMD semiconductors, diminishing the contribution of non-radiative activities to the observed PL lifetime becomes a vital aspect.

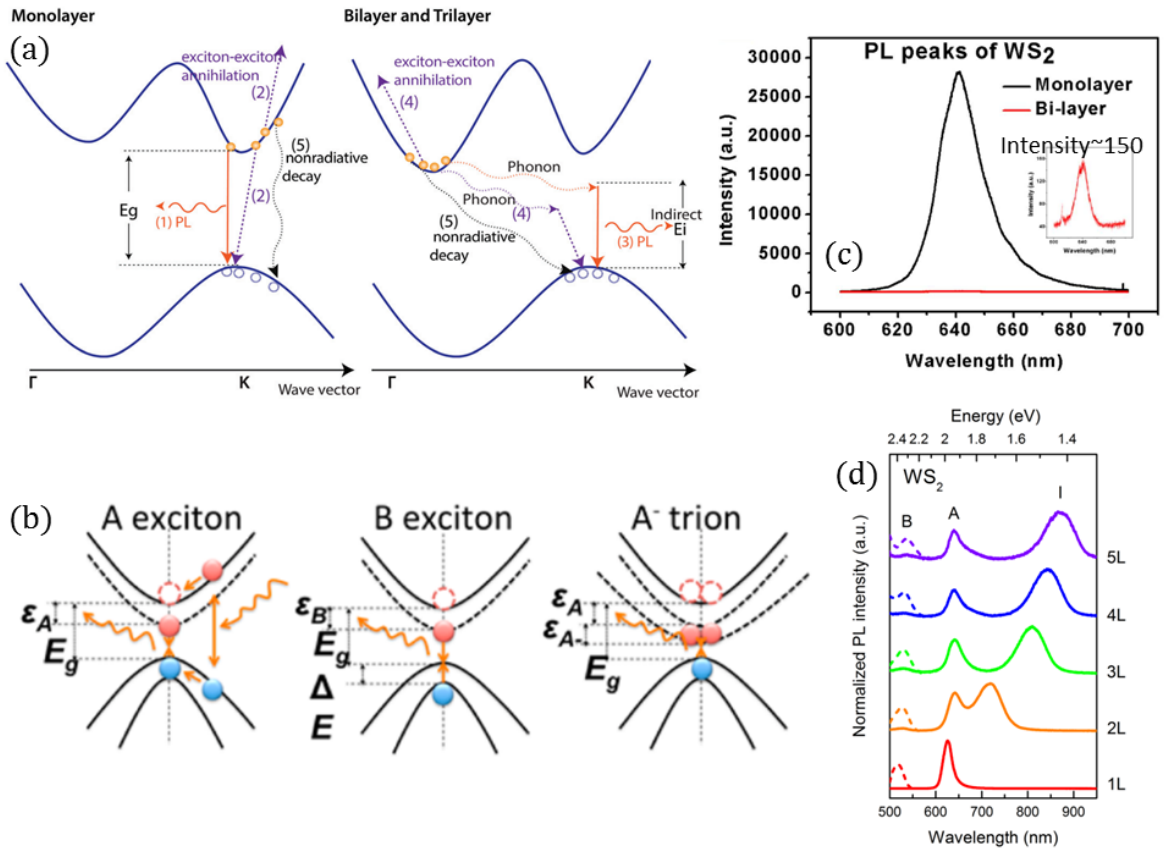

Figure 11. Electron-hole interactions in semiconducting MoS_2 and WS_2 layers. (a) Schematic illustration of electronic relaxation pathways established in band structures of monolayer and few-layer semiconducting TMDs. (b) Three types of exciton-affiliated radiative transition at the K point of Brillouin zone, contributing to the PL. E_g, Δ, ε_A, ε_B, ε_{A^-}, respectively, denotes the bandgap, valence band splitting, the binding energy of A exciton, B exciton and A- trion. (c) Direct comparison between PL spectra of monolayer and bilayer WS_2 grown by CVD method. The inset shows the exact PL intensity of the bilayer WS_2 (~150). (d) Normalized PL spectra of mechanically exfoliated WS_2 in 1-5 layers. Peak I, A, and B represent indirect emission, direct A-exciton emission, and direct B-exciton emission, respectively (the dashed lines: B peaks typically magnified 100 to 1000 times for clarity). Figures reprinted (adapted) with permission from: (a), ref.*(93)*, © The Royal Society of Chemistry 2015; (b), ref.*(75)*, © 2014 American Chemical Society; (c), ref.*(99)*, © 2015 Macmillan Publishers Ltd, OPEN Access; (d), ref.*(18)*, © 2013 American Chemical Society.

2.3 Applications of Monolayer WS_2 (MoS_2)

The direct-bandgap semiconducting behaviour is what equips 2D-TMD semiconductors with a competitive edge in the contest of novelty against graphene. As a result, the majority of semiconducting-TMD applications realized so far lie in the regime of digital electronics, and in particular, optoelectronics. The notion of optoelectronics has never been so recognized in the industry of 2D materials until 2D TMDs. In fact, it is because of this, the prospect of 2D electronic industries was reinstated and is being unceasingly brought to new heights. Existing studies were mostly done on monolayer MoS_2, resulting from the fact that monolayer MoS_2 was the first 2D semiconductor discovered and it is easier to be synthesized. However, what was achieved with monolayer MoS_2 provides a great sense for what would be possible with monolayer WS_2 in applications (*i.e.,* Sulphur-/selenium-based Mo and W can be treated equivalent in terms of semiconducting mechanism). Therefore, in this section, methods feasible in monolayer MoS_2 should be deemed universally beneficial for the remaining 2D semiconductors.

2.3.1 Digital Electronic Devices

Digital electronic circuits are greatly relied upon assemblies of logic gates, where each logic gate consists of several transistors. A transistor acts as a switch to create “on” and “off” current effects through applied voltage, aiming to mimic the Boolean logic algebra that is denoted either true “1” or false “0”. In order to have an effective transistor switch, two as-created current states must be highly distinguishable; in other words, the current on/off ratio ought to be high. At room temperature, the easiest way to accomplish this is by the application of semiconducting materials with band gaps greater than ~1 eV.*(100)* The most common type of transistors in modern digital devices is the metal-oxide-semiconductor field-effect transistor (MOSFET). Given the prominent bandgap size of semiconducting TMDs, WS_2 layered materials with layer-dependent bandgaps are hence of great potential for achieving high on/off-current ratios, as opposed to gapless graphene. The nascent discovery of these 2D TMD semiconductors empowers the development of 2D materials towards digital electronics. The following sections discuss the recent development of FETs fabricated using monolayer MoS_2 and WS_2 (*i.e.,* the two are cross-referable in this context), together with their further advancement into integrated circuits and 2D hybrid devices.

2.3.1.1 Field-Effect Transistors (FETs)

In general, to fabricate a thin TMD-FET requires two metal electrodes (source (S) and drain (D)) deposited on a designated sample for current flow, and an additional electrode (back gate (BG)) for prompting either negatively- or positively-charged carriers to the sample surface through a dielectric material (figure 12a). Figure 12b exhibits a back-gated monolayer WS_2 lithographically patterned to a narrow ribbon (channel) for carrier mobility measurement between S and D. In pursuance of determining the carrier mobility, according to equation 2.2, the relationship between source-drain current (I_{SD}) and back-

gate voltage (V_{BG}) at a specific source-drain voltage (V_{SD}) ought to be generated from the device measurement. However, this method is only accurate when electrode contact resistance is substantially lower than the channel resistance. Choosing an appropriate electrode metal to reduce contact resistance regarding different TMDs has always been one of the major hurdles in the FET device development. Therefore, a four-terminal device configuration (figure 12b), where additional electrodes are introduced at V_1 and V_2 (measuring the voltage drop), is commonly used to retain more precise results of monolayer mobility and also sheet resistance.*(68)* The device design in figure 12a and b also enables the discovery of the Hall Effect in monolayer MoS_2 when simultaneously applying longitudinal (V_{xx}) and transverse voltages (V_{xy}) to the material.*(101,102)*

The back gate is often established by transferring a semiconducting TMD thin film onto a heavily doped silicon (Si) wafer coated with thermal oxide (SiO_2), where Si is the electrode and SiO_2 forms a universal dielectric layer (90 to 300 nm) between the TMD and the back-gate electrode. Although this back-gate method is used most often for graphene FET devices, the measured field-effect mobility for single-layer MoS_2 was discovered to be at least 3 orders of magnitude lower (0.5-3 $cm^2V^{-1}s^{-1}$) than that of graphene.*(103)* It was attested that modifying the dielectric environment can enhance the carrier mobility of graphene.*(104,105)* By moving the dielectric gate from the back to the top (figure 12c) – with a solid dielectric HfO_2 layer deposited by atomic layer deposition (ALD) – the mobility of monolayer MoS_2 FETs has been moderately improved up to ~60-70 $cm^2V^{-1}s^{-1}$ *(106-108)*, generating at room-temperature high current on/off ratios (~10^8).*(4)* In this instance, the ultrathin ALD-deposited dielectric layer (30 nm) and the direct top-gate engagement with monolayer MoS_2 channel have enabled a more effective gate control than back gating, whereby low FET off-current (high switching ratio) is able to be obtained.

In light of section 2.2.2.3, carrier density plays an important role in improving conductivity (switch-on current) and reducing power dissipation of semiconducting TMD devices. The previous solid-top-gate dielectric can help ramp carrier densities up to 10^{13} cm^{-2} in

monolayer MoS_2.*(108)* In recent developments of ionic or electrochemical top-gating (figure 12d), it was declared that TMD FETs can exhibit carrier densities greater than 10^{13} cm^{-2} due to the formation of an electric double layer (EDL).*(109,110)* The direct contact of ionic gel to the TMD channel region and gate electrode, shown in figure 12d, enables the migration of oppositely charged carriers towards the channel/ionic gel interface, establishing an EDL dielectric with less than 1 nm thickness. In comparison to the aforementioned dielectrics, the ionic top-gated FETs can easily retain large capacitance which therefore boosts carrier density across the channel at relatively small voltages. However, gating the TMD FETs using ionic gel has its disadvantages, for example, slow response time and constrained electrochemical stability windows. To gain a better control over charge carrier densities, the ionic top-gate therefore is often employed in conjunction with SiO_2 back gate (figure 12d), as recently reported for MoS_2.*(111,112)* The employment of ionic gating, most importantly, has made the fabrication of functional 2D semiconducting FETs available on flexible substrates.*(113)*

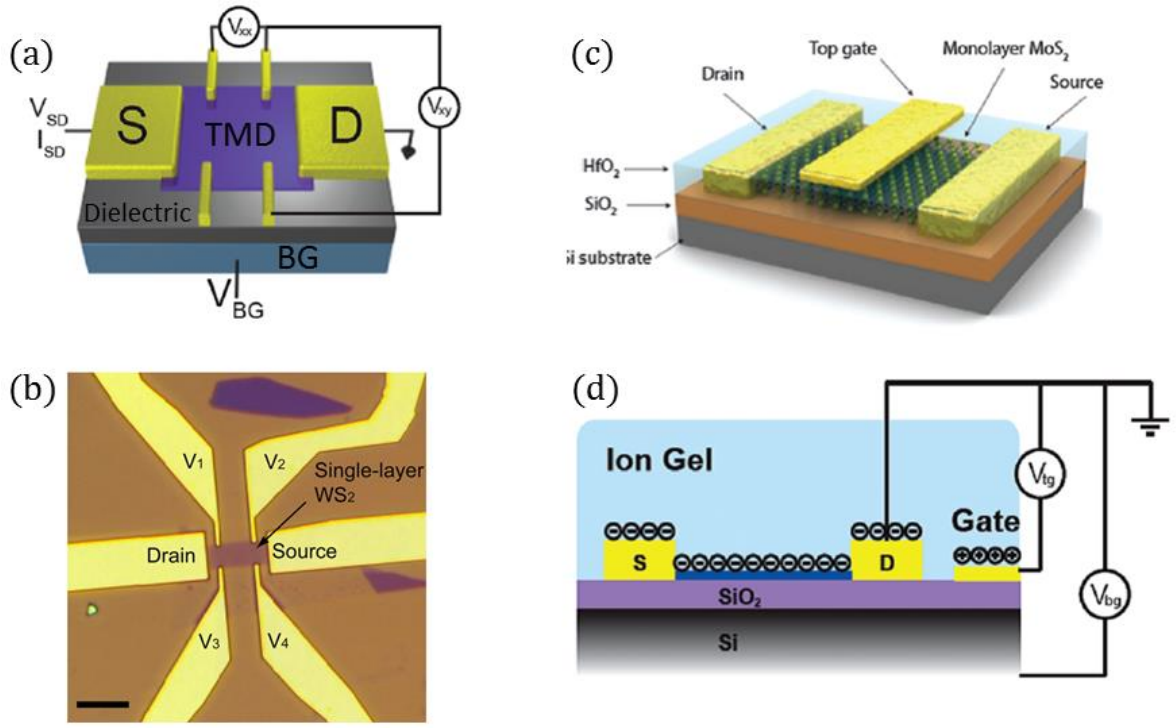

Figure 12. FET Device Structures. (a) Schematic illustration of a back-gated multi-terminal FET, where V_{SD} and I_{SD} are the source (S)–drain (D) voltage and current, respectively; V_{BG} the back gate

voltage needed for electrostatically gating the device channel. (b) Optical image of a standard FET device based on monolayer WS_2. (c) Schematic presentation of a FET device using a solid dielectric (HfO_2) as the top gate. (d) A dual-gate FET device design schematically plotted to indicate ionic gel top gate and Si back gate. Figures reprinted (adapted) with permission from: (a) and (d), ref.*(72)*, © The Royal Society of Chemistry 2015; (b), ref.*(68)*, © 2014 American Chemical Society, OPEN Access; (c), ref.*(4)*, © 2011 Macmillan Publishers Limited.

The carrier mobility of 2D-TMD FETs has formerly shown its strong temperature dependence, owing immensely to the intrinsic phonon and Coulomb scattering effects. The wide spread of carrier mobilities caused by different device fabrication techniques (figure 10a and b), indicates that there must be additional factors affecting the extrinsic conditions of a thin-film FET. Three contacting interfaces that may extrinsically impair semiconducting FET device performance are hence postulated in figure 13a and particularized as follows: First, at ambient/semiconductor interface, oxygen and water are easily adsorbed onto TMD thin films within which the doping level and carrier mobility are subjected to change. The effect exhibits evidently in Figure 13b, where the transfer curve of an as-fabricated monolayer MoS_2 FET device is horizontally shifted to negative gate voltages after annealing the device in vacuum (or N_2). Similar phenomena were revealed in monolayer WS_2 FETs.*(68)* This migration implies there is a significant amount of increase in negatively charged carriers (electrons). Surface adsorbates are extremely in favour of accepting electrons, after they are removed, the electron doping level should supposedly reset to the original value of monolayer MoS_2. As discussed initially, maintaining a high carrier density is crucial to 2D-TMD device efficiency, and more importantly, reduction of doping impurities like ambient adsorbates helps avoid charge scattering that compromises the carrier mobility. In defiance to the device underperformance, it has recently been achieved that the TMD FET-channel can be encapsulated by a stable dielectric layer such as h-BN *(114,115)* (or ionic gel top-gate) to

avoid further atmospheric interference while upholding the 2D FET's great advantage – mechanical flexibility.

Second, it is already widely acknowledged that the SiO_2 dielectric substrate in graphene FETs can evoke charge carrier scattering as a result of resident charged impurities,*(116)* remote interfacial phonons,*(59)* and surface roughness.*(117)* Tantamount effects are expected at the substrate/semiconductor interface of 2D-TMD FETs fabricated directly on SiO_2. In the effort to replace SiO_2, the h-BN layered thin film has quickly found its role in 2D semiconducting devices by virtue of its high surface smoothness and low density of charged impurities.*(69,118,119)* Figure 13c presents a perfect example of boosting the carrier mobility by using h-BN substrates as opposed to SiO_2 in monolayer MoS_2 FETs.

Third, contacting semiconducting TMDs with metal electrodes forms Schottky junctions at the contact interface. The Schottky barrier induces contact resistance that is notably higher than channel resistance, which thus lowers the overall conductance of FET devices. In principle, a metal of low work function ought to be chosen for the purpose of establishing ohmic contacts that are certainly demanded by a high-performance FET. Exceptions can be made for both monolayer WS_2 and MoS_2 FETs deposited with gold (Au) contacts, where linear IV curves featuring ohmic conductance can be derived as figure 13d.*(4,11,68,120,121)* Among commonly used metal contacts, the Au renders the highest work function (5.1 eV) forming the largest Schottky barrier with n-type MoS_2 (electron affinity ~4.0 eV), as depicted in figure 13e. However, upon approaching monolayer TMD thickness, the width of the as-formed Schottky barrier would become so narrow that carriers may tunnel through the barrier, manifesting negligible contact resistance.*(122)* Metals with low work function are still sought-after as a consequence of the ever-changing demand of device adaptability. Figure 13f therefore exemplifies the influence of deploying low-work-function scandium contacts that can help increase the carrier mobility of multi-layer MoS_2 FET devices. In addition to the choice between metal contacts, the chemical interaction at the as-created metal (electrode)/TMD (channel) interface is also a potent

factor that elevates the contact resistance.*(123)* From configuring device structure to selecting metal/dielectric contact materials, additional aspects of improving monolayer WS_2 (or MoS_2) FET device performance may include charge transfer doping, which surpasses the scope of this thesis.

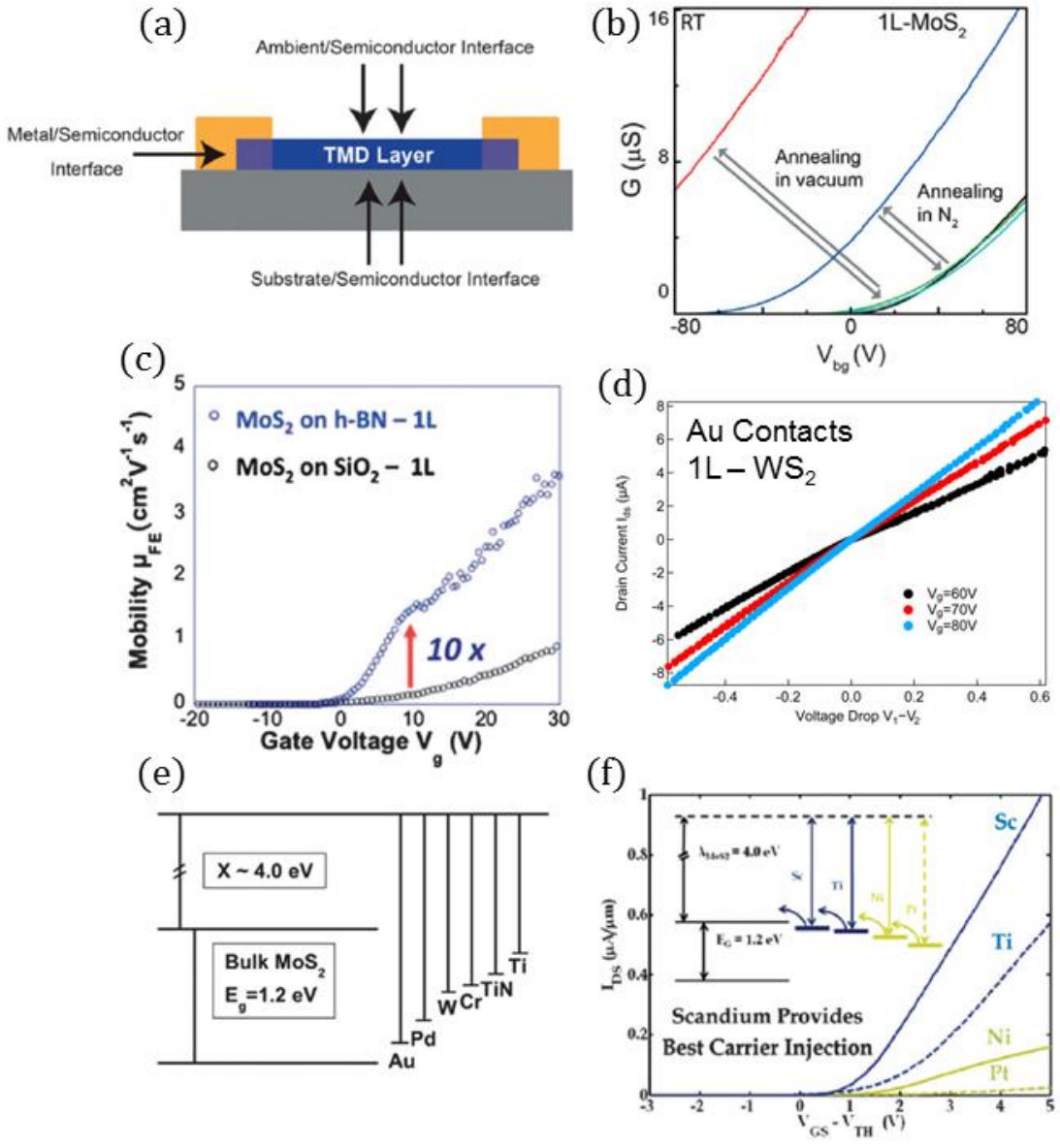

Figure 13. Extrinsic effects for 2D-TMD FET device performance. (a) Schematic of thin-film FET surface and interface that have caused variation in device performance. (b) Transfer curves of a monolayer MoS_2 FET before and after annealing in vacuum and in N_2 environment. (c)Transfer curves of a monolayer MoS_2 FET fabricated on SiO_2 and h-BN/SiO_2. (d) Source-drain IV output curves of a monolayer WS_2 FET with Au contacts (back-gated). (e) Schematic energy-level

alignment between energy bandgap and fermi levels from bulk MoS_2 and various metals, respectively. (f) Transfer curve of MoS_2 FETs fabricated using different metal contacts. Figures reprinted (adapted) with permission from: (a), ref.*(72)*, © The Royal Society of Chemistry 2015; (b), ref.*(124)*, © 2014 American Chemical Society; (c), ref.*(118)*, © The Royal Society of Chemistry 2013. (d), ref.*(68)*, © 2014 American Chemical Society, OPEN Access. (e), ref.*(125)*, 2014 American Chemical Society; (f), ref.*(122)*, © 2013 American Chemical Society.

2.3.1.2 Inverters and Logic Gates

The high current on/off switching ratio demonstrated previously gives semiconducting-TMD FETs access to integrated digital circuitry such as inverters and various types of logic gate. An inverter, the most primitive type of all logic gates, is created from the coalition of two FETs in series. Figure 14a-c explicitly depict a double-gated inverter fabricated using mechanically exfoliated monolayer MoS_2, where the gates of the FETs serve as input voltage (V_{in}) and the middle lead electrode as output voltage (V_{out}). Referring to figure 14d, the inverter is capable of converting high V_{in} to low V_{out} and *vice versa*, resulting from the combining effect of circuitry design and gate-dependent FET conductance. The contrary outcome of input information therefore matches the criteria for NOT logic operation that is used to create logical negation in digital devices (the truth table in figure 14d). Furthermore, the voltage gain, an essential criterion for estimating inverter's performance, where a gain above unity is desired for its further integration in cascaded logic devices. Figure 14e reveals that the voltage gain of this monolayer MoS_2 inverter is above 4. Later development of inverters based on CVD-grown monolayer MoS_2 has shown enhancement of the voltage gain reaching close to 20.*(126)*

These logic gates are of practical use only when 2D semiconducting TMDs can be produced in large-areas by industrially scalable approaches. In this regard, investigating device characteristics of logic gates or even FETs with regard to CVD-grown TMD

semiconductors may seem, as for now, a better pathway for eventually realizing digital products. However, as abovementioned, grain boundaries in CVD-grown polycrystalline TMD thin films, in some case, can diminish the carrier mobility by approximately an order of magnitude. Improvements on CVD techniques have been carried out extensively over the years, and will be addressed individually in the material synthesis section. The current status of CVD synthesis has, nevertheless, enabled the fabrication of centimetre-scale integrated circuits on monolayer MoS_2 (figure 14f). From which, more complex logic-gate geometries such as NAND gates (3 FETs) were successfully demonstrated (figure 14g and h), envisaging the possibility of facilitating the Boolean functions on CVD-grown semiconducting TMD thin films.

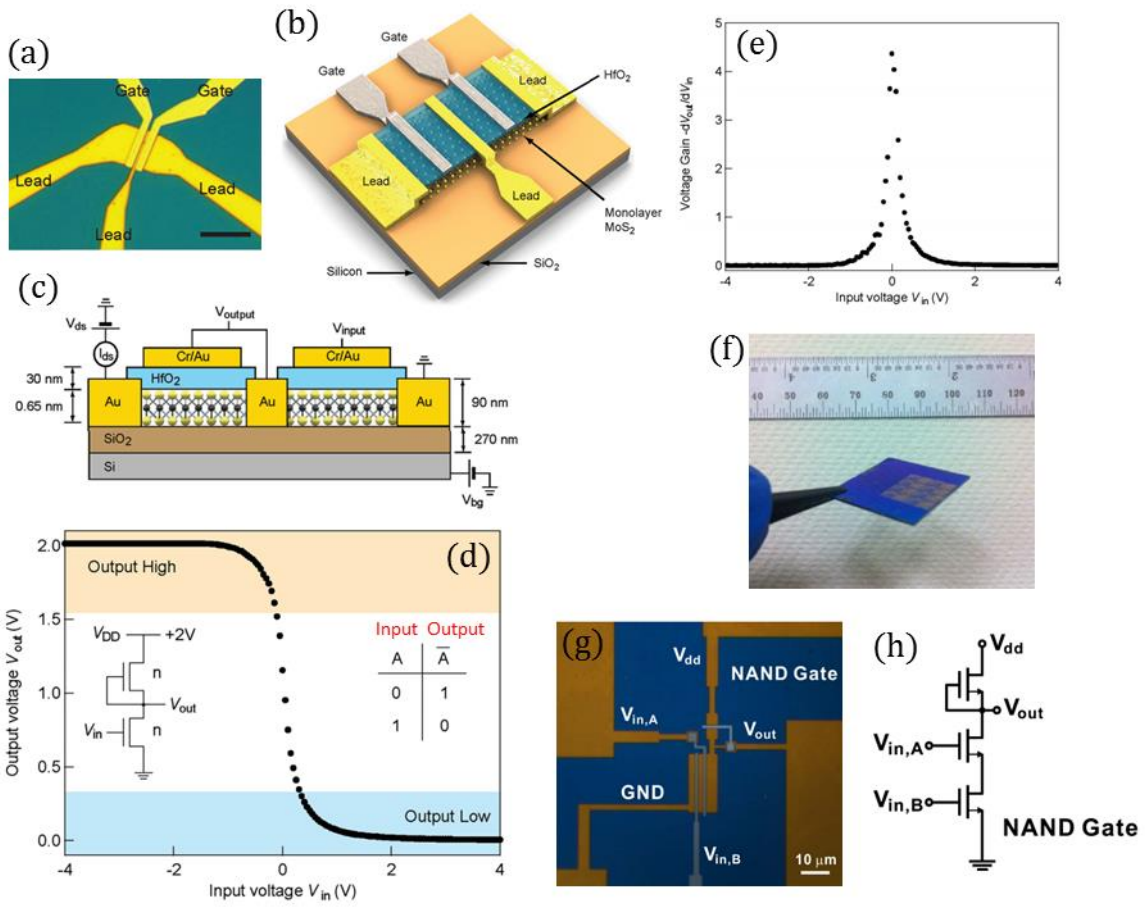

Figure 14. Logic inverter (NOT gate) and NAND (negative-AND) gate fabricated, respectively, on exfoliated and CVD-grown monolayer MoS_2. (a) Optical image of a logic inverter based on exfoliated monolayer MoS_2. Scale bar is 10 μm. (b) and (c) 3D and cross-sectional view of the

inverter structure shown in (a). (d) A plot of output voltage as a function of input voltage generated by the inverter circuit in (a); the inset indicates the inverter schematic and the truth table for NOT logic operation. (e) The inverter voltage gain (negative value of dV_{out}/dV_{in} in (d)) as a function of input voltage. (f) Large-scale fabrication of integrated circuits on a SiO_2/Si wafer using CVD-grown monolayer MoS_2. (g) Optical micrograph of NAND gate from the integrated circuits shown in (f). (h) Schematic of the NAND gate from (g). Figures reprinted (adapted) with permission from: (a)-(e), ref.*(10)*, © 2011 American Chemical Society; (f)-(g), ref.*(126)*, © 2012 Institute of Electrical and Electronics Engineers.

2.3.1.3 Heterostructures and Heterojunctions

The development of electronic devices based on a single 2D material underpins opportunities for creation of 2D material assemblies with unique combination of heterostructures or heterojunctions. In the traditional semiconducting industry, group III (p-type) and group V (n-type) semiconducting crystals are joined together epitaxially to generate various functionalities (e.g. diode, CMOS circuits, solar cells). Here, the chemically and physically versatile TMD semiconductors are potential candidates for substitution of traditional one, as a result of which all devices become significantly thinner, highly transparent as well as mechanically flexible. New functions of electronic device may be also discovered owing to the existing nature of atomically-thin TMDs. Figure 15a presents a ultrathin tunnelling field-effect transistor (TFET) achieved by a vertical heterostructure that comprises a few-layer semiconducting WS_2, two graphene layers and a thin layer of h-BN. The material stacking order of this device is demonstrated in figure 15b. In devices as thin as few layers of atoms, the electric fields can partially penetrate (tunnel) through the entire stack, hence creating a pathway for gate control over the graphene/WS_2 interface.*(127-129)* The few-layer WS_2 acts as a barrier to the tunnelling, which is tuned by gate voltage applied on graphene electrodes. In this set-up, the tunnelling currents upon on/off states are dependent on WS_2 thickness, gate voltage (the

inset in figure 15c) and temperature. Low thickness (1~5 nm) allows large current tunnelling through the WS_2, which leads to higher off-state currents and hence low on/off ratios. On the other hand, low thickness helps gain better gate control over the top layer WS_2 barrier, which renders high on-state current density that increases the on/off ratio (*vice versa* for thickness > 5 nm). Although trade-off between on-current density and off-current tunnelling is to be realized, the circumstances can be substantially alleviated by creating a metal-semiconductor interface at one side (substituting graphene).*(130)* After all, modulating the tunnelling current through few-layer WS_2 by graphene gates has resulted in very promising current on/off ratios – greater than 10^6 at room-temperature. The device performance was also found to be compatible on flexible substrates where bending strains up to 2% was applied.*(127)*

P-n junctions or heterojunctions based on bulk semiconducting TMDs have already been recognized for decades,*(131,132)* whereas fabricating them in pure 2D TMDs remained challenging due to the unrealized techniques of 2D materials synthesis and the limited availability of p-type semiconducting TMD thin films. As a result of the rapid development of CVD techniques, at the beginning, ultrathin TMD p-n heterojunctions are partially demonstrated using n-type monolayer TMDs (MoS_2 and WSe_2) together with p-type semiconducting single-walled carbon nanotubes (s-SWCNT) or conventional semiconductors such as InAs.*(133,134)* Their resulting electrical performance showed good suitability in the application of gate-tunable rectifying diodes. After continuous efforts dedicated to achieving epitaxially-grown semiconducting TMDs on graphene or h-BN,*(83,135-138)* direct CVD growth of pure semiconducting TMD heterostructures (both lateral and vertical) has been achieved recently for WS_2/MoS_2.*(139)* The development of investigating other possible combinations of 2D TMD semiconductors hence became quickly underway. Figure 15d denotes a recently conceived CVD growth mechanism which successfully facilitated the fabrication of 2D $MoS_2/MoSe_2$ and WS_2/WSe_2 lateral (in-plane) heterostructures, as a result of which first epitaxially grown p-n heterojunction in 2D

was accomplished.*(140)* In the as-synthesized lateral heterostructures, monolayer WSe_2 and WS_2 were electrically characterised as p-type and n-type semiconductors, respectively. Adding the fact that the lateral junction of 2D WS_2/WSe_2 are synthetically grown together, the fabrication of a p-n diode using purely 2D TMDs thus becomes a reality, as demonstrated in figure 15e. Additionally, this lateral 2D p-n geometry was also proved ideal for high-performance CMOS inverters, which exhibited a voltage gain as high as 24 (figure 15f).

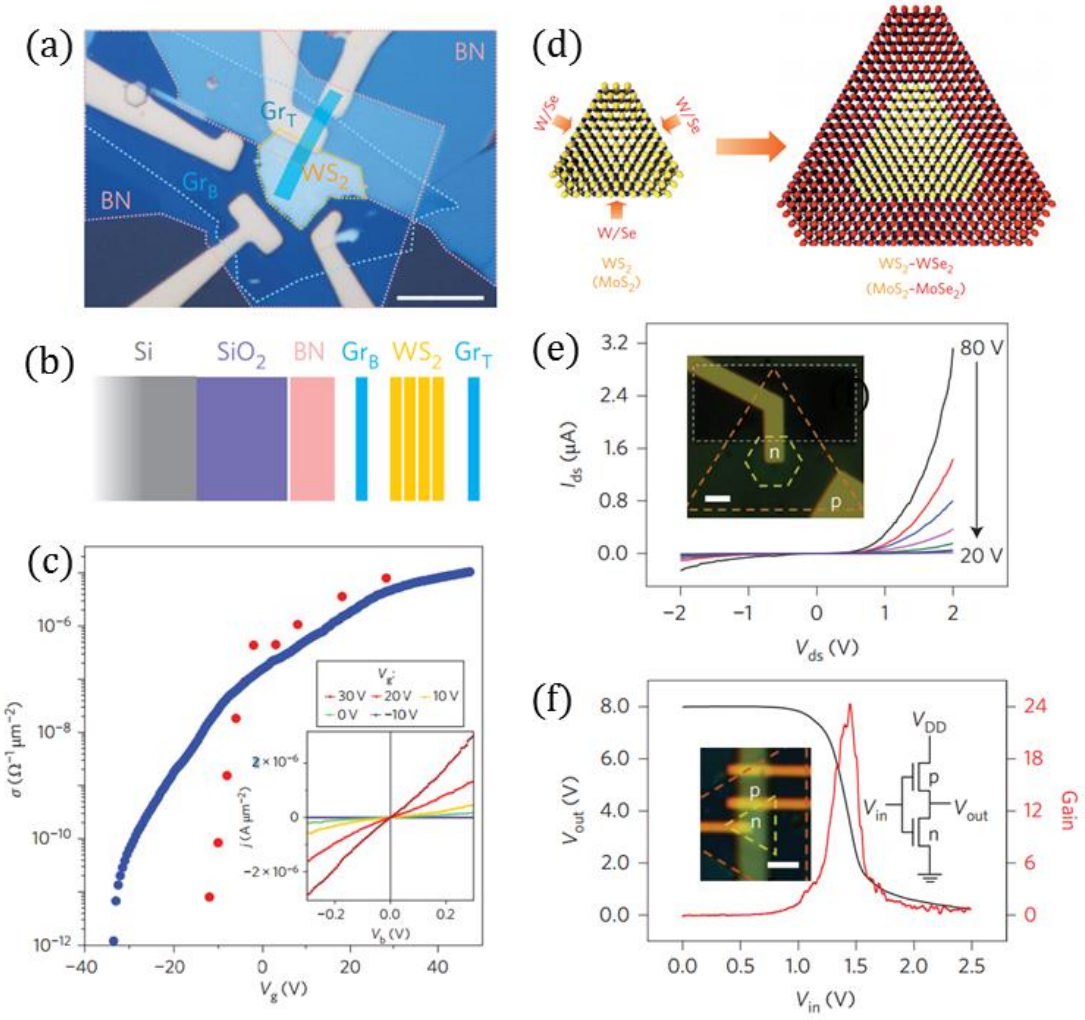

Figure 15. WS_2-based heterostructure and heterojunction devices. (a) Optical image of a graphene/WS_2/graphene/BN heterotransistor (scale bar, 10μm). (b) Schematic of vertical material stacking sequence of the transistor. (c) Red spots: semilog transfer curve of the WS_2-graphene transistor at zero bias; Blue spots: semilog transfer curve at gate-voltage 0.02 V. Inset: Linear-

scale plot of I-V output curves of the transistor at different gate voltages. All measurements were carried at 300K. (d) Schematic of lateral epitaxial growth of monolayer WS_2-WSe_2 and MoS_2-$MoSe_2$ lateral heterostructures in a CVD process. (e) The output characteristics of a 2D in-plane WSe_2-WS_2 heterojunction p-n diode at gate voltages varying from 80 V to 20 V with an interval of 10 V. Inset: An optical image of the heterojunction p-n diode device (scale bar, 2 μm). (f) A 2D CMOS inverter based on the integration of a p-type WSe_2 and an n-type WS_2 FETs. Inset: Optical image of the device on the 2D WSe_2/WS_2 lateral heterostructure and schematic of the CMOS inverter (scale bar, 2 μm). Figures reprinted (adapted) with permission from: (a)-(c), ref.*(127)*, © 2012 Nature Publishing Group; (e)-(g), ref.*(140)*, © 2014 Macmillan Publishers Limited.

2.3.2 Optoelectronics

As they have strong photoluminescence, monolayer semiconducting TMDs should be eligible for detecting, interacting with or generating photons at corresponding energies to their direct bandgaps. These direct bandgaps are of visible-range wavelengths and large exciton binding energies, which make 2D TMD semiconductors ideal candidates for optoelectronic applications in light-emitting devices, photovoltaics and photodetectors. For multi-layer TMDs, the indirect bandgaps require additional photon energy for opto-behaviours that is much less salient than that generated by monolayer TMDs. When electronic devices consist of pure 2D thin films, they retain ultra-high flexibility and transparency. The discovery of 2D TMD semiconductors has, in fact, invigorated the development of optoelectronics towards wearable (flexible and transparent) applications. This section intends to emphasize the uniqueness of the direct bandgap in 2D semiconducting TMDs, through the lens of optoelectronic applications that have exhibited significant advantages over past 2D materials.

2.3.2.1 Photodetectors and Photovoltaics

In a semiconductor, electrons can be excited to the conduction band as a result of photonic excitation facilitated by photon energies greater than the bandgap. The excited electrons and the as-created holes (in valence band) either become free carriers or form excitons (electron-hole pairs) at a strong exciton binding energy. Separating these bound excitons, which normally is achieved through an applied or built-in electric field, will result in generation of photocurrent. For a direct bandgap in 2D TMDs, excitons are created with the least effort from incident photons, but separating them becomes inherently harder owing to their outstanding binding energies (figure 11b). Referring to aforementioned semiconducting TMD FETs and diodes, it is not so difficult to envision that the main categories of semiconducting photodetectors should thus include phototransistors and photodiodes.

2D TMD photo-detecting capability was initially observed in monolayer MoS_2 phototransistors illuminated with photon energies greater than 1.9 eV.*(13)* The fast development of CVD has increased the promise of TMD photodetectors towards large-scale manufacturing, which was highlighted by the fabrication of phototransistors based on CVD-grown WS_2 films.*(141)* In this context, photoresponsivity is an essential parameter to justify the performance of a phototransistor, which is defined as photoresponsivity (R) = generated photocurrent / total incident optical power on the FET channel. Here the preliminary phototransistors based on monolayer MoS_2 and WS_2 films have rendered R = 7.5 mA/W and ~92 μA/W, respectively. Certainly, the performance of 2D/ultra-thin TMD phototransistors needs to be substantially improved as compared to the reported photoresponsivity of other phototransistors based on ZnO nanowires (1.29×10^4 A/W) *(142)* and vertical Si nanowire arrays (~10^5 A/W) *(143)*, but it is already enhanced as opposed to devices fabricated on 2D graphene (~1 mA/W).*(144,145)* Figure 16a-c introduces a monolayer MoS_2 FET configuration for ultrasensitive photodetection *via* large drain biasing, showing a maximum photoresponsivity of 880 A/W at a wavelength of 561

nm and a visible-range photoresponse from 400 to 680 nm. At an exceptionally large drain bias, the as-generated photocurrent is dominated by a large quantity of separated excitons induced by the strong electric field across the FET channel. Figure 16b further shows that the production of photocurrent originates from the area where electron-hole pairs are subjected to the highest separating force – the centre of monolayer MoS_2 FET channel. While most of recent phototransistors can achieve $R > 10^3$ A/W, it is worth mentioning that phototransistors based on vertical heterostructure graphene/MoS_2 channels are eligible for $R > 10^7$ A/W.*(146,147)* In spite of this high photoresponsivity, phototransistors can still underperform owing to prolonged photocurrent response time (*i.e.,* less than 0.6s for the device in figure 16a *(12)*), over which photodiodes are of considerable advantage.*(148)*

To shorten the response time, electron-hole pairs in a photodetector are to be separated and collected by a built-in electric field (photodiode) that is commonly induced *via* junctions, such as metal-semiconductor Schottky junctions, homojunctions between p- and n-doped regions of a semiconductor, and heterojunctions between different p-type and n-type semiconductors.*(100)* Despite Schottky junctions having been shown to be widely effective in enabling photoresponse at low drain bias, the notion of using a metal-semiconductor-metal (M-S-M) configuration has resulted in the fabrication of TMD photodetectors with faster response times.*(149,150)* More importantly, the recent zeal towards flexible devices has invigorated the use of graphene as the metal contacts for an M-S-M photodetector. In Yu *et al.*'s work, the graphene-MoS_2-graphene photodetector, similar to the one with WS_2 shown in figure 16d, has demonstrated prominent reduction of photoresponse time down to <50 μs.*(151)* Nonetheless, p-n heterojunction diodes such as the aforementioned s-SWCNT/monolayer MoS_2 tend to generate even faster photoresponse (<15 μs) with maximum photoresponsivity at 0.1 A/W, as exhibited in figure 16f.*(133)* It is believed that p-n heterojunctions between 2D semiconducting TMDs

will show comparable results, since the measured photoresponse time of the device in figure 15e was beyond the experimental time resolution of 100 μs.*(140)*

On the other hand, the ultra-thin SL-graphene/WS_2/SL-graphene heterostructure (figure 16d) opens pathway to the investigation of prototype TMD photovoltaic performance. An essential parameter in photovoltaic devices is the extrinsic quantum efficiency (EQE), which represents the percentage of the number of as-generated charge carriers over the number of incident photons. According to figure 16e, the EQE of this WS_2 photovoltaic device increases up to ~30% as laser intensity decreases towards zero; meanwhile it remains rather independent as laser wavelength varies between visible ranges. In this regard, the aforementioned graphene-MoS_2-graphene photodetector can escalate the EQE up to 55% with an excitation wavelength of 488 nm.*(151)* The atomically thin heterostructure of semiconducting TMD multi-layers (5-50 nm) can manifest strong light-matter interactions, implying that large photon absorption and photocurrent production are realizable in ultra-thin photovoltaics. However, as predicted, the power conversion efficiency (*i.e.,* a percentage of the incident light energy that is converted into electrical energy) of nanometre-thick TMD solar cells (MoS_2/WS_2 type II heterojunction) remains as low as 1.5%,*(152)* owing to the limited light-matter interaction depth. Engaging the light as exhaustively as possible while interactive space is substantially confined has led to the utilization of light-trapping techniques such as plasmon-enhanced absorption,*(153-155)* strain engineering *(156)* and vertical stacking of multiple thin films. Additionally, note that fabricating ultra-thin TMD solar cells on flexible substrates (instead of SiO_2) may further downgrade the photocurrent output, as pointed out in the inset of figure 16e. This is generally because the light interference in SiO_2 layers augments the optical electric field in the TMD channel.*(157)*

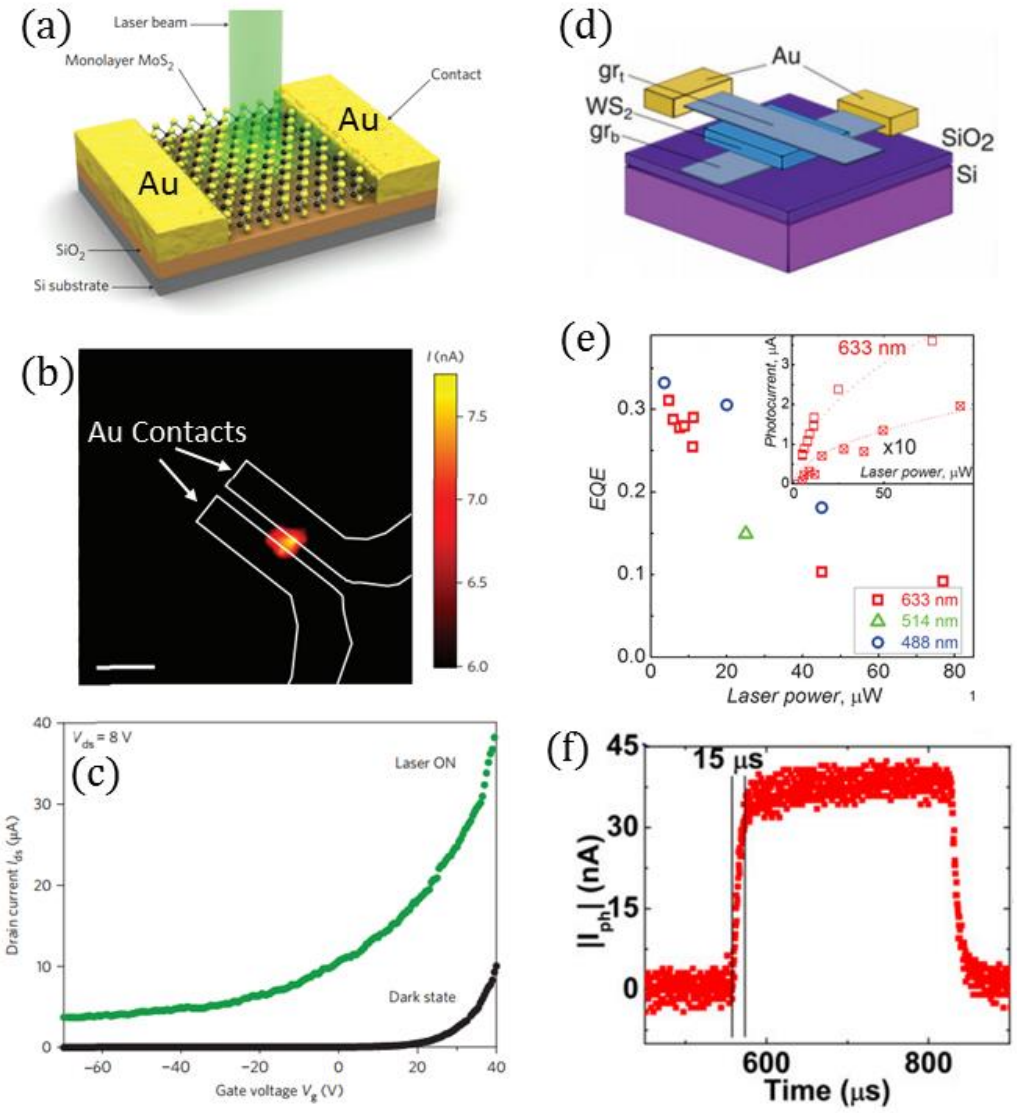

Figure 16. Photodetection in a monolayer MoS_2 FET and photovoltaics in a single-layer (SL) graphene/WS_2/SL-graphene heterostructure. (a) Schematic of a monolayer MoS_2 FET and a focused laser beam employed to activate the device. (b) Spatial photocurrent mapping of the monolayer MoS_2 FET when a focused laser beam is raster-scanned over the surface of the device during biasing. Scale bar, 5 μm. (c) $I_{ds}V_{ds}$ transfer curves of the FET at dark and illuminated states of the laser beam. Illumination power is 0.15 μm. (d) Schematic of a SL-graphene (gr_t)/WS_2/SL-graphene (gr_b) heterostructure FET device for photodetection and photovoltaics. (e) The EQE of the device as a function of laser power at optical absorption wavelength 633 nm, 514 nm and 488 nm, respectively. Inset: as-generated photocurrent of the photovoltaic device as a function of laser intensity (633 nm); open and crossed symbols are referred as a device measured on a Si/SiO_2 substrate and a flexible substrate, respectively. (f) Photocurrent as a function of photon incident

time showing fast photoresponse (15 μm) generated by an s-SWCNT/monolayer MoS_2 p-n heterojunction diode. Figures reprinted (adapted) with permission from: (a)-(c), ref.*(12)*, © 2013 Macmillan Publishers Limited; (d) and (e), ref.*(153)*, © 2013 American Association for the Advancement of Science; (f), ref.*(133)*, © 2013 National Academy of Sciences.

2.3.2.2 Light-Emitting Devices

Another important application of semiconducting p-n junctions encompasses a wide range of light-emitting diodes (LEDs) with diverse emission spectra. Photo-induced electron-hole pairs in device channels can be electrically separated to create current gain, so should electrons and holes be electrically redirected (injected back to the channel) to generate light through radiative recombination. In this contest, the direct-bandgap TMD monolayers are particularly efficient (PL in figure 11). It is alleged that the involvement of semiconducting TMD monolayers will drive the industry of LEDs to revolutionary heights, where ultrathin, flexible and highly efficient LED devices are attainable. Nevertheless, recent development of TMD optoelectronics has exposed a fundamental obstacle to this ambition – the deficiency of controlled chemical doping approaches for semiconducting TMDs. As rule of thumb, stimulating light-emission in semiconductors under bias, in general, must be accompanied with majority quantities of both electrons and holes that originate from n- and p-doped semiconductors, respectively. This hence diverted the path of functioning pure TMD LEDs using chemically doped p-n junctions to using metallic Schottky junctions or electrostatically induced p-n homojunctions, which has appeared to be increasingly preferable in recent years.

Sundaram *et al.* successfully demonstrated electroluminescence (EL) in monolayer MoS_2 by using an ordinary FET device set-up equipped with inverted optical channel for a single photon counting detector (figure 17a). In the device, a split top-gate was employed initially to electrostatically create p- and n-type regions in the monolayer MoS_2 channel. Given

that the Cr/Au contacts inherently form Schottky barriers with the monolayer MoS_2, electron/hole injection therefore ought to be modulated through the application of the respective split gate voltages. However, the results have shown that the proposed gating configuration is incompetent for establishing a p-n junction in the device, due to large bandgap size (1.8 eV) and low doping levels (carrier density $<2\times10^{12}$ cm^{-2}) in the corresponding monolayer MoS_2. In lieu of injection of electrons and holes independently, electron-hole pairs can be generated *via* impact excitation evoked by highly-biased electrons injected at the substantially deformed metal-MoS_2 band interface. Under this circumstance, electrons (majority carriers) are easily backscattered towards the drain electrode, instigating hole (minority carries) leakage at the drain, as a result of which the radiative recombination should be expected to localize at the Schottky-junction drain. Upon applying source-drain voltage, the spatial distribution of EL intensity within this split-top-gate FET device was obtained using single-photon raster scanning (figure 17b), where previous predictions have been experimentally approved. Figure 17c exhibits the light wavelength emitted in monolayer MoS_2 due to this device set-up falls in the visible-red spectrum range. Although the EL intensity is easily observable under the photon detector, the estimated exciton-to-photon conversion efficiency is only of $\sim10^{-5}$, that is more than an order of magnitude lower than that of individual semiconducting single walled nanotubes.*(158)*

The ineffectiveness of split gates has led to the exploration of more powerful FET gating systems that can render a larger density of carriers. Ionic liquid (IL) gating hence has become an ideal candidate due to its extremely large gate capacitance (nanometre-scale EDL in figure 12d), which permits the possibility of facilitating a dramatic increase of carrier density in TMDs at rather low gating voltages ($>10^{14}$ cm^{-2}).*(71,113,159)* With this idea in mind, figure 17d presents an IL-gated FET device based on monolayer WS_2, by which strong EL intensity (figure 17e) joined with ambipolar transport characteristics (figure 17f and g) was accomplished, despite that monolayer WS_2 is of the largest

bandgap in the semiconducting TMD group (~2.1 eV). The EL emission in this device requires simultaneous electron- and hole-injection, respectively, at source and drain contacts (figure 17d). As profoundly studied in organic light-emitting transistors,*(160-163)* an originally electron-populated device channel at positive V_G could be partially introduced with holes (or *vice versa*) by inverting the potential of the channel through an adequate source-drain bias. The starting point of the simultaneous electron-hole injection is easily noted in an $I_{SD}V_{SD}$ output diagram. For example, in figure 17f and g, the I_{SD} quickly saturates in the monolayer WS_2 FET at low V_{SD} regardless of the gating voltage, owing to the accumulation of electrons (figure 17f) or of holes (figure 17g). A sudden increase of I_{SD} at high V_{SD} signifies the occurrence of simultaneous electron/hole injection, which therefore leads to the light emission. Due to the fact that the EL intensity from the monolayer WS_2 device is observable directly from the optical microscope with naked eyes, not too surprisingly, its EL spectrum peak manifests as at least 50 times greater than that from bilayer, while bulk WS_2 remains as non-luminescent (figure 17h).

Besides the attainment of IL gating on monolayer WS_2, the possibility of using split gating to create electrostatically-induced p-n homojunctions has, however, been realized on monolayer WSe_2.*(164-166)* In particular, the calculation of EL efficiency, defined as the ratio of emitted optical power to electrical input power, was demonstrated for the first-time for monolayer TMD light-emitting devices. It is thus claimed that the homojunction light-emitting diode based on monolayer WSe_2 can generate EL with 0.1% efficiency.*(165)* In comparison to the previous monolayer MoS_2 Schottky junction, the monolayer WSe_2 has provided 10 times larger in photon emission rate while using 1000 times smaller injection current.*(164)* Given commercial organic LEDs performing at 20% emission efficiencies, the concept of 2D LEDs based on semiconducting TMD monolayers is still far behind realization and therefore demands further improvements.

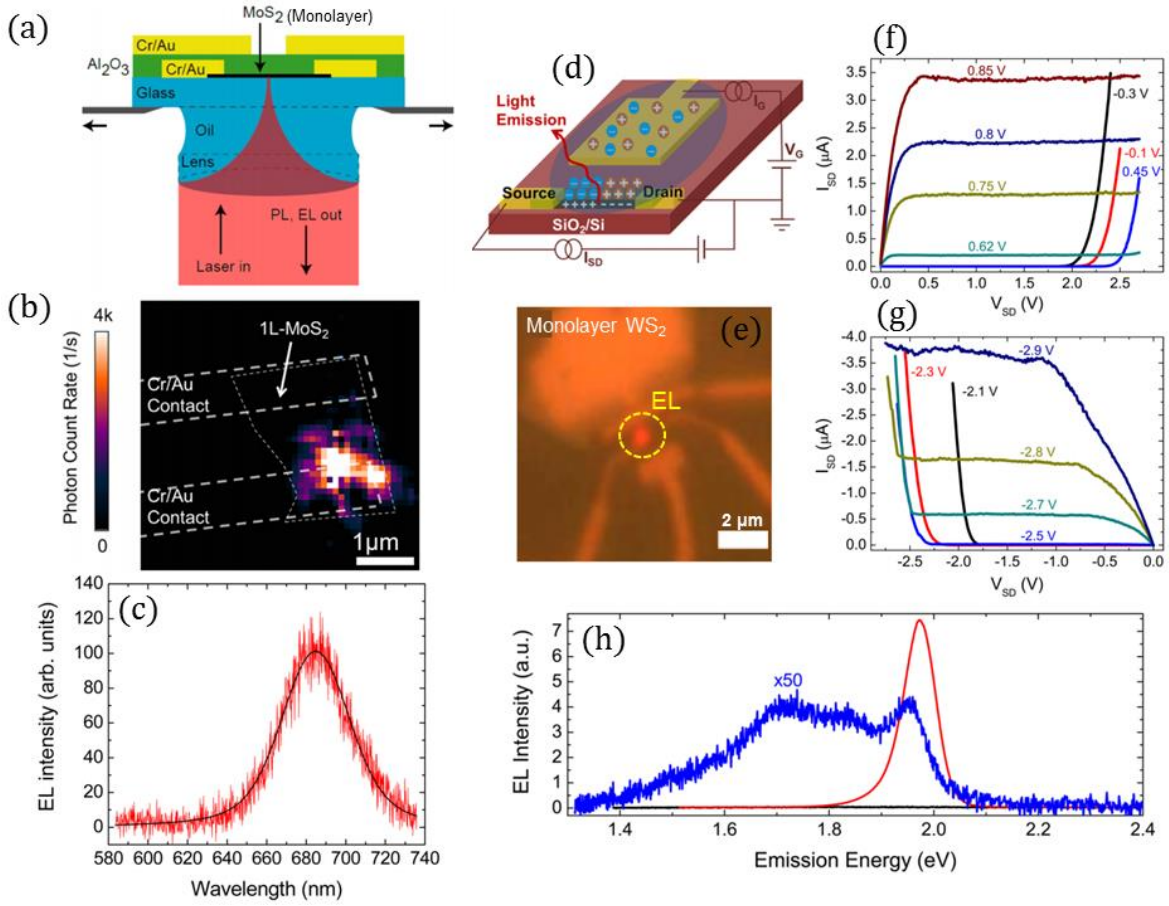

Figure 17. Light-emission in monolayer MoS_2 and WS_2 FET Devices. (a) Schematic of a top-gated (Al_2O_3) monolayer MoS_2 FET with dedicated optical observation channel. (b) False-colour image of EL emission instigated in close proximity to the Cr/Au (white dashed line) where a MoS_2 monolayer (grey dashed line) is laid underneath. (c) EL spectrum (red) of a monolayer MoS_2, fitted with a Voigt algorithm (black). (d) Schematic of a monolayer WS_2 FET device top-gated with ionic liquid. (e) Optical image of a red EL emission spot in the monolayer WS_2 device channel. (f) and (g) Evolution of source-drain current (I_{SD}) as function of source-drain voltage (V_{SD}) at different gate voltages (V_G). At low V_{SD}, positive V_G prepares the channel with electrons and vice versa for holes. (h) EL spectra obtained from monolayer (red), bilayer (blue), and bulk WS_2 (black) light-emitting devices. Figures reprinted (adapted) with permission from: (a)-(c), ref.*(14)*, © 2013 American Chemical Society; (d)-(h), ref.*(70)*, © 2014 American Chemical Society.

2.3.3 Sensors

Electronic sensors generally function to detect analytes by exhibiting a change in resistance. Figure 18a depicts a FET device based on monolayer MoS_2, where the MoS_2-channel causes the variation in conductivity due to its interaction with the analytes. If it were a bulk material in the channel, the device resistance will become less susceptible to change because the interaction is confined to the surface only. However, the atomically-thin TMD monolayers embody a surface-to-volume ratio that is close to unity, by which changes of electrical behaviour become noticeable upon submonolayer analyte adsorption. Initial studies indicated that ultra-thin MoS_2 FETs were eligible for detecting NO, NO_2, NH_3 and H_2O gaseous analytes.*(167,168)* Among which, it was discovered that the sensitivity of these MoS_2 sensors was layer-dependent, where 5-layer thickness was shown to have the highest sensitivity to the above analytes. The origin of resistance variation is commonly referred to as the effect of charge transfer that is accordingly induced by the doping of gaseous products. In addition to inorganics, monolayer-MoS_2 FETs also show advantageous selectivity in organic molecule analytes (*i.e.,* sensitive to reducing and polar analytes while insensitive to oxidizing analytes) as opposed to carbon nanotube (CNT) network sensors (figure 18b). As to the increasing demand of large-scale TMD applications, later development of chemical sensors has quickly shed light on TMD semiconductors grown by CVD.*(169,170)*

Furthermore, the interaction between analytes and monolayer TMD semiconductors also encourages variation in light-emission intensity. Figure 18c elucidates the influence of gaseous physisorption (e.g. O_2, H_2O and ambient air) on the light-emission intensity photo-induced (*i.e.,* PL) from monolayer MoS_2. As a consequence, the drastic distinction between PL intensity in vacuum and at ambient conditions implies a future creation of 2D-TMD photonic sensors. The enhancement of PL efficiency originates from the charge transfer of n-type monolayer MoS_2 caused by the electrophilic analytes (e.g. O_2 and H_2O), where p-type WSe_2 encounters degradation.*(171)* Nonetheless, it is confirmed that the

photonic sensitivity of n-type monolayer MoS_2 (or WS_2) corresponding to electrophilic analytes will not be functionalized, unless the as-synthesized materials are thermally annealed in vacuum (figure 18d). In comparison to aforementioned electronic devices based on semiconducting TMDs, the development of their sensor functionality still remains premature, owing to the perplexity in improving selectivity and reset-ability of ultra-thin TMD semiconductors.

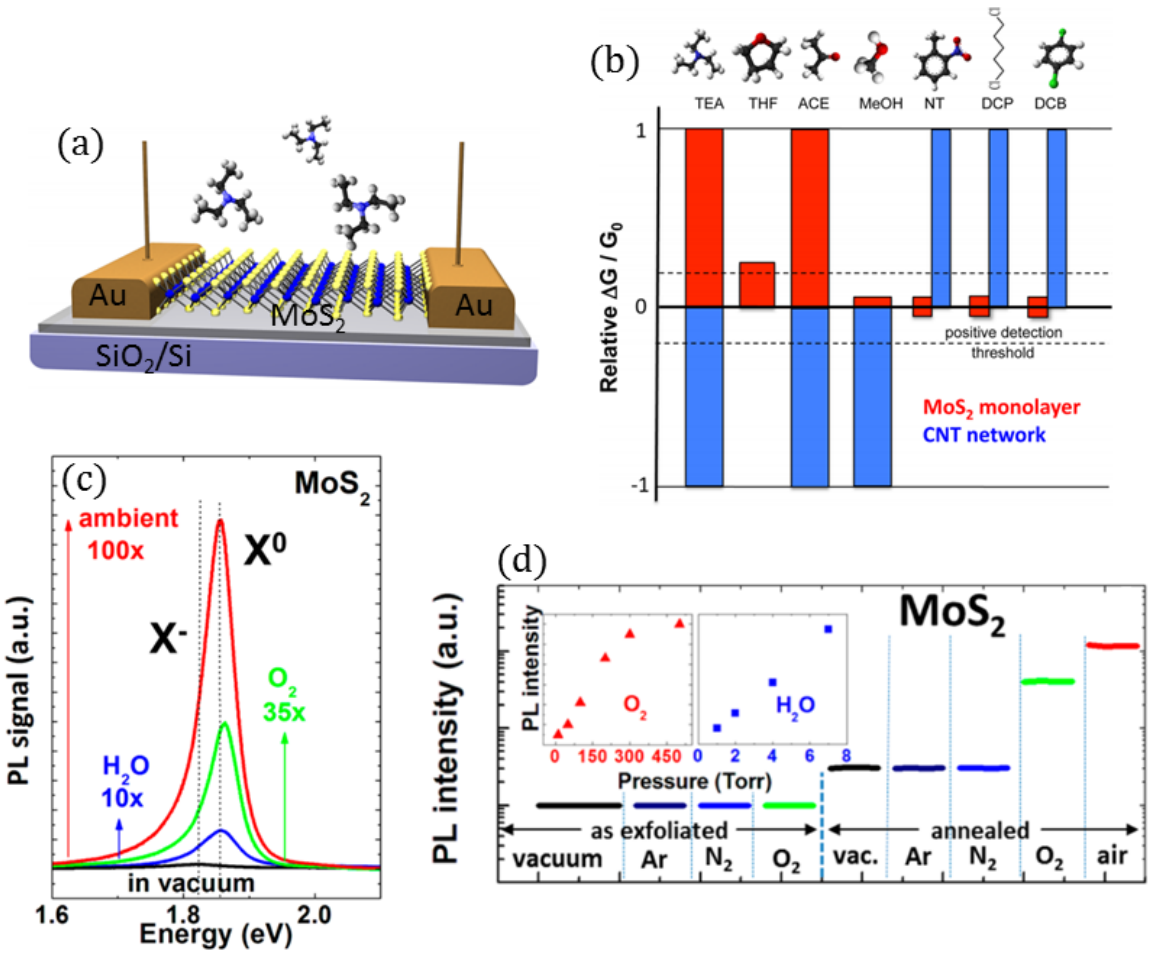

Figure 18. Sensors based on semiconducting TMD monolayers. (a) Schematic of a monolayer MoS_2 FET sensor for detecting organic vapours. (b) Histogram of change-in-percentile of the monolayer-MoS_2-FET conductivity ($\Delta G/G_0$) regarding the indicated analytes for monolayer MoS_2 and CNT-network sensors. (c) Change in photoluminescence (PL) intensity when monolayer MoS_2 is upon exposure to the designated gas environments. X^- and X^0 are trion and exciton peak positions, respectively. (d) Influence of vacuum, Ar, N_2, O_2 gaseous environments on as-exfoliated and annealed monolayer MoS_2. Inset: The PL intensity increases with O_2 or H_2O vapour pressure

in monolayer MoS_2. Figures reprinted (adapted) with permission from: (a) and (b), ref.*(172)*, © 2013 American Chemical Society; (c) and (d), ref.*(171)*, © 2013 American Chemical Society.

2.4 Synthesis of WS_2 (MoS_2) Monolayers

All of aforesaid applications of monolayer WS_2 (MoS_2) would not be accessible if reproducible synthetic means were not realized. Similar to graphene, the synthesis of 2D TMDs can generally be divided into two groups: top-down and bottom-up. The top-down approaches enable microscale production of high-quality TMD monolayers *via* mechanical or chemical exfoliation from bulk TMDs. It is commonly appreciated that the mechanically exfoliated (chemical free) 2D materials generate better device performance and they are ideal for laboratory researches. If ever 2D TMDs will be industrialized, the synthesis of TMD monolayers must be achieved over large-area with high controllability. In this respect, the bottom-up approaches, which include chemical vapour deposition (CVD), thermolysis, physical vapour transport, and surface chemical conversion, have recently shown promising advantages.

2.4.1 Exfoliation and Chemical Processing

In the development of exfoliating 2D materials, mechanical exfoliation using the Scotch-tape method has always been able to offer the cleanest and the highest-crystallinity monolayer samples for high-performance electronic applications and studies.*(5,100)* To mechanically exfoliate a monolayer TMD, it generally requires an adhesive Scotch tape and a bulk TMD single crystal (*i.e.,* MoS_2 in Figure 2c). Single- to multi-layer TMD thin flakes are peeled off from the bulk crystal due to the adhesiveness of the Scotch tape. The cleaved TMD thin flakes are transferred onto a desired substrate by repeatedly rubbing the Scotch tape/TMD film against the substrate until the thin flakes are fully

adhered to the substrate surface. An optical image of a MoS_2 monolayer flake mechanically exfoliated and transferred onto a SiO_2/Si substrate is presented in figure 2d. This physical approach of monolayer TMD synthesis empowers the investigation of monolayer TMD properties without the interference of chemical dopants and crystalline defects that are commonly introduced in material synthesis and processing.

However, the greatest disadvantage of mechanical exfoliation is its low production volume. The application of layered materials in areas such as electrochemical energy storage, catalysis, composite fillers, demands materials produced in large quantities. Graphene was first produced in large quantities by liquid exfoliation where bulky graphite powder was directly sonicated in either dimethylformamide or N-methyl-2-pyrrolidone solvents.*(173)* As new layered materials starting to emerge, this method was quickly adopted and proved effective for fabricating monolayer and multi-layer nanosheets of h-BN as well as a wide range of TMDs including MoS_2 and WS_2 (figure 19a). The as-exfoliated nanosheets are basically dispersed in suspension of the sonicated solvent after centrifuging. Any type of layered-material suspensions can be subsequently transformed into free-standing films using vacuum filtration or spraying (figure 19a: bottom). The efficacy of isolating individual layers by the direct sonication is heavily dependent on the solvents or surfactants that are used to overcome the van der Waals bonding between the monolayers. Therefore, the solvents used for this method must possess comparable or greater surface energies than the bonding energy.*(174)* Nevertheless, the greatest obstacle of this method is fabricating monolayer structure in large quantities as well as retaining large lateral dimensions of the exfoliated nanosheets. Figure 19b unveils the random thickness variation and average lateral size of the exfoliated nanosheets obtained from a single type of layered-material suspension. Sonication breaks apart layered crystals but also tears them to shreds, due to which optimization of the liquid-exfoliating process was developed for graphene and MoS_2 regarding the aspects of starting

precursor mass, sonication duration and centrifuging rate.*(173,175)* As a result, the monolayer yield percentage and flake size are considerably improved.

Only until recently, the monolayer productivity of liquid exfoliation was substantially improved for TMD crystals that were pre-treated with lithium (Li)-intercalation processing. Initially, the Li intercalation treatment was enabled by soaking sulphur-based TMDs (MoS_2 and WS_2) in a solvent of n-butyl lithium in hexane provided with nitrogen atmosphere.*(176)* The as-formed Li_xXS_2 (X=Mo, W) compound was extracted from the solvent and then sonicated in water to produce nearly 100% exfoliated MoS_2 monolayers.*(84)* Despite the high monolayer throughput, this lithiation process had to be carried at 100 ºC for three days, where averting the formation of metal nanoparticles and precipitation of Li_2S was given a substantial effort. To further improve on these issues, Zeng *et al.* developed a straightforward electrochemical approach for facilitating the Li intercalation of sulphur-based TMDs (cathode) directly from a Li-foil anode, as depicted in figure 19c. In comparison to the former method, the Li ions here are provided over a galvanostatic discharge, where the intercalation process can be naturally monitored and precisely controlled from the applied voltage. After sonicating the Li-intercalated TMDs in water or ethanol, the TMD monolayers were not only produced in 100% quantity but also in the form of least chemical contamination. Figure 19d (monolayer WS_2) reveals an exemplary topology of these exfoliated TMD monolayers using AFM.

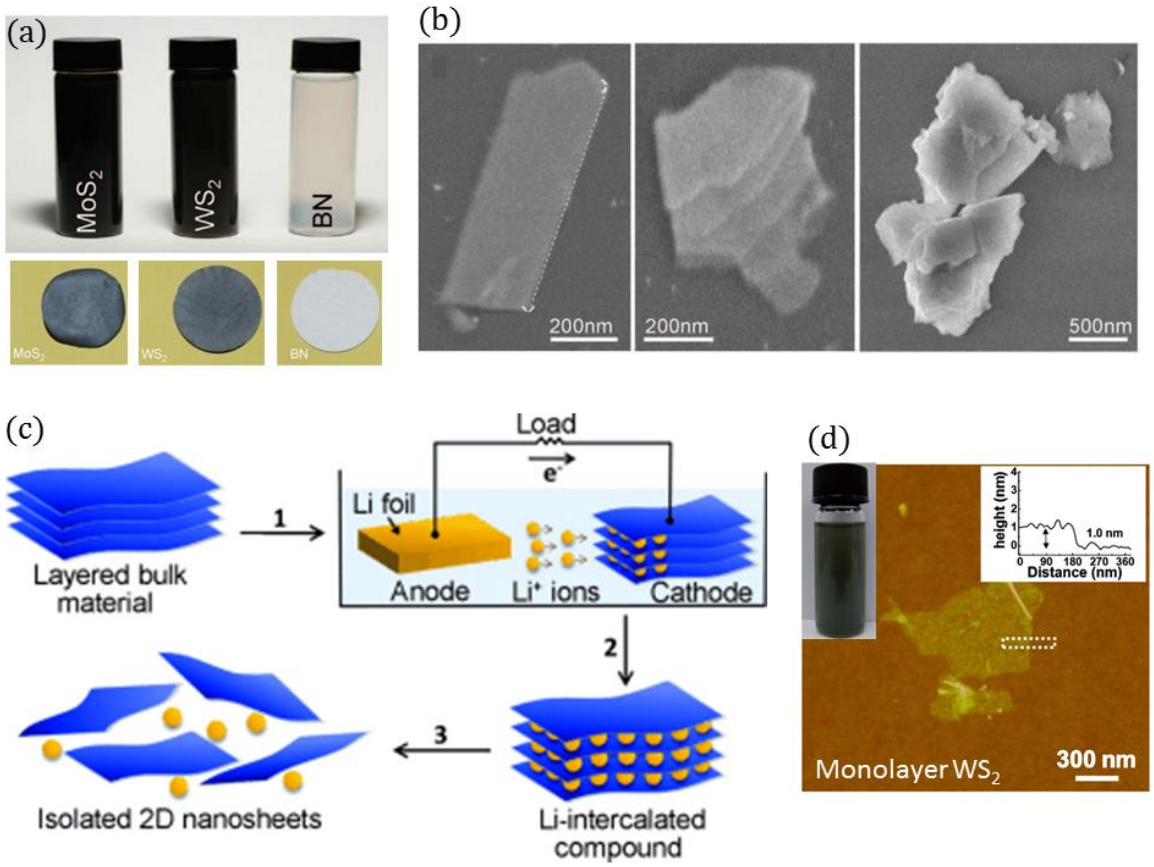

Figure 19. Synthesis of WS_2 thin flakes (multilayer to monolayer) using chemical exfoliation and processing. (a) Top: Photographs of exfoliated MoS_2 (in NMP), WS_2 (in NMP), and h-BN (in IPA) thin flakes dispersed in a range of suspensions. Bottom: Photographs of free-standing films developed from corresponding suspensions above. (b) Morphology (under scanning electron microscopy) of exfoliated thin flakes obtained in (a): a few-layer, a multi-layer, and an aggregation of layered flakes (from left to right). (c) Schematic illustration of liquid exfoliation of 2D TMDs enabled by an electrochemical lithiation process. (d) The monolayer thickness of a WS_2 nanosheet confirmed by the atomic force microscopy. Inset: A photograph of monolayer WS_2 nanosheets dispersed in water. Figures reprinted (adapted) with permission from: (a) and (b), ref.*(177)*, © 2011 American Association for the Advancement of Science; (c) and (d), ref.*(178)*, © 2011 Wiley.

2.4.2 Vapour Phase Deposition

The vapour-phase-deposition (bottom-up) methods have been developed to meet the industrial demand of large-area monolayers with high uniformity. Large-area graphene was realized largely owing to the success of CVD synthesis using copper substrates.*(179,180)* However, the vapour-phase synthesis of monolayer TMDs is more complicated resulting from the chemistry of constituent elements in inorganic TMD crystals. For example, the growth of graphene in CVD requires a metal-catalytic surface while TMD monolayers mostly develop without catalytic assistance (on SiO_2), due to which maintaining a good controllability of 2D-TMD formation in CVD becomes particularly challenging. This section intends to focus on introducing the majority of vapour-phase approaches developed so far for growing large-area semiconducting WS_2 thin layers, where some techniques developed for monolayer MoS_2 are also used to help gain a boarder perspective.

2.4.2.1 Physical Vapour Deposition (PVD) Using Solid TMDs

Probably the easiest approach to start with fabricating monolayer TMDs in vapour phase deposition is achieved through direct vaporization of the relevant TMD bulk crystals onto target substrates. As a result, Wu *et al.* first demonstrated that monolayer MoS_2 domains with high optical quality could be produced by physical vapour transport of MoS_2 powder in a low-pressure evaporating chamber (Figure 20a).*(181)* The MoS_2 powder was evaporated at ~900 ºC, from which the MoS_2 vapour was delivered by Ar gas to the as-prepared substrate that was left at a lower-temperature region, ~650 ºC. Due to the nature of this synthetic approach, the formation of monolayer MoS_2 is prone to not only develop on SiO_2 surface (Si wafer) but also on other insulating substrates with similar surface smoothness, for example, sapphire or glass (figure 20b). Figure 20b also embodies that the as-formed monolayer MoS_2 domains are sparsely distributed on the chosen substrates

over small regions (100×100 μm). The high synthetic temperature needed for evaporating the MoS_2 precursor undermined the productivity of MoS_2 monolayer over large areas, although the optimization of Ar flow rate and substrate/source positioning was extensively carried out. During the deposition, the nucleation density was so low that the pre-deposited MoS_2 monolayers started to grow vertically instead of growing laterally to form continuous films, as shown in figure 20b. In essence, the PVD enabled the synthesis of monolayer MoS_2 with high crystallinity (*i.e.,* triangular domains are widely known as single crystals for TMDs), but it may not be ideal for synthesizing monolayer WS_2 since the solid WS_2 requires even higher evaporating temperature.

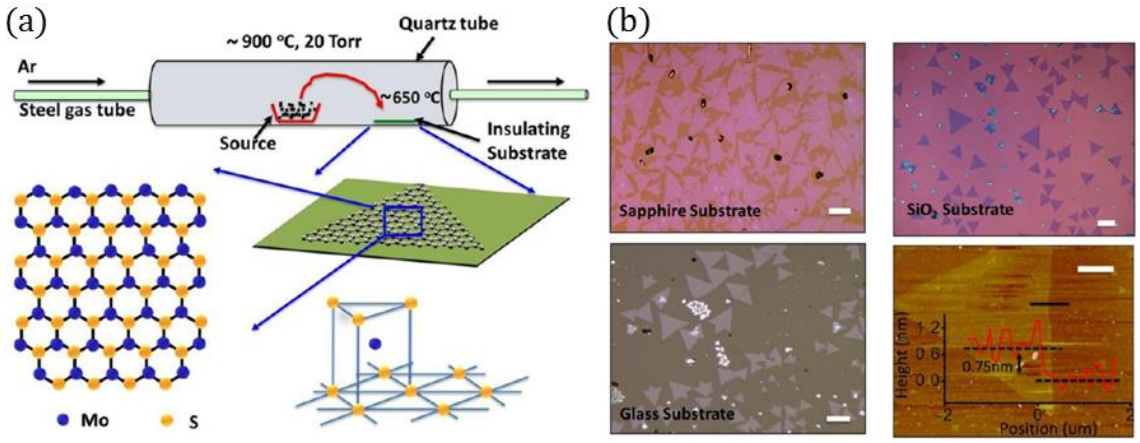

Figure 20. PVD synthesis of monolayer TMDs. (a) Schematic of the synthesis and growth conditions of the monolayer MoS_2 domains by having solid MoS_2 powder as the source. (b) Optical images (scale bar, 10 μm) of MoS_2 monolayers directly grown on insulating substrates such as sapphire, SiO_2 ,and glass, where average crystal thickness is confirmed to be ~0.75 nm (monolayer) by atomic force microscopy (AFM) (scale bar, 3 μm). Figures reprinted (adapted) with permission from: (a) and (b), ref.*(181)*, © 2013 American Chemical Society.

2.4.2.2 Thermal Decomposition of Thiosalts

By just relying on gas flow rate, sample positioning and reaction temperature during a non-catalytic (substrate) vapour deposition, gaining control over the uniformity and

coverage of the TMD layers seemed non-realistic. Efforts therefore went into the investigation of surface-treatment techniques for catalysing the insulating substrates. It was then demonstrated by Liu *et al.* that the thermal decomposition of ammonium thiomolybdate can lead to large-area formation of MoS_2 few-layer-thick thin films (figure 21a).*(182)* In the fabrication process, the insulating substrate was first dip-coated with the thiosalt and then thermally annealed in hydrogen environment at 500 ºC for 1 hr (1^{st} anneal), conforming to the reaction in figure 21 - equation 3. The involvement of H_2 in this reaction effectively prevented the thermal decomposition (figure 21 - equations 1 and 2) from oxidation. However, it was noted that the as-formed MoS_2 could meanwhile decompose in the H_2 gas environment. The synthetic approach hence took in a 2^{nd} annealing treatment at 1000 ºC, where Ar gas and sulphur (S) vapour were introduced to revamp the decomposed MoS_2 regions.

Pre-depositing a TMD-based precursor on desired substrates has empowered the fabrication of TMDs thin layers in the aspect of large-area production, but not in the realm of monolayer uniformity and crystallinity. Evidently, the dip-coating method for the precursor deposition is not ideal for layer control, as a result of which the as-formed MoS_2 thin films in this study are found not in monolayer thickness (figure 21b). Thus, alternative deposition techniques equipped with thickness control are yet to be explored. For the very first time, Liu *et al.* was able to demonstrate FET device performance based on ultra-thin TMD films that were not obtained from exfoliation. The transistor devices adopted a bottom gate geometry which led to the discovery of n-type behaviours with an on/off current ratio of ~10^5 and electron mobility up to 6 $cm^2V^{-1}s^{-1}$ (room-temperature). It is still rational to postulate that the mobility here is jeopardized by the low crystallinity or the incomplete thermolysis upon obtaining the MoS_2 thin films, as compared to the aforementioned exfoliated ones (figure 10a).

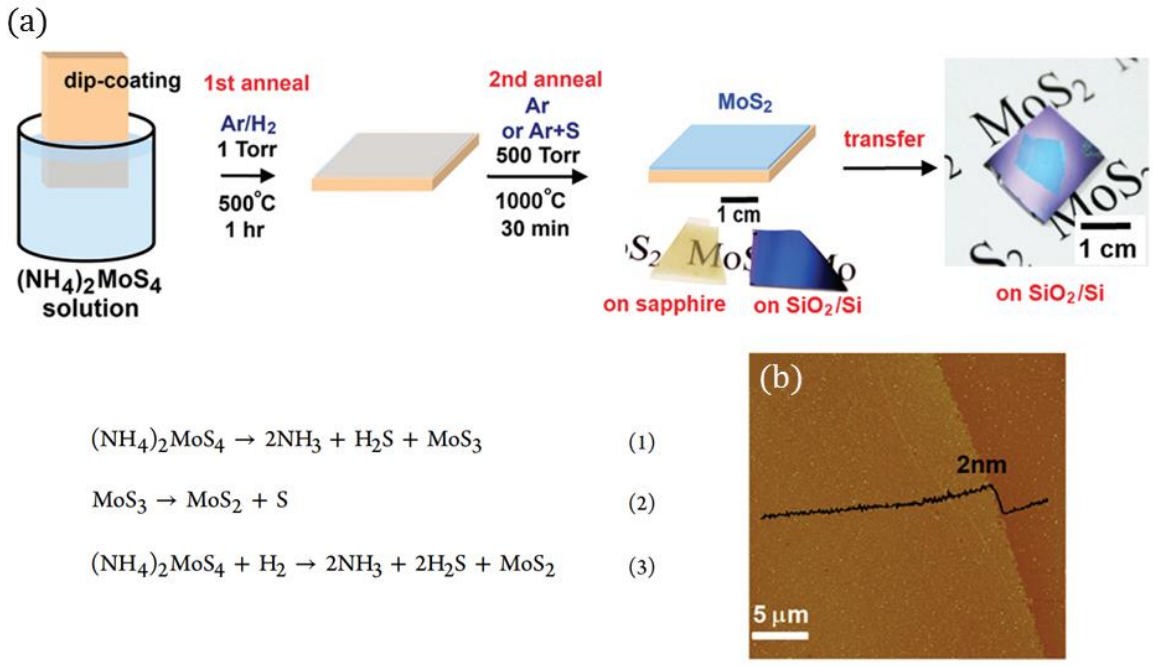

Figure 21. Synthesis of TMD thin films by thermal decomposition. (a) Schematic demonstration of the two-step thermolysis process for the synthesis of large-area MoS_2 thin films on insulating substrates. Either the SiO_2/Si or sapphire substrate was dip-coated in $(NH_4)_2MoS_4$ solution and then processed according to the two-step annealing protocols that are designed to facilitate the reactions presented in equation (1)-(3). The as-developed MoS_2 thin films can be transferred onto other arbitrary substrates. (b) AFM image showing that the MoS_2 thin film is of few-layer thickness. Figures reprinted (adapted) with permission from: (a) and (b), ref.*(182)*, © 2012 American Chemical Society.

2.4.2.3 Vapour Phase Sulphurization of Metal or Metal Oxide Thin films

Quantitative attempts of depositing ultra-thin TMD precursors with atomic precision were found to be viable with transition metals or transition metal oxides. In 2012, Lou's group produced large-area MoS_2 layers *via* the sulphurization of atomically-thin Mo layer (1-5 nm) that was pre-deposited on SiO_2 by an e-beam evaporator (figure 22a). The synthetic process is accomplished when the Mo thin layer is fully transformed into a MoS_2 thin film. In other words, the thickness and dimensions of the as-obtained MoS_2 thin film are totally

subjected to the pre-deposition conditions of the Mo layer. Figure 22b presents a typical distribution of the as-formed MoS_2 layers from mono- (yellow arrow) to few-layers. Despite this method providing a promising opportunity for TMD large-area synthesis on arbitrary insulating substrates, the instability of Mo layer deposition has led to low throughput in monolayer MoS_2 as well as large variation in layer thickness. Additionally, the FET devices based on this material rendered metallic transport behaviour with a substantially low on/off current ratio, which underlines the fact that this synthetic approach can potentially lead to incomplete sulphurization of the metallic Mo layers.

Thermal evaporation of TMD precursors entails the implementation of templates for large-area TMD synthesis but not for TMD growth with high crystallinity (large single-crystal size). To improve this, Wang *et al.* managed to deposit MoO_2 rhomboidal microcrystals (templates) on SiO_2/Si substrates for the growth of bilayer MoS_2 crystals (*i.e.,* occasionally monolayers were observed). Figure 22c helps elaborate that the nucleation and growth of the MoO_2 microcrystals were initiated by the sulphur-reduced MoO_3 precursor that was delivered in a mixture of Ar and S vapour at 650-850 ºC. The bilayer/monolayer MoS_2 was then grown on top of these MoO_2 templates *via* further sulphurization at 850-950 ºC for 0.5 h (figure 22d: left). Longer growth times resulted in thicker MoS_2 crystals, where the growth of additional layers was limited by the diffusion rate of S atoms through the pre-existing MoS_2 layer. After the reaction, the as-grown MoS_2 layers were peeled-off from the MoO_2 templates and placed onto arbitrary insulating substrates (SiO_2/Si in figure 22d: right) by the polymethylmethacrylate (PMMA)-assisted nanotransfer printing technique.*(183)* Owing to these crystalline templates for sulphurization, the as-obtained MoS_2 bilayers are of high crystallinity, based on which the FET devices demonstrated on/off current ratios from 10^4 to 10^6 and field-effect mobilities from 0.1 to 0.7 $cm^2V^{-1}s^{-1}$ (room-temperature). It is viable to reflect that the PMMA-pealing process may cause damage to the MoS_2 crystalline quality after transfer, which consequently manifests as low carrier mobility in FETs. Above all, the greatest disadvantage for this method is that the

as-grown MoS_2 crystals are strongly dependent on the nature of the pre-existing MoO_2 templates (isolated and small), whereby the fabrication of TMD continuous films with large single-crystal sizes is inexecutable.

As a result of the work in figure 22a, the thermal evaporation technique was quickly improved for the synthesis of monolayer WS_2 domains *via* sulphurization of WO_3 atomic layers deposited on SiO_2/Si with only 5-20 Å thickness. Similar to the set-up in figure 22c, the WS_2 monolayers were formed by heating the WO_3/SiO_2 sample at 800 ºC for 30 min while the sulphurization was induced by heating solid S powder placed upstream at 250 ºC (*i.e.,* Ar was used as the delivery gas at atmospheric pressure). Although this improvement has quantitatively increased the production of highly crystalline monolayers, the thin-film continuity over large area was compromised (figure 22e and f), likely owing to the reduced amount of the WO_3 precursor and the non-uniform WO_3 deposition. Irrefutably, the inconsistent deposition thickness provided by the thermal evaporation technique has led to a trade-off between the layer thickness and thin-film continuity of the as-synthesized TMD layers.

Recently, a new set of techniques for metal-oxide deposition was developed to alleviate the previous bewilderment. Figure 22g represents that the WO_3 metal oxide can be deposited onto SiO_2/Si substrates using the atomic-layer-deposition (ALD) technique, by which high thickness controllability and wafer-scale uniformity become viable in practice. The WO_3 films were introduced onto the substrates *via* the reaction between O_2 plasma and the $WH_2(iPrCp)_2$ precursor at a growth temperature of 300 ºC. Subsequently, as opposed to the common sulphurization approach, the WO_3 films here were sulphurized by the H_2S gas at 1000 ºC for 30 min. The outcome of this approach was iconic, in which mono- to few-layer TMD (WS_2) thin films were produced for the first-time with wafer-scale uniformity, as shown in figure 22h. The WS_2 layer number across the wafer-dimension was precisely tuned by the number of WO_3-ALD cycles. As to intrinsic characteristics, the monolayer WS_2 exhibited an electron mobility (3.9 $cm^2V^{-1}s^{-1}$ at room-temperature) that

was two orders of magnitude higher than the CVD-produced WS_2 FET device.*(184)* However, it is worthwhile to argue that this method could be industrially inapplicable since the precursor is not widely available and the WO_3 growth is limited to chemically active substrates only.*(185)* In spite of the fact that the average single-crystal size within the wafer-scale WS_2 monolayers was not determined, the methodology used (metal/metal-oxide sulphurization) was not so different from the above ones after all. Following the trend of graphene development, the prospect of TMD applications may potentially lie with the CVD approach facilitating the wafer-scale production of single crystalline monolayers.

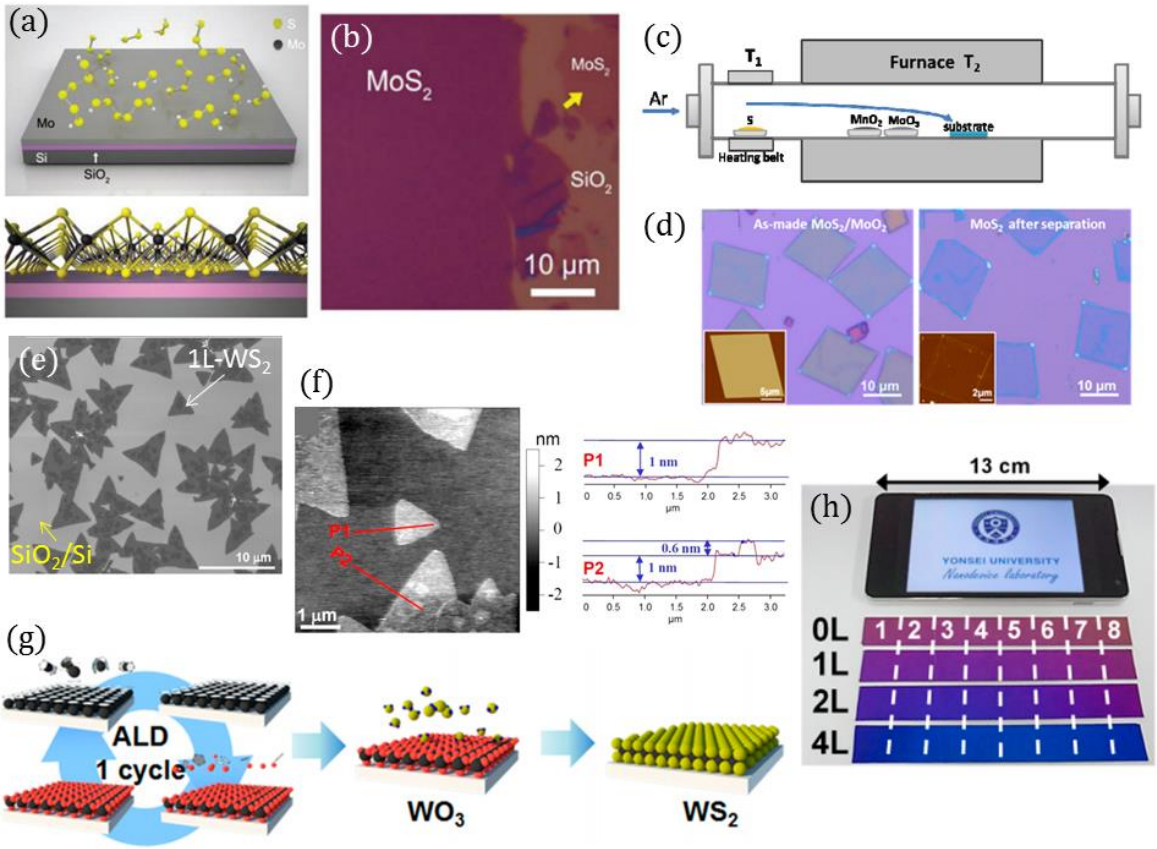

Figure 22. Synthesis of mono- to few-layer MoS_2 and WS_2 through direct sulphurization. (a) Schematic illustration of sulphurizing the Mo metallic thin film that was pre-deposited on the SiO_2/Si substrate for the synthesis of MoS_2 thin layers. (b) Optical image of the as-formed MoS_2 thin layers on the SiO_2/Si substrate. Yellow arrow highlights the monolayer MoS_2 region while darker contrast represents few-layer MoS_2 regions. (c) Schematic of the synthetic set-up used for growing MoS_2/MoO_2 thin flakes shown in (d). (d) Optical images of the as-synthesized MoS_2/MoO_2 thin

flakes (left) and the bilayer MoS_2 flakes (right) that were transferred from the MoS_2/MoO_2. The insets: AFM images of the corresponding thin flakes, where the thickness of MoS_2/MoO_2 and MoS_2 is ~120 nm and ~1.5 nm, respectively. (e) SEM images of the monolayer (1L) WS_2 domains that were formed under the sulfurization of ultra-thin WO_3 (5-20Å) thermally deposited on SiO_2/Si substrates. (f) AFM images of the monolayer WS_2 domains with line profiles P1 and P2 confirming 1-nm monolayer thickness. (g) Synthetic procedures for fabricating large-area WS_2 thin sheets on SiO_2/Si substrates through sulphurization of WO_3 films prepared by ALD. (h) Photograph of mono-, bi-, tri-layer WS_2 sheets synthesized on SiO_2/Si substrates achieving a 13-cm large-scale coverage. Figures reprinted (adapted) with permission from: (a) and (b), ref.*(186)*, © 2012 Wiley; (c) and (d), ref.*(187)*, © 2013 American Chemical Society; (e) and (f), ref.*(19)*, © 2012 American Chemical Society; (g) and (h), ref.*(188)*, © 2013 American Chemical Society.

2.4.2.4 Vapour Phase Reaction of Transition Metal Oxides with Chalcogen

The very first attempt for fabricating monolayer TMDs using the CVD approach was demonstrated for MoS_2 by Lee *et al.*, where a chemical vapour reaction of MoO_3 and S precursors was directly introduced at the SiO_2/Si substrate placed directly above the MoO_3 precursor with the SiO_2 side faced-down (figure 23a).*(184,189)* In this all-vapour-precursor environment, it is believed that the MoO_3 vapour was first reduced by the S vapour to an intermediate compound, MoO_{3-x}, which further reacted with S to form MoS_2 crystals on the substrate. While graphene CVD synthesis uses copper as the catalytic substrate, the MoS_2 here employs seed-implemented SiO_2/Si substrates for high-throughput monolayer production (*i.e.,* seeding reagents generally include graphene oxide (rGO), perylene-3,4,9,10-tetracarboxylic acid tetrapotassium salt (PTAS), perylene-3,4,9,10-tetracarboxylic dianhydride (PTCDA)). More importantly, the as-obtained MoS_2 monolayers were found in large quantity of triangular single crystals, as a result of which the CVD approach has been used most frequently in the recent TMD development. Thanks to the fact that the as-developed CVD approach was not substrate-dependent,

later CVD synthesises of TMD were successfully conducted on a variety of other insulating substrates (figure 23).

By inheriting the previous techniques, Kong's group managed to demonstrate the atmospheric-pressure CVD (APCVD) synthesis for both MoS_2 and WS_2 monolayers on insulating substrates such as sapphire, quartz and SiO_2/Si (figure 23b-e). The WO_3 precursor was used for the synthesis of monolayer WS_2, which hence led to the rise of CVD-synthetic temperature from 650 (MoO_3) to 800 ºC. As to the quality of the monolayers, the MoS_2 FET showed the highest on/off current ratio so far, exceeding 10^7, while having carrier mobility at 1.2 $cm^2V^{-1}s^{-1}$; meanwhile the WS_2 FET generated ~10^5 and a surprisingly low-mobility 0.01 $cm^2V^{-1}s^{-1}$(all at room-temperature).*(184)* On the other hand, it is easy to notice that the CVD method not only produced large quantities of MoS_2 (or WS_2) single crystals but also provided potential opportunities for the realization of monolayer thin films over large-area. Accordingly, Liu's group introduced, in figure 23f, a low-pressure CVD (LPCVD) system provided with independently temperature-controlled precursor regions, by which a centimetre-scale uniform monolayer MoS_2 (figure 23g and h) was synthesized on the freshly-made fluorophlogopite mica ($KMg_3AlSi_3O_{10}F_2$). In lieu of seeding the substrate, the mica substrate is able to instigate monolayer growth due to its atomic flatness as well as chemical inertness joined with its hexagonally arranged in-plane lattice structure. This work implicates the fact that the fabrication of monolayer TMDs over large-area (centimetre-scale) is indeed viable using the CVD approach.

There has been a rising concern for the seeding pre-treatment, which may reduce the performance of the as-synthesized TMD FETs, especially in carrier mobility. Najmaei *et al.* then explored the possibility of using MoO_3 nanoribbons both as the precursor and as the growth initiators.*(190)* Consequently, the FETs fabricated using the as-formed MoS_2 monolayers performed at carrier mobilities that were an order of magnitude higher than the seed-assisted ones, while on/off current ratio was kept at >10^6 (room-temperature). Besides, it was also noted in this study that either the SiO_2/Si substrate edges (figure 23i)

or the edges on SiO_2 surface (figure 23j) could preferentially become the nucleation sites for MoS_2, resulting in non-uniform MoS_2 multi-layer continuous films. For a non-seeded growth substrate, surface smoothness and cleanness are therefore vital to the uniform growth of monolayer TMDs over large-area. Van der Zande *et al.* quickly presented experimental evidences to emphasize this issue, from which extra-large monolayer MoS_2 single crystals (up to 123 μm) were grown directly on ultra-clean SiO_2/Si substrates using freshly prepared precursors (figure 23k and l). The synthetic process was completed by adopting the CVD step-up shown in figure 23a, except using N_2 as the carrier gas. In the pursuit of high-quality TMD synthesis, the surface cleanness and smoothness of provided growth substrates could be more important than the substrate seeding options.

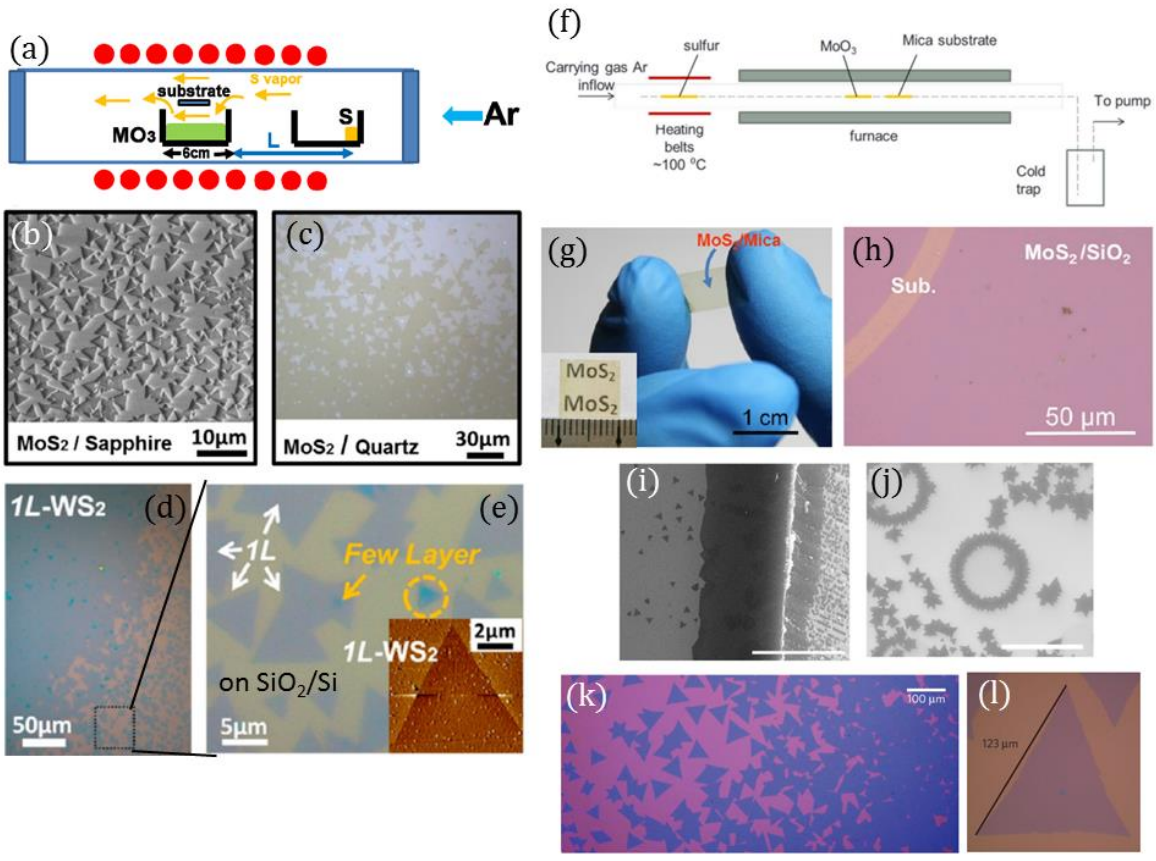

Figure 23. CVD synthesis of monolayer MoS_2 and WS_2 on diverse insulating surfaces. (a) Schematic of the CVD set-up for the synthesis of monolayer MoS_2 on faced-down insulating substrates. M = Mo or W. (b) SEM image of monolayer MoS_2 on the sapphire substrate. (c) Optical

image of monolayer MoS_2 on the quartz substrate. (d) Optical image of monolayer WS_2 on the SiO_2/Si substrate. (e) Enlarged optical image of the marked region in (d), where the inset shows the corresponding monolayer AFM image. (f) Schematic illustration of the CVD method for the production of monolayer MoS_2 thin films on mica substrates. (g) Photograph of a centimetre-scale monolayer MoS_2 thin film deposited on Mica. (h) Optical image of the monolayer MoS_2 thin film transferred onto the SiO_2 substrate (Sub.). (i) SEM image of showing MoS_2 preferentially nucleated along the substrate (SiO_2/Si) edge and over the cross-sectional rough surfaces. Scale bar, 10 μm. (j) SEM image of triangular MoS_2 domains preferentially formed around the artificially-made circular edges on SiO_2 surface. Scale bar, 50 μm. (k) Optical image of large MoS_2 triangular domains merging into continuous films, developed by the CVD method. (l) Example (optical image) of a large monolayer MoS_2 single crystal from (k). Figures reprinted (adapted) with permission from: (a)-(e), ref.*(184)*, © 2013 American Chemical Society; (f)-(h), ref.*(191)*, © 2013 American Chemical Society; (i) and (j), ref.*(190)*, © 2013 Macmillan Publishers Ltd.; (k) and (l), ref.*(36)*, © 2013 Macmillan Publishers Ltd.

By harnessing the CVD techniques developed for the MoS_2 synthesis, it was then possible to produce monolayer WS_2 for the same quality or if not better. As derived from the LPCVD used for growing MoS_2 on mica, Liu's group further proved that the centimetre-scale monolayer growth was likewise feasible for WS_2 (figure 24a and c). In analogy to the characteristic of mica substrate, the hexagonal (0001) plane of sapphire (Al_2O_3) was used as the growth substrate (figure 24b). In addition to the use of S vapour as the reducing agent, it was revealed in Liu's study that the more reductive H_2 (or as-formed H_2S) could expedite the reduction of WO_3 to WO_{3-x} at ~900 ºC, resulting in a more WO_{3-x}-rich environment for WS_2 growth. Intriguingly, monolayer WS_2 domains grown without (figure 24d) or with H_2 (figure 24e) displayed different morphology. The as-obtained FET devices based on WS_2 monolayer thin films showed a considerably lower on/off current ratio, ~10^2, and improved electron mobility, 0.46 $cm^2V^{-1}s^{-1}$ at room-temperature.

An alternative approach to create a WO_{3-x}-rich environment during the CVD process was conceived by Yu's group in 2014. It is depicted in figure 24f that the WO_3 precursor can be reduced thoroughly by an enhanced S concentration environment, which is achieved by enclosing substrates and all precursors in a one-end sealed quartz tube. This small half-sealed deposition chamber was placed in a bigger Ar-ventilated quartz tube with the open end facing the Ar flow direction. The effectiveness of this approach entails the fabrication of monolayer WS_2 single crystals with sizes up to ~178 μm (figure 24g and h). Nevertheless, the synthesis did not render the merge of monolayer WS_2 crystals towards continuous films, which could be referred to either the non-epitaxial SiO_2/Si substrates used or the atmospheric-pressure conditions applied. In other words, it is sensible to propose that, in order to fulfil monolayer TMD uniform thin films, two prerequisites are required; low-pressure (vacuum) environment and epitaxial growth substrate.

Monolayer MoS_2 and WS_2 synthesized on the abovementioned insulating substrates were faced with a dilemma – large single crystals but not continuous thin films or *vice versa*. This is largely due to the catalytic limitations of the insulating substrates, considering the role of metallic substrates in graphene CVD synthesis.*(180,192,193)* It has been difficult for sulphur-based TMDs because there are hardly any metals that do not react with S, but with one exception – gold (Au). Having taken all the previous CVD techniques into consideration, Gao *et al.* actualized the first TMD-CVD synthesis using metallic substrates (Au) for self-limited WS_2 growth (figure 24i). During the synthesis, the Au substrate assisted the dissociation of S_2 dimer which catalytically lowered the barrier energies for the sulphurization of WO_3. The amount of precursors needed, therefore, was reduced significantly, which benefited the formation of monolayer WS_2 with higher uniformity and larger single-crystal size. Figure 24j and k shows the as-obtained single crystals are as large as 400 μm (*i.e.,* the largest ever formed in TMD synthesis). Furthermore, the low solubility of W (< 0.1 atomic% at 800 ºC) in Au prohibited the multi-layer WS_2 growth on the Au substrate caused by the W segregation or precipitation.*(194)* The growth of

monolayer WS_2 on a flexible Au foil has also given access to the large-scale roll-to-roll production that was developed for graphene.*(179)* In back-gated FET devices, the high-quality WS_2 monolayers exhibited the best transport properties hitherto in terms of CVD-synthesized sulphur-based TMD monolayers: a mobility of 1.7 $cm^2V^{-1}s^{-1}$ and an on/off current ratio of ~10^7 at room-temperature.

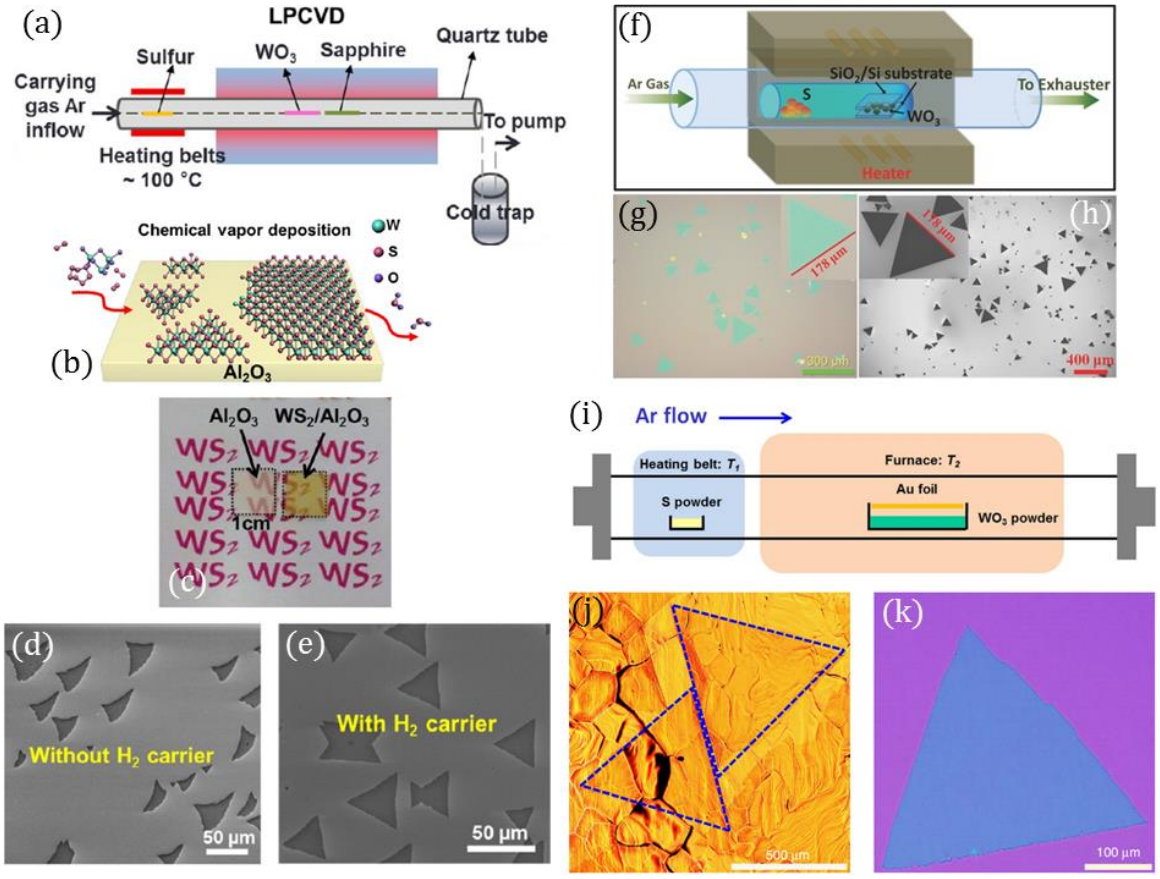

Figure 24. CVD synthesis of large monolayer WS_2 domains. (a) Schematic of the CVD set-up for the synthesis of monolayer WS_2 on sapphire substrates. (b) Schematic demonstration of the involved chemical reactions during the CVD synthesis. (c) Photograph of sapphire substrates with and without the deposition of monolayer WS_2 films. (d) SEM image of monolayer WS_2 flakes produced without H_2 gas. (e) SEM image of monolayer WS_2 domains synthesized with H_2 gas. (f) Schematic of the CVD design for the synthesis of large monolayer WS_2 domains on SiO_2/Si substrates. (g) and (h) Optical and SEM images of monolayer WS_2 domains, with the inset showing an exceptionally large single crystal (~178 μm). (i) The CVD system used for the synthesis of extra-large monolayer WS_2 single crystals on Au foils. (j) and (k) Optical images of the as-obtained

monolayer WS_2 single crystals on the Au and SiO_2/Si substrates, respectively. Figures reprinted (adapted) with permission from: (a)-(e), ref.*(26)*, © 2013 American Chemical Society; (f)-(h), ref.*(195)*, © 2013 Wiley; (i)-(k), ref.*(81)*, © 2015 Macmillan Publishers Ltd, OPEN Access.

From an industrial perspective, using Au for large-scale production of monolayer WS_2 (or MoS_2) could be overly expensive. Park's group hence designed a completely new CVD approach, which is more cost effective, for the synthesis of wafer-scale MoS_2 and WS_2 monolayers directly on insulating SiO_2 (silica) substrates or SiO_2/Si wafers (figure 25a-c). As schematically illustrated in figure 25d, this nascent CVD approach employed gas-phase metal organic (MO) reagents as the precursors for the growth of MoS_2 and WS_2 under the influence of H_2 gas concentration. For the MOCVD, the growth of MS_2 (M = W or Mo) on the non-catalytic wafer substrate was affirmed to be a layer-by-layer growth mechanism that is crucial for high monolayer uniformity (figure 25e). Corresponding to the growth time in figure 25e, figure 25f optically reveals the growth evolution, starting from the nucleation of isolated MS_2 domains, to the formation of full monolayer coverage, and finally to the nucleation of second-layer domains at the grain boundaries of the first layer. In this method, the concentration of H_2 influenced the MX_2 crystallinity differently (figure 25g), as compared to figure 24d and e. Although the MX_2 domain size decreased with increasing H_2 concentration, the domains became perfectly triangular without merging with neighbouring domains at the low H_2 concentration. By optimizing the H_2 concentration together with the S-precursor $(C_2H_5)_2S$, Kang et al. managed to fabricate continuous monolayer MX_2 with high-quality inter-domain stitching over wafer-scale. With respect to the electrical performance, both MoS_2 and WS_2 monolayer FETs showed extraordinary electron mobilities at room-temperature (*i.e.,* higher than those produced by the traditional CVD methods), where MoS_2 and WS_2 were ~29 $cm^2V^{-1}s^{-1}$ at ~10^6 and 18 $cm^2V^{-1}s^{-1}$ at ~10^6, respectively.

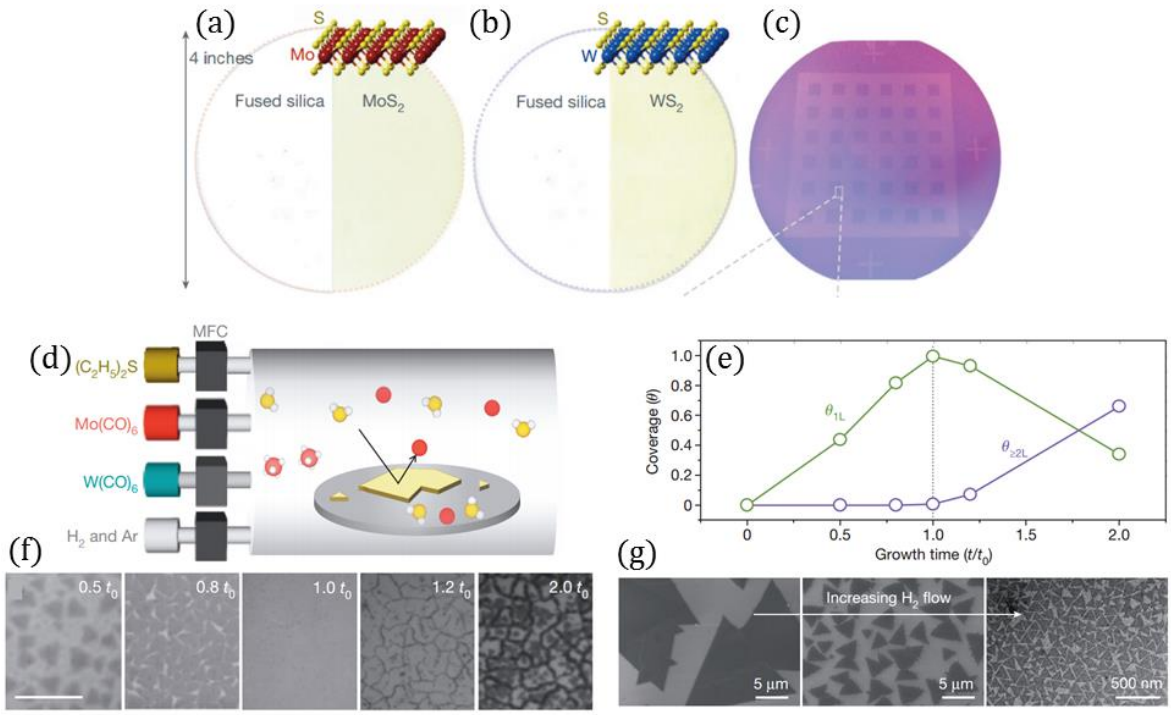

Figure 25. Wafer-scale metal-organic (MO) CVD synthesis of monolayer MoS_2 and WS_2 thin films. (a) and (b) Photographs of monolayer MoS_2 and WS_2 thin films synthesized on 4-inch fused silica substrates, respectively. (c) Photograph of a monolayer MoS_2 thin film grown on the patterned 4-inch SiO_2/Si wafer. (d) Schematic of the MOCVD synthesis set-up, where precursors were introduced by individual mass flow controllers (MFC). The reaction chamber: white ball, carbonyl or ethyl ligand; red ball, Mo or W atom; yellow ball, S atom. (e) Coverage ratio of monolayer and multi-layer (≥two layers) MoS_2 or WS_2 as a function of growth time (t)/optimal growth time (t_0). Optimal growth time meant for full monolayer coverage. (f) Optical images of the as-grown monolayer MoS_2 at corresponding times shown in (e). Scale bar is 10 μm. (g) The evolution of monolayer MoS_2 grain size as a function of increasing H_2 gas flow. From left to right: 5 standard cm^3 min^{-1} (sccm) (SEM image), 20 sccm (SEM) and 200 sccm (TEM). Figures reprinted (adapted) with permission from: (a)-(g), ref.*(196)*, © 2015 Macmillan Publishers Ltd.

2.4.2.5 CVD Fabrication of Monolayer TMD Alloys and Heterostructures

Tuning the bandgap of semiconductors through controllable means has long been carried out to fulfil the demands from the optoelectronic industry. In regard to the semiconducting TMD monolayers, bandgap tuning can be achieved *via* the selection of transition metals and the substitution doping of chalcogenides.*(197)* Given the fact that the semiconducting TMDs are highly isomorphic, manipulating TMD bandgaps with stoichiometry becomes applicable, by which the TMDs can be transformed into ternary van der Waals alloys without phase separation.*(198-200)* These ternary alloys are categorized into two groups: transition metal sublattice (e.g. $Mo_xW_{1-x}S_2$) and chalcogen sublattice (e.g. $MoS_{2(1-x)}Se_{2x}$). They were initially produced by mechanically exfoliating pre-prepared CVD-synthesized TMD alloy bulk crystals.*(199,200)* However, owing to the rapid development of TMD-CVD synthesis, it was hence reasonable that the ternary alloys should be synthesized directly from bottom-up, where monolayer TMD alloys with high crystallinity were attainable, as demonstrated by Gong *et al.* in figure 26a and b. Figure 26c and d exemplify the typical distribution of Se doping sites in the $MoS_{2(1-x)}Se_{2x}$ monolayer alloy under atomic resolution. The as-produced alloy single crystals and continuous thin films were of few-tens and hundreds micrometres, respectively. Although these are premature conditions, this synthetic advancement has added new possibilities to the large-scale application of TMD optoelectronics.

Interestingly, the mixed chalcogen or transition-metal precursors in a CVD reaction do not necessarily generate the types of TMD alloy mentioned above. Instead, they can readily transform the assumed synthetic reaction into a process that leads to the fabrication of epitaxially-grown TMD monolayer heterostructures. In derivation of their CVD process shown in figure 26a, Gong *et al.* mixed transition metals Te and W (as opposed to S and Se) together for the hypothetical synthesis of monolayer $Mo_xW_{1-x}S_2$ alloy (figure 26e). In reality, the differences in nucleation and growth rates between MoS_2 and WS_2 have led to a creation of monolayer MoS_2/WS_2 vertical and in-plane heterostructures (figure 26f-i).

The end product of this synthesis was dominated by the reaction temperature controlled by the single-temperature-zone furnace (same in figure 26a). Accordingly, the vertically stacked bilayers were obtained at 850 ºC while the in-plane lateral heterojunctions were produced at 650 ºC. The establishment of these epitaxially-grown (clean) vertical/in-plane monolayer semiconductor hetero-interfaces, without involving any transfer processes, is particularly desired in high-performance 2D digital electronics and optoelectronics (as pointed out in section 3). As a result, the FETs based on the bilayer MoS_2/WS_2 reached average carrier mobility 25 $cm^2V^{-1}s^{-1}$ and on/off ratio > 10^6 under vacuum; meanwhile the monolayer MoS_2/WS_2 exhibited p-n junction and photovoltaic effect that were reported first-time in non-gated monolayer materials.

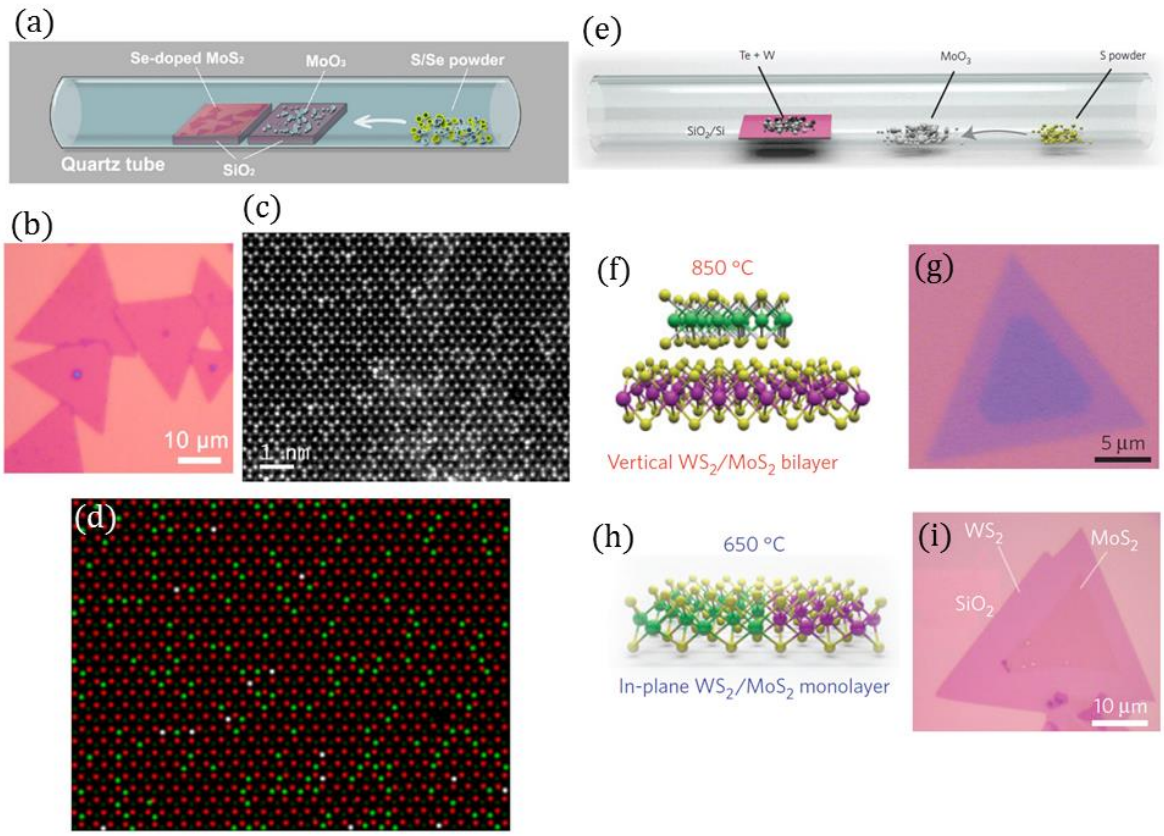

Figure 26. CVD synthesis of monolayer TMD alloys and heterostructures. (a) CVD schematic of the controlled synthesis of monolayer $MoS_{2(1-x)}Se_{2x}$ alloys on SiO_2/Si substrates, achieved by having the S/Se powder placed in the low-temperature region while having MoO_3 at the centre (high-temperature) region of the single furnace (*i.e.,* reaction temperature set at ~800 ºC). (b)

Optical image of the merged monolayer $MoS_{2(1-x)}Se_{2x}$ (x = 0.1) single crystals grown on the SiO_2/Si. (c) ADF-STEM image of the Se-doped MoS_2 monolayer with ~12% local Se concentration. (d) Atomic structure model obtained to show the distribution of single- and double-Se substituted S_2 sites in the Se-doped (~12%) MoS_2 monolayer, where red is Mo site; dark green S_2 site; bright green Se+S site; white, Se_2 site. (e) Schematic of the CVD approach that facilitated the synthesis of vertical and in-plane (all-TMD) MoS_2/WS_2 monolayer heterostructures. (f)-(i) Schematic and optical demonstration of the vertical and in-plane MoS_2/WS_2 monolayer heterostructures in (f) and (g), and (h) and (i), respectively. Figures reprinted (adapted) with permission from: (a)-(d), ref.*(198)*, © 2013 American Chemical Society; (e)-(i), ref. *(139)*, © 2014 Macmillan Publishers Ltd.

The realization of flexible or transparent optoelectronics requires much more than just ultra-thin/2D TMD semiconductors. As covered in the previous chapter, it calls for integrating different classes of 2D materials with distinct properties, in which graphene has been an ideal candidate for electrodes whereas h-BN has been a promising dielectric material. Upon combining them together, the repeating transfer processes involved can introduce unwanted material defects and chemical dopants that are detrimental to the device performance. Therefore, it is looked-for that the CVD synthesis of epitaxially-grown 2D heterostructures is still applicable beyond the regime of TMD materials. Shi *et al.* developed the first monolayer TMD(MoS_2)/graphene heterostructure by conducting the thermolysis approach (figure 21) directly on top of the graphene that was still deposited on copper foil (figure 27a). Although the lattice spacing of MoS_2 is 28% greater than that of graphene, the graphene served well as an epitaxial substrate for MoS_2 monolayers, as shown in figure 27a (the diffraction pattern). The reason to this was that the van der Waals gap between MoS_2 and graphene was able to compensate the large strains caused by the lattice mismatch.

As to the h-BN substrates, Warner's group provided a scalable CVD approach for the growth of monolayer MoS_2 on CVD-grown h-BN multi-layers (figure 27b). The h-BN

continuous films were grown on copper by CVD and then PMMA-transferred on the SiO_2/Si substrates for the CVD-deposition of monolayer MoS_2 (figure 27c). The prerequisite for a monolayer MoS_2 growth was that the MoS_2-growth surface of the h-BN films must be kept PMMA-free. In figure 27d, whether the truncated MoS_2 domains were epitaxially grown on the h-BN is ambiguous in this study. On the other hand, by using the equivalent approach, it was not possible to grow monolayer WS_2 on the h-BN substrates, because the growth temperature of WS_2 would cause the decomposition of the h-BN films. In this context, Okada *et al.* successfully obtained monolayer WS_2 on exfoliated h-BN flakes by modifying the previous CVD system for WS_2 growth (figure 27e and f). There were two adjustments specifically done to lower the WS_2 growth temperature, namely the use of a new solid precursor WCl_6, and an individual low-temperature furnace (Furnace 3) for h-BN/SiO_2. With this approach, the as-formed WS_2 triangular monolayers were epitaxially grown on the h-BN substrate, shown in figure 27g. The comprehension of these hybrid CVD approaches symbolizes a significant advancement in the post-graphene CVD development. Nonetheless, neither the pure TMD nor TMD/graphene (or h-BN) heterostructures are in place to compete with the CVD-produced homostructures, considering their production scale and crystalline quality. New opportunities concomitantly generated in terms of their electronic and optoelectronic applications will, however, invigorate more interest in tackling these challenges.

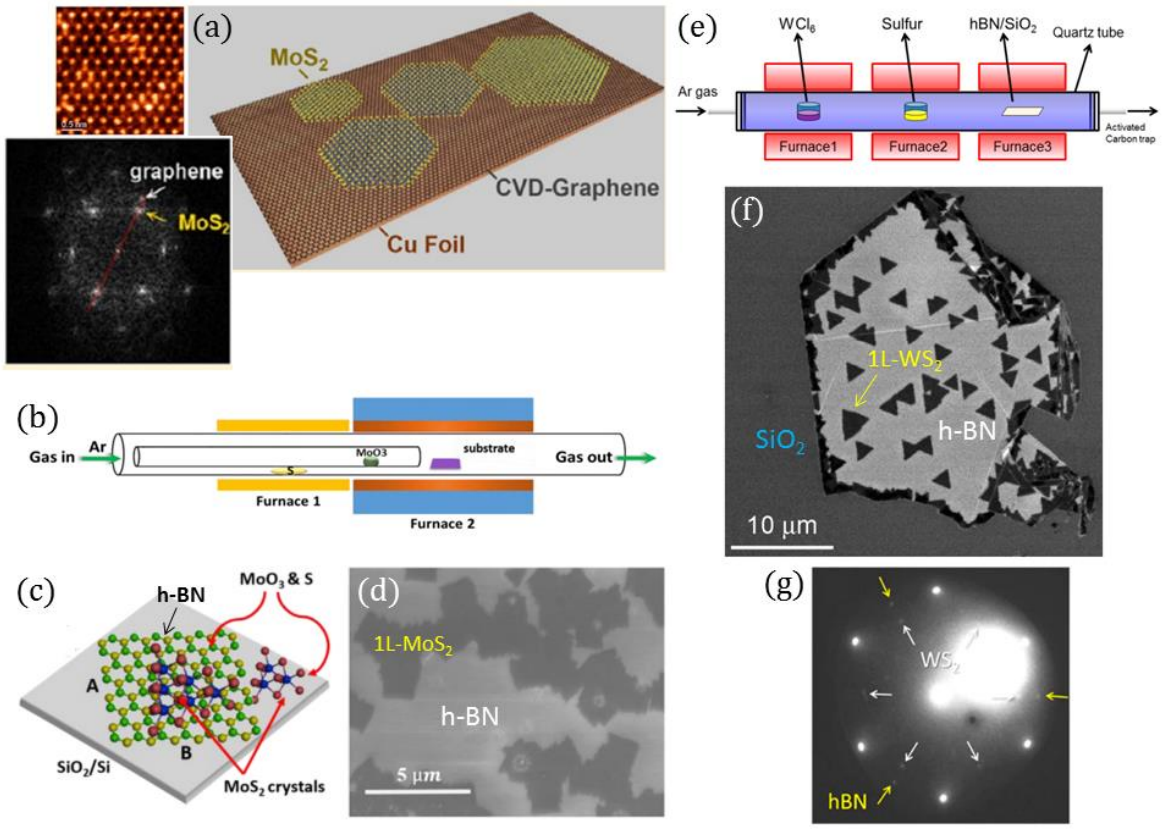

Figure 27. Growth of monolayer TMDs on graphene and h-BN layers. (a) Schematic of the epitaxial growth of monolayer MoS_2 on CVD-grown graphene substrates. The insets: TEM image of the monolayer MoS_2 grown on graphene (top); the electron diffraction pattern indicating the MoS_2/graphene epitaxial growth. (b) Schematic of the CVD set-up for the synthesis of monolayer MoS_2 directly on CVD-grown h-BN substrates. (c) Schematic model of the growth process in (b). (d) SEM image of the MoS_2 monolayer grown on the h-BN multi-layer substrate. (e) Schematic of the CVD system for the epitaxial growth of monolayer WS_2 domains on mechanically exfoliated h-BN multi-layers. (f) SEM image of the triangular WS_2 domains deposited epitaxially on the h-BN flake. (g) Low-energy electron diffraction (LEED) pattern of the WS_2/h-BN heterostructure. Figures reprinted (adapted) with permission from: (a), ref.*(135)*, © 2012 American Chemical Society; (b)-(d), ref.*(83)*, © 2015 American Chemical Society; (e)-(g), ref.*(136)*, © 2014 American Chemical Society.

2.4.2.6 Post-Synthesis Transfer

In furtherance of various TMD thin film applications, the TMD layers synthesized either on insulating or metallic substrates are expected to be transferred intact onto arbitrary substrates. Similar to graphene transfer, PMMA has been widely chosen to act as a temporary scaffold for the TMD transfer processes. The developed TMD transfer methods, thus far, only vary from substrate to substrate, meaning that a transfer approach based on one type of growth substrate is universally applicable for all layered TMD varieties. Accordingly, this section intends to only cover the transfer studies carried on monolayer WS_2, which nevertheless epitomizes the development of transfer techniques in all TMDs.

As schematically elaborated in figure 28a, the first step of the transfer entailed a WS_2 monolayer film (deposited on the SiO_2/Si substrate) being spin-coated with the PMMA dissolved in anisole solution.*(201)* The as-coated PMMA/WS_2 thin film were then lifted-off by the action of an appropriate etchant, such as hydrofluoric acid (HF), as shown in figure 28b. After rinsing in deionized water, the lifted-off film was transferred onto desired surface for WS_2 curing (baking in air at ~180 ºC) and PMMA removal. The PMMA was removed by the action of immersing the cured PMMA/WS_2/new substrate into a solvent such as acetone. Figure 28a and c demonstrated the appearance of the monolayer WS_2 thin film transferred onto a new SiO_2/Si substrate. Note that the HF etchant could be also applied to the detachment of TMD films from other insulating substrates such as micas *(191)*. In addition, alternative choices of the etchant for insulating substrates have also been proven effective, for example, KOH for SiO_2/Si *(19)* and NaOH (or NaOH/NaF) for sapphire.*(26,202)*

In an ideal 2D transfer, the use of chemical processing is maintained at the minimum level. The involvement of the etching process inevitably introduces chemical contaminants or damage to the TMD materials, which potentially undermines their electrical or opto-performance. Xu *et al.* recently developed an etchant-reduced transfer technique for the

WS_2 monolayers CVD-grown on sapphire substrates (figure 28d). The WS_2/sapphire sample was first spin-coated with a thin layer (~100 nm) of polystyrene (PS) instead of PMMA. Subsequent to a brief pre-etching in hot NaOH solution, the PS/WS_2 was promptly (several seconds) peeled-off from the substrate by dropping the PS-coated sample into deionized water. The peeling-off process was a self-initiated process dependent on the capillary force between the hydrophobic PS and the hydrophilic substrate. This rapid PS-mediated transfer has enabled the reduction of damages to the WS_2 samples and the substrates incurred by the long-time etching reactions. As a consequence, the sapphire substrates were able to be used repeatedly for the WS_2 growth, leading to a reduced synthesis cost. After baking on the targeted substrates at 120 ºC (30 min), the WS_2 transfer was completed with the removal of PS in toluene solution.

In response to the large-scale CVD synthesis of high-quality WS_2 monolayers on Au substrates, a different transfer method, electrochemical H_2 bubbling, was developed on the basis of water electrolysis reaction that was tested to be effective in graphene transfer.*(193)* By virtue of the weak interaction between the monolayer WS_2 and the Au substrate, the PMMA-supported monolayer WS_2 film was separated from the Au foil by H_2 bubbles generated by the water electrolysis (figure 28e and f).*(81)* Following the standard procedure of PMMA transfer/removal, the monolayer WS_2 was easily transferred onto polyethylene terephthalate (PET) (figure 28g) and SiO_2/Si substrates (figure 28h) with a highly uniform thickness. Furthermore, it was emphasized that the WS_2-removed Au foil was not involved with the water electrolysis reaction (*i.e.,* Au is chemically inert), which thus highlighted the fact that the Au substrate here could be used repeatedly. In opposition to the previous destructive transfer methods, the reusability of Au substrates was as high as ~700 times in terms of monolayer WS_2 synthesis-transfer cycles. Given the high price of Au, this particular feature has made the large-scale production of monolayer WS_2 using the CVD method more achievable. Besides, Gao *et al.* also integrated the electrochemical bubbling into the roll-to-roll transfer set-up developed

previously for graphene,*(179)* as depicted in figure 28i. In substitution to the PMMA scaffold, the monolayer WS_2 (on Au) was covered roll-to-roll with the thermal release tape (TRT), which was subsequently rolled into the bubbling transfer for the TRT/WS_2 detachment. By roll-to-roll releasing the TRT (with WS_2) on the flexible PET substrate, this high-throughput transfer of monolayer WS_2 has therefore laid the foundation of the large-scale production of transparent flexible electronics and optoelectronics based on monolayer TMDs.

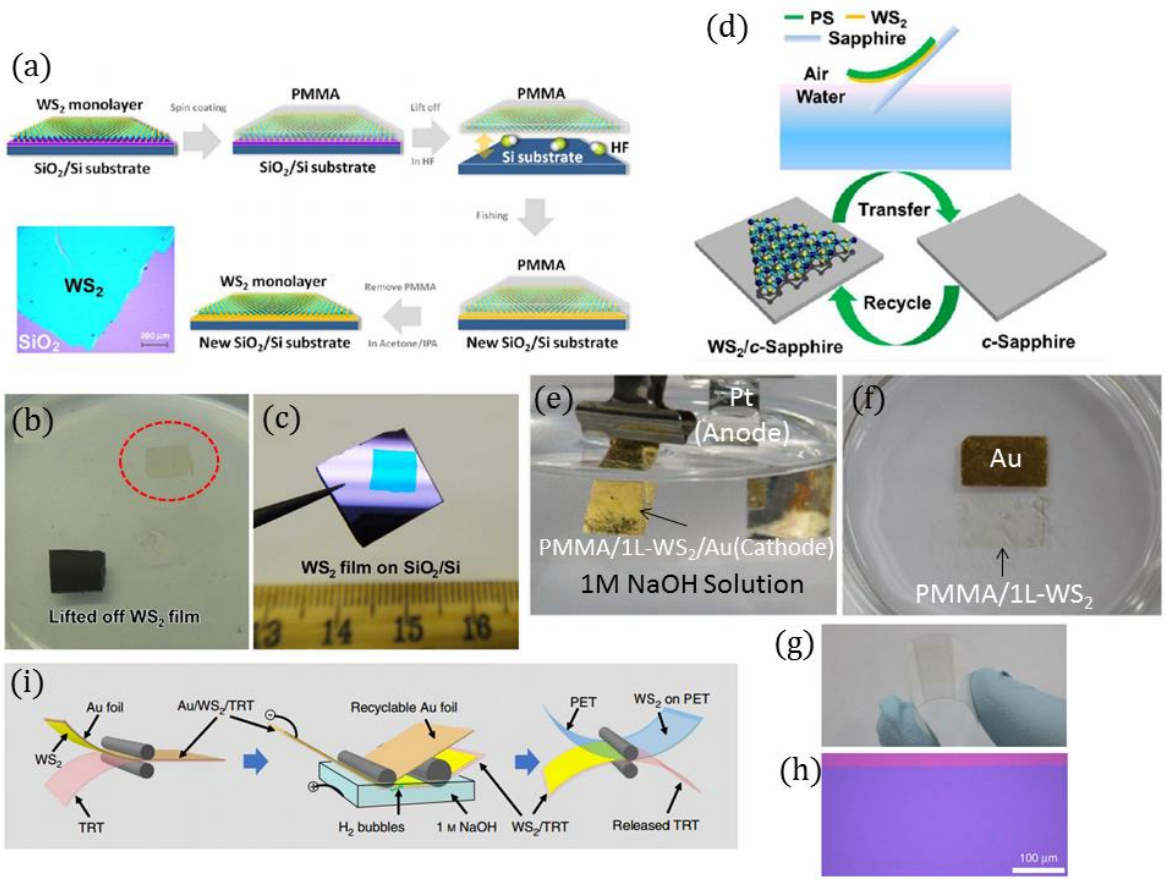

Figure 28. Transfer methods for TMDs (*i.e.*, WS_2) CVD-grown on SiO_2/Si, sapphire, and Au substrates. (a) Schematic of the PMMA-assisted transfer of monolayer WS_2 grown on SiO_2/Si. (b) Photograph of the peeled-off PMMA/WS_2 film floating on hydrofluoric acid (HF). (c) Photograph of the WS_2 monolayer film transferred onto the new SiO_2/Si substrate with PMMA removed in acetone. (d) Schematic of the polystyrene (PS)-mediated transfer of monolayer WS_2/sapphire assisted by the capillary force at air/water interface. (e) Photograph of the electrochemical H_2 bubbling transfer of monolayer (1L) WS_2 grown on the Au substrate (PMMA coated). (f) Photograph of the peeled-off

PMMA/1L-WS_2 film floating on NaOH solution. (g) Photograph of the monolayer WS_2 continuous thin film transferred onto the PET substrate, demonstrating a good flexibility (using the method in (i)). (h) Optical image of the edge region of the monolayer WS_2 thin film transferred onto the SiO_2/Si substrate. (i) Schematic illustration of the roll-to-roll transfer method equipped with the H_2 bubbling process for the WS_2/Au films. Figures reprinted (adapted) with permission from: (a)-(c), ref.*(201)*, © 2013 American Chemical Society; (d), ref.*(22)*, © 2013 American Chemical Society; (e)-(i), ref.*(81)*, © 2015 Macmillan Publishers Ltd.

2.5 Characterisation of WS_2 (MoS_2) Monolayers

All of the abovementioned works on monolayer WS_2 or MoS_2 were sought-after due to the great respect paid towards understanding the fundamental properties of 2D TMDs. To exploit different properties, from physical to chemical, one must have access to a combination of characterisation techniques; such as optical, scanning electron, atomic force, (scanning) transmission electron microscopy, photoluminescence and Raman spectroscopy, and a wide range of electronic device fabrication techniques. A typical characterisation process for monolayer WS_2 as well as for the rest of 2D TMD semiconductors often starts with identification. It is only useful when a 2D material of interest has first been confirmed to be correct (*i.e.,* chemical composition and layer thickness) before accrediting the as-discovered properties. This review only intends to discuss the identification aspect that is vested in characterisation tools pertaining to the research interest of the thesis. Specifically, they are optical, atomic force, scanning electron and (scanning) transmission electron microscopy, joined by Raman (PL) spectroscopy.

2.5.1 Optical Microscopy

Monolayer WS_2 (or MoS_2) is merely three-atom-thick, with a transparency of 95%, due to which one would suspect it to be simply non-characterisable by optical microscopy (OM). This is indeed the case, unless the TMDs are placed on a type of substrate that evokes a large optical contrast between the substrate material and the TMD of interest. In the majority of works the enhanced optical contrast of TMD mono- to multi-layers is created using 90 nm or 300 nm thick SiO_2 on Si wafer substrates, knowing that the thin layer of oxide can provide an additional distance for optical interactions. Except being able to optically observe TMD thin flakes on the SiO_2/Si substrates, OM was demonstrated to have the ability to precisely characterise TMD layer thickness with the help of the optical contrast value uniquely possessed by each TMD layer number (figure 29).*(203)* As one example from Li *et al.*'s work, the optical identification of layer numbers in MoS_2 thin flakes placed on both 90 nm and 300 nm SiO_2/Si substrates was feasible from monolayers all the way to 15-layers (figure 29a, d and e). Whether optically observing in colour or individual RGB channels, the contrast difference (C_D) was able to be determined as the optical contrast of the TMD thin film subtracting with that of the chosen SiO_2/Si substrate. Hence, the variation of C_D values (RGB channels) plotted as a function of layer number was generated, shown in figure 29c and f. By referring to these quantitative values, a quick and high-throughput realization of the MoS_2 layer thicknesses was possible.

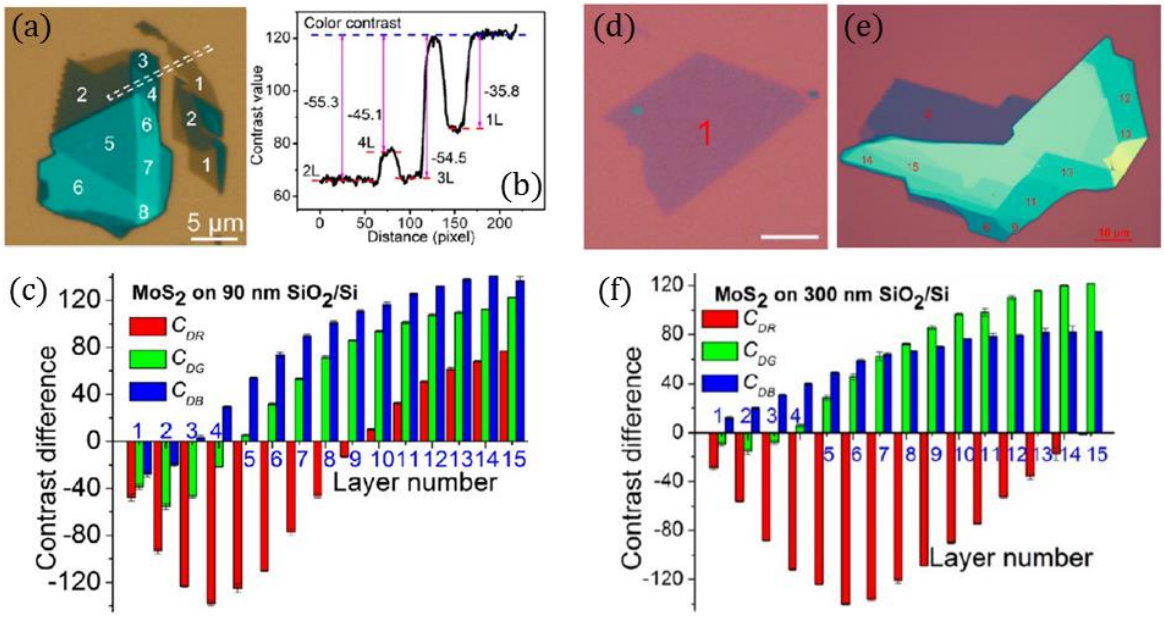

Figure 29. Thickness identification of mechanically-exfoliated MoS_2 flakes on SiO_2/Si substrates using optical microscopy. (a) Colour optical image of the MoS_2 flakes on the SiO_2 (90 nm) /Si provided with highlighted layer numbers and the corresponding contrast profile shown in (b). (c) Optical contrast differences of 1-15L MoS_2 on 90 nm SiO_2/Si measured in red (C_{DR}), green (C_{DG}) and blue (C_{DB}) channels, plotted against MoS_2 layer number. (d) and (e) Colour optical images of the monolayer (1L) MoS_2 flake and 2-15L MoS_2 flakes deposited on the SiO_2 (300 nm)/Si. Scale bar, 5 μm (d) and 10 μm (e). (f) The plot in (c) but on 300 nm SiO_2/Si. Figures reprinted (adapted) with permission from: (a)-(f), ref.*(203)*, © 2013 American Chemical Society.

In supplement to the previous work, Jo *et al.* investigated the optical contrast differences in mono-, bi-, and tri-layer WS_2 (figure 30). The thickness of SiO_2 was preferred to be 90 nm for the purpose of maintaining the best optical contrast for WS_2 layers under the optical microscope. Likewise, the optical contrast of mono- to tri-layer WS_2 was quantitatively analysed with respect to the as-obtained RGB images (figure 30c). It is worthwhile noting that the intensity of the WS_2 (or MoS_2) contrasts against the 90 nm (or 300 nm) SiO_2/Si substrate is strongly dependent on the quality of the CCD camera employed to acquire the image. As a result, there is a reason to believe that the efficacy of

the TMD optical characterisation can vary from system to system, for which other qualitative characterisation methods has been conjunctively implemented too.

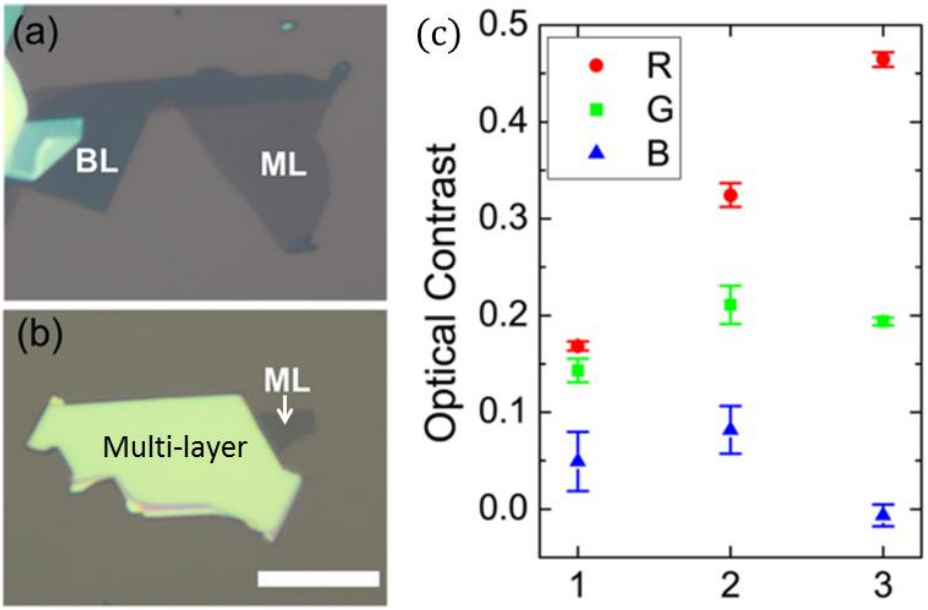

Figure 30. Thickness identification of monolayer (ML), bilayer (BL), and multi-layer (>2L) WS_2 on SiO_2/Si using optical microscopy. (a) and (b) Colour optical images of MLs, BLs and multi-layers deposited the SiO_2 (90 nm)/Si substrates. Scale bar, 10 μm. (c) The average optical contrast in red, green and blue channels for mono-, bi-, and trilayer WS_2 flakes. Figures reprinted (adapted) with permission from: (a)-(c), ref.*(70)*, © 2014 American Chemical Society.

2.5.2 Raman Spectroscopy

Raman spectroscopy is another non-destructive method for quantifying TMDs' layer number, and also for identifying a material as one of the TMDs. This characterisation technique is not only fast in acquiring structural and electronic information that are of high-spectral and -spatial resolution, but also widely applicable in both laboratory and industrial conditions. It is a technique that has been used extensively on graphene in respect of identifying structural damage, functional groups, layer numbers and chemical modifications caused by synthetic processing, material handling and electronic

doping.*(204,205)* All of which are understood through a quantitative analysis of different peak positions and compositions in the Raman spectrum obtained upon laser excitation. Raman spectroscopy provides signature information about one lattice system through its built-in spectrometer that is able to detect energy variations from the incident optical photons caused by inelastic scattering from the vibrational phonons in the lattice. The vibrational mode of these phonons is however subjected to change with the lattice structure and the incident photonic energy (laser wavelength). Different vibrational modes result in different Raman peak intensities and peak positions. For layered materials, it is the layer thickness that influences the Raman peak profiles greatly.

Figure 31 a and b, respectively, demonstrate a typical Raman spectrum of monolayer WS_2 obtained at 514.5 nm (green) and 488 nm (blue) excitation wavelength (λ_{ex}). In majority of reports, the $E^1_{2g}(\Gamma)$ and $A_{1g}(\Gamma)$ at the Brillouin zone centre (Γ) were defined as the most prominent first-order vibrational modes in WS_2 (the inset in figure 31b). In addition, a zone-edge mode was characterised as the longitudinal acoustic mode at the M point of the Brillouin Zone (LA(M)). The vibration of longitudinal acoustic phonons is a collective effort of atomic compression and expansion along the direction of propagation. While the Raman spectrum of monolayer WS_2 at λ_{ex} = 488 nm was dominated by the first-order modes (figure 31b), Terrones's group was able to reveal many other second-order peaks using resonant Raman scattering at λ_{ex} = 514.5 nm (figure 31a). Among which, a new second-order mode, 2LA(M), was separated first-time from the contribution of the $E^1_{2g}(\Gamma)$ mode at 356 cm^{-1} using the Lorentzian fitting, even though the two modes were overlapped in the spectrum. Note that observing the high-intensity 2LA(M) was only possible because of the as-claimed double-resonant Raman process that was specifically limited to the electronic band structure of the monolayer at the excitation of 514.5 nm.*(206)* All the remaining peaks were from the hybrid effects of phonon vibrational modes mentioned formerly.

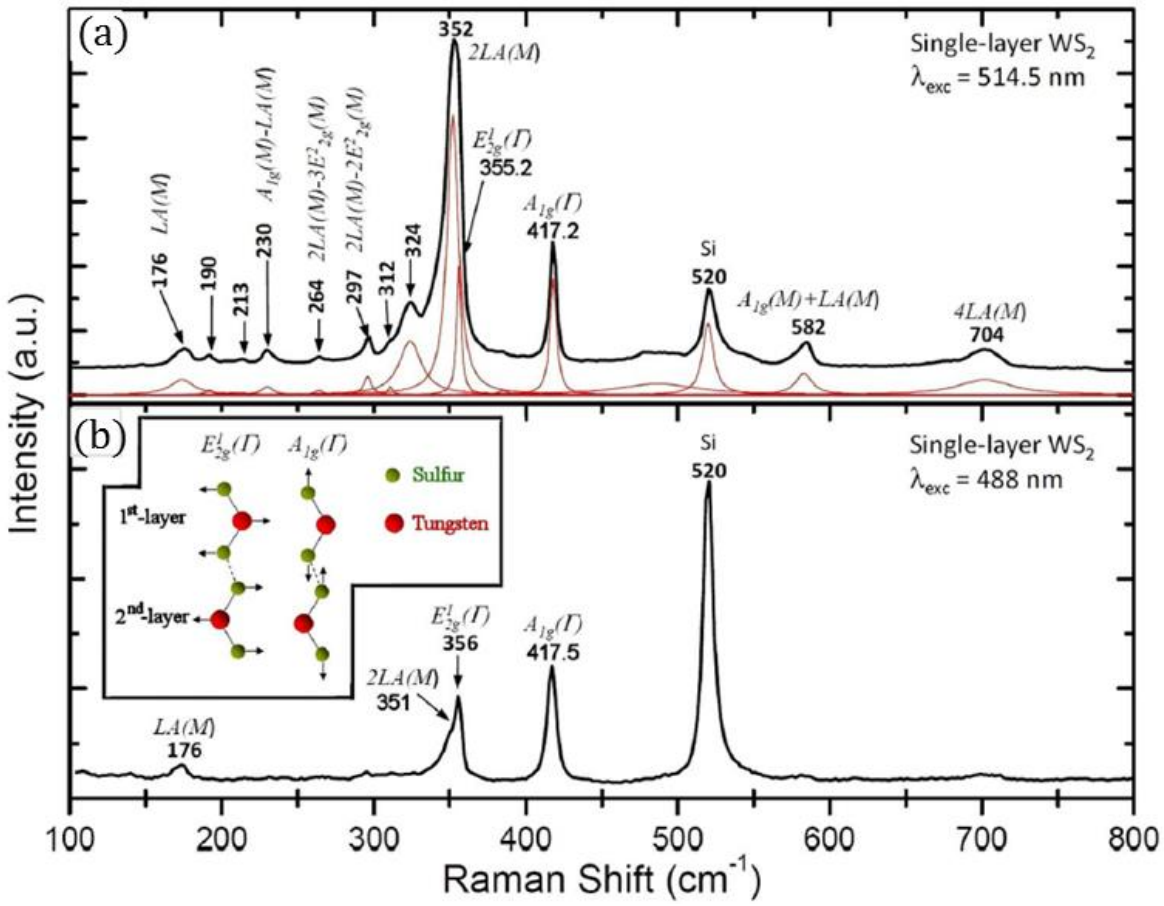

Figure 31. Room-temperature Raman Spectra acquired from a monolayer WS_2 using the 514.5 nm (green) and 488 nm (blue) laser excitation, respectively. The spectral peaks in (a) are fitted with Lorentz algorithm. The inset in (b) illustrates the vibrational displacement of WS_2 atoms caused by the in-plane phonon mode $E^1_{2g}(\Gamma)$ and the out-of-plane phonon mode $A_{1g}(\Gamma)$ in neighbouring WS_2 layers, where the dashed line represents the weak interlayer van der Waals force. Figures reprinted (adapted) with permission from: (a) and (b), ref.*(206)*, © 2013 Macmillan Publishers Ltd, OPEN Access.

Taking into account the major WS_2 Raman peaks obtained at different λ_{ex}, figure 32a unveils the transition of signature peak positions (frequencies) as the layer thickness increases from monolayer to bulk. It is not difficult to notice that the $A_{1g}(\Gamma)$ mode blue-shifts (hardening) when increasing the WS_2 layer number. This was attributed to the fact that the out-of-plane vibrations were increasingly counteracted by the accumulating van

der Waals interactions among layers. On the contrary, the $E^1_{2g}(\Gamma)$ and 2LA(M) modes demonstrate negligible redshifts upon increasing layer thickness. Due to the close proximity of these two peaks, it was claimed that their shift in peak position was of the same order of magnitude as the error bar, meaning that the dependency of these two peak positions on layer thickness might be inconclusive. In this study, all λ_{ex} provided the same peak-shift tendencies.

The intensity of the abovementioned signature peaks at respective λ_{ex} is compared at the layer numbers indicated in figure 32b. In spectra acquired at λ_{ex} = 488 and 647 nm, the ratio of the two most intense peak features, $E^1_{2g}(\Gamma)$ and $A_{1g}(\Gamma)$, does not exhibit significant changes as the layer number increases. At λ_{ex} = 514 nm, the two dominating peak intensities are found in the as-separated 2LA(M) and $A_{1g}(\Gamma)$ phonon modes. As a result, the relative intensity of 2LA(M)/$A_{1g}(\Gamma)$ has experienced a soaring increase in monolayer WS_2. This distinct difference for monolayer WS_2 as opposed to that for greater thicknesses gives a unique access to monolayer characterisation of WS_2 using Raman spectroscopy at λ_{ex} = 514 nm. In cases that the resonant Raman scattering is not activated but a green laser is used for excitation (*i.e.,* 2LA(M) is not eligible to be separated), the intensity ratio of $E^1_{2g}(\Gamma)$/$A_{1g}(\Gamma)$ could be used instead for the monolayer characterisation, owing to their overlapping peak positions.

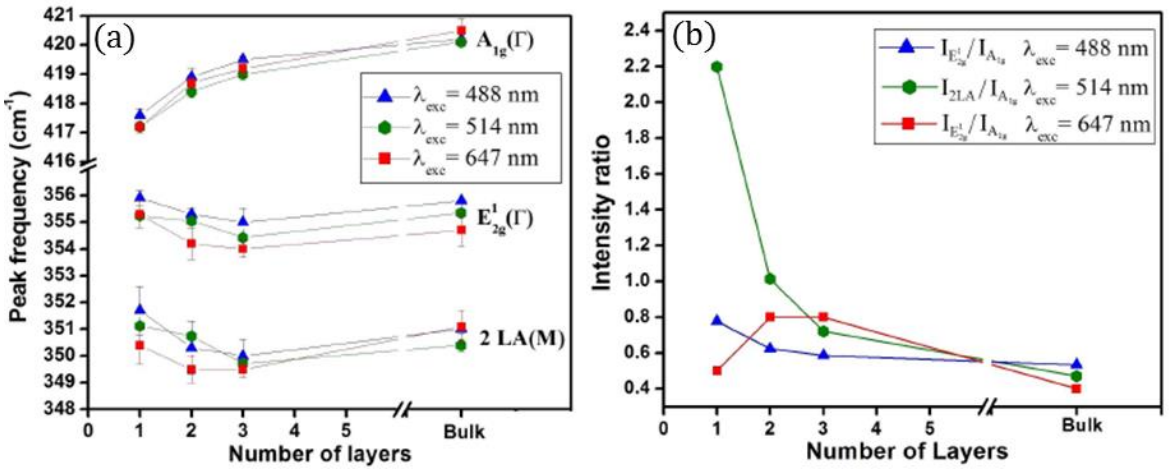

Figure 32. Raman peak frequencies (a) and peak intensity ratios (b) of WS_2 from monolayer to bulk WS_2 at 488 nm (blue), 514 nm (green), and 647 nm (red) laser excitation wavelength. Figures reprinted (adapted) with permission from: (a) and (b), ref.*(206)*, © 2013 Macmillan Publishers Ltd, OPEN Access.

2.5.3 Atomic Force Microscopy

Atomic force microscopy (AFM) is particularly powerful when measuring the roughness of a sample surface and is capable of producing lateral (XY-coordination) mapping of surface topologies at sub-nanometre resolution. So in the research of 2D materials, AFM has been often employed to examine the surface smoothness and layer thickness of an as-synthesized thin film before and after the transfer. As opposed to Raman spectroscopy, AFM generates numerical layer thicknesses that lead to determination of all layer numbers in TMD thin films. According to surface conditions and application demands, the operation of AFM takes the form of three different modes: contact, tapping and non-contact. It has been widely acknowledged that atom-thin materials are susceptible to surface adsorbates, which has given rise to variable thickness measurements in graphene (on SiO_2/Si) using the non-contact mode.*(207)* Although this problem has not been pointed out specifically in TMDs, contact mode is hence suggested in order to obtain conclusive AFM results (as demonstrated in graphene). However, there are times that the non-contact or tapping mode must be employed to prevent the sample from getting damaged by the AFM tip. For instance, free-standing monolayer MoS_2 was preferred in piezoelectric device applications owing to the fact that substrates incur unwanted doping and parasitic charges.*(208)* Besides, free-standing (suspended) TMD ultra-thin layers are essential for experiments that help investigate the innate electronic and physical properties.*(209-211)* Regardless contact or non-contact mode, the measured thickness of monolayer WS_2 varies for from 0.7 nm to 1nm on SiO_2/Si substrates, depending on the

synthetic approach used.*(19,26,68,195,212)* Since mechanical exfoliation always provides the cleanest/smoothest monolayers, the thickness of WS_2 monolayers grown by CVD is always slightly higher due to the accumulation of adsorbates from the chemical reaction at low-energy sites (*i.e.,* grain boundaries and domain edges). With the knowledge of the actual monolayer WS_2 thickness, the layer number of WS_2 thin films at a given thickness ought to be accurately derived. Thus, the layer-dependency of WS_2 Raman spectra is often confirmed with the corresponding AFM profiles.

2.5.4 Scanning Electron Microscopy

In characterising layered TMD materials, the purpose of using scanning electron microscopy (SEM) is similar to what is expected from OM, that is to examine the crystallinity and domain size of as-grown (often CVD-grown) TMDs on a range of substrates mentioned previously. SEM is as high-throughput as OM but more capable of observing nanoscale objects that are certainly beyond ordinary OM's magnification. SEM imaging takes place when a sample surface is raster-scanned by an electron beam, with which secondary electrons emitted from the electron-excited atoms are collected by an Everhart-Thornley detector located aside. As a result, the same ideology found in OM for layer identification is no longer viable in this context. SEM generates strong topographic contrast due to its noteworthy depth of field (on the order of millimetres). In respect of probing low-energy surface structures (2D materials or carbon nanotubes), one requires the application of an in-column (in-lens) secondary electron detector from which the layer number of graphene was quantitatively identified relying on the as-generated thickness-dependent SEM contrast. After all, the necessity for characterising TMD layers under SEM with regard to the layer thickness is not yet recognized.*(213)*

When using SEM for 2D TMD characterisations, one particular challenge arises in observing the ultra-thin TMDs on insulating substrates (*i.e.,* SiO_2, sapphire and mica)

resulting from the nature of TMD synthesises and applications. In order to prevent electron charging across the non-conductive surface of these substrates, a low accelerating voltage (ranging from 1 to 3 kV) has been always preferred in probing TMD surface structures. For example, Zhang *et al.* successfully characterised monolayer WS_2 grain boundaries on the sapphire substrate after exposure to mild oxidation.*(26)* On the other hand, recent zeal towards using Au substrates for high-quality MoS_2 and WS_2 growth has given an easy access to SEM imaging, and also leveraged the role of SEM in 2D TMD studies.*(81,212,214)* The high-contrast SEM images generated from metallic Au (polycrystalline) substrates provide a unique opportunity to observe monolayer MoS_2 (or WS_2) domains whilst realizing their correlation to the crystallographic orientation of Au grains.

2.5.5 (Scanning) Transmission Electron Microscopy

Transmission electron microscopy (TEM) is a characterisation tool that discloses the crystalline information of an ultra-thin specimen at the atomic level. Compared to other optical and electron microscopy techniques, TEM's resolution is neither limited by the large optical wavelength nor the random scattering of surface electrons. Its high-resolution imaging capability originates from the interaction of electron beams (at accelerating voltages from 80 to 200 kV) transmitted through the specimen, from which electron density, phase and periodicity are generated on relevant analytical devices for display. In a modern TEM set-up, the transmitted electrons are processed by a charge-coupled device (CCD) camera, through which TEM images are recorded consecutively so that the evolution of the specimen under electron irradiation can be captured at a high temporal resolution. A TEM apparatus capable of resolving nanoscale lattice structures at both high spatial and temporal resolution is often referred as high-resolution TEM (HRTEM). To further boost the resolution down to angstrom scale, recent developments have led to the

aberration corrected HRTEM (AC-TEM), that is operating HRTEM with corrections for spherical aberration and reduced chromatic aberration.*(215)*

In general, TEM characterisation can be difficult in terms of sample preparation. An adequate TEM sample must be transparent enough for electrons to pass through, which hence provokes sample thinning processes such as mechanical grinding, electro-polishing and ion milling. In this regard, however, the high-crystallinity and atom-thick 2D materials are of the best thickness one can get, provided that they are also facile to be obtained. Therefore, monolayer WS_2 as well as other 2D TMDs is a perfect and ready specimen for HRTEM imaging and related characterisations.

Many characteristic phenomena can be made use of when a high-energy beam of electrons strike through a few-nanometre-thick material. During HRTEM imaging, signature X-rays constantly emit from the specimen as a result of the high-energy electron bombardment. In the interest of understanding the specimen's composition, they can be harnessed and analysed by a built-in energy-dispersive X-ray (EDX) spectrometer. Figure 33a shows a characteristic EDX spectrum for monolayer WS_2, as to which SEM has struggled to provide. It is because the depth of field provided by SEM is significantly greater than a monolayer TMD (~1 nm), whereas the EDX signal from the ultra-thin TMD is easily overwhelmed by that from its supporting substrate. Furthermore, the wavelength of high-energy electrons is known to be a few thousandths of a monolayer TMD thickness. The TMD atoms hence are diffraction gratings for the electrons, and some of which are diffracted according to the crystal structure. On the TEM CCD camera, these diffracted electrons manifest as diffraction patterns, which are particularly useful information for studying crystalline structures and orientations. In figure 33b-d, Terrones's group utilized a common feature in HRTEM – the selected area aperture – to block the electron beam except for the region of the triangular WS_2 single crystal shown in figure 33c. The as-generated electron diffraction pattern (figure 33d) is a so-called selected area electron diffraction (SAED) pattern, where each pair (red line) of spots represents a direction/plane

within the crystal (*i.e.,* [100] direction helps confirm the triangular WS_2 edges are zigzag-terminated). In a folded monolayer WS_2 region (figure 33e), the SAED pattern tends to show multi-pairs of spots (figure 33f) due to the skew-stacked WS_2 layers provoking disoriented planes for additional electron diffraction patterns. It is also well-known that overlaid 2D crystal planes that are rotated from one another entail the observation of Moiré patterns in HRTEM (figure 33g). In contrast, a non-folded monolayer WS_2 should render direct imaging of the honeycomb-like WS_2 lattice structure, shown in figure 33h. The folded regions of monolayer WS_2 on a TEM grid are, nonetheless, valuable when it comes to identifying the layer thickness. Figure 33i depicts a typical HRTEM image taken at the edge of a folded WS_2 monolayer film, in which a single dark line contrast embodies the monolayer crystallinity.

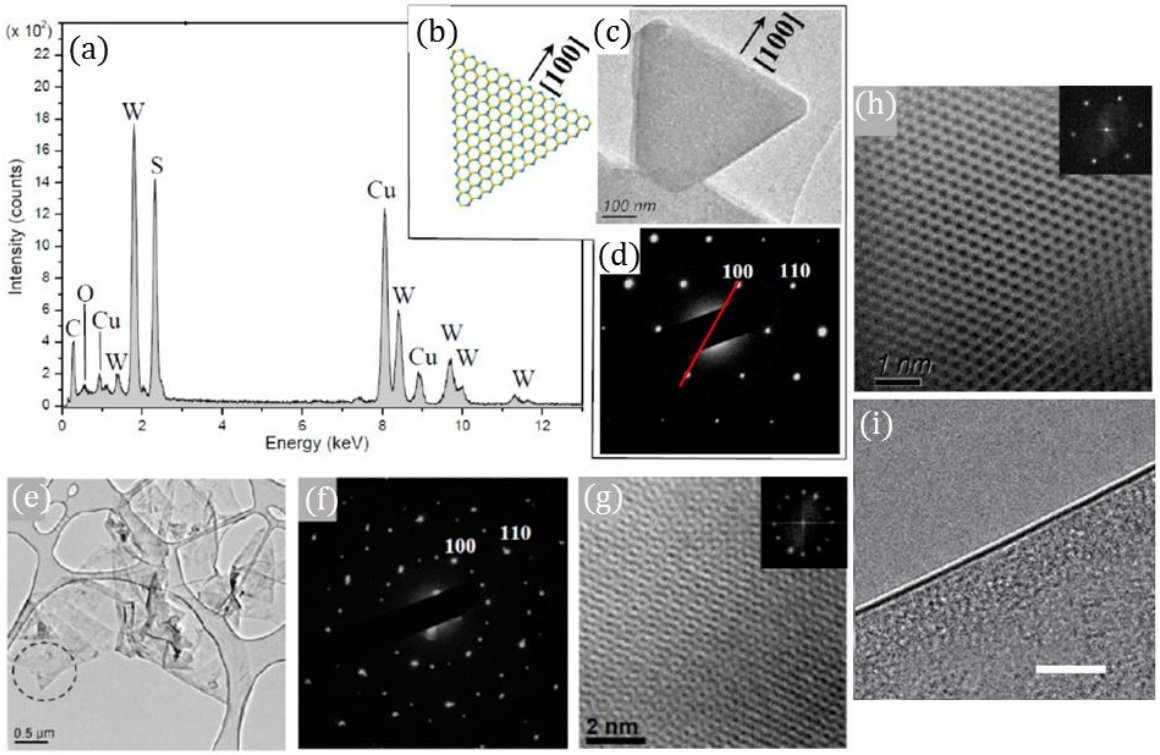

Figure 33. TEM characterisation of monolayer WS_2. (a) EDX spectrum from a single-domain monolayer WS_2 crystal. (b)-(d) Atomic model, low-magnification TEM image, and SAED pattern, respectively, of a triangular WS_2 monolayer single crystal confirming the zigzag-edge termination (*i.e.,* perpendicular to the [100] crystalline direction). (e)-(g) Low-magnification TEM image, SAED

pattern, HRTEM phase-contrast image, respectively, of monolayer WS_2 folded after transferring onto the TEM grid. (h) A HRTEM image obtained from a monolayer WS_2 single crystal. (i) HRTEM image of a folded WS_2 edge confirming the monolayer nature. Figures reprinted (adapted) with permission from: (a)-(h), ref.*(19)*, © 2012 American Chemical Society; (i), ref.*(216)*, © 2013 Macmillan Publishers Ltd.

The single crystallinity is an important index for the quality of 2D-TMD CVD synthesis. Polycrystallinity is formed because of single crystals that are CVD-grown in different crystal orientations. In this category, HRTEM-SAED should be the most qualified characterisation approach. Figure 34a-c demonstrate that a large-area single crystallinity (~400 μm) can be mapped out by tracking the change of crystalline direction in SAED patterns collected individually. This lateral SAED mapping technique has been the most common approach for realizing the single-crystal size across large-areas (dark-field HRTEM image is useful when crystal domains are smaller than the selected area aperture).*(20,21,36,81)*

In addition to HRTEM characterisation, more related works have been done by using TEM equipped with scanning operational mode (STEM). Instead of focusing the electron beam at one place, the STEM's imaging beam is raster-scanned across the specimen. By taking on an annular dark-field (ADF) detector, this added scanning mode is especially powerful for TMDs (*i.e.,* asymmetric atomic weight) because it allows the STEM to acquire atomic contrast that is subjected to atomic weight. While providing atomic resolution by scanning atom-by-atom, the detector is able to collect scattered electrons that are strongly dependent on atomic weight. The indistinguishable W or S atom contrast from phase-contrast-based HRTEM can therefore be identified directly using this imaging technique in STEM (figure 34d-g), often known as high-angle annular dark-field (HAADF) imaging. In many occasions, a HRTEM is built exclusively for STEM imaging, but it should still possess all the functionalities discussed in figure 33. The STEM imaging shown in figure

34f and g implies that the SAED technique could also be used to detect or characterize tilt (high-/low-angle) grain boundaries on the basis of the misorientation angles unveiled in SAED patterns.

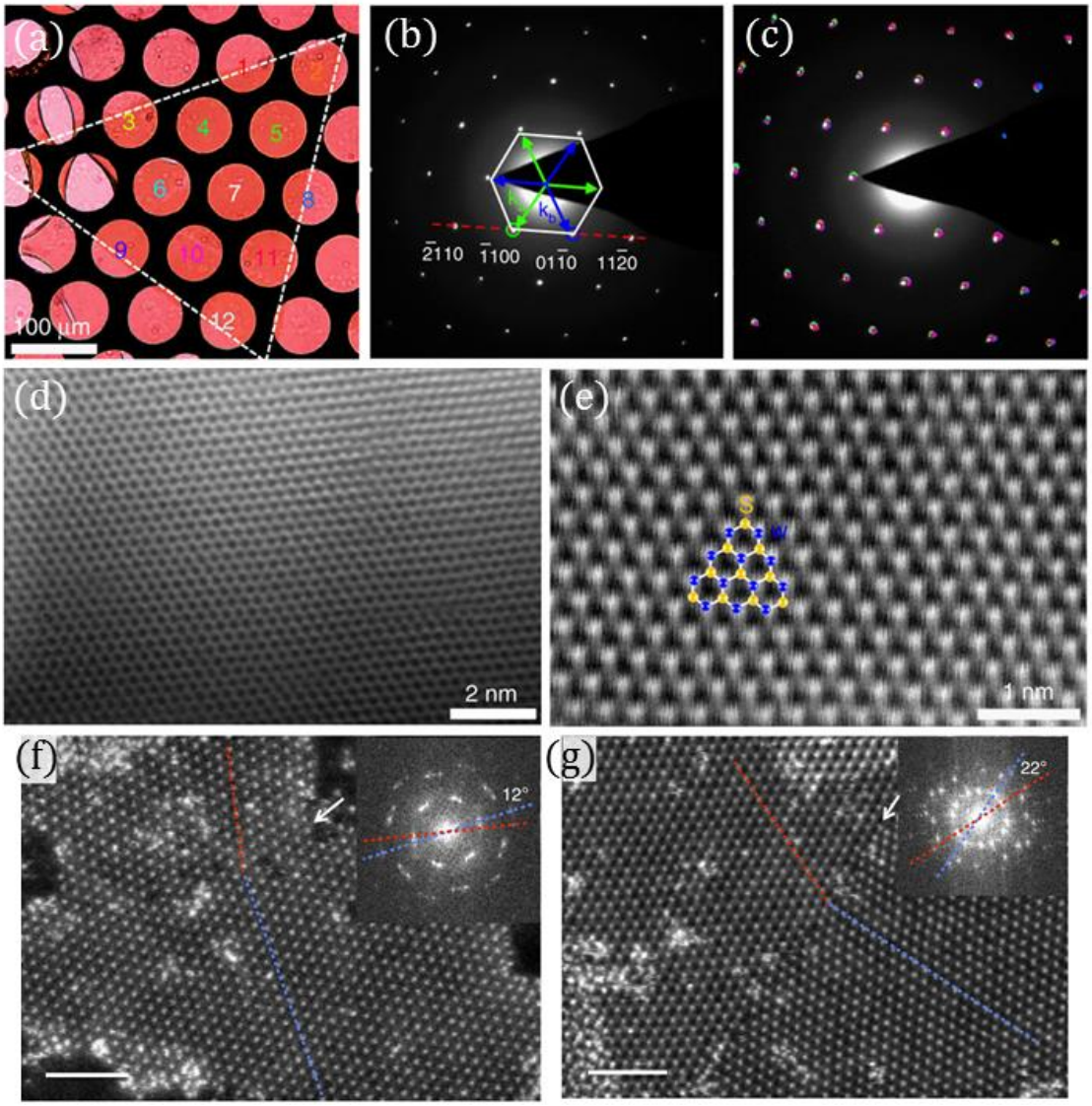

Figure 34. STEM characterisation of monolayer WS_2. (a) Optical image of a 400μm-WS_2 monolayer single crystal transferred on the TEM grid. (b) An example of SAED patterns obtained from the monolayer WS_2 in (a) demonstrating a hexagonal crystalline structure. (c) Overlaid images of colour-coded 12 SAED patterns corresponding to the colour-coded hole numbers shown in (a). (d) and (e) Aberration-corrected ADF-STEM images of the monolayer WS_2 in (a), provided with highlighted W and S atoms in (e). (f) and (g) ADF-STEM images, respectively, of low- (12º) and high-angle (22º) grain boundary, along with the insets showing the relevant SAEDs. Figures

reprinted (adapted) with permission from: (a)-(e), ref.*(81)*, © 2015 Macmillan Publishers Ltd; (f) and (g), ref.*(35)*, © 2014 Macmillan Publishers Ltd.

2.6 Conclusion

It took more than a decade of global research in order for graphene to be produced in large-scale and used in a variety of applications. In comparison to graphene, 2D TMDs did not enter the mainstream research until only a few years ago, underlining that it is too premature to envision the industrialization of 2D TMDs. However, it is possible that the learning curve for 2D TMDs is much steeper than it was for graphene. This may be attributed to a few facts: first, graphene's synthesis techniques are transferrable for 2D TMDs; second, the application framework of 2D materials has already been established by graphene in some areas; third, instead of one material the 2D-TMD category is much more diversified, leading to a collective advancement due to highly cross-referable experiments carried out on 2D TMDs. On the other hand, the unique semiconducting property of some 2D TMDs demands a whole set of new application and characterisation tools that have never been encountered with graphene, which yet thwarts the progression of 2D TMDs. Above all, regardless of the application, further development of 2D TMDs will need improvement of synthesis techniques that can be readily industrialized. In this context, developing the synthesis of monolayer WS_2, though for one, has implications for all 2D TMDs. Relevant studies being carried out on individuals are in fact part of the collective efforts bringing 2D TMDs beyond academia.

2.7 Reference

1. Geim, A. K.; Novoselov, K. S. The Rise of Graphene. *Nat. Mater.* **2007***, 6*, 183-191.

2. Chhowalla, M.; Shin, H. S.; Eda, G.; Li, L.; Loh, K. P.; Zhang, H. The Chemistry of Two-Dimensional Layered Transition Metal Dichalcogenide Nanosheets. *Nat. Chem.* **2013***, 5*, 263-275.
3. Yang, J.; Lu, T.; Myint, Y. W.; Pei, J.; Macdonald, D.; Zheng, J.; Lu, Y. Robust Excitons and Trions in Monolayer $MoTe_2$. *ACS Nano* **2015***, 9*, 6603-6609.
4. Radisavljevic, B.; Radenovic, A.; Brivio, J.; Giacometti, V.; Kis, A. Single-Layer MoS_2 Transistors. *Nat. Nanotechnol.* **2011***, 6*, 147-150.
5. Wang, Q. H.; Kalantar-Zadeh, K.; Kis, A.; Coleman, J. N.; Strano, M. S. Electronics and Optoelectronics of Two-Dimensional Transition Metal Dichalcogenides. *Nat. Nanotechnol.* **2012***, 7*, 699-712.
6. Benameur, M. M.; Radisavljevic, B.; Heron, J. S.; Sahoo, S.; Berger, H.; Kis, A. Visibility of Dichalcogenide Nanolayers. *Nanotechnology* **2011***, 22*, 125706.
7. Castro Neto, A. H.; Novoselov, K. Two-Dimensional Crystals: Beyond Graphene. *Materials Express* **2011***, 1*, 10-17.
8. Tsirlina, T.; Feldman, Y.; Homyonfer, M.; Sloan, J.; Hutchison, J. L.; Tenne, R. Synthesis and Characterization of Inorganic Fullerene-Like WSe_2 Material. *Fullerene. Sci. Technol.* **1998***, 6*, 157-165.
9. Lu, X.; Utama, M. I. B.; Lin, J.; Gong, X.; Zhang, J.; Zhao, Y.; Pantelides, S. T.; Wang, J.; Dong, Z.; Liu, Z.; Zhou, W.; Xiong, Q. Large-Area Synthesis of Monolayer and Few-Layer $MoSe_2$ Films on SiO_2 Substrates. *Nano Lett.* **2014***, 14*, 2419-2425.
10. Radisavljevic, B.; Whitwick, M. B.; Kis, A. Integrated Circuits and Logic Operations Based on Single-Layer MoS_2. *ACS Nano* **2011***, 5*, 9934-9938.
11. Jariwala, D.; Sangwan, V. K.; Late, D. J.; Johns, J. E.; Dravid, V. P.; Marks, T. J.; Lauhon, L. J.; Hersam, M. C. Band-Like Transport in High Mobility Unencapsulated Single-Layer MoS_2 Transistors. *Appl. Phys. Lett.* **2013***, 102*, 173107.
12. Lopez-Sanchez, O.; Lembke, D.; Kayci, M.; Radenovic, A.; Kis, A. Ultrasensitive Photodetectors Based on Monolayer MoS_2. *Nat. Nanotechnol.* **2013***, 8*, 497-501.
13. Yin, Z.; Li, H.; Li, H.; Jiang, L.; Shi, Y.; Sun, Y.; Lu, G.; Zhang, Q.; Chen, X.; Zhang, H. Single-Layer MoS_2 Phototransistors. *ACS Nano* **2012***, 6*, 74-80.
14. Sundaram, R. S.; Engel, M.; Lombardo, A.; Krupke, R.; Ferrari, A. C.; Avouris, P.; Steiner, M. Electroluminescence in Single Layer MoS_2. *Nano Lett.* **2013***, 13*, 1416-1421.
15. Liu, L.; Kumar, S. B.; Ouyang, Y.; Guo, J. Performance Limits of Monolayer Transition Metal Dichalcogenide Transistors. *IEEE Trans. Electron Dev.* **2011***, 58*, 3042-3047.
16. Zhu, Z. Y.; Cheng, Y. C.; Schwingenschloegl, U. Giant Spin-Orbit-Induced Spin Splitting in Two-Dimensional Transition-Metal-Dichalcogenide Semiconductors. *Phys. Rev. B* **2011***, 84*, 153402.
17. Xiao, D.; Liu, G.; Feng, W.; Xu, X.; Yao, W. Coupled Spin and Valley Physics in Monolayers of MoS_2 and Other Group-VI Dichalcogenides. *Phys. Rev. Lett.* **2012***, 108*, 196802.

18. Zhao, W.; Ghorannevis, Z.; Chu, L.; Toh, M.; Kloc, C.; Tan, P.; Eda, G. Evolution of Electronic Structure in Atomically Thin Sheets of WS_2 and WSe_2. *ACS Nano* **2013***, 7*, 791-797.
19. Gutierrez, H. R.; Perea-Lopez, N.; Elias, A. L.; Berkdemir, A.; Wang, B.; Lv, R.; Lopez-Urias, F.; Crespi, V. H.; Terrones, H.; Terrones, M. Extraordinary Room-Temperature Photoluminescence in Triangular WS_2 Monolayers. *Nano Lett.* **2013***, 13*, 3447-3454.
20. Rong, Y.; He, K.; Pacios, M.; Robertson, A. W.; Bhaskaran, H.; Warner, J. H. Controlled Preferential Oxidation of Grain Boundaries in Monolayer Tungsten Disulfide for Direct Optical Imaging. *ACS Nano* **2015***, 9*, 3695-3703.
21. Rong, Y.; Fan, Y.; Koh, A. L.; Robertson, A. W.; He, K.; Wang, S.; Tan, H.; Sinclair, R.; Warner, J. H. Controlling Sulphur Precursor Addition for Large Single Crystal Domains of WS_2. *Nanoscale* **2014***, 6*, 12096-12103.
22. Xu, Z.; Zhang, Y.; Lin, S.; Zheng, C.; Zhong, Y. L.; Xia, X.; Li, Z.; Sophia, P. J.; Fuhrer, M. S.; Cheng, Y.; Bao, Q. Synthesis and Transfer of Large-Area Monolayer WS_2 Crystals: Moving Toward the Recyclable Use of Sapphire Substrates. *ACS Nano* **2015***, 9*, 6178-6187.
23. Yu, Y.; Li, C.; Liu, Y.; Su, L.; Zhang, Y.; Cao, L. Controlled Scalable Synthesis of Uniform, High-Quality Monolayer and Few-layer MoS_2 Films. *Sci. Rep.* **2013***, 3*, 1866.
24. Jeon, J.; Jang, S. K.; Jeon, S. M.; Yoo, G.; Jang, Y. H.; Park, J.; Lee, S. Layer-Controlled CVD Growth of Large-Area Two-Dimensional MoS_2 Films. *Nanoscale* **2015***, 7*, 1688-1695.
25. Wang, S.; Rong, Y.; Fan, Y.; Pacios, M.; Bhaskaran, H.; He, K.; Warner, J. H. Shape Evolution of Monolayer MoS_2 Crystals Grown by Chemical Vapor Deposition. *Chem. Mater.* **2014***, 26*, 6371-6379.
26. Zhang, Y.; Zhang, Y.; Ji, Q.; Ju, J.; Yuan, H.; Shi, J.; Gao, T.; Ma, D.; Liu, M.; Chen, Y.; Song, X.; Hwang, H. Y.; Cui, Y.; Liu, Z. Controlled Growth of High-Quality Monolayer WS_2 Layers on Sapphire and Imaging Its Grain Boundary. *ACS Nano* **2013***, 7*, 8963-8971.
27. Gao, L.; Ni, G.; Liu, Y.; Liu, B.; Castro Neto, A. H.; Loh, K. P. Face-to-Face Transfer of Wafer-Scale Graphene Films. *Nature* **2014***, 505*, 190-194.
28. Yazyev, O. V.; Louie, S. G. Electronic Transport in Polycrystalline Graphene. *Nat. Mater.* **2010***, 9*, 806-809.
29. Grantab, R.; Shenoy, V. B.; Ruoff, R. S. Anomalous Strength Characteristics of Tilt Grain Boundaries in Graphene. *Science* **2010***, 330*, 946-948.
30. Plummer, J. D.; Deal, M. D.; Griffin, P. B. Silicon VLSI Technology. *Prentice Hall* **2000**.
31. Li, X.; Magnuson, C. W.; Venugopal, A.; An, J.; Suk, J. W.; Han, B.; Borysiak, M.; Cai, W.; Velamakanni, A.; Zhu, Y.; Fu, L.; Vogel, E. M.; Voelkl, E.; Colombo, L.; Ruoff, R. S. Graphene Films with Large Domain Size by a Two-Step Chemical Vapor Deposition Process. *Nano Lett.* **2010***, 10*, 4328-4334.
32. Zhou, H.; Yu, W. J.; Liu, L.; Cheng, R.; Chen, Y.; Huang, X.; Liu, Y.; Wang, Y.; Huang, Y.; Duan, X. Chemical Vapour Deposition Growth of Large Single Crystals of Monolayer and Bilayer Graphene. *Nat. Commun.* **2013***, 4*, 2096.

33. Petrone, N.; Dean, C. R.; Meric, I.; van der Zande, A. M.; Huang, P. Y.; Wang, L.; Muller, D.; Shepard, K. L.; Hone, J. Chemical Vapor Deposition-Derived Graphene with Electrical Performance of Exfoliated Graphene. *Nano Lett.* **2012***, 12*, 2751-2756.
34. Dinh Loc Duong; Han, G. H.; Lee, S. M.; Gunes, F.; Kim, E. S.; Kim, S. T.; Kim, H.; Quang Huy Ta; So, K. P.; Yoon, S. J.; Chae, S. J.; Jo, Y. W.; Park, M. H.; Chae, S. H.; Lim, S. C.; Choi, J. Y.; Lee, Y. H. Probing Graphene Grain Boundaries with Optical Microscopy. *Nature* **2012***, 490*, 235-239.
35. Azizi, A.; Zou, X.; Ercius, P.; Zhang, Z.; Elias, A. L.; Perea-Lopez, N.; Stone, G.; Terrones, M.; Yakobson, B. I.; Alem, N. Dislocation Motion and Grain Boundary Migration in Two-Dimensional Tungsten Disulphide. *Nat. Commun.* **2014***, 5*, 4867.
36. van der Zande, A. M.; Huang, P. Y.; Chenet, D. A.; Berkelbach, T. C.; You, Y.; Lee, G.; Heinz, T. F.; Reichman, D. R.; Muller, D. A.; Hone, J. C. Grains and Grain Boundaries in Highly Crystalline Monolayer Molybdenum Disulphide. *Nat. Mater.* **2013***, 12*, 554-561.
37. Huang, C.; Wu, S.; Sanchez, A. M.; Peters, J. J. P.; Beanland, R.; Ross, J. S.; Rivera, P.; Yao, W.; Cobden, D. H.; Xu, X. Lateral Heterojunctions within Monolayer $MoSe_2$-WSe_2 Semiconductors. *Nat. Mater.* **2014***, 13*, 1096-1101.
38. Elias, D. C.; Gorbachev, R. V.; Mayorov, A. S.; Morozov, S. V.; Zhukov, A. A.; Blake, P.; Ponomarenko, L. A.; Grigorieva, I. V.; Novoselov, K. S.; Guinea, F.; Geim, A. K. Dirac Cones Reshaped by Interaction Effects in Suspended Graphene. *Nat. Phys.* **2011***, 7*, 701-704.
39. Mayorov, A. S.; Gorbachev, R. V.; Morozov, S. V.; Britnell, L.; Jalil, R.; Ponomarenko, L. A.; Blake, P.; Novoselov, K. S.; Watanabe, K.; Taniguchi, T.; Geim, A. K. Micrometer-Scale Ballistic Transport in Encapsulated Graphene at Room Temperature. *Nano Lett.* **2011***, 11*, 2396-2399.
40. Li, X.; Wang, X.; Zhang, L.; Lee, S.; Dai, H. Chemically Derived, Ultrasmooth Graphene Nanoribbon Semiconductors. *Science* **2008***, 319*, 1229-1232.
41. Han, M. Y.; Oezyilmaz, B.; Zhang, Y.; Kim, P. Energy Band-Gap Engineering of Graphene Nanoribbons. *Phys. Rev. Lett.* **2007***, 98*, 206805.
42. Balog, R.; Jorgensen, B.; Nilsson, L.; Andersen, M.; Rienks, E.; Bianchi, M.; Fanetti, M.; Laegsgaard, E.; Baraldi, A.; Lizzit, S.; Sljivancanin, Z.; Besenbacher, F.; Hammer, B.; Pedersen, T. G.; Hofmann, P.; Hornekaer, L. Bandgap Opening in Graphene Induced by Patterned Hydrogen Adsorption. *Nat. Mater.* **2010***, 9*, 315-319.
43. Zhang, Y.; Tang, T.; Girit, C.; Hao, Z.; Martin, M. C.; Zettl, A.; Crommie, M. F.; Shen, Y. R.; Wang, F. Direct Observation of a Widely Tunable Bandgap in Bilayer Graphene. *Nature* **2009***, 459*, 820-823.
44. Perdew, J. P.; Burke, K.; Ernzerhof, M. Generalized Gradient Approximation Made Simple. *Phys. Rev. Lett.* **1996***, 77*, 3865-3868.
45. Kuc, A.; Zibouche, N.; Heine, T. Influence of Quantum Confinement on the Electronic Structure of the Transition Metal Sulfide TS_2. *Phys. Rev. B* **2011***, 83*, 245213.
46. Mattheis.Lf Band Structures of Transition-Metal-Dichalcogenide Layer Compounds. *Phys. Rev. B* **1973***, 8*, 3719-3740.

47. Frey, G. L.; Tenne, R.; Matthews, M. J.; Dresselhaus, M. S.; Dresselhaus, G. Optical Properties of MS_2 (M = Mo, W) Inorganic Fullerene-Like and Nanotube Material Optical Absorption and Resonance Raman Measurements. *J. Mater. Res.* **1998***, 13*, 2412-2417.
48. Frey, G. L.; Elani, S.; Homyonfer, M.; Feldman, Y.; Tenne, R. Optical-Absorption Spectra of Inorganic Fullerenelike MS_2 (M = Mo, W). *Phys. Rev. B* **1998***, 57*, 6666-6671.
49. Ballif, C.; Regula, M.; Schmid, P. E.; Remskar, M.; Sanjines, R.; Levy, F. Preparation and Characterization of Highly Oriented, Photoconducting WS_2 Thin Films. *Appl. Phys. A Mater. Sci. Process.* **1996***, 62*, 543-546.
50. Xiao, D.; Yao, W.; Niu, Q. Valley-Contrasting Physics in Graphene: Magnetic Moment and Topological Transport. *Phys. Rev. Lett.* **2007***, 99*, 236809.
51. Yao, W.; Xiao, D.; Niu, Q. Valley-Dependent Optoelectronics from Inversion Symmetry Breaking. *Phys. Rev. B* **2008***, 77*, 235406.
52. Yao, Y.; Ye, F.; Qi, X.; Zhang, S.; Fang, Z. Spin-Orbit Gap of Graphene: First-Principles Calculations. *Phys. Rev. B* **2007***, 75*, 041401.
53. Mak, K. F.; He, K.; Shan, J.; Heinz, T. F. Control of Valley Polarization in Monolayer MoS_2 by Optical Helicity. *Nat. Nanotechnol.* **2012***, 7*, 494-498.
54. Sie, E. J.; McIver, J.; Lee, Y.; Fu, L.; Kong, J.; Gedik, N. Valley-Selective Optical Stark Effect in Monolayer WS_2. *Nat. Mater.* **2015***, 14*, 290-294.
55. Yuan, H.; Wang, X.; Lian, B.; Zhang, H.; Fang, X.; Shen, B.; Xu, G.; Xu, Y.; Zhang, S.; Hwang, H. Y.; Cui, Y. Generation and Electric Control of Spin-Valley-Coupled Circular Photogalvanic Current in WSe_2. *Nat. Nanotechnol.* **2014***, 9*, 851-857.
56. Zeng, H.; Dai, J.; Yao, W.; Xiao, D.; Cui, X. Valley Polarization in MoS_2 Monolayers by Optical Pumping. *Nat. Nanotechnol.* **2012***, 7*, 490-493.
57. Ando, T.; Fowler, A. B.; Stern, F. Electronic-Properties of Two-Dimensional Systems. *Rev. Mod. Phys.* **1982***, 54*, 437-672.
58. Ridley, B. K. The Electron Phonon Interaction in Quasi-2-Dimensional Semiconductor Quantum-Well Structures. *J. Phys. C* **1982***, 15*, 5899-5917.
59. Chen, J.; Jang, C.; Xiao, S.; Ishigami, M.; Fuhrer, M. S. Intrinsic and Extrinsic Performance Limits of Graphene Devices on SiO_2. *Nat. Nanotechnol.* **2008***, 3*, 206-209.
60. Hwang, E. H.; Adam, S.; Das Sarma, S. Carrier Transport in Two-Dimensional Graphene Layers. *Phys. Rev. Lett.* **2007***, 98*, 186806.
61. Kaasbjerg, K.; Thygesen, K. S.; Jacobsen, K. W. Phonon-Limited Mobility in n-type Single-Layer MoS_2 from First Principles. *Phys. Rev. B* **2012***, 85*, 115317.
62. Castro, E. V.; Ochoa, H.; Katsnelson, M. I.; Gorbachev, R. V.; Elias, D. C.; Novoselov, K. S.; Geim, A. K.; Guinea, F. Limits on Charge Carrier Mobility in Suspended Graphene due to Flexural Phonons. *Phys. Rev. Lett.* **2010***, 105*, 266601.
63. Sakaki, H.; Noda, T.; Hirakawa, K.; Tanaka, M.; Matsusue, T. Interface Roughness Scattering in GaAs/AlAs Quantum-Wells. *Appl. Phys. Lett.* **1987***, 51*, 1934-1936.
64. Adam, S.; Hwang, E. H.; Das Sarma, S. Scattering Mechanisms and Boltzmann Transport in Graphene. *Physica E: Low-Dimensional Systems & Nanostructures* **2008***, 40*, 1022-1025.

65. Brivio, J.; Alexander, D. T. L.; Kis, A. Ripples and Layers in Ultrathin MoS_2 Membranes. *Nano Lett.* **2011***, 11*, 5148-5153.
66. Kim, S.; Konar, A.; Hwang, W.; Lee, J. H.; Lee, J.; Yang, J.; Jung, C.; Kim, H.; Yoo, J.; Choi, J.; Jin, Y. W.; Lee, S. Y.; Jena, D.; Choi, W.; Kim, K. High-Mobility and Low-Power Thin-Film Transistors Based on Multilayer MoS_2 Crystals. *Nat. Commun.* **2012***, 3*, 1011.
67. Novoselov, K. S.; Geim, A. K.; Morozov, S. V.; Jiang, D.; Katsnelson, M. I.; Grigorieva, I. V.; Dubonos, S. V.; Firsov, A. A. Two-Dimensional Gas of Massless Dirac fermions in Graphene. *Nature* **2005***, 438*, 197-200.
68. Ovchinnikov, D.; Allain, A.; Huang, Y.; Dumcenco, D.; Kis, A. Electrical Transport Properties of Single-Layer WS_2. *ACS Nano* **2014***, 8*, 8174-8181.
69. Withers, F.; Bointon, T. H.; Hudson, D. C.; Craciun, M. F.; Russo, S. Electron Transport of WS_2 Transistors in A Hexagonal Boron Nitride Dielectric Environment. *Sci. Rep.* **2014***, 4*, 4967.
70. Jo, S.; Ubrig, N.; Berger, H.; Kuzmenko, A. B.; Morpurgo, A. F. Mono- and Bilayer WS_2 Light-Emitting Transistors. *Nano Lett.* **2014***, 14*, 2019-2025.
71. Braga, D.; Lezama, I. G.; Berger, H.; Morpurgo, A. F. Quantitative Determination of the Band Gap of WS_2 with Ambipolar Ionic Liquid-Gated Transistors. *Nano Lett.* **2012***, 12*, 5218-5223.
72. Schmidt, H.; Giustiniano, F.; Eda, G. Electronic Transport Properties of Transition Metal Dichalcogenide Field-Effect Devices: Surface and Interface Effects. *Chem. Soc. Rev.* **2015***, Advance Article*.
73. Cheiwchanchamnangij, T.; Lambrecht, W. R. L. Quasiparticle Band Structure Calculation of Monolayer, Bilayer, and Bulk MoS_2. *Phys. Rev. B* **2012***, 85*, 205302.
74. Berghaeuser, G.; Malic, E. Analytical Approach to Excitonic Properties of MoS_2. *Phys. Rev. B* **2014***, 89*, 125309.
75. Lin, Y.; Ling, X.; Yu, L.; Huang, S.; Hsu, A. L.; Lee, Y.; Kong, J.; Dressehaus, M. S.; Palacios, T. Dielectric Screening of Excitons and Trions in Single-Layer MoS_2. *Nano Lett.* **2014***, 14*, 5569-5576.
76. Komsa, H.; Krasheninnikov, A. V. Effects of Confinement and Environment on the Electronic Structure and Exciton Binding Energy of MoS_2 from First Principles. *Phys. Rev. B* **2012***, 86*, 241201.
77. Ramasubramaniam, A. Large Excitonic Effects in Monolayers of Molybdenum and Tungsten Dichalcogenides. *Phys. Rev. B* **2012***, 86*, 115409.
78. Mak, K. F.; Lee, C.; Hone, J.; Shan, J.; Heinz, T. F. Atomically Thin MoS_2: A New Direct-Gap Semiconductor. *Phys. Rev. Lett.* **2010***, 105*, 136805.
79. Peimyoo, N.; Shang, J.; Cong, C.; Shen, X.; Wu, X.; Yeow, E. K. L.; Yu, T. Nonblinking, Intense Two-Dimensional Light Emitter: Monolayer WS_2 Triangles. *ACS Nano* **2013***, 7*, 10985-10994.
80. Chow, P. K.; Jacobs-Gedrim, R. B.; Gao, J.; Lu, T.; Yu, B.; Terrones, H.; Koratkar, N. Defect-Induced Photoluminescence in Monolayer Semiconducting Transition Metal Dichalcogenides. *ACS Nano* **2015***, 9*, 1520-1527.

81. Gao, Y.; Liu, Z.; Sun, D.; Huang, L.; Ma, L.; Yin, L.; Ma, T.; Zhang, Z.; Ma, X.; Peng, L.; Cheng, H.; Ren, W. Large-Area Synthesis of High-Quality and Uniform Monolayer WS_2 on Reusable Au Foils. *Nat. Commun.* **2015***, 6*, 8569.
82. Peimyoo, N.; Yang, W.; Shang, J.; Shen, X.; Wang, Y.; Yu, T. Chemically Driven Tunable Light Emission of Charged and Neutral Excitons in Monolayer WS_2. *ACS Nano* **2014***, 8*, 11320-11329.
83. Wang, S.; Wang, X.; Warner, J. H. All Chemical Vapor Deposition Growth of MoS_2:h-BN Vertical van der Waals Heterostructures. *ACS Nano* **2015***, 9*, 5246-5254.
84. Eda, G.; Yamaguchi, H.; Voiry, D.; Fujita, T.; Chen, M.; Chhowalla, M. Photoluminescence from Chemically Exfoliated MoS_2. *Nano Lett.* **2011***, 11*, 5111-5116.
85. Ross, J. S.; Wu, S.; Yu, H.; Ghimire, N. J.; Jones, A. M.; Aivazian, G.; Yan, J.; Mandrus, D. G.; Xiao, D.; Yao, W.; Xu, X. Electrical Control of Neutral and Charged Excitons in A Monolayer Semiconductor. *Nat. Commun.* **2013***, 4*, 1474.
86. Jones, A. M.; Yu, H.; Ghimire, N. J.; Wu, S.; Aivazian, G.; Ross, J. S.; Zhao, B.; Yan, J.; Mandrus, D. G.; Xiao, D.; Yao, W.; Xu, X. Optical Generation of Excitonic Valley Coherence in Monolayer WSe_2. *Nat. Nanotechnol.* **2013***, 8*, 634-638.
87. Bellus, M. Z.; Ceballos, F.; Chiu, H.; Zhao, H. Tightly Bound Trions in Transition Metal Dichalcogenide Heterostructures. *ACS Nano* **2015***, 9*, 6459-6464.
88. Zhu, B.; Zeng, H.; Dai, J.; Gong, Z.; Cui, X. Anomalously Robust Valley Polarization and Valley Coherence in Bilayer WS_2. *Proc. Natl. Acad. Sci. U. S. A.* **2014***, 111*, 11606-11611.
89. Ye, Z.; Cao, T.; O'Brien, K.; Zhu, H.; Yin, X.; Wang, Y.; Louie, S. G.; Zhang, X. Probing Excitonic Dark States in Single-Layer Tungsten Disulphide. *Nature* **2014***, 513*, 214-218.
90. Wang, Y.; Cong, C.; Yang, W.; Shang, J.; Peimyoo, N.; Chen, Y.; Kang, J.; Wang, J.; Huang, W.; Yu, T. Strain-Induced Direct-Indirect Bandgap Transition and Phonon Modulation in Monolayer WS_2. *Nano Res.* **2015***, 8*, 2562-2572.
91. Mitioglu, A. A.; Plochocka, P.; Jadczak, J. N.; Escoffier, W.; Rikken, G. L. J. A.; Kulyuk, L.; Maude, D. K. Optical Manipulation of The Exciton Charge State in Single-Layer Tungsten Disulfide. *Phys. Rev. B* **2013***, 88*, 245403.
92. Zhu, B.; Chen, X.; Cui, X. Exciton Binding Energy of Monolayer WS_2. *Sci. Rep.* **2015***, 5*, 9218.
93. Yuan, L.; Huang, L. Exciton Dynamics and Annihilation in WS_2 2D Semiconductors. *Nanoscale* **2015***, 7*, 7402-7408.
94. Kozawa, D.; Kumar, R.; Carvalho, A.; Amara, K. K.; Zhao, W.; Wang, S.; Toh, M.; Ribeiro, R. M.; Castro Neto, A. H.; Matsuda, K.; Eda, G. Photocarrier Relaxation Pathway in Two-Dimensional Semiconducting Transition Metal Dichalcogenides. *Nat. Commun.* **2014***, 5*, 4543.
95. Salehzadeh, O.; Tran, N. H.; Liu, X.; Shih, I.; Mi, Z. Exciton Kinetics, Quantum Efficiency, and Efficiency Droop of Monolayer MoS_2 Light-Emitting Devices. *Nano Lett.* **2014***, 14*, 4125-4130.

96. Sun, D.; Rao, Y.; Reider, G. A.; Chen, G.; You, Y.; Brezin, L.; Harutyunyan, A. R.; Heinz, T. F. Observation of Rapid Exciton-Exciton Annihilation in Monolayer Molybdenum Disulfide. *Nano Lett.* **2014***, 14*, 5625-5629.
97. Kumar, N.; Cui, Q.; Ceballos, F.; He, D.; Wang, Y.; Zhao, H. Exciton-Exciton Annihilation in $MoSe_2$ Monolayers. *Phys. Rev. B* **2014***, 89*, 125427.
98. Mouri, S.; Miyauchi, Y.; Toh, M.; Zhao, W.; Eda, G.; Matsuda, K. Nonlinear Photoluminescence in Atomically Thin Layered WSe_2 Arising from Diffusion-Assisted Exciton-Exciton Annihilation. *Phys. Rev. B* **2014***, 90*, 155449.
99. Kang, K. N.; Godin, K.; Yang, E. The Growth Scale and Kinetics of WS_2 Monolayers under Varying H_2 Concentration. *Sci. Rep.* **2015***, 5*, 13205.
100. Jariwala, D.; Sangwan, V. K.; Lauhon, L. J.; Marks, T. J.; Hersam, M. C. Emerging Device Applications for Semiconducting Two-Dimensional Transition Metal Dichalcogenides. *ACS Nano* **2014***, 8*, 1102-1120.
101. Baugher, B. W. H.; Churchill, H. O. H.; Yang, Y.; Jarillo-Herrero, P. Intrinsic Electronic Transport Properties of High-Quality Monolayer and Bilayer MoS_2. *Nano Lett.* **2013***, 13*, 4212-4216.
102. Neal, A. T.; Liu, H.; Gu, J.; Ye, P. D. Magneto-Transport in MoS_2: Phase Coherence, Spin-Orbit Scattering, and the Hall Factor. *ACS Nano* **2013***, 7*, 7077-7082.
103. Novoselov, K.; Jiang, D.; Schedin, F.; Booth, T.; Khotkevich, V.; Morozov, S.; Geim, A. Two-Dimensional Atomic Crystals. *Proc. Natl. Acad. Sci. U. S. A.* **2005***, 102*, 10451-10453.
104. Konar, A.; Fang, T.; Jena, D. Effect of High-Kappa Gate Dielectrics on Charge Transport in Graphene-Based Field Effect Transistors. *Phys. Rev. B* **2010***, 82*, 115452.
105. Ponomarenko, L. A.; Yang, R.; Mohiuddin, T. M.; Katsnelson, M. I.; Novoselov, K. S.; Morozov, S. V.; Zhukov, A. A.; Schedin, F.; Hill, E. W.; Geim, A. K. Effect of a High-kappa Environment on Charge Carrier Mobility in Graphene. *Phys. Rev. Lett.* **2009***, 102*, 206603.
106. Fuhrer, M. S.; Hone, J. Measurement of Mobility in Dual-Gated MoS_2 Transistors. *Nat. Nanotechnol.* **2013***, 8*, 146-147.
107. Radisavljevic, B.; Kis, A. Measurement of Mobility in Dual-Gated MoS_2 Transistors. *Nat. Nanotechnol.* **2013***, 8*, 147-148.
108. Radisavljevic, B.; Kis, A. Mobility Engineering and A Metal-Insulator Transition in Monolayer MoS_2. *Nat. Mater.* **2013***, 12*, 815-820.
109. Ming-Wei Lin; Lezhang Liu; Qing Lan; Xuebin Tan; Dhindsa, K. S.; Peng Zeng; Naik, V. M.; Cheng, M. M. -.; Zhixian Zhou Mobility Enhancement and Highly Efficient Gating of Monolayer MoS_2 Transistors with Polymer Electrolyte. *J. Phys. D* **2012***, 45*, 345102 (6 pp.)-345102 (6 pp.).
110. Perera, M. M.; Lin, M.; Chuang, H.; Chamlagain, B. P.; Wang, C.; Tan, X.; Cheng, M. M.; Tomanek, D.; Zhou, Z. Improved Carrier Mobility in Few-Layer MoS_2 Field-Effect Transistors with Ionic-Liquid Gating. *ACS Nano* **2013***, 7*, 4449-4458.

111. Chu, L.; Schmidt, H.; Pu, J.; Wang, S.; Oezyilmaz, B.; Takenobu, T.; Eda, G. Charge Transport in Ion-Gated Mono-, Bi-, and Trilayer MoS_2 Field Effect Transistors. *Sci. Rep.* **2014***, 4*, 7293.
112. Pu, J.; Yomogida, Y.; Liu, K.; Li, L.; Iwasa, Y.; Takenobu, T. Highly Flexible MoS_2 Thin-Film Transistors with Ion Gel Dielectrics. *Nano Lett.* **2012***, 12*, 4013-4017.
113. Zhang, Y. J.; Ye, J. T.; Yornogida, Y.; Takenobu, T.; Iwasa, Y. Formation of a Stable p-n Junction in a Liquid-Gated MoS_2 Ambipolar Transistor. *Nano Lett.* **2013***, 13*, 3023-3028.
114. Liu, Y.; Wu, H.; Cheng, H.; Yang, S.; Zhu, E.; He, Q.; Ding, M.; Li, D.; Guo, J.; Weiss, N. O.; Huang, Y.; Duan, X. Toward Barrier Free Contact to Molybdenum Disulfide Using Graphene Electrodes. *Nano Lett.* **2015***, 15*, 3030-3034.
115. Lee, G.; Cui, X.; Kim, Y. D.; Arefe, G.; Zhang, X.; Lee, C.; Ye, F.; Watanabe, K.; Taniguchi, T.; Kim, P.; Hone, J. Highly Stable, Dual-Gated MoS_2 Transistors Encapsulated by Hexagonal Boron Nitride with Gate-Controllable Contact, Resistance, and Threshold Voltage. *ACS Nano* **2015***, 9*, 7019-7026.
116. Chen, J. -.; Jang, C.; Adam, S.; Fuhrer, M. S.; Williams, E. D.; Ishigami, M. Charged-Impurity Scattering in Graphene. *Nat. Phys.* **2008***, 4*, 377-381.
117. Dean, C. R.; Young, A. F.; Meric, I.; Lee, C.; Wang, L.; Sorgenfrei, S.; Watanabe, K.; Taniguchi, T.; Kim, P.; Shepard, K. L.; Hone, J. Boron Nitride Substrates for High-Quality Graphene Electronics. *Nat. Nanotechnol.* **2010***, 5*, 722-726.
118. Chan, M. Y.; Komatsu, K.; Li, S.; Xu, Y.; Darmawan, P.; Kuramochi, H.; Nakaharai, S.; Aparecido-Ferreira, A.; Watanabe, K.; Taniguchi, T.; Tsukagoshi, K. Suppression of Thermally Activated Carrier Transport in Atomically Thin MoS_2 on Crystalline Hexagonal Boron Nitride Substrates. *Nanoscale* **2013***, 5*, 9572-9576.
119. Lee, G.; Yu, Y.; Cui, X.; Petrone, N.; Lee, C.; Choi, M. S.; Lee, D.; Lee, C.; Yoo, W. J.; Watanabe, K.; Taniguchi, T.; Nuckolls, C.; Kim, P.; Hone, J. Flexible and Transparent MoS_2 Field-Effect Transistors on Hexagonal Boron Nitride-Graphene Heterostructures. *ACS Nano* **2013***, 7*, 7931-7936.
120. Buscema, M.; Barkelid, M.; Zwiller, V.; van der Zant, H. S. J.; Steele, G. A.; Castellanos-Gomez, A. Large and Tunable Photothermoelectric Effect in Single-Layer MoS_2. *Nano Lett.* **2013***, 13*, 358-363.
121. Ghatak, S.; Pal, A. N.; Ghosh, A. Nature of Electronic States in Atomically Thin MoS_2 Field-Effect Transistors. *ACS Nano* **2011***, 5*, 7707-7712.
122. Das, S.; Chen, H.; Penumatcha, A. V.; Appenzeller, J. High Performance Multilayer MoS_2 Transistors with Scandium Contacts. *Nano Lett.* **2013***, 13*, 100-105.
123. Guo, Y.; Han, Y.; Li, J.; Xiang, A.; Wei, X.; Gao, S.; Chen, Q. Study on the Resistance Distribution at the Contact between Molybdenum Disulfide and Metals. *ACS Nano* **2014***, 8*, 7771-7779.
124. Schmidt, H.; Wang, S.; Chu, L.; Toh, M.; Kumar, R.; Zhao, W.; Neto, A. H. C.; Martin, J.; Adam, S.; Oezyilmaz, B.; Eda, G. Transport Properties of Monolayer MoS_2 Grown by Chemical Vapor Deposition. *Nano Lett.* **2014***, 14*, 1909-1913.

125. McDonnell, S.; Addou, R.; Buie, C.; Wallace, R. M.; Hinkle, C. L. Defect-Dominated Doping and Contact Resistance in MoS_2. *ACS Nano* **2014***, 8*, 2880-2888.
126. Wang, H.; Yu, L.; Lee, Y. -.; Fang, W.; Hsu, A.; Herring, P.; Chin, M.; Dubey, M.; Li, L. -.; Kong, J.; Palacios, T. Large-Scale 2D Electronics Based on Single-Layer MoS_2 Grown by Chemical Vapor Deposition. *2012 IEEE International Electron Devices Meeting (IEDM)* **2012**.
127. Georgiou, T.; Jalil, R.; Belle, B. D.; Britnell, L.; Gorbachev, R. V.; Morozov, S. V.; Kim, Y.; Gholinia, A.; Haigh, S. J.; Makarovsky, O.; Eaves, L.; Ponomarenko, L. A.; Geim, A. K.; Novoselov, K. S.; Mishchenko, A. Vertical Field-Effect Transistor Based on Graphene-WS_2 Heterostructures for Flexible and Transparent Electronics. *Nat. Nanotechnol.* **2013***, 8*, 100-103.
128. Yang, H.; Heo, J.; Park, S.; Song, H. J.; Seo, D. H.; Byun, K.; Kim, P.; Yoo, I.; Chung, H.; Kim, K. Graphene Barristor, A Triode Device with A Gate-Controlled Schottky Barrier. *Science* **2012***, 336*, 1140-1143.
129. Britnell, L.; Gorbachev, R. V.; Geim, A. K.; Ponomarenko, L. A.; Mishchenko, A.; Greenaway, M. T.; Fromhold, T. M.; Novoselov, K. S.; Eaves, L. Resonant Tunnelling and Negative Differential Conductance in Graphene Transistors. *Nat. Commun.* **2013***, 4*, 1794.
130. Yu, W. J.; Li, Z.; Zhou, H.; Chen, Y.; Wang, Y.; Huang, Y.; Duan, X. Vertically Stacked Multi-Heterostructures of Layered Materials for Logic Transistors and Complementary Inverters. *Nat. Mater.* **2013***, 12*, 246-252.
131. Spah, R.; Luxsteiner, M.; Obergfell, M.; Bucher, E.; Wagner, S. n-$MoSe_2$/p-WSe_2 Heterojunctions. *Appl. Phys. Lett.* **1985***, 47*, 871-873.
132. Spah, R.; Elrod, U.; Luxsteiner, M.; Bucher, E.; Wagner, S. Pn Junctions in Tungsten Diselenide. *Appl. Phys. Lett.* **1983***, 43*, 79-81.
133. Jariwala, D.; Sangwan, V. K.; Wu, C.; Prabhumirashi, P. L.; Geier, M. L.; Marks, T. J.; Lauhon, L. J.; Hersam, M. C. Gate-Tunable Carbon Nanotube-MoS_2 Heterojunction p-n Diode. *Proc. Natl. Acad. Sci. U. S. A.* **2013***, 110*, 18076-18080.
134. Chuang, S.; Kapadia, R.; Fang, H.; Chang, T. C.; Yen, W.; Chueh, Y.; Javey, A. Near-Ideal Electrical Properties of InAs/WSe_2 van der Waals Heterojunction Diodes. *Appl. Phys. Lett.* **2013***, 102*, 242101.
135. Shi, Y.; Zhou, W.; Lu, A.; Fang, W.; Lee, Y.; Hsu, A. L.; Kim, S. M.; Kim, K. K.; Yang, H. Y.; Li, L.; Idrobo, J.; Kong, J. van der Waals Epitaxy of MoS_2 Layers Using Graphene As Growth Templates. *Nano Lett.* **2012***, 12*, 2784-2791.
136. Okada, M.; Sawazaki, T.; Watanabe, K.; Taniguch, T.; Hibino, H.; Shinohara, H.; Kitaura, R. Direct Chemical Vapor Deposition Growth of WS_2 Atomic Layers on Hexagonal Boron Nitride. *ACS Nano* **2014***, 8*, 8273-8277.
137. Yan, A.; Velasco, J. J.; Kahn, S.; Watanabe, K.; Taniguchi, T.; Wang, F.; Crommie, M. F.; Zettl, A. Direct Growth of Single- and Few-Layer MoS_2 on h-BN with Preferred Relative Rotation Angles. *Nano Lett.* **2015***, 15*, 6324-31.

138. Kobayashi, Y.; Sasaki, S.; Mori, S.; Hibino, H.; Liu, Z.; Watanabe, K.; Taniguchi, T.; Suenaga, K.; Maniwa, Y.; Miyata, Y. Growth and Optical Properties of High-Quality Monolayer WS_2 on Graphite. *ACS Nano* **2015***, 9*, 4056-4063.
139. Gong, Y.; Lin, J.; Wang, X.; Shi, G.; Lei, S.; Lin, Z.; Zou, X.; Ye, G.; Vajtai, R.; Yakobson, B. I.; Terrones, H.; Terrones, M.; Tay, B. K.; Lou, J.; Pantelides, S. T.; Liu, Z.; Zhou, W.; Ajayan, P. M. Vertical and In-Plane Heterostructures from WS_2/MoS_2 Monolayers. *Nat. Mater.* **2014***, 13*, 1135-1142.
140. Duan, X.; Wang, C.; Shaw, J. C.; Cheng, R.; Chen, Y.; Li, H.; Wu, X.; Tang, Y.; Zhang, Q.; Pan, A.; Jiang, J.; Yu, R.; Huang, Y.; Duan, X. Lateral Epitaxial Growth of Two-Dimensional Layered Semiconductor Heterojunctions. *Nat. Nanotechnol.* **2014***, 9*, 1024-1030.
141. Perea-Lopez, N.; Elias, A. L.; Berkdemir, A.; Castro-Beltran, A.; Gutierrez, H. R.; Feng, S.; Lv, R.; Hayashi, T.; Lopez-Urias, F.; Ghosh, S.; Muchharla, B.; Talapatra, S.; Terrones, H.; Terrones, M. Photosensor Device Based on Few-Layered WS_2 Films. *Adv. Funct. Mater.* **2013***, 23*, 5511-5517.
142. Weng, W. Y.; Chang, S. J.; Hsu, C. L.; Hsueh, T. J. A ZnO-Nanowire Phototransistor Prepared on Glass Substrates. *ACS Appl. Mater. Interfaces* **2011***, 3*, 162-166.
143. Zhang, A.; Kim, H.; Cheng, J.; Lo, Y. Ultrahigh Responsivity Visible and Infrared Detection Using Silicon Nanowire Phototransistors. *Nano Lett.* **2010***, 10*, 2117-2120.
144. Xia, F.; Mueller, T.; Lin, Y.; Valdes-Garcia, A.; Avouris, P. Ultrafast Graphene Photodetector. *Nat. Nanotechnol.* **2009***, 4*, 839-843.
145. Xia, F.; Mueller, T.; Golizadeh-Mojarad, R.; Freitag, M.; Lin, Y.; Tsang, J.; Perebeinos, V.; Avouris, P. Photocurrent Imaging and Efficient Photon Detection in a Graphene Transistor. *Nano Lett.* **2009***, 9*, 1039-1044.
146. Roy, K.; Padmanabhan, M.; Goswami, S.; Sai, T. P.; Ramalingam, G.; Raghavan, S.; Ghosh, A. Graphene-MoS_2 Hybrid Structures for Multifunctional Photoresponsive Memory Devices. *Nat. Nanotechnol.* **2013***, 8*, 826-830.
147. Zhang, W.; Chuu, C.; Huang, J.; Chen, C.; Tsai, M.; Chang, Y.; Liang, C.; Chen, Y.; Chueh, Y.; He, J.; Chou, M.; Li, L. Ultrahigh-Gain Photodetectors Based on Atomically Thin Graphene-MoS_2 Heterostructures. *Sci. Rep.* **2014***, 4*, 3826.
148. Sze, S. M.; Ng, K. K., Eds.; In *Physics of Semiconductor Devices;* Wiley: New York, 2007; Vol. 3rd Edition.
149. Tsai, D.; Lien, D.; Tsai, M.; Su, S.; Chen, K.; Ke, J.; Yu, Y.; Li, L.; He, J. Trilayered MoS_2 Metal-Semiconductor-Metal Photodetectors: Photogain and Radiation Resistance. *IEEE J. Sel. Topics Quantum Electron.* **2014***, 20*, 3800206.
150. Tsai, D.; Liu, K.; Lien, D.; Tsai, M.; Kang, C.; Lin, C.; Li, L.; He, J. Few-Layer MoS_2 with High Broadband Photogain and Fast Optical Switching for Use in Harsh Environments. *ACS Nano* **2013***, 7*, 3905-3911.
151. Yu, W. J.; Liu, Y.; Zhou, H.; Yin, A.; Li, Z.; Huang, Y.; Duan, X. Highly Efficient Gate-Tunable Photocurrent Generation in Vertical Heterostructures of Layered Materials. *Nat. Nanotechnol.* **2013***, 8*, 952-958.

152. Bernardi, M.; Palummo, M.; Grossman, J. C. Extraordinary Sunlight Absorption and One Nanometer Thick Photovoltaics Using Two-Dimensional Monolayer Materials. *Nano Lett.* **2013***, 13*, 3664-3670.
153. Britnell, L.; Ribeiro, R. M.; Eckmann, A.; Jalil, R.; Belle, B. D.; Mishchenko, A.; Kim, Y. -.; Gorbachev, R. V.; Georgiou, T.; Morozov, S. V.; Grigorenko, A. N.; Geim, A. K.; Casiraghi, C.; Castro Neto, A. H.; Novoselov, K. S. Strong Light-Matter Interactions in Heterostructures of Atomically Thin Films. *Science* **2013***, 340*, 1311-1314.
154. Eda, G.; Maier, S. A. Two-Dimensional Crystals: Managing Light for Optoelectronics. *ACS Nano* **2013***, 7*, 5660-5665.
155. Lin, J.; Li, H.; Zhang, H.; Chen, W. Plasmonic Enhancement of Photocurrent in MoS_2 Field-Effect-Transistor. *Appl. Phys. Lett.* **2013***, 102*, 203109.
156. Feng, J.; Qian, X.; Huang, C.; Li, J. Strain-Engineered Artificial Atom as a Broad-Spectrum Solar Energy Funnel. *Nature Photon.* **2012***, 6*, 865-871.
157. Gorbachev, R. V.; Riaz, I.; Nair, R. R.; Jalil, R.; Britnell, L.; Belle, B. D.; Hill, E. W.; Novoselov, K. S.; Watanabe, K.; Taniguchi, T.; Geim, A. K.; Blake, P. Hunting for Monolayer Boron Nitride: Optical and Raman Signatures. *Small* **2011***, 7*, 465-468.
158. Mueller, T.; Kinoshita, M.; Steiner, M.; Perebeinos, V.; Bol, A. A.; Farmer, D. B.; Avouris, P. Efficient Narrow-Band Light Emission from a Single Carbon Nanotube p-n Diode. *Nat. Nanotechnol.* **2010***, 5*, 27-31.
159. Zhang, Y.; Ye, J.; Matsuhashi, Y.; Iwasa, Y. Ambipolar MoS_2 Thin Flake Transistors. *Nano Lett.* **2012***, 12*, 1136-1140.
160. Meijer, E. J.; De Leeuw, D. M.; Setayesh, S.; Van Veenendaal, E.; Huisman, B. H.; Blom, P. W. M.; Hummelen, J. C.; Scherf, U.; Klapwijk, T. M. Solution-Processed Ambipolar Organic Field-Effect Transistors and Inverters. *Nat. Mater.* **2003***, 2*, 678-682.
161. Dinelli, F.; Capelli, R.; Loi, M. A.; Murgia, M.; Muccini, M.; Facchetti, A.; Marks, T. J. High-Mobility Ambipolar Transport in Organic Light-Emitting Transistors. *Adv. Mater.* **2006***, 18*, 1416.
162. Zaumseil, J.; Friend, R. H.; Sirringhaus, H. Spatial Control of The Recombination Zone in An Ambipolar Light-Emitting Organic Transistor. *Nat. Mater.* **2006***, 5*, 69-74.
163. Bisri, S. Z.; Takenobu, T.; Yomogida, Y.; Shimotani, H.; Yamao, T.; Hotta, S.; Iwasa, Y. High Mobility and Luminescent Efficiency in Organic Single-Crystal Light-Emitting Transistors. *Adv. Funct. Mater.* **2009***, 19*, 1728-1735.
164. Ross, J. S.; Klement, P.; Jones, A. M.; Ghimire, N. J.; Yan, J.; Mandrus, D. G.; Taniguchi, T.; Watanabe, K.; Kitamura, K.; Yao, W.; Cobden, D. H.; Xu, X. Electrically Tunable Excitonic Light-Emitting Diodes Based on Monolayer WSe_2 p-n Junctions. *Nat. Nanotechnol.* **2014***, 9*, 268-272.
165. Pospischil, A.; Furchi, M. M.; Mueller, T. Solar-Energy Conversion and Light Emission in An Atomic Monolayer p-n Diode. *Nat. Nanotechnol.* **2014***, 9*, 257-261.

166. Baugher, B. W. H.; Churchill, H. O. H.; Yang, Y.; Jarillo-Herrero, P. Optoelectronic Devices Based on Electrically Tunable p-n Diodes in a Monolayer Dichalcogenide. *Nat. Nanotechnol.* **2014***, 9*, 262-267.

167. Li, H.; Yin, Z.; He, Q.; Li, H.; Huang, X.; Lu, G.; Fam, D. W. H.; Tok, A. I. Y.; Zhang, Q.; Zhang, H. Fabrication of Single- and Multilayer MoS_2 Film-Based Field-Effect Transistors for Sensing NO at Room Temperature. *Small* **2012***, 8*, 63-67.

168. Late, D. J.; Huang, Y.; Liu, B.; Acharya, J.; Shirodkar, S. N.; Luo, J.; Yan, A.; Charles, D.; Waghmare, U. V.; Dravid, V. P.; Rao, C. N. R. Sensing Behavior of Atomically Thin-Layered MoS_2 Transistors. *ACS Nano* **2013***, 7*, 4879-4891.

169. Liu, B.; Chen, L.; Liu, G.; Abbas, A. N.; Fathi, M.; Zhou, C. High-Performance Chemical Sensing Using Schottky-Contacted Chemical Vapor Deposition Grown Mono layer MoS_2 Transistors. *ACS Nano* **2014***, 8*, 5304-5314.

170. Lee, K.; Gatensby, R.; McEvoy, N.; Hallam, T.; Duesberg, G. S. High-Performance Sensors Based on Molybdenum Disulfide Thin Films. *Adv. Mater.* **2013***, 25*, 6699-6702.

171. Tongay, S.; Zhou, J.; Ataca, C.; Liu, J.; Kang, J. S.; Matthews, T. S.; You, L.; Li, J.; Grossman, J. C.; Wu, J. Broad-Range Modulation of Light Emission in Two-Dimensional Semiconductors by Molecular Physisorption Gating. *Nano Lett.* **2013***, 13*, 2831-2836.

172. Perkins, F. K.; Friedman, A. L.; Cobas, E.; Campbell, P. M.; Jernigan, G. G.; Jonker, B. T. Chemical Vapor Sensing with Monolayer MoS_2. *Nano Lett.* **2013***, 13*, 668-673.

173. Hernandez, Y.; Nicolosi, V.; Lotya, M.; Blighe, F. M.; Sun, Z.; De, S.; McGovern, I. T.; Holland, B.; Byrne, M.; Gun'ko, Y. K.; Boland, J. J.; Niraj, P.; Duesberg, G.; Krishnamurthy, S.; Goodhue, R.; Hutchison, J.; Scardaci, V.; Ferrari, A. C.; Coleman, J. N. High-Yield Production of Graphene by Liquid-Phase Exfoliation of Graphite. *Nat. Nanotechnol.* **2008***, 3*, 563-568.

174. Smith, R. J.; King, P. J.; Lotya, M.; Wirtz, C.; Khan, U.; De, S.; O'Neill, A.; Duesberg, G. S.; Grunlan, J. C.; Moriarty, G.; Chen, J.; Wang, J.; Minett, A. I.; Nicolosi, V.; Coleman, J. N. Large-Scale Exfoliation of Inorganic Layered Compounds in Aqueous Surfactant Solutions. *Adv. Mater.* **2011***, 23*, 3944.

175. O'Neill, A.; Khan, U.; Coleman, J. N. Preparation of High Concentration Dispersions of Exfoliated MoS_2 with Increased Flake Size. *Chem. Mater.* **2012***, 24*, 2414-2421.

176. Matte, H. S. S. R.; Gomathi, A.; Manna, A. K.; Late, D. J.; Datta, R.; Pati, S. K.; Rao, C. N. R. MoS_2 and WS_2 Analogues of Graphene. *Angew. Chem. Int. Ed.* **2010***, 49*, 4059-4062.

177. Coleman, J. N.; Lotya, M.; O'Neill, A.; Bergin, S. D.; King, P. J.; Khan, U.; Young, K.; Gaucher, A.; De, S.; Smith, R. J.; et al. Two-Dimensional Nanosheets Produced by Liquid Exfoliation of Layered Materials. *Science* **2011***, 331*, 568-571.

178. Zhiyuan Zeng; Zongyou Yin; Xiao Huang; Hai Li; Qiyuan He; Gang Lu; Boey, F.; Hua Zhang Single-layer Semiconducting Nanosheets: High-yield Preparation and Device Fabrication. *Angew. Chem. Int. Ed.* **2011***, 50*, 11093-7.

179. Bae, S.; Kim, H.; Lee, Y.; Xu, X.; Park, J.; Zheng, Y.; Balakrishnan, J.; Lei, T.; Kim, H. R.; Song, Y. I.; Kim, Y.; Kim, K. S.; Ozyilmaz, B.; Ahn, J.; Hong, B. H.; Iijima, S. Roll-to-Roll

Production of 30-inch Graphene Films for Transparent Electrodes. *Nat. Nanotechnol.* **2010**, *5*, 574-578.

180. Li, X.; Cai, W.; An, J.; Kim, S.; Nah, J.; Yang, D.; Piner, R.; Velamakanni, A.; Jung, I.; Tutuc, E.; Banerjee, S. K.; Colombo, L.; Ruoff, R. S. Large-Area Synthesis of High-Quality and Uniform Graphene Films on Copper Foils. *Science* **2009**, *324*, 1312-1314.
181. Wu, S.; Huang, C.; Aivazian, G.; Ross, J. S.; Cobden, D. H.; Xu, X. Vapor-Solid Growth of High Optical Quality MoS_2 Monolayers with Near-Unity Valley Polarization. *ACS Nano* **2013**, *7*, 2768-2772.
182. Liu, K.; Zhang, W.; Lee, Y.; Lin, Y.; Chang, M.; Su, C.; Chang, C.; Li, H.; Shi, Y.; Zhang, H.; Lai, C.; Li, L. Growth of Large-Area and Highly Crystalline MoS_2 Thin Layers on Insulating Substrates. *Nano Lett.* **2012**, *12*, 1538-1544.
183. Jiao, L.; Fan, B.; Xian, X.; Wu, Z.; Zhang, J.; Liu, Z. Creation of Nanostructures with Poly(methyl methacrylate)-Mediated Nanotransfer Printing. *J. Am. Chem. Soc.* **2008**, *130*, 12612.
184. Lee, Y.; Yu, L.; Wang, H.; Fang, W.; Ling, X.; Shi, Y.; Lin, C.; Huang, J.; Chang, M.; Chang, C.; Dresselhaus, M.; Palacios, T.; Li, L.; Kong, J. Synthesis and Transfer of Single-Layer Transition Metal Disulfides on Diverse Surfaces. *Nano Lett.* **2013**, *13*, 1852-1857.
185. Shi, Y.; Li, H.; Li, L. Recent Advances in Controlled Synthesis of Two-Dimensional Transition Metal Dichalcogenides via Vapour Deposition Techniques. *Chem. Soc. Rev.* **2015**, *44*, 2744-2756.
186. Zhan, Y.; Liu, Z.; Najmaei, S.; Ajayan, P. M.; Lou, J. Large-Area Vapor-Phase Growth and Characterization of MoS_2 Atomic Layers on a SiO_2 Substrate. *Small* **2012**, *8*, 966-971.
187. Wang, X.; Feng, H.; Wu, Y.; Jiao, L. Controlled Synthesis of Highly Crystalline MoS_2 Flakes by Chemical Vapor Deposition. *J. Am. Chem. Soc.* **2013**, *135*, 5304-5307.
188. Song, J.; Park, J.; Lee, W.; Choi, T.; Jung, H.; Lee, C. W.; Hwang, S.; Myoung, J. M.; Jung, J.; Kim, S.; Lansalot-Matras, C.; Kim, H. Layer-Controlled, Wafer-Scale, and Conformal Synthesis of Tungsten Disulfide Nanosheets Using Atomic Layer Deposition. *ACS Nano* **2013**, *7*, 11333-11340.
189. Lee, Y.; Zhang, X.; Zhang, W.; Chang, M.; Lin, C.; Chang, K.; Yu, Y.; Wang, J. T.; Chang, C.; Li, L.; Lin, T. Synthesis of Large-Area MoS_2 Atomic Layers with Chemical Vapor Deposition. *Adv. Mater.* **2012**, *24*, 2320-2325.
190. Najmaei, S.; Liu, Z.; Zhou, W.; Zou, X.; Shi, G.; Lei, S.; Yakobson, B. I.; Idrobo, J.; Ajayan, P. M.; Lou, J. Vapour Phase Growth and Grain Boundary Structure of Molybdenum Disulphide Atomic Layers. *Nat. Mater.* **2013**, *12*, 754-759.
191. Ji, Q.; Zhang, Y.; Gao, T.; Zhang, Y.; Ma, D.; Liu, M.; Chen, Y.; Qiao, X.; Tan, P.; Kan, M.; Feng, J.; Sun, Q.; Liu, Z. Epitaxial Monolayer MoS_2 on Mica with Novel Photoluminescence. *Nano Lett.* **2013**, *13*, 3870-3877.
192. Chae, S. J.; Guenes, F.; Kim, K. K.; Kim, E. S.; Han, G. H.; Kim, S. M.; Shin, H.; Yoon, S.; Choi, J.; Park, M. H.; Yang, C. W.; Pribat, D.; Lee, Y. H. Synthesis of Large-Area Graphene

Layers on Poly-Nickel Substrate by Chemical Vapor Deposition: Wrinkle Formation. *Adv. Mater.* **2009***, 21*, 2328.

193. Gao, L.; Ren, W.; Xu, H.; Jin, L.; Wang, Z.; Ma, T.; Ma, L.; Zhang, Z.; Fu, Q.; Peng, L.; Bao, X.; Cheng, H. Repeated Growth and Bubbling Transfer of Graphene with Millimetre-Size Single-Crystal Grains Using Platinum. *Nat. Commun.* **2012***, 3*, 699.
194. Li, X.; Cai, W.; Colombo, L.; Ruoff, R. S. Evolution of Graphene Growth on Ni and Cu by Carbon Isotope Labeling. *Nano Lett.* **2009***, 9*, 4268-4272.
195. Cong, C.; Shang, J.; Wu, X.; Cao, B.; Peimyoo, N.; Qiu, C.; Sun, L.; Yu, T. Synthesis and Optical Properties of Large-Area Single-Crystalline 2D Semiconductor WS_2 Monolayer from Chemical Vapor Deposition. *Adv. Opt. Mater.* **2014***, 2*, 131-136.
196. Kang, K.; Xie, S.; Huang, L.; Han, Y.; Huang, P. Y.; Mak, K. F.; Kim, C.; Muller, D.; Park, J. High-Mobility Three-Atom-Thick Semiconducting Films With Wafer-Scale Homogeneity. *Nature* **2015***, 520*, 656-660.
197. Mann, J.; Ma, Q.; Odenthal, P. M.; Isarraraz, M.; Le, D.; Preciado, E.; Barroso, D.; Yamaguchi, K.; Palacio, G. v. S.; Andrew Nguyen; et al. 2-Dimensional Transition Metal Dichalcogenides with Tunable Direct Band Gaps: $MoS_{2(1-x)}Se_{2x}$ Monolayers. *Adv. Mater.* **2014***, 26*, 1399-1404.
198. Gong, Y.; Liu, Z.; Lupini, A. R.; Shi, G.; Lin, J.; Najmaei, S.; Lin, Z.; Elias, A. L.; Berkdemir, A.; You, G.; Terrones, H.; Terrones, M.; Vajtai, R.; Pantelides, S. T.; Pennycook, S. J.; Lou, J.; Zhou, W.; Ajayan, P. M. Band Gap Engineering and Layer-by-Layer Mapping of Selenium-Doped Molybdenum Disulfide. *Nano Lett.* **2014***, 14*, 442-449.
199. Chen, Y.; Xi, J.; Dumcenco, D. O.; Liu, Z.; Suenaga, K.; Wang, D.; Shuai, Z.; Huang, Y.; Xie, L. Tunable Band Gap Photoluminescence from Atomically Thin Transition-Metal Dichalcogenide Alloys. *ACS Nano* **2013***, 7*, 4610-4616.
200. Zhang, M.; Wu, J.; Zhu, Y.; Dumcenco, D. O.; Hong, J.; Mao, N.; Deng, S.; Chen, Y.; Yang, Y.; Jin, C.; Chaki, S. H.; Huang, Y.; Zhang, J.; Xie, L. Two-Dimensional Molybdenum Tungsten Diselenide Alloys: Photoluminescence, Raman Scattering, and Electrical Transport. *ACS Nano* **2014***, 8*, 7130-7137.
201. Elias, A. L.; Perea-Lopez, N.; Castro-Beltran, A.; Berkdemir, A.; Lv, R.; Feng, S.; Long, A. D.; Hayashi, T.; Kim, Y. A.; Endo, M.; Gutierrez, H. R.; Pradhan, N. R.; Balicas, L.; Houk, T. E. M.; Lopez-Urias, F.; Terrones, H.; Terrones, M. Controlled Synthesis and Transfer of Large-Area WS_2 Sheets: From Single Layer to Few Layers. *ACS Nano* **2013***, 7*, 5235-5242.
202. Ji, Q.; Kan, M.; Zhang, Y.; Guo, Y.; Ma, D.; Shi, J.; Sun, Q.; Chen, Q.; Zhang, Y.; Liu, Z. Unravelling Orientation Distribution and Merging Behavior of Mono layer MoS_2 Domains on Sapphire. *Nano Lett.* **2015***, 15*, 198-205.
203. Li, H.; Wu, J.; Huang, X.; Lu, G.; Yang, J.; Lu, X.; Zhang, Q.; Zhang, H. Rapid and Reliable Thickness Identification of Two-Dimensional Nanosheets Using Optical Microscopy. *ACS Nano* **2013***, 7*, 10344-10353.
204. Dresselhaus, M. S.; Jorio, A.; Hofmann, M.; Dresselhaus, G.; Saito, R. Perspectives on Carbon Nanotubes and Graphene Raman Spectroscopy. *Nano Lett.* **2010***, 10*, 751-758.

205. Ferrari, A. C.; Meyer, J. C.; Scardaci, V.; Casiraghi, C.; Lazzeri, M.; Mauri, F.; Piscanec, S.; Jiang, D.; Novoselov, K. S.; Roth, S.; Geim, A. K. Raman Spectrum of Graphene and Graphene Layers. *Phys. Rev. Lett.* **2006***, 97*, 187401.

206. Berkdemir, A.; Gutierrez, H. R.; Botello-Mendez, A. R.; Perea-Lopez, N.; Elias, A. L.; Chia, C.; Wang, B.; Crespi, V. H.; Lopez-Urias, F.; Charlier, J.; Terrones, H.; Terrones, M. Identification of Individual and Few Layers of WS_2 Using Raman Spectroscopy. *Sci. Rep.* **2013***, 3*, 1755.

207. Novoselov, K. S.; Geim, A. K.; Morozov, S. V.; Jiang, D.; Zhang, Y.; Dubonos, S. V.; Grigorieva, I. V.; Firsov, A. A. Electric Field Effect in Atomically Thin Carbon Films. *Science* **2004***, 306*, 666-669.

208. Zhu, H.; Wang, Y.; Xiao, J.; Liu, M.; Xiong, S.; Wong, Z. J.; Ye, Z.; Ye, Y.; Yin, X.; Zhang, X. Observation of Piezoelectricity in Free-Standing Monolayer MoS_2. *Nat. Nanotechnol.* **2015***, 10*, 151-155.

209. Peimyoo, N.; Shang, J.; Yang, W.; Wang, Y.; Cong, C.; Yu, T. Thermal Conductivity Determination of Suspended Mono- and Bilayer WS_2 by Raman Spectroscopy. *Nano Res.* **2015***, 8*, 1210-1221.

210. Eknapakul, T.; King, P. D. C.; Asakawa, M.; Buaphet, P.; He, R. -.; Mo, S. -.; Takagi, H.; Shen, K. M.; Baumberger, F.; Sasagawa, T.; Jungthawan, S.; Meevasana, W. Electronic Structure of a Quasi-Freestanding MoS_2 Monolayer. *Nano Lett.* **2014***, 14*, 1312-1316.

211. Shi, H.; Yan, R.; Bertolazzi, S.; Brivio, J.; Gao, B.; Kis, A.; Jena, D.; Xing, H. G.; Huang, L. Exciton Dynamics in Suspended Monolayer and Few-Layer MoS_2 2D Crystals. *ACS Nano* **2013***, 7*, 1072-1080.

212. Yun, S. J.; Chae, S. H.; Kim, H.; Park, J. C.; Park, J.; Han, G. H.; Lee, J. S.; Kim, S. M.; Oh, H. M.; Seok, J.; Jeong, M. S.; Kim, K. K.; Lee, Y. H. Synthesis of Centimeter-Scale Monolayer Tungsten Disulfide Film on Gold Foils. *ACS Nano* **2015***, 9*, 5510-5519.

213. Kochat, V.; Pal, A. N.; Sneha, E. S.; Sampathkumar, A.; Gairola, A.; Shivashankar, S. A.; Raghavan, S.; Ghosh, A. High Contrast Imaging and Thickness Determination of Graphene with In-Column Secondary Electron Microscopy. *J. Appl. Phys.* **2011***, 110*, 014315.

214. Shi, J.; Zhang, X.; Ma, D.; Zhu, J.; Zhang, Y.; Guo, Z.; Yao, Y.; Ji, Q.; Song, X.; Zhang, Y.; Li, C.; Liu, Z.; Zhu, W.; Zhang, Y. Substrate Facet Effect on the Growth of Monolayer MoS_2 on Au Foils. *ACS Nano* **2015***, 9*, 4017-4025.

215. Urban, K. W. Studying Atomic Structures by Aberration-Corrected Transmission Electron Microscopy. *Science* **2008***, 321*, 506-510.

216. Qiu, H.; Xu, T.; Wang, Z.; Ren, W.; Nan, H.; Ni, Z.; Chen, Q.; Yuan, S.; Miao, F.; Song, F.; Long, G.; Shi, Y.; Sun, L.; Wang, J.; Wang, X. Hopping Transport through Defect-Induced Localized States in Molybdenum Disulphide. *Nat. Commun.* **2013***, 4*, 2642.

Chapter 3

Methodology

3.1 Introduction

This research project was initiated as the result of devoted interest towards synthesizing high-quality WS_2 monolayers and probing their unique properties. Some experimental and analytical techniques dilated in the review were therefore chosen to help fulfil these endeavours. In lieu of providing an overview, this chapter intends to elaborate specific methods/protocols in techniques that are exclusively employed to aid the progression of this project. For example, the section on chemical vapour deposition (CVD) will renounce discussions addressed to how the system delivers monolayer WS_2 or why a specific method is chosen. Rather, it will focus on delivering operational details, such as CVD recipes, sample preparation and transfer procedures.

3.2 CVD Synthesis and Transfer

As the first objective of this project, a CVD system was constructed for WS_2 synthesis (figure 1) by referring to existing reports (*Chapter 2*). The CVD system uses two tubular furnaces, which are dubbed low-temperature (LT) and high-temperature (HT) furnace. This dual-temperature-zone system is needed for heating sulphur (S) and tungsten trioxide (WO_3) precursors, respectively, at low and high temperatures (*i.e.,* S melting point is ~ 115 ºC while WO_3 is ~1473 ºC). The S and WO_3 powder are placed in their respective ceramic containers for evaporation, from which S and WO_3 vapour are delivered to target

substrates (2×2 cm SiO_2/Si) by an inert carrier gas (Ar) controlled precisely *via* a mass flow controller (MFC). The substrates supported by an additional ceramic container are located at the downstream of Ar gas for deposition of WS_2. All precursors and substrates are kept within the confines of a 1-inch-diameter quartz tube that is normally replaced after several cycles of CVD reactions. During the CVD reaction, the quartz tube was properly sealed by vacuum fittings which were connected to the Ar supply gas line on one end and an exhaust outlet on the other. The exhaust pipeline is prone to solidification of S vapour (non-heated region), thus it is inspected regularly for signs of S congestion in order to avoid over-pressurized CVD chamber. In *Chapter 5 and 6*, WS_2 monolayers were synthesized in a double-walled quartz tube, where a 1-cm-diameter short quartz tube was placed within the original tube to isolate S and WO_3 precursors (see *Chapter 5* – figure 1 for the corresponding schematic).

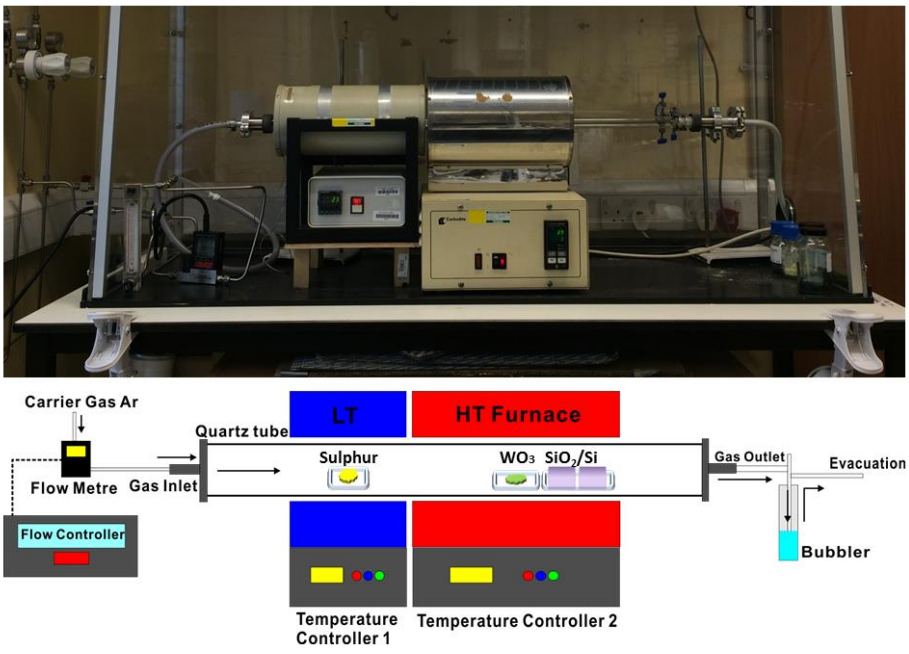

Figure 1. Photograph and schematic of the CVD system used throughout the duration of this project.

3.2.1 Preparation and Growth of Monolayer WS_2

On top of the WS_2 (MoS_2) growth mechanisms depicted in *Chapter 2*, further exploration of CVD parameter space has led to discovery of novel CVD techniques for synthesis of high-quality WS_2 monolayers. Exact preparation and CVD recipes for producing monolayer WS_2 in this project are enumerated as follows:

For substrate preparation, 2-by-2 (cm) Si substrates with a 300 nm (or 90 nm) SiO_2 layer were cleaned in acetone and subsequently in isopropanol *via* sonication. Before loading into the reaction chamber, substrates were further cleaned by oxygen plasma. In regard to the single-walled CVD reaction, 1g S powder (Sigma-Aldrich, purum grade ≥ 99.5%) was placed in the LT furnace sublimating at ~180 ºC while 1g WO_3 powder (Sigma-Aldrich, puriss grade > 99.9%) was heated at ~1070 ºC in the HT furnace. The cleaned SiO_2/Si substrates were required to be placed at the downstream of S and WO_3 vapour (*i.e.,* 10 cm from the centre of the HT furnace), where furnace temperature was kept at ~860 ºC. Prior to vaporizing the precursors, CVD chamber was purged with 500 sccm flow rate of Ar gas for 30 min. The flow rate was then adjusted down to 100 sccm for WS_2 growth on SiO_2/Si substrates, when S and WO_3 temperature started to ramp up, respectively, at ~30 ºC min^{-1} and 40 ºC min^{-1}. Upon reaching the target temperatures, the CVD system was given an extra 60 min such that WO_{3-x} and S could react and migrate on the substrate to form large monolayer WS_2 domains. The WS_2 sample was quickly cooled as soon as the reaction finished. However, obtaining high-quality WS_2 monolayers requires delicate control over S introduction timing, discussed in *Chapter 4*. The production of optimal WS_2 samples was achieved by ramping S at 15 min (-10 min S introduction time) before WO_3 reaching 1070 ºC. For the double-walled CVD set-up, the added inner quart tube has resulted in alteration of Ar flow rate (at growth stage), growth time and precursor quantities. Both S and WO_3 remained at the original positions but were contained, respectively, in the original tube and the inner tube. Accordingly, the amount of S and WO_3 powder used was able to reduce to 400 mg and 200 mg, respectively. After purging

the system, 250 sccm Ar flow rate was adopted for the WS_2 synthesis, where the growth of large monolayer domains was achieved by using a 3 min growth time while 5 min was needed to acquire regional monolayer continuous films.

3.2.2 Transfer of Monolayer WS_2

In this project, the as-grown monolayer WS_2 from CVD was transferred off the SiO_2/Si substrate for TEM characterisations. The WS_2 sample (on SiO_2/Si) was first spin coated with a thin layer of poly-methyl-methacrylate (PMMA, 8% wt. in anisole, 495k molecular weight) as the supportive scaffold. The spin coater was set at 4700 rpm for 60 seconds. Subsequently, the as-coated PMMA was cured onto monolayer WS_2 by heating at 150 ºC for 15 minutes. As exhibited in figure 2, the underlying SiO_2/Si substrate was detached by floating the PMMA-cured WS_2 sample on a 1M KOH (Sigma-Aldrich reagent grade 90%) solution at room temperature. Further rinsing of the PMMA/WS_2 thin film was carried out by several deionized water baths, and then transferred to a designated substrate, such as a holey silicon nitride TEM grid (Agar Scientific Y5385). The PMMA/WS_2 was left to dry overnight in air on the TEM grid, and then baked at 150 ºC for 15 min to improve sample adhesion. Finally, the WS_2 transferred sample was prepared ready by removing the PMMA *via* a 2-hour acetone solution bath at 45 ºC.

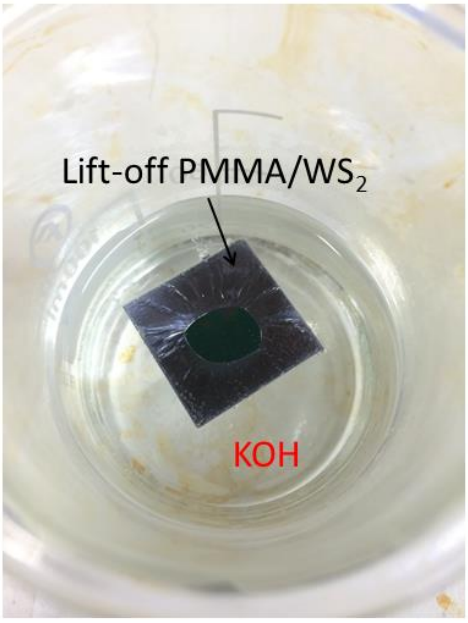

Figure 2. Transfer of WS_2 layers from a SiO_2/Si substrate in 1M KOH solution.

3.3 Optical Microscopy

Optical Microscopy (OM) was used frequently for characterisation of monolayer WS_2 due to its unique layer-dependent optical contrast (section 2.5.1) and high-throughput ability at low-cost. Two different OM set-ups were employed for this project, namely the eVue Pro 40X digital imaging system lens built-in for the Cascade MicroTech probe station, and the Mitutoyo objective lens with a 50x magnification attached to the CMOS camera (DCC1645C Thorlabs high-resolution 1280×1024 CMOS camera with colour sensor). The former is capable of providing high-contrast OM images with respect to different WS_2 layer thicknesses on a SiO_2/Si substrate. Therefore it was used for preliminary examination of WS_2 monolayers after synthesis, and observation of oxidized WS_2 grain boundaries (GBs) in *Chapter 5*. The latter is inferior in terms of optical contrast, but it was implemented easily into the bespoke built probe station in our lab and used for recording electrically induced dynamics (electroburning and electroluminescence) in monolayer WS_2 (*Chapter 5*

and 6). Optical images were frequently brightness/contrast enhanced to show information of interest using the image processing tool, “ImageJ”.

3.4 Raman Spectroscopy

Monolayer characteristic of WS_2 can be identified saliently by Raman spectroscopy, as introduced in section 2.5.2. The JY Horiba Labram Aramis imaging confocal Raman spectrometer was used to analyse spectral signals of monolayer WS_2 (on SiO_2/Si) excited by a 532 nm frequency doubled Nd:YAG laser. In the meantime, the laser excitation induced photoluminescence (PL), which was also measured *via* the same Raman spectrometer. Switching between Raman and PL measurement mode was accessible from the software package installed. Upon using Raman mode, spectra were normally taken from 200 to 600 cm^{-1} range with the fine resolution 1800 slits per mm grating. The incident laser intensity was filtered to 10%, and the acquisition time was kept within 10 seconds. As a result of the high PL efficiency from monolayer WS_2, the laser filter and acquisition time were in need to be further reduced to 1% and less than 1 second, respectively. The PL intensity as a function of wavelength (*i.e.,* 500-800 nm) was captured by using the coarse resolution 600 slits per mm grating. To investigate the uniformity of as-grown WS_2 monolayers, this instrument was able to provide Raman and PL multi-point spectra across lateral dimensions (XY coordinates) in a fixed step size, namely Raman and PL mapping. In a Raman mapping mode, the acquisition time was 0.5 second so as to expedite the acquisition process, much in the same way that 0.1 second of acquisition time was employed for the PL mapping.

In *Chapter 6*, the PL spectrum (overlaid on the EL) was not obtained from the instrument above. Instead, it was developed from the bespoke built probe station coupled to the spectrometer with the attached CCD (Princeton Instruments Acton SP-2300 spectrometer with a Princeton Instruments, PIXIS 100 CCC). The PL measurement was then conducted

using a 532 nm laser with 0.5 mW power focused by the 50x objective lens to a sport of ~5 μm. The electroluminescence (EL) signal was collected by the same spectrometer *via* the microscopy system but without any laser excitation.

3.5 Scanning Electron Microscopy

Since OM provided access to high-contrast observation of WS_2 domains on SiO_2/Si substrates, the major function of scanning electron microscopy (SEM) in this project was investigating nanoscale geometry of as-grown WS_2 domains which were undetectable *via* OM. There were two SEM model used, namely the Hitachi-4300 and the Zeiss Merlin Analytical. Both SEMs operated at low accelerating voltages (2-3 kV), but the Hitachi was inferior when comparing to the Zeiss in terms of resolution. The Hitachi was good enough for characterizing WS_2 domain size and configuration, whereas observing WS_2 micro-/nanoribbons within GBs was only possible with the Zeiss.

All SEM characterisations were done on WS_2 samples deposited on SiO_2/Si substrates. In preparing an SEM sample, silver paste or carbon sticky pads are used most often for pasting the WS_2 sample on a SEM sample stub, as a result of which the WS_2 sample suffers less from surface charging. Despite that the silver paste was of better conductivity, the carbon sticky pad was more favourable due to its easy recovery of samples from SEM stubs. The removal of silver paste involves organic solvent rinsing, which could potentially contaminate the WS_2 sample and prevent it from being used in succeeding experiments.

3.6 Atomic Force Microscopy

The number of layers in as-grown WS_2 domains is not affirmatively characterised if relying on Raman intensity profiles only. Hence, it often demands further confirmation provided by

atomic force microscopy (AFM). The fact that WS_2 domains were grown directly on rigid SiO_2/Si substrates facilitated a quick AFM investigation, excluding the necessity of transferring samples. The topological variation of WS_2 samples was detected by the silicon AFM probe *via* the tapping mode. In *Chapter 4*, the AFM characterisation was performed on the Veeco Park CP AutoProbe SPM (*i.e.,* date was collected by Mr. Fan), while in *Chapter 5 and 6*, the Asylum Research MFP-3D AFM was used instead (*i.e.,* data was collected by Dr. Pacios). The AFM mapping and height/thickness profiles were generated by using the "Gwyddion" software.

3.7 Transmission Electron Microscopy

Unravelling crystal orientation and lattice structure in monolayer WS_2 domains entailed employing a range of transmission electron microscopy (TEM) instruments. Selected area electron diffraction (SAED) of WS_2 triangular domains was done on the JEOL 2100 TEM operated at accelerating voltage of 80kV, which contributed to the determination of monolayer WS_2 single crystallinity and GB location, as shown in *Chapter 4 and 5*. Aberration-corrected (AC) TEM (operated at 80 kV), that is the Stanford's FEI Titan 80-300 environmental TEM, was employed to deliver the energy dispersive X-ray (EDX) spectroscopy as well as the high-resolution (HR) TEM image in *Chapter 4*. In *Chapter 5*, the ACTEM was used again but with a different model to capture WS_2 monolayers in atomic resolution, which was realized by the Oxford's JEOL JEM-2200MCO field emission gun TEM, fitted with a CEOS probe, image aberration correctors, and a double Wien Filter monochromator operated at 80 kV. The TEM experiments depicted here were carried out by Dr. Robertison (the Oxford's JEOL), Dr. Ai Leen Koh (the Stanford's FEI Titan) and Mr. He (the JEOL 2100), respectively. Nevertheless, the TEM samples prepared using the method introduced in section 3.2.2 provoked formation of an amorphous carbon layer above the WS_2 sample, which had blocked the electron beam during imaging. Thanks to

the dry-cleaning method,*(1)* high-quality TEM samples were prepared *via* active-carbon baking, where a WS_2 TEM sample was gradually heated up in a smidgen of active carbon powder and baked at 200 ºC for 30-40 min.

3.8 Electrical Measurement

Electrical measurement, such as the source-drain output measurement, was conducted on the bespoke built probe station mentioned earlier in section 3.3. The probe station was equipped with a pair of ultrafine W probe tips (Signatone, SE-T, 5 μm in diameter) controlled by micro-manipulators. Upon carrying out the measurement, the probes were lowered onto the surface of a monolayer WS_2 domain to make initial contact and then moved slightly horizontally to produce a good stable contact. When source-drain bias started to ramp, the GB electroburning (*Chapter 6*) and the EL process (*Chapter 7*) were observed by the probe station's optical system. The source-drain bias/current was programmed to run at designated values through the Keithley source-measurement unit (2400-LV).

3.9 Reference

1. Algara-Siller, G.; Lehtinen, O.; Turchanin, A.; Kaiser, U. Dry-Cleaning of Graphene. *Appl. Phys. Lett.* **2014***, 104*, 153115.

Chapter 4

Controlling Sulphur Precursor Addition for Large Single Crystal Domains of WS_2

4.1 Introduction

Atomically-thin transition metal dichalcogenides (TMDs) have expanded two-dimensional (2D) materials beyond graphene and invigorated the promise of 2D materials in electronics.*(1-7)* While the zero-band-gap nature has limited graphene's implementation in electronics,*(8)* single layered atomic TMD materials are direct band-gap semiconductors with applications in electronics, optoelectronics *(9-12)* and valleytronics.*(13,14)* In recent years, single-layer MoS_2 and WS_2 have been fabricated *via* several methods such as mechanical exfoliations,*(3,15-17)* liquid exfoliation,*(4,5,18)* and sulfurization of transition metal oxides.*(19-23)* However, producing synthetic large-area high-quality monolayers of TMDs is possibly more challenging than graphene due to the propensity for the formation of nanoparticles *(24,25)* or multilayers.*(26)* Chemical vapour deposition (CVD) growth of monolayer MoS_2 crystal domains and films has been realised,*(19,27-29)* which has facilitated extensive studies regarding their unique photoluminescence and electrical transport properties.*(28,30,31)*

The CVD synthesis of WS_2 monolayer crystals is slightly more challenging than MoS_2 because of the higher melting points of the W-based precursors, such as WO_3, compared to the Mo-based precursor counterparts, and the resulting higher growth temperatures needed. In the past decade, the CVD approach has proved extremely useful for production of large-area single crystalline graphene domains which can diminish grain boundary defects for transport devices.*(32,33)* Although the creation of a single crystalline

structure of monolayer WS_2 has been recently achieved,*(34,35)* the controlled CVD growth of large-area monolayers with homogenous crystallinity still remains an experimental challenge and requires further investigation.

The approach for most reports of CVD growth of WS_2 relies on the reaction of S vapour with a W-precursor at elevated temperatures, with both precursors placed in a single furnace. Not having individual control over each precursor's temperature limits the parameter space of chemical reaction. To overcome this limitation, we utilize a CVD approach that separates the two precursors into different furnaces, one containing the elemental S and the other containing both the W-precursor and the growth substrates. Both the S vapour and W-precursor vapour are carried downstream to the growth substrate by pure Ar gas. We examine how the timing of when the S precursor is heated relative to the WO_3 precursor to release S vapour influences the domain size, crystal thickness and homogeneity.

4.2 Results and Discussion

Figure 1a presents a schematic illustration of the double-furnace 1inch quartz tube atmospheric pressure CVD system designed for allowing the abundant supply of S vapour both before and during the formation of WS_2 thin crystals on SiO_2/Si substrates. The S powder was heated at ~180°C in low temperature (LT) furnace which generates vapour carried by pure Ar gas to the reaction furnace with high temperature (HT). The HT furnace contains both WO_3 and the growth substrates. The WO_3 precursor is placed in the center of the HT furnace and heated to ~1070°C for the crystal growth on the substrate. The SiO_2/Si substrate was placed downstream from WO_3 where WS_2 nucleation and growth were enabled at a lower temperature (~860°C).

Figure 1b shows the temperature profiles employed for ramping or cooling of S and WO_3 precursors to the reaction temperatures (*i.e.,* temperature profile for the SiO_2/Si substrate simultaneously ramps and cools along with that of the WO_3 precursor). With regard to the WS_2 growth stage, all WS_2 formation reactions were equally given 60 min growth time starting at 0 min when the temperature of the HT furnace reached 1070°C (WO_3)/860°C (substrate). The solid S powder in the LT zone was heated and carried downstream using Ar to the reaction chamber at times of 0, 10 or 20 min before the HT furnace (and WO_3 precursor) reached 1070°C. These different introduction timings of S vapour prior to the WS_2 growth stage were important in the controlled growth of thin crystal domains on as-prepared substrates.*(27)* By optimization of the reaction variables, such as the amount of precursors used, the reaction temperature and the positioning of the growth substrate, we have improved synthesis of WS_2 domains so that they are large enough to be visible with the naked eye, shown in Figure 1c-e.

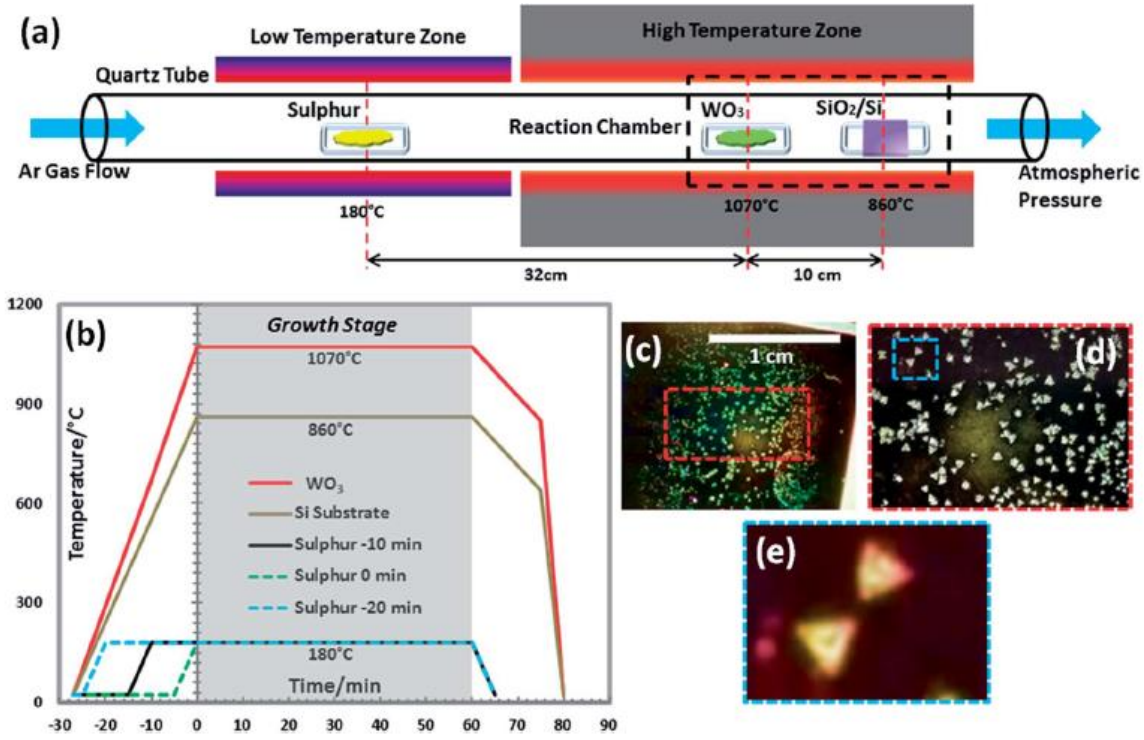

Figure 1. Atmospheric pressure CVD synthesis of large-area WS_2 crystal domains on the SiO_2/Si substrate. (a) Schematic presentation of the corresponding CVD experimental set-up with a highlighted WS_2 reaction chamber (black dashed line). (b) Temperature profiles employed for

formation of WS_2 on the SiO_2/Si substrate with sulphur introduced at 0, -10 and -20 min due to the target reaction temperature at 1070°C/860°C. (c) Photo of large triangular WS_2 crystals deposited on a 2cm SiO_2/Si substrate. (d) and (e) Zoom-in images chosen from the selected area (red dashed line) in (c) and (blue dashed line) in (d), respectively, showing triangular WS_2 domains.

Figure 2a presents an overview of large WS_2 crystal domains (200~300μm) deposited on the SiO_2 surface where sulphur (S) was introduced 10 min prior to growth, the black line in figure 1b. The WS_2 domains are scattered across the SiO_2/Si substrate with low nucleation density which can permit the large crystal domain size. However, the distribution of domain sizes and crystallinity across the substrate is due to the dynamics of the local supply of vapourized precursors. As a close kin to WS_2, previously reported vapour phase growth of monolayer MoS_2 triangular crystals has also inevitably encountered similar phenomena.*(23,28)* In figure 2b and c, we particularly demonstrate an as-deposited area where a triangular WS_2 domain as large as ~370μm was formed under the aforementioned conditions. Figure 2d shows an example of the optical contrast from one of these large WS_2 triangles (~300μm) on the SiO_2/Si substrate. The majority of as-obtained WS_2 single domains have sizes varying from ~200 to ~350μm excluding relatively small domains that are not fully crystallized. Characterization using AFM was performed at a selected region of a WS_2 triangular domain (figure 2e). Figure 2f shows an AFM image that correlates with the selected region in figure 2e and a line profile which determines the thickness of the as-grown WS_2 crystal to be ~1nm which is in good agreement with the reported thickness for monolayer WS_2 triangular crystals.*(22)* The WS_2 domains were primarily monolayer, but there were some bilayer and few layer domains as well. The monolayer domains were easily identified from the multi-layered domains by their substantially more intense photoluminescence (PL) emission, as illustrated in figure 3b. In this approach to synthesis of WS_2 atomically-thin crystals, we were able to produce the largest monolayer triangular single domain (~370μm) in the

recent development of large-area 2D dichalcogenides.*(28,34,36)* Some small particular materials are occasionally observed on the substrates post-growth and it is likely that these are formed during the cooling stages of the CVD, since they did not cause nucleation of WS_2 domains as it would be expected that they were present before or during growth.

Raman spectroscopy was used to confirm that the triangles were indeed WS_2. The Raman spectrum from a WS_2 single domain using an excitation laser with a wavelength (λ_{ex}) of 532 nm is shown in figure 2g, which demonstrates the characteristic in-plane vibrational (E^1_{2g}) mode and the out-of-plane vibrational (A_{1g}) mode at ~350 and ~416 cm^{-1}, respectively, for WS_2. The frequency difference between the E^1_{2g} mode and A_{1g} mode is shown to be ~66 cm^{-1} which matches the Raman spectroscopic characteristics of single-layer-thick WS_2 films on SiO_2/Si substrates.*(17)* PL spectroscopy using a 532nm laser for excitation was undertaken, figure 2h, which revealed a strong PL peak between 550 and 750 nm, typical for a monolayer WS_2 crystal. The peak has maxima at the wavelength of 636 nm (direct band gap~1.95eV) which falls in the range of reported PL peak positions for monolayer WS_2 thin films.*(16,17,22,37)*

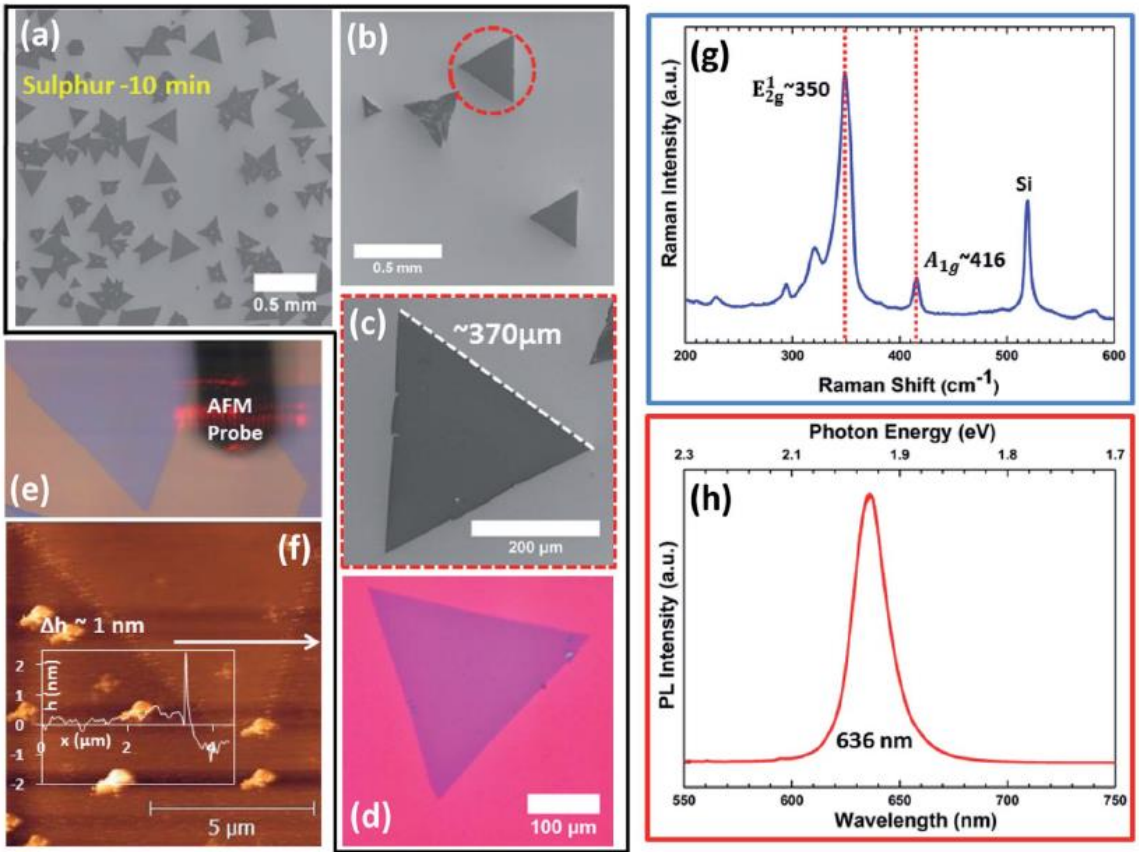

Figure 2. SEM, AFM, Optical, Raman, and PL characterization of WS_2 single crystals obtained from growth achieved with -10 min sulphur introduction. (a) SEM image of overall coverage of monolayer WS_2 crystals on SiO_2/Si. (b) and (c) SEM images of the as-deposited area chosen to show extraordinary large WS_2 single crystal domains. (d) Optical image of a monolayer WS_2 single crystal on the SiO_2/Si substrate. (e) and (f) AFM result of the selected region of the as-grown large WS_2 crystal domain in (e). (g) and (h) Characteristic Raman and PL spectra of as-produced monolayer WS_2 domains exhibited in (d).

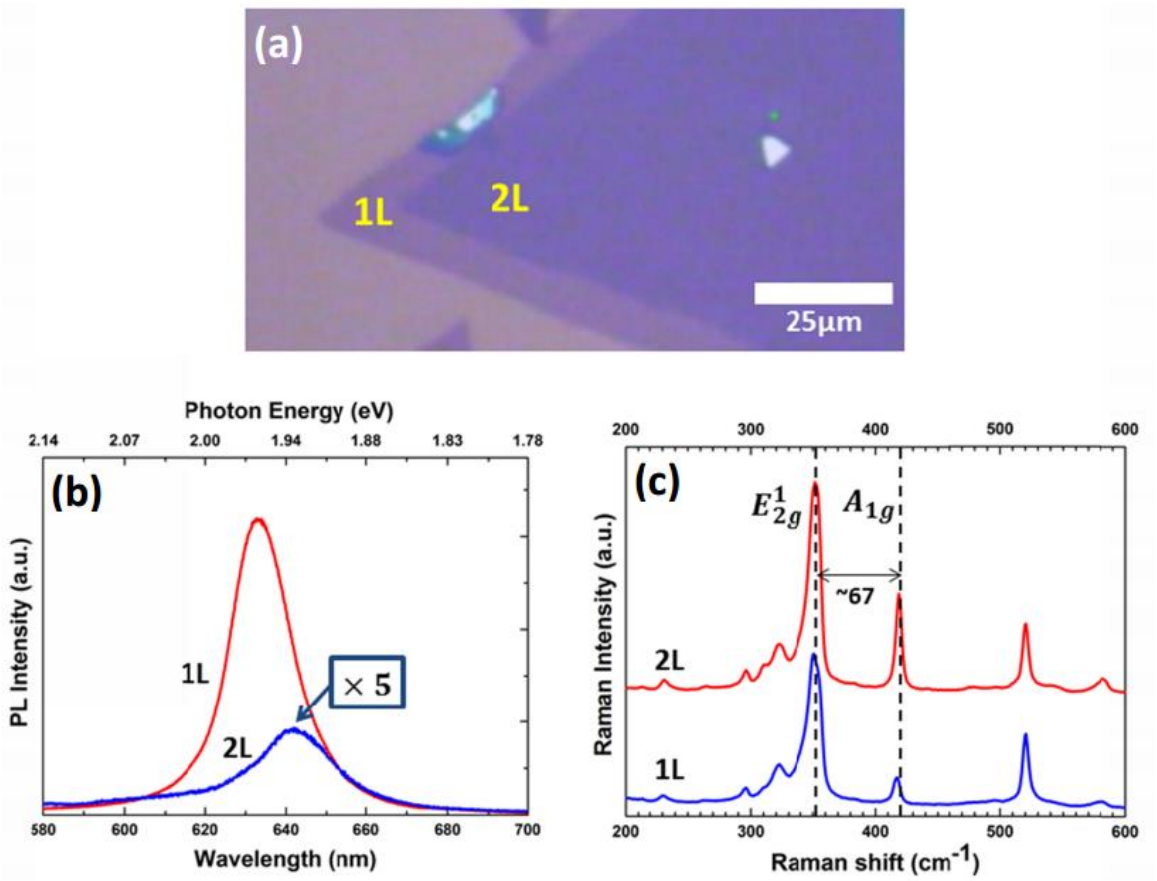

Figure 3. PL and Raman characterization of WS_2 monolayer (1L) and bi-layer (2L) domains. (a) Optical image of the as-examined WS_2 domain. (b) and (c) Characteristic PL and Raman profiles of the corresponding 1L and 2L WS_2 domains indicated in (a).

In the interest of studying uniformity and crystallinity of the as-formed crystals, PL and Raman mapping were executed on three major types of the large monolayer WS_2 domains presented in Figure 4a-c. As provided in the figure 3c, the most prominent difference between single- and bi-layer WS_2 regarding their Raman spectrum is the ratio of E^1_{2g} peak intensity and A_{1g} intensity. For a bilayer, the E^1_{2g}/A_{1g} ratio is of ~2 whereas the ratio for a single-layer can be of three times greater. Therefore, we have plotted the ratio of these two characteristic Raman peaks against *XY* coordinates where multi-point Raman analysis was conducted on WS_2 crystal domains shown in Figure 4a-c. As a result, the high consistency of E^1_{2g}/A_{1g} peak intensity ratio of ~6 across the single domains is

shown respectively in Figure 4d-f. This has ascertained that a high uniformity of the monolayer WS_2 single domain over an area of up to ~0.05 mm^2 is plausible.*(22,28,34,35)* Figure 4g-i elaborate the integrated PL peak intensity of monolayer WS_2 plotted with regard to the *XY* coordinates of PL multi-point analysis. Accordingly, it is confirmed that the lateral PL yield of these as-formed WS_2 monolayer domains is of good efficacy. It is noteworthy that the PL efficiency varies due to different WS_2 monolayer domain configurations. Furthermore, the PL intensity showed no signs of increased PL yield at the edge of the crystal domains.*(22,34)* In contrast, an increase in PL intensity from the edge towards the central body was discovered through analysis of single-point PL spectrum which is demonstrated in Figure 4j-l. Moreover, the relatively deteriorated PL as well as the slightly red-shifted peak position due to the edge of WS_2 monolayer domains has indicated that there might be an edge passivation incurred by impurities from the reaction chamber or localized oxidation in air.*(35)*

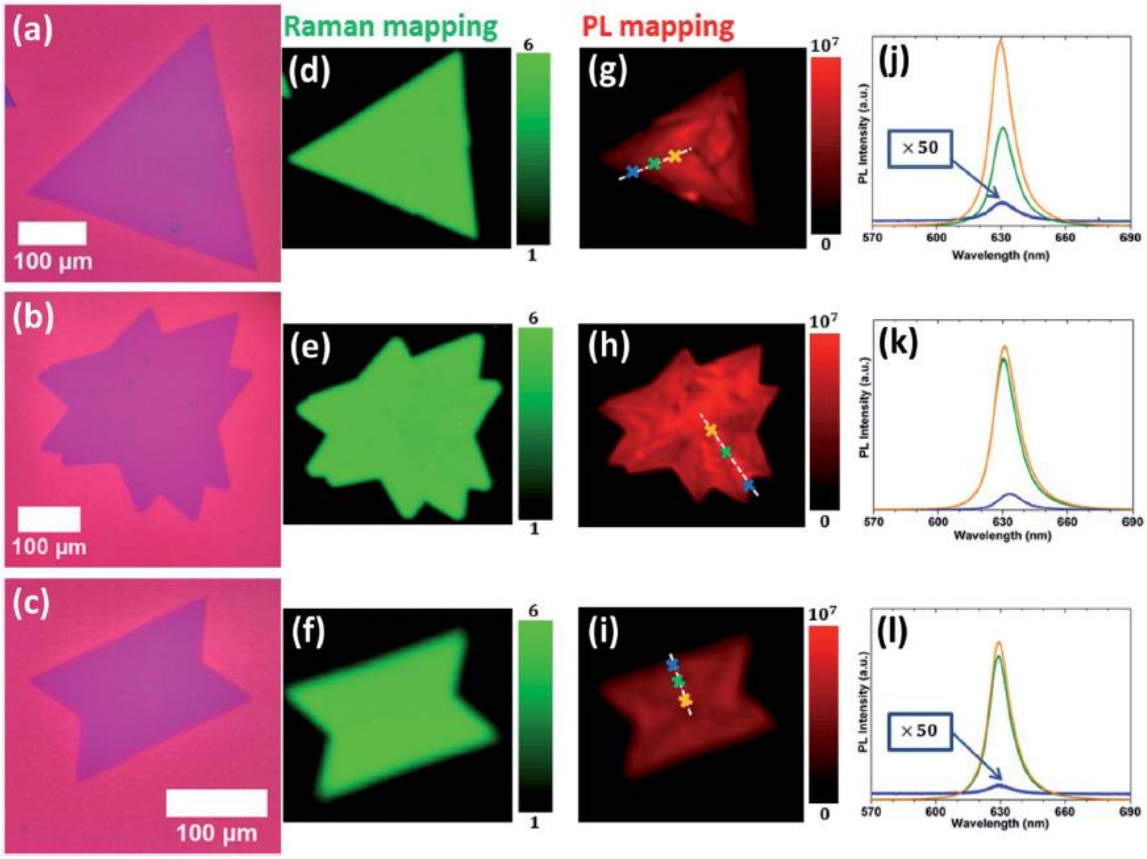

Figure 4. Raman and PL mapping of major configurations of as-grown monolayer WS_2 crystals. (a)-(c) Optical images of different WS_2 domain configurations. (d)-(f) Raman mapping of WS_2 crystals shown in (a)-(c) plotted with regard to the ratio of integrated E_{2g} peaks (330-370 cm^{-1}) / integrated A_{1g} peaks (400~430 cm^{-1}) at a 532 nm excitation laser. (g)-(i) PL mapping of WS_2 crystals in (a)-(c) plotted according to integrated characteristic photon emission intensities from wavelength 600 to 660 nm. (j)-(l) PL spectra of the colour-indicated characterization points selected from the edge towards the crystal center in (g)-(i) respectively.

The large WS_2 monolayer domains characterized in figure 1, 2 and 4 were grown for the S introduction time of -10 min, the black line in figure 1b. In order to demonstrate that the introduction time of S is important, we present results where the time is changed to 0 min and also -20 min, dashed green line and dashed blue line in figure 1b, respectively. Figures 5a-c show SEM images of the samples produced when sulphur is introduce at time = 0 min, the dashed green line in figure 1b. We observed defected or incomplete triangular WS_2 crystals formed close to the regions where possible deposition of WS_2 nanowires was facilitated. The regions covered with WS_2 nanowires are very susceptible to further deposition of WS_2 crystals as the nanowires are energetically favourable to act as WS_2 nucleation seeds. Figure 5c shows a large incomplete WS_2 triangle with a size of ~200μm being deposited. Figure 5d-f show SEM images of the samples when the sulphur introduction time was changed to -20 min, the blue dashed line in figure 1b. This case has the sulphur vapour introduced at almost the very beginning of WO_3 temperature ramping stage. In contrast to figure 5a, the WS_2 nanowires were no longer fabricated. Figures 5e and f show two different examples of WS_2 triangular crystals produced by this approach. One, shown in figure 5e, has uniform regions within a larger triangular crystal that is ~200μm. The other domain, figure 5f, shows relatively thick edges towards the crystal centre, which is likely to be due to the early stage of formation of a monolayer WS_2 single crystal that normally provides WS_{2+x} in the thick regions.*(34)*

The results in figures 1, 2, 4 and 5 demonstrate that the timing of the sulphur introduction is very important for the growth of large monolayer crystals of WS_2. If S is introduced too early, then there is not sufficient WO_3 precursor on the growth substrate to obtain large uniform WS_2 domains and if S is introduced too late, then there is too much WO_3 precursor on the substrate and WS_2 ends up to a thick multi-layer and nanotubes also form. The key step is the balance of WO_3 precursor concentration on the growth substrate. The WS_2 formation on the growth substrate occurs within a sulphur rich atmosphere and therefore growth is controlled by the WO_3 precursor. If the S vapour is introduced into the system before the bulk WO_3 precursor reaches the elevated temperature, then it can react to form bulk WS_2 which does not sublimate in our conditions easily and the result is no material on the growth substrate, and a large amount of bulk WS_2 powder where the WO_3 powder originated.

The position of the growth substrate within the HT furnace is also important. In figure 5g, we have carried out WS_2 deposition with the substrate face-down in comparison with the previous face-up approach. Face-down synthesis was achieved by placing the SiO_2/Si substrate above the WO_3 precursor with SiO_2-side facing downward. The precursor and the face-down substrate were both heated at 1070°C in the reaction chamber under equivalent conditions to that of the black line in figure 1b (-10 min). As a result, it can be seen in figure 5h that only very few WS_2 domains had deposited at the very edge of the SiO_2/Si substrate with almost none in the main central region of the substrate.

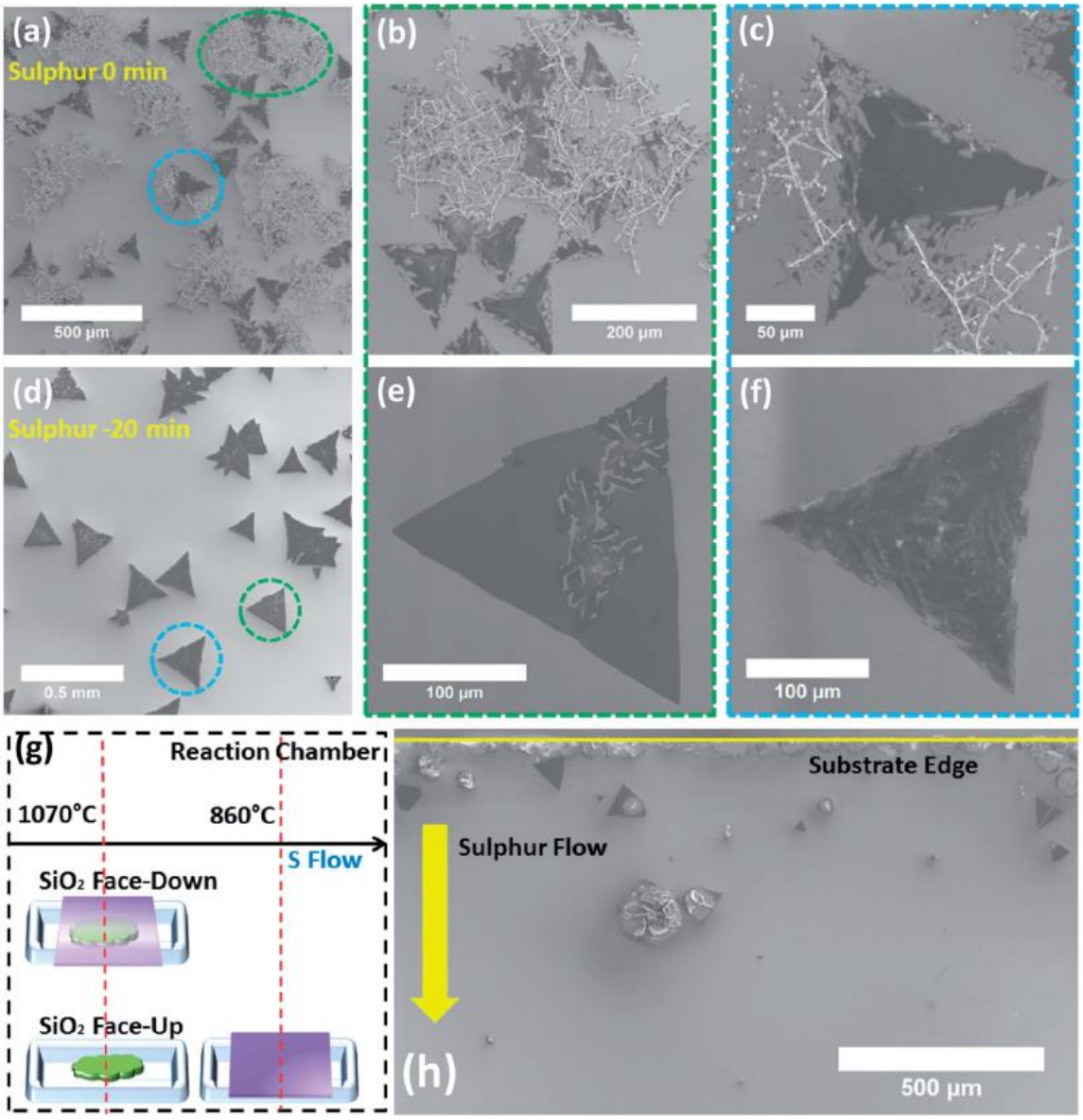

Figure 5. Influence of S introduction timing as well as face-up/face-down substrate positioning on WS_2 crystallization. (a)-(c) SEM images of WS_2 triangular crystals formed using 0 min sulphur introduction. (d)-(f) SEM images of WS_2 triangular crystal domains obtained from -20 min sulphur introduction. (g) Schematic illustration of the substrate face-down configuration in the reaction chamber with respect to the substrate face-up. (h) A SEM image taken at the edge of the SiO_2/Si substrate produced by the substrate face-down approach.

High-resolution transmission electron microscopy (HRTEM) combined with selected area electron diffraction (SAED) was used to investigate the crystallinity of the CVD-

synthesized WS_2 domains. Figure 6a shows an optical microscopy image of a selected region of a WS_2 crystal transferred onto a holey SiN TEM grid. Figure 6b provides a zoomed-in view of the WS_2 thin film region on the TEM grid. A comprehensive study of the SAED pattern was conducted along the array of 20 consecutive holes of the TEM grid highlighted in Figure 6a (red dashed line). Figure 6c-h show a selected group of the SAED patterns that correspond to the numbered holes in Figure 6a. All SAED patterns demonstrate the single crystalline structure except the last hole, number 20, as shown in figure 7. It showed a polycrystalline pattern due to the back-folded edge of the WS_2 triangle. The continuity of the single-crystal WS_2 diffraction pattern and lattice orientation occurs across dimensions of ~86 μm. Furthermore, the energy dispersive X-ray (EDX) spectrum in figure 6i shows that the domain consists of tungsten (W) and sulphur (S) with minor contamination (Ca) from the solvent used in the transfer process. Figure 5j is an aberration-corrected HRTEM image from a WS_2 domain showing a typical hexagonal lattice structure.

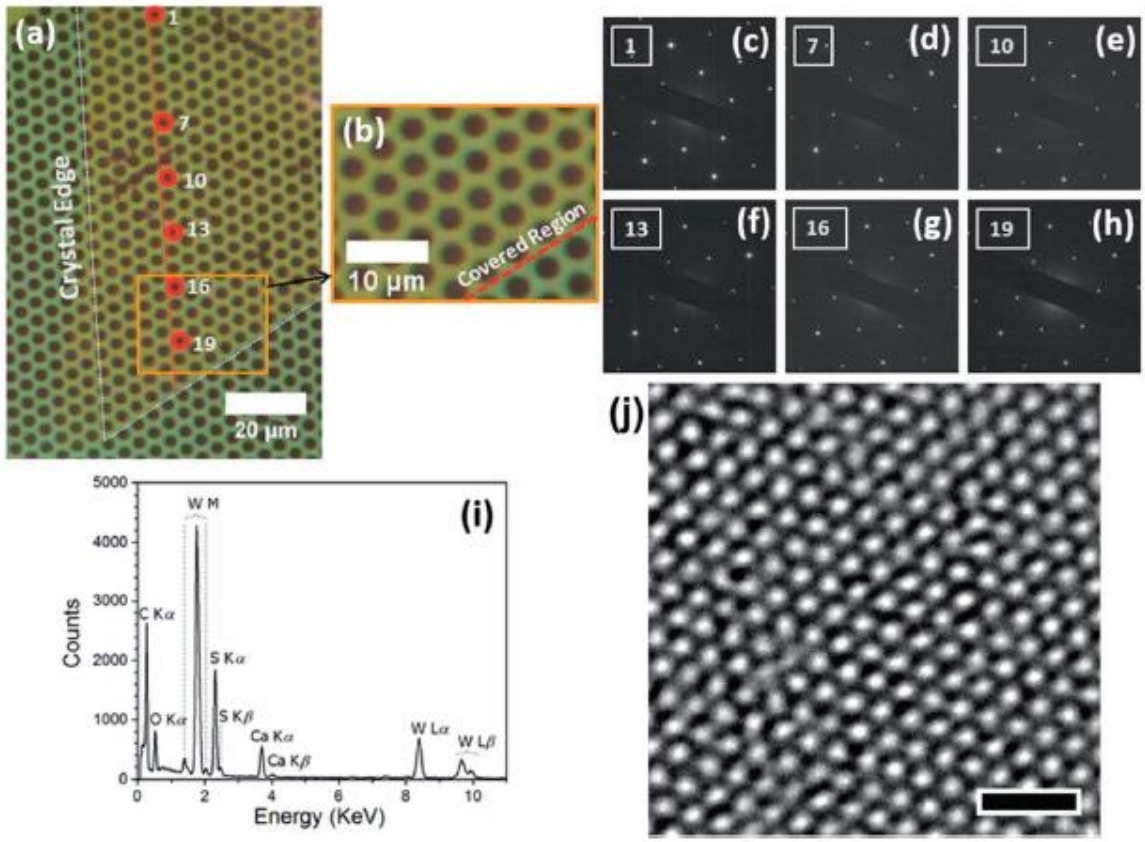

Figure 6. Single crystallinity and HRTEM characterisation of as-produced WS_2 domains. (a) Optical microscopy image of a region of the WS_2 triangular domain transferred onto a holey SiN TEM grid. (b) Higher magnification optical image of a covered and uncovered region of the WS_2 domain on the TEM grid. (c)-(h) SAED patterns from the WS_2 domain taken from regions marked in (a). (i) EDX spectroscopy from a WS_2 domain. (j) Aberration-corrected HRTEM image of a WS_2 showing a hexagonal lattice structure. The scale bar is 1nm.

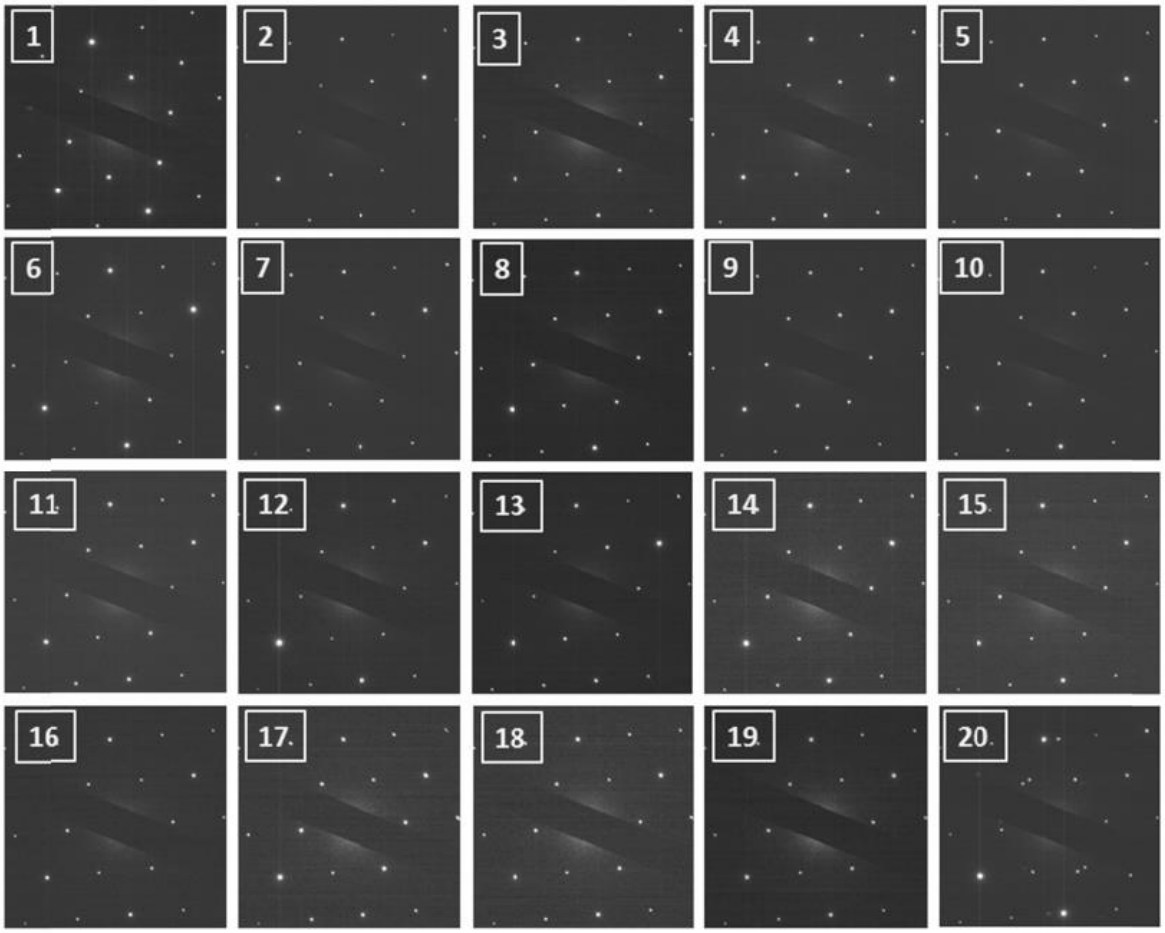

Figure 7. Full exhibition of SAED patterns obtained from the TEM grid holes highlighted in figure 6a.

4.3 Conclusion

We have demonstrated that the heating profile of the S precursor influences the growth of WS_2 domains by CVD. Using two separate furnaces was crucial in optimizing the growth conditions to achieve large triangular monolayer domains of WS_2 directly grown on silicon wafers with an oxide surface. The WS_2 crystals were photoluminescent and are therefore suitable for use in opto-electronic applications. These results provide important insights into the delicate factors that influence the growth of high-quality TMD semiconducting 2D materials. Further work will involve extending these growth methods to achieve full uniform monolayer coverage of WS_2 directly on device compatible substrates. One major challenge for growing continuous sheets of monolayer WS_2 using the current approach is that the S vapour reacts with the bulk WO_3 precursor and turns it into WS_2 bulk powder. This results in the quenching of the WO_3 precursor and the CVD growth of WS_2 domains stop, limiting their size. The key to moving this forward will be the ability to introduce S and WO_3 precursors into the growth chamber separately and therefore the WO_3 bulk powder will not quench and this should lead to the continuous growth.

4.4 Reference

1. Butler, S. Z.; Hollen, S. M.; Cao, L.; Cui, Y.; Gupta, J. A.; Gutierrez, H. R.; Heinz, T. F.; Hong, S. S.; Huang, J.; Ismach, A. F.; *et al.* Progress, Challenges, and Opportunities in Two-Dimensional Materials Beyond Graphene. *ACS Nano,* **2013***, 7*, 2898-2926.
2. Novoselov, K.; Jiang, D.; Schedin, F.; Booth, T.; Khotkevich, V.; Morozov, S.; Geim, A. Two-Dimensional Atomic Crystals. *Proc.Natl.Acad.Sci. U.S.A.,* **2005***, 102*, 10451-10453.
3. Mak, K. F.; Lee, C.; Hone, J.; Shan, J.; Heinz, T. F. Atomically Thin MoS_2: A New Direct-Gap Semiconductor. *Phys.Rev.Lett.,* **2010***, 105*, 136805.

4. Coleman, J. N.; Lotya, M.; O'Neill, A.; Bergin, S. D.; King, P. J.; Khan, U.; Young, K.; Gaucher, A.; De, S.; Smith, R. J.; Shvets, I. V.; Arora, S. K.; Stanton, G.; Kim, H.; Lee, K.; Kim, G. T.; Duesberg, G. S.; Hallam, T.; Boland, J. J.; Wang, J. J.; Donegan, J. F.; Grunlan, J. C.; Moriarty, G.; Shmeliov, A.; Nicholls, R. J.; Perkins, J. M.; Grieveson, E. M.; Theuwissen, K.; McComb, D. W.; Nellist, P. D.; Nicolosi, V. Two-Dimensional Nanosheets Produced by Liquid Exfoliation of Layered Materials. *Science,* **2011***, 331*, 568-571.
5. Matte, H. S. S. R.; Gomathi, A.; Manna, A. K.; Late, D. J.; Datta, R.; Pati, S. K.; Rao, C. N. R. MoS_2 and WS_2 Analogues of Graphene. *Angew.Chem.Int.Edit.,* **2010***, 49*, 4059-4062.
6. Chhowalla, M.; Shin, H. S.; Eda, G.; Li, L.; Loh, K. P.; Zhang, H. The Chemistry of Two-Dimensional Layered Transition Metal Dichalcogenide Nanosheets. *Nat.Chem.,* **2013***, 5*, 263-275.
7. Geim, A. K.; Novoselov, K. S. The Rise of Graphene. *Nat.Mater.,* **2007***, 6*, 183-191.
8. Palacios, T. Graphene Electronics Thinking Outside the Silicon Box. *Nat.Nanotechnol.,* **2011***, 6*, 464-465.
9. Wang, Q. H.; Kalantar-Zadeh, K.; Kis, A.; Coleman, J. N.; Strano, M. S. Electronics and Optoelectronics of Two-dimensional Transition Metal Dichalcogenides. *Nat.Nanotechnol.,* **2012***, 7*, 699-712.
10. Eda, G.; Maier, S. A. Two-Dimensional Crystals: Managing Light for Optoelectronics. *ACS Nano,* **2013***, 7*, 5660-5665.
11. Sundaram, R. S.; Engel, M.; Lombardo, A.; Krupke, R.; Ferrari, A. C.; Avouris, P.; Steiner, M. Electroluminescence in Single Layer MoS_2. *Nano Lett.,* **2013***, 13*, 1416-1421.
12. Bernardi, M.; Palummo, M.; Grossman, J. C. Extraordinary Sunlight Absorption and One Nanometer Thick Photovoltaics Using Two-Dimensional Monolayer Materials. *Nano Lett.,* **2013***, 13*, 3664-3670.
13. Mak, K. F.; He, K.; Shan, J.; Heinz, T. F. Control of Valley Polarization in Monolayer MoS_2 by Optical Helicity. *Nat.Nanotechnol.,* **2012***, 7*, 494-498.
14. Zeng, H.; Dai, J.; Yao, W.; Xiao, D.; Cui, X. Valley Polarization in MoS_2 Monolayers by Optical Pumping. *Nat.Nanotechnol.,* **2012***, 7*, 490-493.
15. Splendiani, A.; Sun, L.; Zhang, Y.; Li, T.; Kim, J.; Chim, C.; Galli, G.; Wang, F. Emerging Photoluminescence in Monolayer MoS_2. *Nano Lett.* **2010***, 10*, 1271-1275.
16. Zhao, W.; Ghorannevis, Z.; Chu, L.; Toh, M.; Kloc, C.; Tan, P.; Eda, G. Evolution of Electronic Structure in Atomically Thin Sheets of WS_2 and WSe_2. *ACS Nano,* **2013***, 7*, 791-797.
17. Zeng, H.; Liu, G.; Dai, J.; Yan, Y.; Zhu, B.; He, R.; Xie, L.; Xu, S.; Chen, X.; Yao, W.; Cui, X. Optical Signature of Symmetry Variations and Spin-Valley Coupling in Atomically Thin Tungsten Dichalcogenides. *Sci.Rep.,* **2013***, 3*, 1608.
18. Eda, G.; Yamaguchi, H.; Voiry, D.; Fujita, T.; Chen, M.; Chhowalla, M. Photoluminescence from Chemically Exfoliated MoS_2. *Nano Lett.,* **2011***, 11*, 5111-5116.
19. Zhan, Y.; Liu, Z.; Najmaei, S.; Ajayan, P. M.; Lou, J. Large-Area Vapor-Phase Growth and Characterization of MoS_2 Atomic Layers on a SiO_2 Substrate. *Small,* **2012***, 8*, 966-971.

20. Song, J.; Park, J.; Lee, W.; Choi, T.; Jung, H.; Lee, C. W.; Hwang, S.; Myoung, J. M.; Jung, J.; Kim, S.; Lansalot-Matras, C.; Kim, H. Layer-Controlled, Wafer-Scale, and Conformal Synthesis of Tungsten Disulfide Nanosheets Using Atomic Layer Deposition. *ACS Nano,* **2013***, 7*, 11333-11340.
21. Elias, A. L.; Perea-Lopez, N.; Castro-Beltran, A.; Berkdemir, A.; Lv, R.; Feng, S.; Long, A. D.; Hayashi, T.; Kim, Y. A.; Endo, M.; Gutierrez, H. R.; Pradhan, N. R.; Balicas, L.; Houk, T. E. M.; Lopez-Urias, F.; Terrones, H.; Terrones, M. Controlled Synthesis and Transfer of Large-Area WS_2 Sheets: From Single Layer to Few Layers. *ACS Nano,* **2013***, 7*, 5235-5242.
22. Gutierrez, H. R.; Perea-Lopez, N.; Elias, A. L.; Berkdemir, A.; Wang, B.; Lv, R.; Lopez-Urias, F.; Crespi, V. H.; Terrones, H.; Terrones, M. Extraordinary Room-Temperature Photoluminescence in Triangular WS_2 Monolayers. *Nano Lett.,* **2013***, 13*, 3447-3454.
23. Najmaei, S.; Liu, Z.; Zhou, W.; Zou, X.; Shi, G.; Lei, S.; Yakobson, B. I.; Idrobo, J.; Ajayan, P. M.; Lou, J. Vapour Phase Growth and Grain Boundary Structure of Molybdenum Disulphide Atomic Layers. *Nat.Mater.,* **2013***, 12*, 754-759.
24. Wiesel, I.; Arbel, H.; Albu-Yaron, A.; Popovitz-Biro, R.; Gordon, J. M.; Feuermann, D.; Tenne, R. Synthesis of WS_2 and MoS_2 Fullerene-Like Nanoparticles from Solid Precursors. *Nano Res.* **2009***, 2*, 416-424.
25. Rapoport, L.; Bilik, Y.; Feldman, Y.; Homyonfer, M.; Cohen, S.; Tenne, R. Hollow Nanoparticles of WS_2 as Potential Solid-State Lubricants. *Nature* **1997***, 387*, 791-793.
26. Kim, S.; Konar, A.; Hwang, W.; Lee, J. H.; Lee, J.; Yang, J.; Jung, C.; Kim, H.; Yoo, J.; Choi, J.; Jin, Y. W.; Lee, S. Y.; Jena, D.; Choi, W.; Kim, K. High-Mobility and Low-Power Thin-Film Transistors Based on Multilayer MoS_2 Crystals. *Nat.Commun.,* **2012***, 3*, 1011.
27. Lee, Y.; Zhang, X.; Zhang, W.; Chang, M.; Lin, C.; Chang, K.; Yu, Y.; Wang, J. T.; Chang, C.; Li, L.; Lin, T. Synthesis of Large-Area MoS_2 Atomic Layers with Chemical Vapor Deposition. *Adv.Mater.,* **2012***, 24*, 2320-2325.
28. van der Zande, A. M.; Huang, P. Y.; Chenet, D. A.; Berkelbach, T. C.; You, Y.; Lee, G.; Heinz, T. F.; Reichman, D. R.; Muller, D. A.; Hone, J. C. Grains and Grain Boundaries in Highly Crystalline Monolayer Molybdenum Disulphide. *Nat.Mater.,* **2013***, 12*, 554-561.
29. Wang, X.; Feng, H.; Wu, Y.; Jiao, L. Controlled Synthesis of Highly Crystalline MoS_2 Flakes by Chemical Vapor Deposition. *J.Am.Chem.Soc.,* **2013***, 135*, 5304-5307.
30. Zhang, W.; Huang, J.; Chen, C.; Chang, Y.; Cheng, Y.; Li, L. High-Gain Phototransistors Based on a CVD MoS_2 Monolayer. *Adv.Mater.,* **2013***, 25*, 3456-3461.
31. Lee, Y.; Yu, L.; Wang, H.; Fang, W.; Ling, X.; Shi, Y.; Lin, C.; Huang, J.; Chang, M.; Chang, C.; Dresselhaus, M.; Palacios, T.; Li, L.; Kong, J. Synthesis and Transfer of Single-Layer Transition Metal Disulfides on Diverse Surfaces. *Nano Lett.,* **2013***, 13*, 1852-1857.
32. Zhou, H.; Yu, W. J.; Liu, L.; Cheng, R.; Chen, Y.; Huang, X.; Liu, Y.; Wang, Y.; Huang, Y.; Duan, X. Chemical Vapour Deposition Growth of Large Single Crystals of Monolayer and Bilayer Graphene. *Nat.Commun.,* **2013***, 4*, 2096.
33. Yazyev, O. V.; Louie, S. G. Electronic Transport in Polycrystalline Graphene. *Nat.Mater.,* **2010***, 9*, 806-809.

34. Cong, C.; Shang, J.; Wu, X.; Cao, B.; Peimyoo, N.; Qiu, C.; Sun, L.; Yu, T. Synthesis and Optical Properties of Large-Area Single-Crystalline 2D Semiconductor WS_2 Monolayer from Chemical Vapor Deposition. *Adv.Opt.Mater.,* **2014***, 2*, 131-136.
35. Zhang, Y.; Zhang, Y.; Ji, Q.; Ju, J.; Yuan, H.; Shi, J.; Gao, T.; Ma, D.; Liu, M.; Chen, Y.; Song, X.; Hwang, H. Y.; Cui, Y.; Liu, Z. Controlled Growth of High-Quality Monolayer WS_2 Layers on Sapphire and Imaging Its Grain Boundary. *ACS Nano,* **2013***, 7*, 8963-8971.
36. Huang, J.; Pu, J.; Hsu, C.; Chiu, M.; Juang, Z.; Chang, Y.; Chang, W.; Iwasa, Y.; Takenobu, T.; Li, L. Large-Area Synthesis of Highly Crystalline WSe_2 Monolayers and Device Applications. *ACS Nano,* **2014***, 8*, 923-930.
37. Peimyoo, N.; Shang, J.; Cong, C.; Shen, X.; Wu, X.; Yeow, E. K. L.; Yu, T. Nonblinking, Intense Two-Dimensional Light Emitter: Monolayer WS_2 Triangles. *ACS Nano,* **2013***, 7*, 10985-10994.
38. Rong, Y.; Fan, Y.; Koh, A.; Robertson, A.; He, K.; Wang, S.; Tan, H.; Sinclair, R.; Warner, J. Controlling Sulphur Precursor Addition for Large Single Crystal Domains of WS_2. *Nanoscale*, **2014**, 6, 12096-12103.

Chapter 5

Controlled Preferential Oxidation of Grain Boundaries in Monolayer WS_2 for Direct Optical Imaging

5.1 Introduction

Development of chemical vapour deposition (CVD) techniques has enabled the growth of large-scale high-quality two-dimensional (2D) materials such as single-atom-thick graphene.*(1-4)* However, grain boundaries (GBs) in the as-synthesized 2D films are easily formed due to the merger of randomly oriented crystalline domains during the growth of the polycrystalline films.*(5,6)* The GBs play an important role in influencing electron transport properties.*(4,7-10)* Therefore there is an urgent need for not only realizing lateral GB distributions across a given sized sample, but also being able to detect them on a large-scale and in a time-efficient manner. GBs in graphene have been extensively imaged and studied at the atomic scale using transmission electron microscopy (TEM) *(11,12)* or scanning tunnelling microscopy (STM).*(7,13,14)* This approach is limited to studying only small regions of the sample and was substantially improved in terms of the through-put and area examined by using optical microscopy for graphene GBs directly on copper. This was achieved by a straightforward moisture-rich oxidation to the sample.*(15)*

Recent advancement in CVD for producing two-dimensional metal dichalcogenide (TMDs) domains and thin films over large areas,*(16-20)* and application of these 2D TMDs in optical studies *(21-24)* and optoelectronics,*(25-28)* have promoted the need for determining their grain boundaries. GBs and grain structures of monolayer MoS_2 have

been successfully examined using a colour-coded overlay of dark-field-TEM images.*(8)* GBs in WS_2 domains on sapphire substrates were made partially visible by scanning electron microscopy (SEM) using mild oxidation under moisture-rich ambient conditions, taking up to 20 days to emerge.*(29)* However this was a random process with no control and took excessively long for GBs to emerge as visible. Several parts of the WS_2 domains also showed deterioration, making the unambiguous assignment of the GBs challenging. Recent work has shown that UV exposure leads to deterioration of the GBs in TMDs, and it is likely that this is the driving cause of GB deterioration when TMDs are left in room lights and in air.*(30)* The GBs of the 2D materials are not easily detectable using optical microscopy because of their nanometre-sized widths.*(16-18,31,32)* An approach to reveal GBs in 2D TMDs directly on as-deposited substrates with rapid throughput time using large-area examination methods such as imaging by optical microscopy is still important.

5.2 Results and Discussion

Here we demonstrate a reproducible rapid technique for revealing GBs in CVD grown monolayer WS_2 domains and continuous films on SiO_2/Si substrates under a standard optical microscope. This controlled approach relies on simple heating in air to cause preferential structural changes localised on the WS_2 GBs, shown schematically in Figure 3a. High quality CVD growth of TMDs provides isolated domains that can grow from between 20~400 µm. However, detecting the size of the grains within TMD continuous films has been limited due to the absence of suitable techniques that can detect the GBs on the micro- to millimetre scale. We have improved our CVD approach shown in *Chapter 4* to enable control of either isolated domain or continuous film growth of WS_2 monolayers by isolating sulphur (S) and WO_3 precursors in a double-walled quartz tube (figure 1). This gives us the ability to probe both types of TMD crystal forms: isolated single crystals or polycrystalline films. Raman spectroscopy and photoluminescence (PL) spectroscopy

confirmed that both the isolated domains and the continuous films are predominantly monolayer (Figure 2). We explored several heating conditions to reach the conclusion that 20 min at 380 ˚C provided both rapid transformation and achieving clear GB appearance. Figures 3b and c show that before heat treatment there are no lines of contrast, but after heat treatment strong contrast lines associated with GBs appear in the WS_2. For isolated WS_2 domains there are several shapes grown during the CVD. In Figure 3c we show the results from heating a perfect triangular-shaped domain, most likely a single crystal, and then two multifaceted structures, likely formed from several crystals merging together. Multi-faceted WS_2 domains after heat treatment show strong contrast lines in locations where one would expect GBs to have formed based on the faceted structures. In contrast, the single crystal triangle in Figure 3c does not show any contrast lines after heat treatment, which provides a strong indication that the contrast lines are GBs. The heat treatment of the continuous films shows similar strong contrast lines and we can extrapolate from our findings that these lines are the GBs in these films.

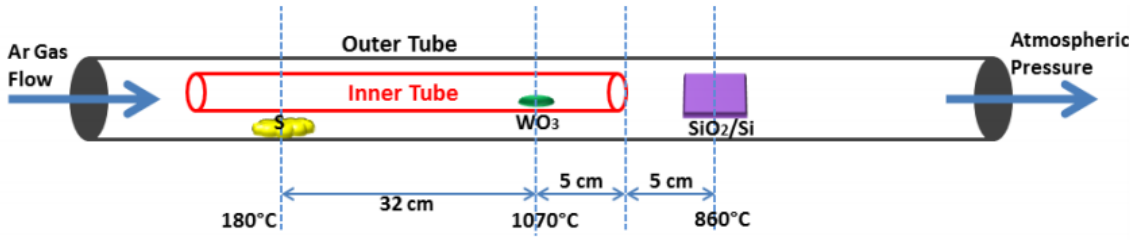

Figure 1. Schematic demonstration of the CVD system set-up employed for the growth of monolayer WS_2 domains and continuous films.

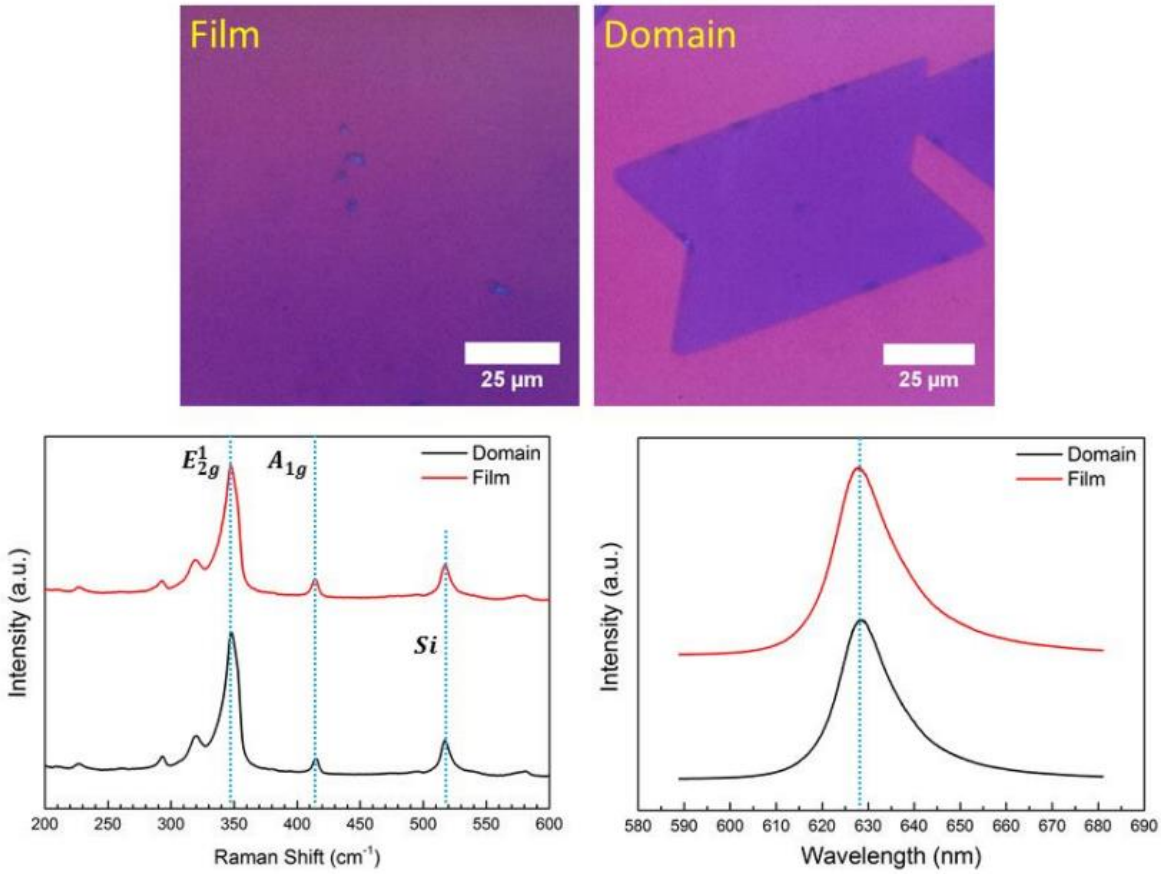

Figure 2. Characteristic Raman and PL intensity profiles for monolayer WS_2 domains and films.

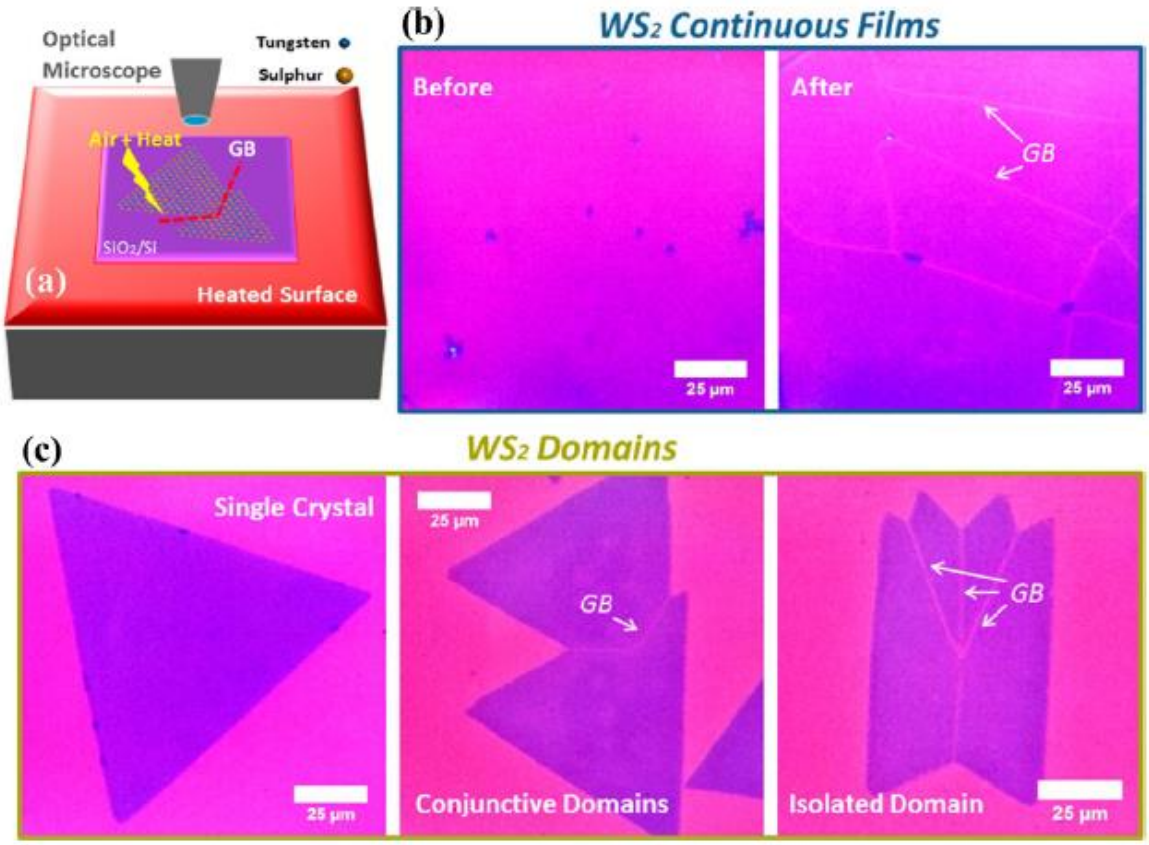

Figure 3. Grain boundaries revealed in monolayer WS_2 continuous films and crystalline domains using the as-developed thermal treatment in air (380°C for 20 min) and observed by an optical microscope. (a) Schematic illustration of the thermal treatment that enabled direct imaging of WS_2 GBs using optical microscope. (b) Optical images of a monolayer WS_2 continuous film before and after the thermal treatment in air, resulting in the appearance of WS_2 GBs. (c) Optical images of WS_2 GBs in other monolayer configurations of the as-formed WS_2 crystal, which can be generally summarized as single crystal, conjunctive domains and isolated domain.

We used selected area electron diffraction (SAED) within a TEM to map out the crystal structure within two connected monolayer WS_2 domains transferred onto a holey SiN TEM grid, figure 4. A hole was introduced into the WS_2 using the 80kV electron beam, and the atomic resolution image taken by an aberration-corrected TEM, figure 4b, shows the hole opens to vacuum, confirming it is monolayer thickness. Examination of the back folded WS_2 edge also shows only a single line of contrast, expected for folded monolayer 2D

materials, figure 4c. Taking SAED patterns from each hole provides accurate tracking of the crystal orientation and reveals a grain boundary running through locations A43, B26 and between C31 and C32 (figure 4e-n). According to a full range of SAED patterns in figure 5, the as-transferred WS_2 domain has only two crystal orientations across approximately ~324μm. This confirms our findings in figure 3.

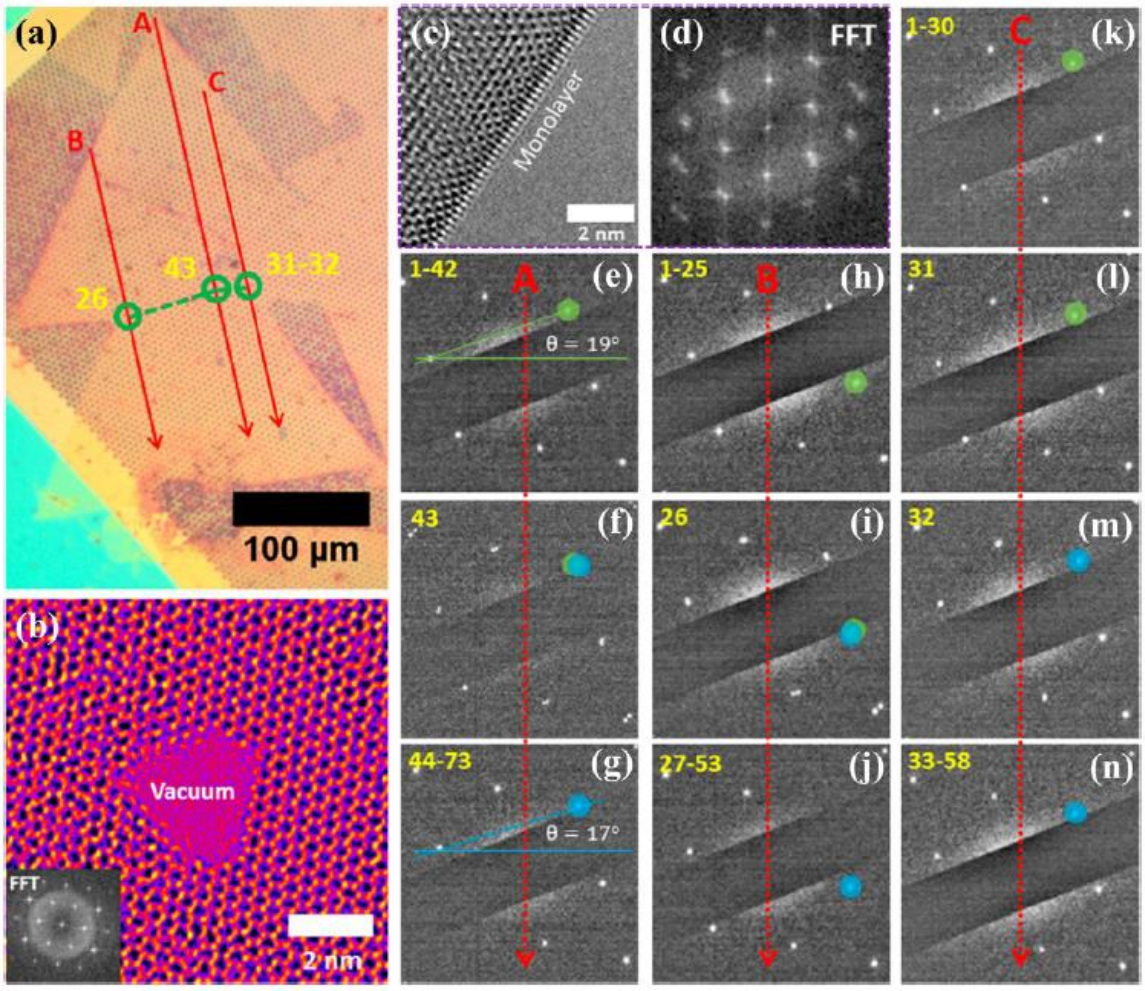

Figure 4. TEM characterizations of monolayer WS_2 domains with regard to the GB locations and crystallinity performed on a holey SiN TEM grid. (a) Optical microscopy image of a WS_2 domain transferred onto the SiN TEM grid with highlighted (red) hole-arrays (A, B and C) for SAED characterisations. Green circles indicate as-determined WS_2 GB positions across the domain with highlighted numbered holes for corresponding SAED diffractions patterns in (f), (i), (l) and (m) respectively. (b) Aberration-corrected (AC)-TEM image of the WS_2 domain showing a hexagonal lattice structure with a hole created by electron beam to show it is a monolayer and the

corresponding FFT pattern is introduced in the inset (a colour look-up-table of “Fire” is used to improve visual inspection). (c) Smoothed AC-TEM image taken on the back folded edge of a monolayer WS_2 with part (d) showing its corresponding FFT image. (e)-(g) SAED diffraction patterns taken from the hole-array A, which spans from hole number 1 to 73. (h) - (j) SAED patterns obtained from hole number 1 to 53 of the hole-array B. (k)-(n) Hole number 1 to 58 SAED patterns acquired from the hole-array C. The corresponding WS_2 crystal orientations relative to the horizontal level are presented in (e) and (g) as 19° in green and 17° in blue, respectively, which also applies to the colour coding in parts (h) to (n). This SiN TEM grid has a hole-centre to adjacent hole-centre distance of 4.5μm.

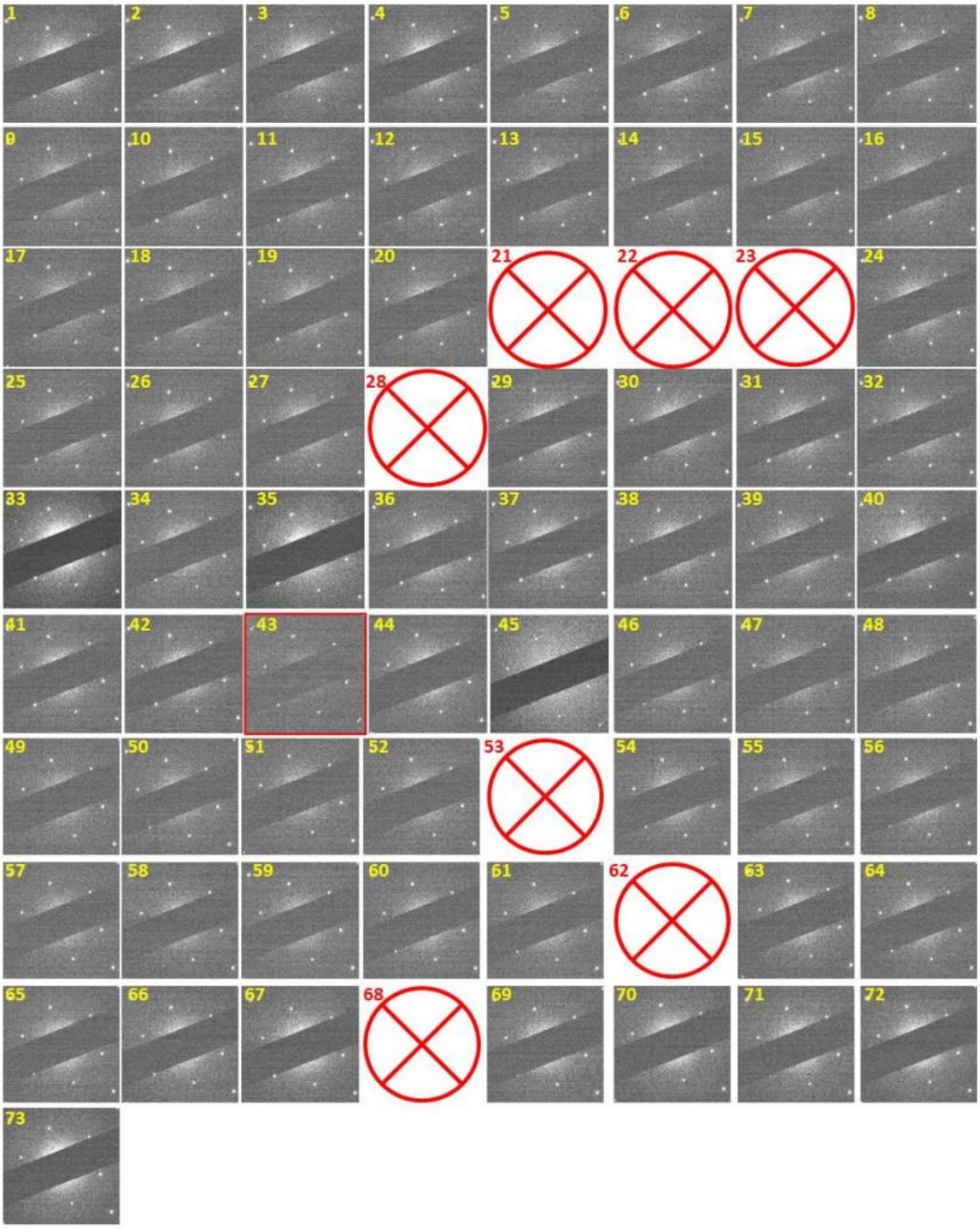

Figure 5. HRTEM-SAED investigation carried consecutively across the whole monolayer WS_2 domain (hole-array A in figure 4a), resulting in determination of the GB location (hole A43 in red box) as well as large areas of single crystallinity. Red-cross circles denote vacant TEM-grid holes in which WS_2 thin films are broken due to transfer.

In figure 6, another example of GB mapping by SAED measurements is conducted on a conjunctive WS_2 domain. From hole-number 1 to 25, SAED patterns show a consistent crystal orientation of 28º. The crystal orientation then changes 31º at hole-number 26, meaning that there is a low-angle GB (equivalent to the one in figure 4) between hole-number 25 and 26 (yellow line). In the meantime, a high-angle GB is also noted at the adjacent TEM-grid hole, number 27, showing two distinct sets of SAED patterns. As a result, the spatial distribution of GBs in this WS_2 domain further confirms the findings in figure 3.

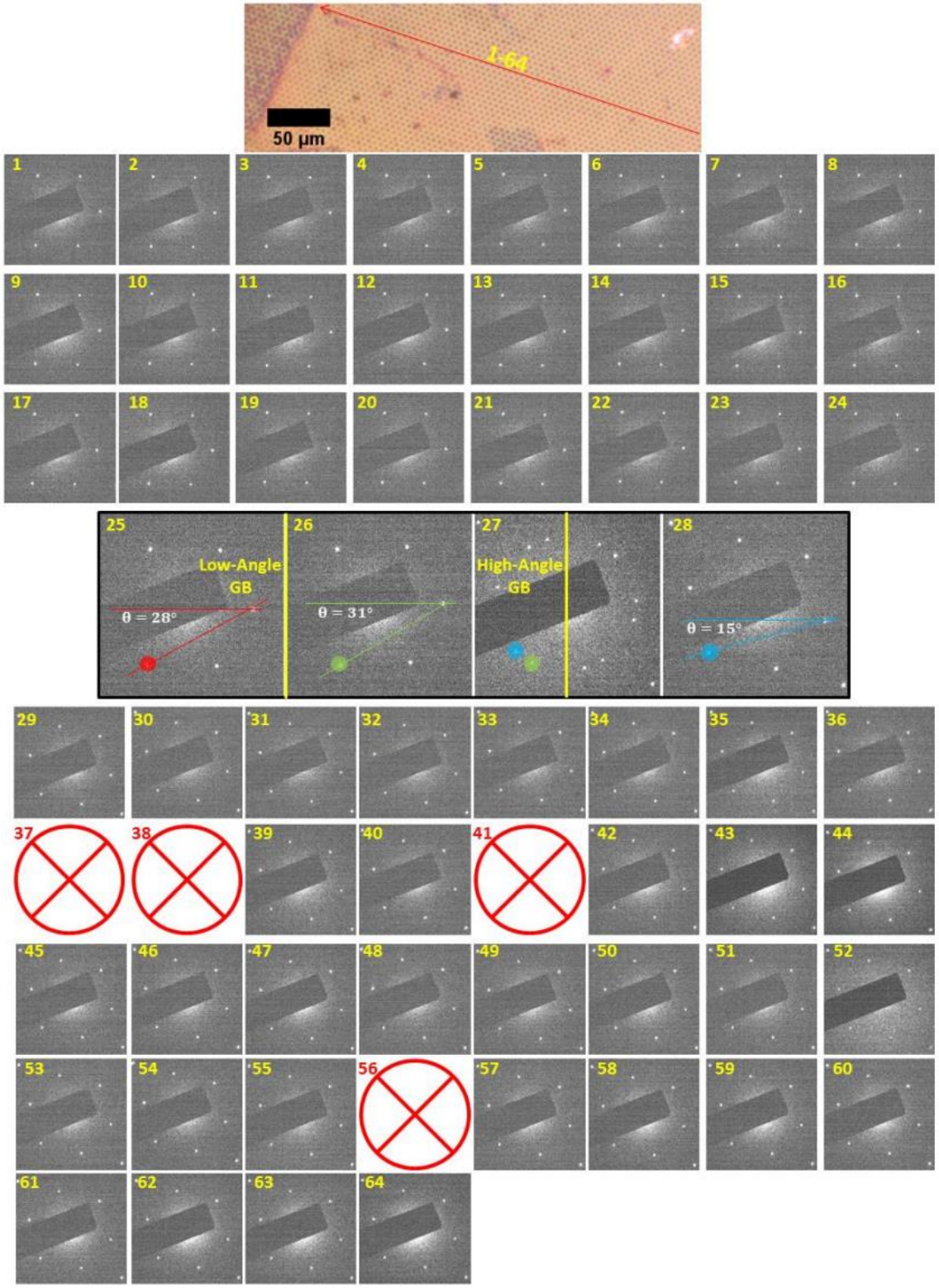

Figure 6. HRTEM-SAED patterns obtained from a monolayer WS_2 domain area of ~284 µm lateral length (red arrow), showing the existence of low- and high-angle GBs between single crystals.

We have carried out an extensive study of how heating temperature in air over time affects the appearance of WS_2 GBs under optical microscopy, as demonstrated in figure 7. Figure 8a depicts the unveiling of GBs in monolayer WS_2 domains after 90 min exposure to a heating temperature of 250 ºC in air. If the heating temperature is lower than 250 °C, in our study, the GBs in WS_2 domains are not observable with optical microscopy after 90 min (figure 7a-c). On the other hand, the efficiency of this particular approach can be much improved by having a higher heating temperature as shown in figure 8b. By treating the WS_2 domains at 380 °C in air, the amount of time needed for GBs to be visible by optical microscope can be shortened to 20 min. This provided a pathway for more time-efficient GB imaging of monolayer WS_2 domains or films in this context. Further increase in the heating temperature or prolongation of the treatment can eventually result in damaging the crystal domains, instead allowing GBs to only mildly develop (figure 9), and makes the unambiguous identification of GBs challenging. In addition to the control of heating temperature, the environment in which to process monolayer WS_2 domains or films is also of great importance. Figure 8c demonstrates that using the same heating temperature and the same duration as in Figure 8b but processing instead in an Ar atmosphere led to failure in observing WS_2 GBs optically. This reveals that the thermal treatment for the GB imaging of monolayer WS_2 domains with optical microscopy should be done in an oxidizing atmosphere.

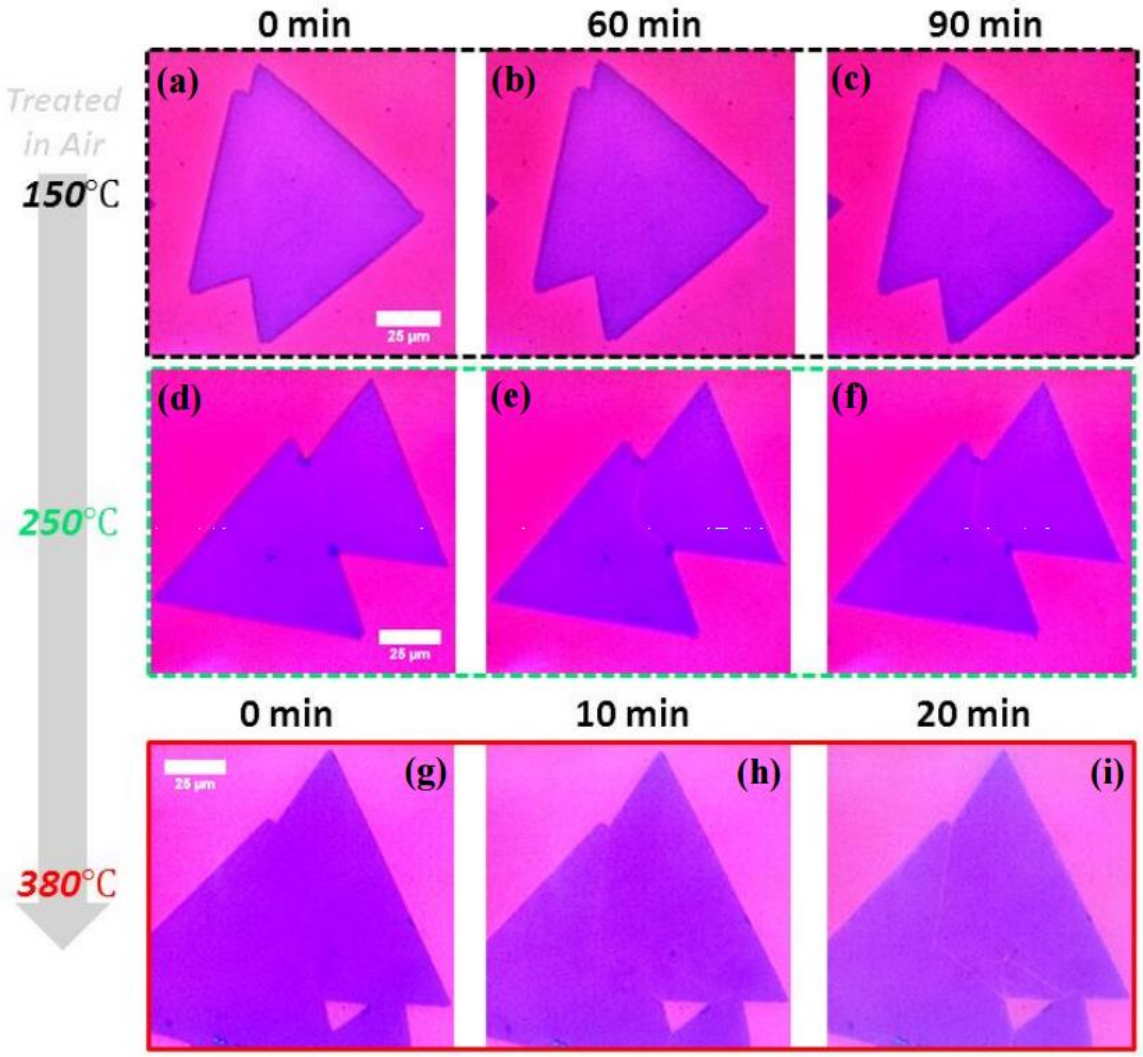

Figure 7. Evolution of monolayer WS_2 domains demonstrated with regard to different timings or temperatures. (a)-(c) Optical images of an as-formed WS_2 domain treated at 150 ºC in air after 0 min, 60 min and 90 min, respectively. (d)-(f) Optical images of the chosen WS_2 domain treated at 250 ºC in air after 0 min, 60 min and 90 min, respectively. (g)-(i) Optical images of the designated WS_2 domain treated at 380 ºC in air after 0 min, 10 min and 20 min, respectively.

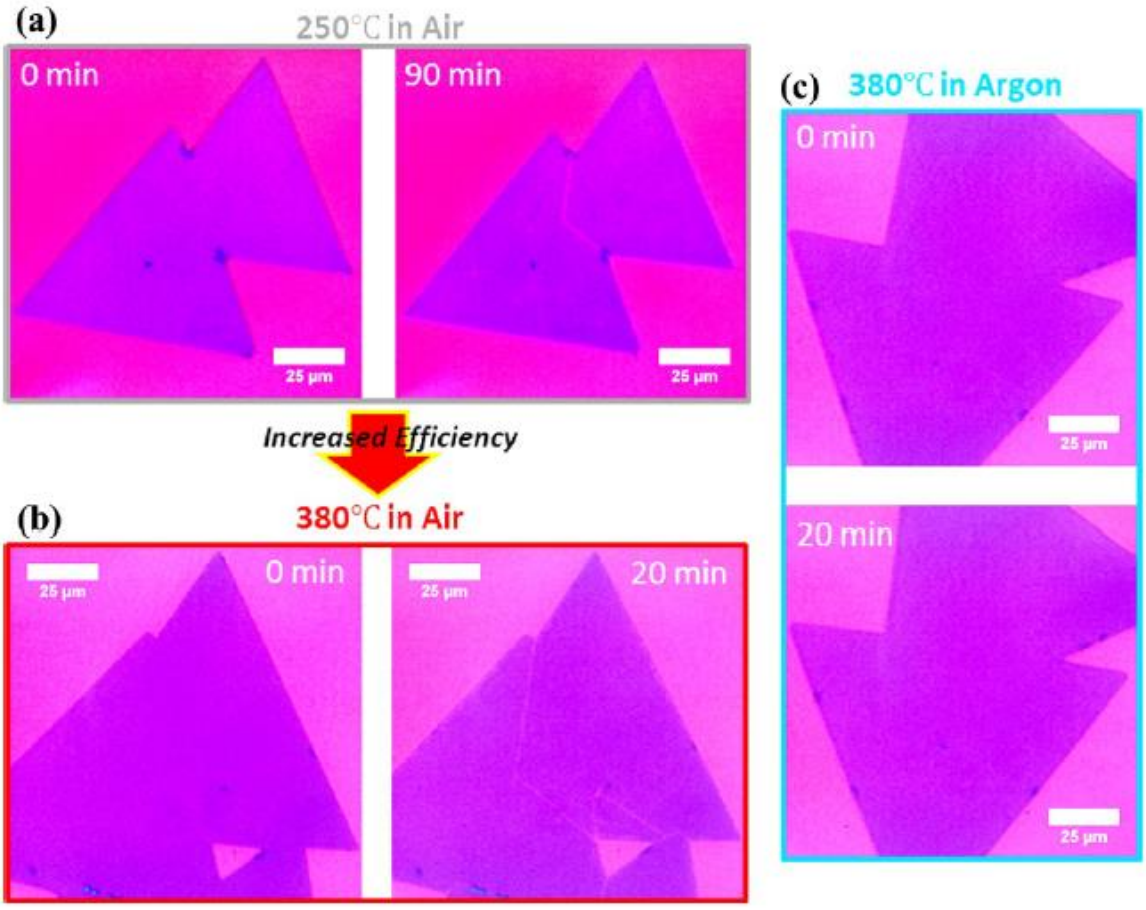

Figure 8. Optical images of WS_2 domains showing the effect of time and heating temperature in air or in an inert argon atmosphere on GB visualization. (a) Before and after 90 min in air at a heating temperature of 250 ˚C. (b) Before and after 20 min in air at a heating temperature of 380 ˚C. (c) Before and after 20 min in argon at a heating temperature of 380 ˚C.

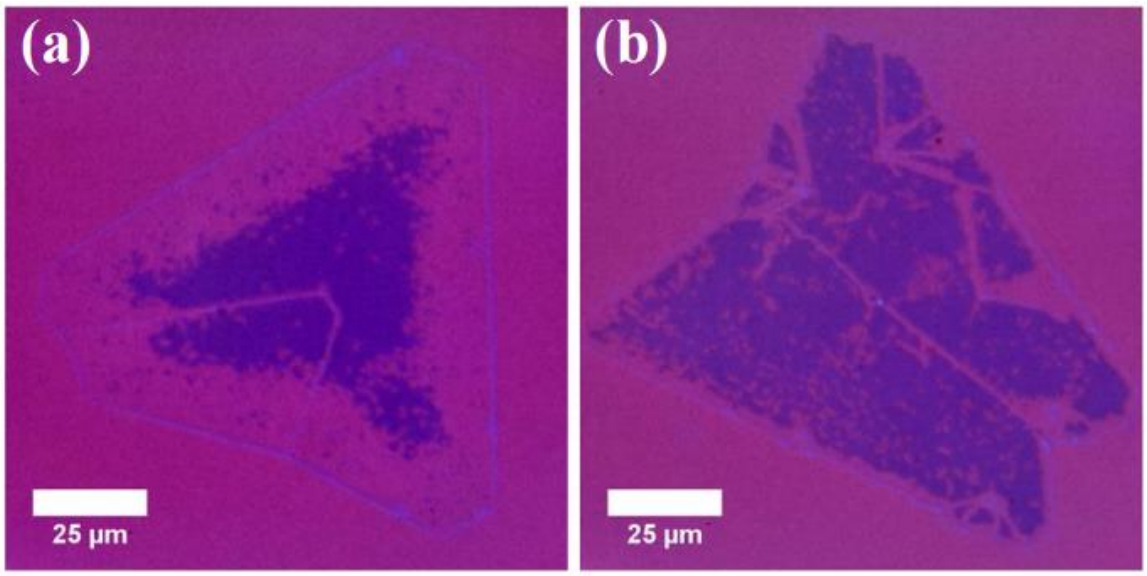

Figure 9. Demonstration of damaged monolayer WS_2 domains due to over-heating and prolonged heat treatment. (a) Optical image of a WS_2 domain treated at 450 ºC in air for 20 min. (b) Optical image of a WS_2 domain treated at 380 ºC in air for 60 min.

Raman spectroscopy and PL spectroscopy were used to probe the GBs after the heat treatment, figure 10. Figure 10a shows that there is a small decrease in PL peak intensity of the bulk region of the treated WS_2 domains compared to the pristine domains. Moreover, the PL emission of the GBs of the treated WS_2 shows nearly a 2-fold decrease in signal relative to that of the central part of the treated domains. Thermal treatment with air may cause adsorption of O_2/H_2O from air or defect creation due to applied thermal energy at WS_2 GBs, which may result in either PL enhancement *(33,34)* or quenching.*(8,29)* We have found only a small peak shift of 1 nm between the pristine and treated WS_2 domains and GBs. We were also able to detect the WS_2 GBs from a PL map of a treated domain, figure 10b. (*i.e.*, PL mapping was generated by plotting integrated PL peak intensities against XY coordinates where multi-point PL analysis was carried in that specific area of the WS_2 domain). Raman spectroscopy and 2D Raman mapping can also detect changes of crystallinity either in monolayer WS_2 domains or GBs after heating in air

at the designated temperature, figure 10c-f. The pristine and treated WS_2 domains show similar monolayer characteristic Raman profiles of WS_2 with an in-plane vibrational (E^1_{2g}) mode of ~351 cm^{-1} and an out-of-plane vibrational (A_{1g}) mode ~418 cm^{-1}, with no peak shifting or quenched intensities observed.*(35)* For the treated WS_2 GBs, the intensity of E^1_{2g} and A_{1g} peaks were reduced by two-fold as compared to the central part of the treated WS_2 domains (and pristine WS_2 domains). Similar to the PL mapping of WS_2 GBs, both E^1_{2g} and A_{1g} peak intensities from the treated GBs can be used in 2D Raman mapping to see the GBs, figure 10d and e. In addition, the WS_2 GBs after the treatment can also be mapped out using the ratio of E^1_{2g} to A_{1g}, figure 10f. Without heating the WS_2 domains, as we have done, PL and Raman 2D mappings cannot clearly reveal the GBs (figure 11).*(17,29)*

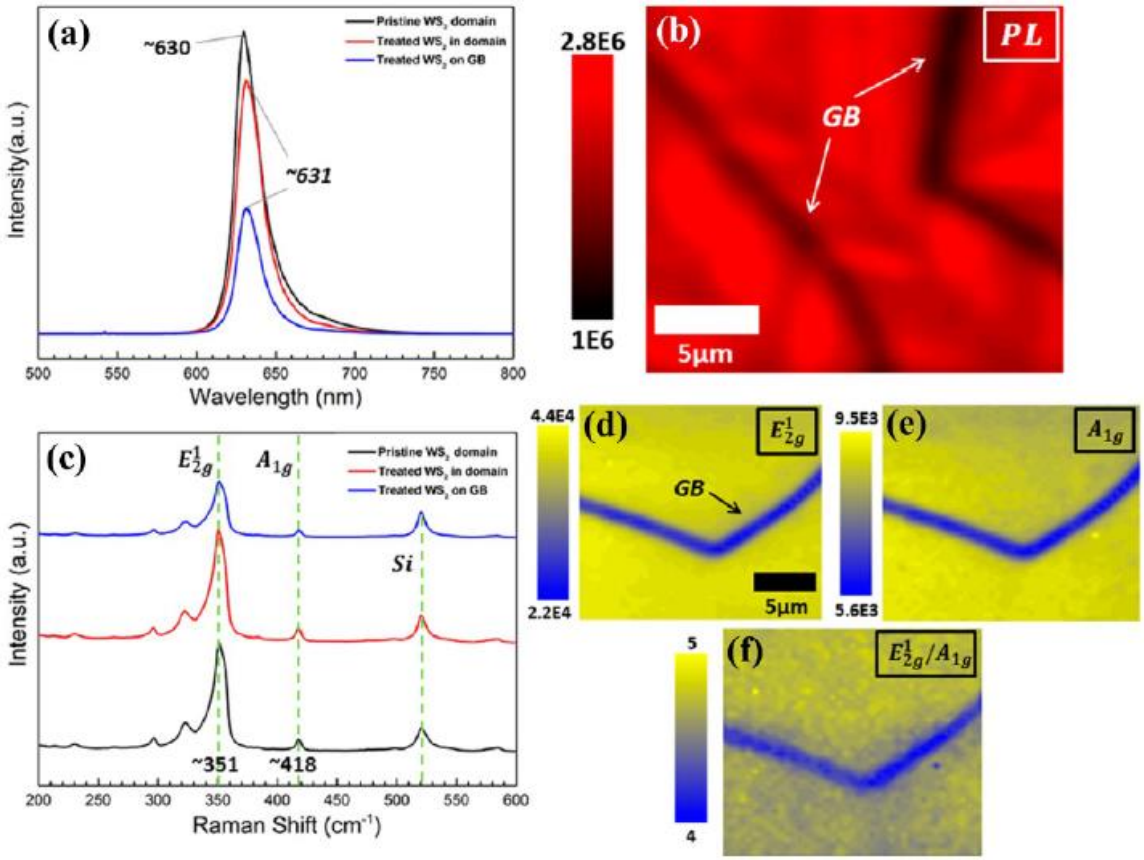

Figure 10. PL and Raman characterizations for as-treated monolayer WS_2 domains at a 532 nm excitation laser. (a) PL emission profiles obtained in a pristine monolayer WS_2 domain as

opposed to the treated monolayer WS_2 on a GB or in domain. (b) PL 2D mapping of the as-developed WS_2 GBs according to the integrated characteristic photon emission intensities from wavelengths 600 to 660 nm. (c) Raman spectra obtained in a pristine monolayer WS_2 domain in comparison with the treated monolayer WS_2 on a GB or in domain, with highlighted Si peak and WS_2 characteristic peaks, E^1_{2g} and A_{1g}. (d) Raman 2D mapping of the WS_2 GBs with regard to the integrated characteristic E^1_{2g} peak intensities from 330 to 370 cm^{-1}. (e) Raman mapping of the WS_2 GBs executed for the A_{1g} characteristic peak with integrated intensities from 400 to 430 cm^{-1}. (f) Raman mapping of the WS_2 GBs corresponding to the ratio of integrated E^1_{2g} peak intensities (330-370 cm^{-1}) / integrated A_{1g} peak intensities (400-430 cm^{-1}).

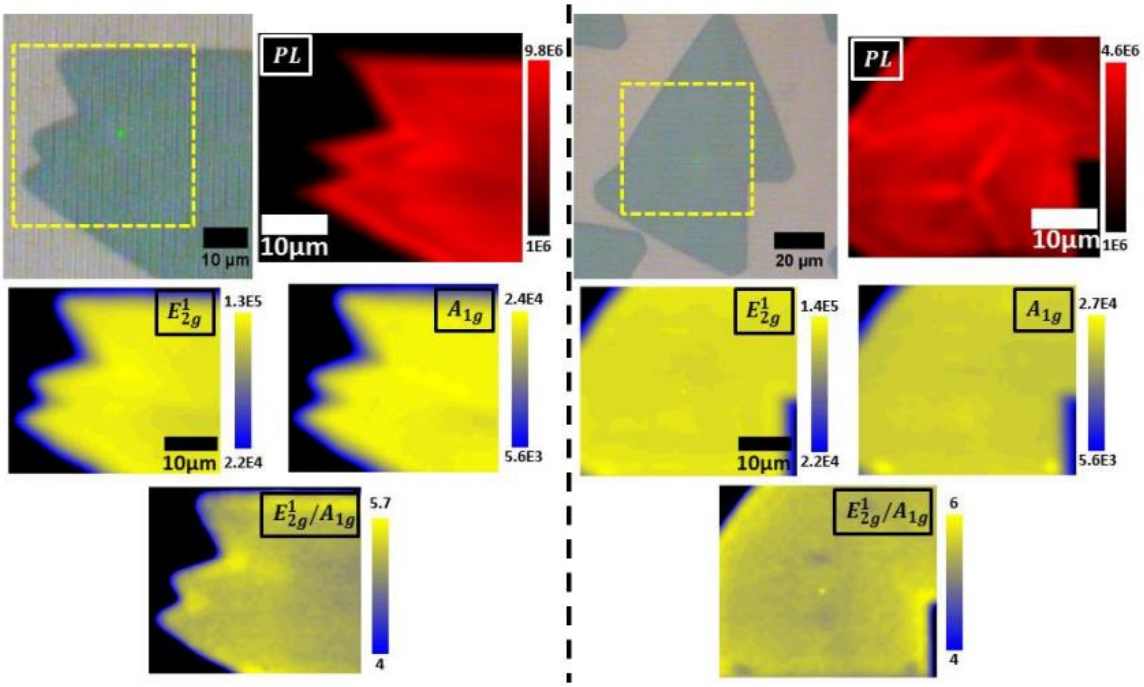

Figure 11. Raman and PL 2D mappings (same method as in figure 10) for untreated monolayer WS_2 domains.

GBs in as-produced high-quality CVD monolayer WS_2 domains and polycrystalline films are difficult to detect even under SEM, figure 12a. However, in certain cases of CVD

growth of 2D TMD crystals, some contrast can be detected from the GBs under SEM *(29,36)* or optical microscopy *(10,32)* due to unwanted multi-layer crystal growth or contamination, as shown in the case of figure 12b.*(10,36)* After our controlled heat treatment in air, a strong contrast (blisters) from the GBs in SEM (figure 12c) may arise from balling of as-formed WO_x in the GB defect area due to reduction of surface energy. Atomic force microscopy (AFM) revealed that the GBs increased in width after heating in air, figure 12d-i. The actual width of the GB after heating, figure 12g, is approximately 0.55μm, figure 12i, which is large enough to be detected under an optical microscope.*(15)*

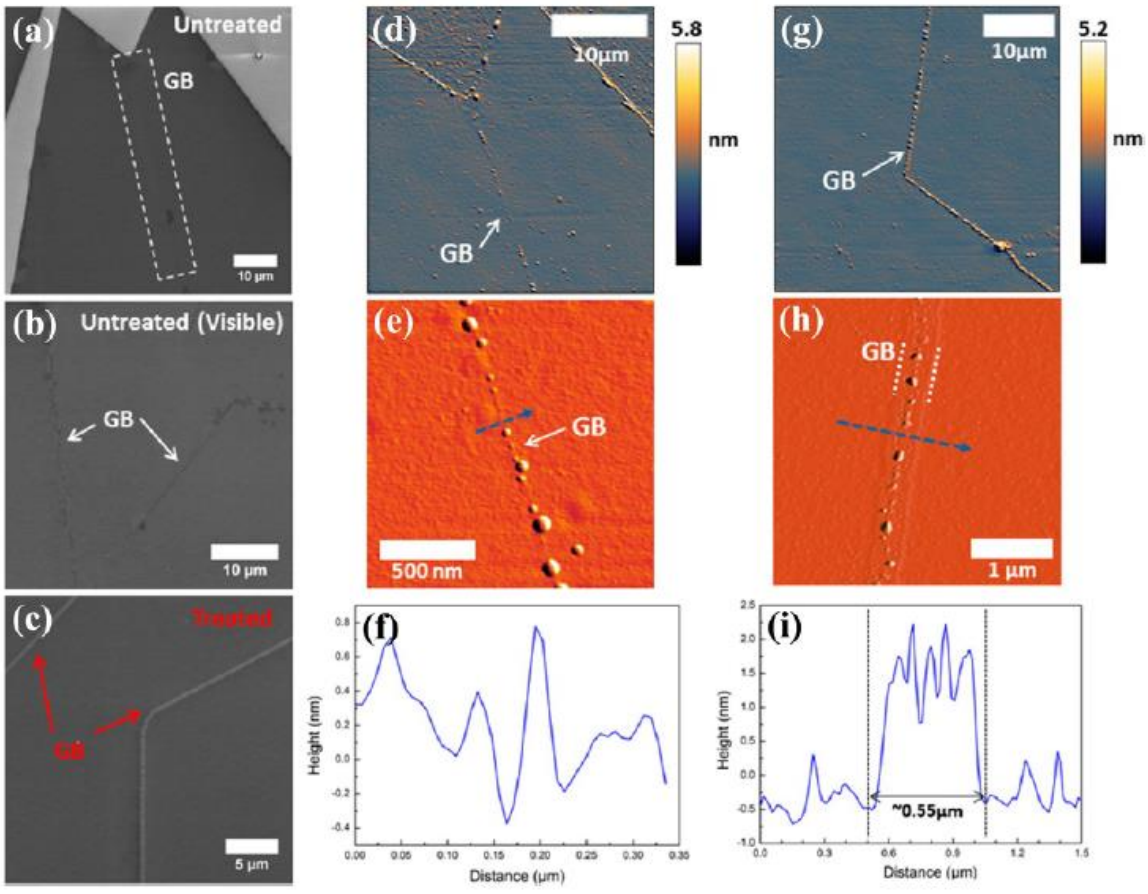

Figure 12. Topological characterisations of the treated WS_2 GBs using SEM and AFM. (a) Untreated WS_2 GBs that are invisible under the SEM observation. (b) Untreated WS_2 GBs that are partially visible with SEM. (c) Treated WS_2 GBs that show strong contrast with SEM. (d) AFM topological mapping of the untreated WS_2 GB. (e) Close-up mapping of the untreated WS_2 GB. (f) Corresponding line profile indicated (blue) in (e). (g) AFM topological mapping of the as-treated

WS_2 GBs. (h) Finer AFM mapping specifically carried for determination of the topography within the as-treated WS_2 GBs. (i) As-obtained topological line profile indicated (blue) in (h).

The ability to measure the GBs in a large number of WS_2 domains under an optical microscope enabled a statistical study of their relative orientation with respect to the WS_2 triangle orientation. We found that mirror GBs (*i.e.,* GB formed at half angle (θ) of the two neighbouring domain zigzag edge (α)) dominated (Figure 13a). Figure 13b plots the α/θ ratio distribution for 100 GBs measured in oxidization-treated joined domains, fitted with the Lorentz curve (red). In Figure 13c, typical optical images of GBs are shown, emphasizing that the α/θ ratio is mostly 2. The creation of GB defects occurs when one single crystal merges with another single crystal of different orientation (Figure 13d-e). While the GBs may appear straight at the microscopic level, previous work using STEM has shown that mirror GBs predominantly consist of 8- and 4-membered rings at atomic level in MoS_2 (Figure 13e).*(8,37)* Given that the mirror GBs form for all domains, regardless of their initial relative orientation and separation of domain centres, it is likely that the mirror GBs do not represent the region where the two domains initially meet and connect, but rather that the system reconstructs after two domains merge together and the GBs adjust until reaching the mirror symmetry.

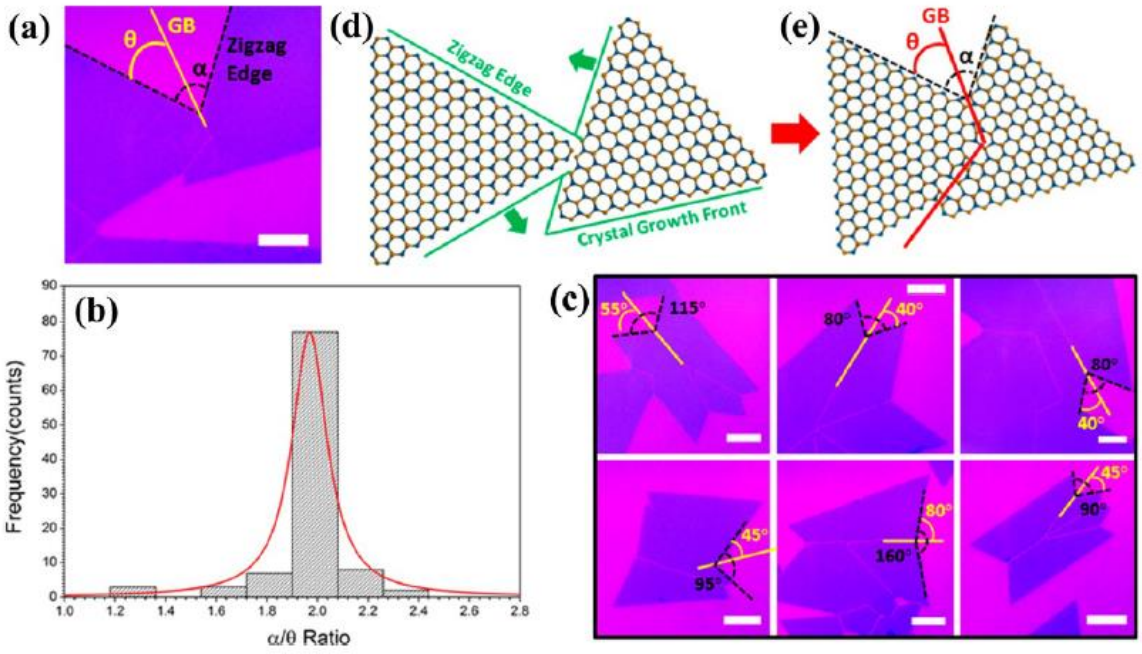

Figure 13. Preferential GB orientations incurred from mismatching of as-grown monolayer WS_2 domains. (a) Schematic illustration of GB angle (θ = angle between the GB and the neighbouring domain edge) bisecting domain angle (α = angle between two neighbouring zigzag edges). Scale bar = 20μm (b) Domain angle (α)/GB angle (θ) ratio distribution in 100 monolayer WS_2 domains obtained from our CVD approach. (c) Optical images showing that the majority of GB θ angles bisect the domain α angles in as-synthesized WS_2 joined domains (all scale bars are 20μm). (d) Schematic illustration of two pristine WS_2 triangular single crystals with zigzag edges merging together to form a GB. (e) Schematic atomic model showing the formation of a GB structure at an orientation that bisects the domain edge angle.

The large size of the CVD-grown WS_2 domains enables electrical contacts using sharp W probes in a probe-station brought directly into the crystals without any lithography needed and thus reduces contamination. Figure 14a and b show the typical IV electrical properties of the as-grown WS_2 domain as well as domains that were oxidized in air. Probes were placed in specified regions likely to be the same crystal to ensure no grain boundary would lie in-between the probes. Both pristine and heat-treated WS_2 domains are conductive at applied source-drain bias of 10V onwards (*i.e.,* a current compliance of 500

nA was used to avoid excess current, which heats the sample and causes irreversible deterioration). The W probes form a Schottky barrier with the WS_2 and result in a nonlinear IV curve and large onset bias voltage. The similar IV response of the WS_2 before and after oxidization shows that the material conductivity of WS_2 domain after heat treatment was not greatly affected by the mild oxidation.

Electrical measurements were then taken across a GB for the as-grown WS_2 domains by placing the probe tips either side of a GB. Upon applying the bias, current started to flow, as in the case of the non-GB area, but surprisingly, the GB started to emerge visibly under the optical microscope after a period of current flow, shown in the sequence of images in Figure 14c. The optically invisible GB junction at two domains was found vulnerable to further increase of source-drain bias until two domains became fully separated at the GB site. The corresponding IV measurement shown in Figure 14d monitors how the level of current across the WS_2 GB increases at first (source-drain bias stages I to IV), but then drops suddenly to zero when source-drain bias reaches ~30V and remains zero for further ramping of source-drain bias (stages V to VI). This correlates in the optical images of Figure 14c to the increase of WS_2 GB width, resulting in formation of two isolated WS_2 domain with no current flowing between. To further study this, W probes were placed either side of a GB made visible by the heat-treatment process in WS_2 and bias was applied to monitor the IV response. Figure 14e and f show that no current flows across the oxidized GB as the bias is increased, but that the width of the GB increases substantially after ramping the bias up to 40V (as in Figure 14c). Another identical example is provided in figure 15. We repeated these measurements on more than 100 domains and found qualitatively consistent behaviour.

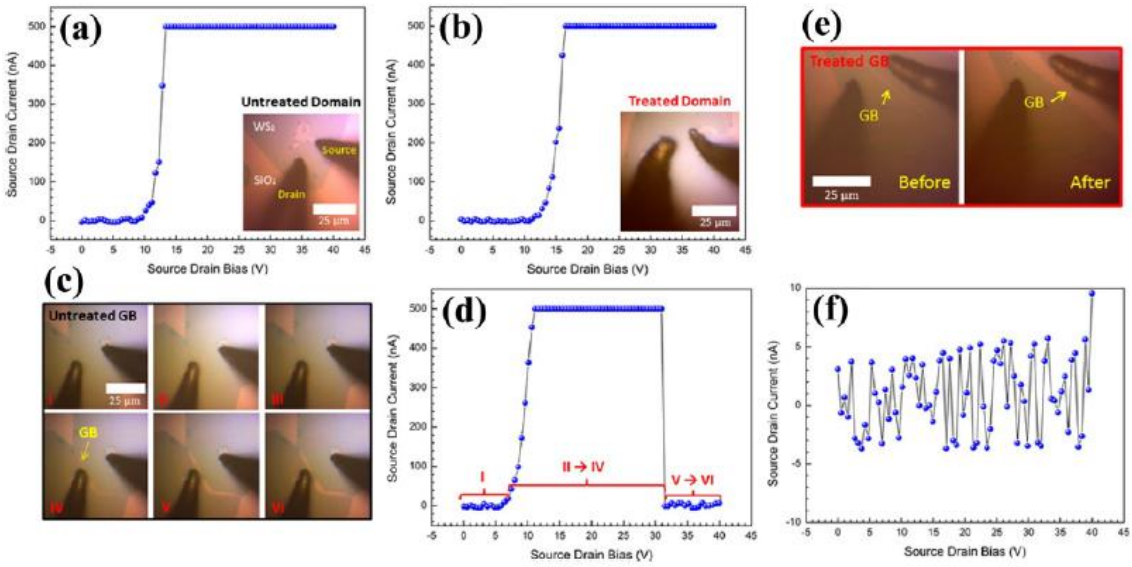

Figure 14. IV source-drain electrical measurements of monolayer WS_2 against its domain (or GB) that is pristine and heat-treated, respectively. (a) and (b) Output $I_{sd}V_{sd}$ curves of an as-grown WS_2 domain that is unprocessed and processed by heat treatment in air, respectively. (c) Optical images I to VI showing untreated WS_2 GB being revealed under optical microscope at elevated source-drain biases applied against the pristine GB. (d) Corresponding output profile of the untreated WS_2 GB appearing in (c). (e) Optical images showing before and after applying source-drain bias against a thermally treated WS_2 GB. (f) Corresponding output profile of the WS_2 GB presented in (e). All measurements were conducted at source-drain-bias increase rate of approximately 1.24V/s.

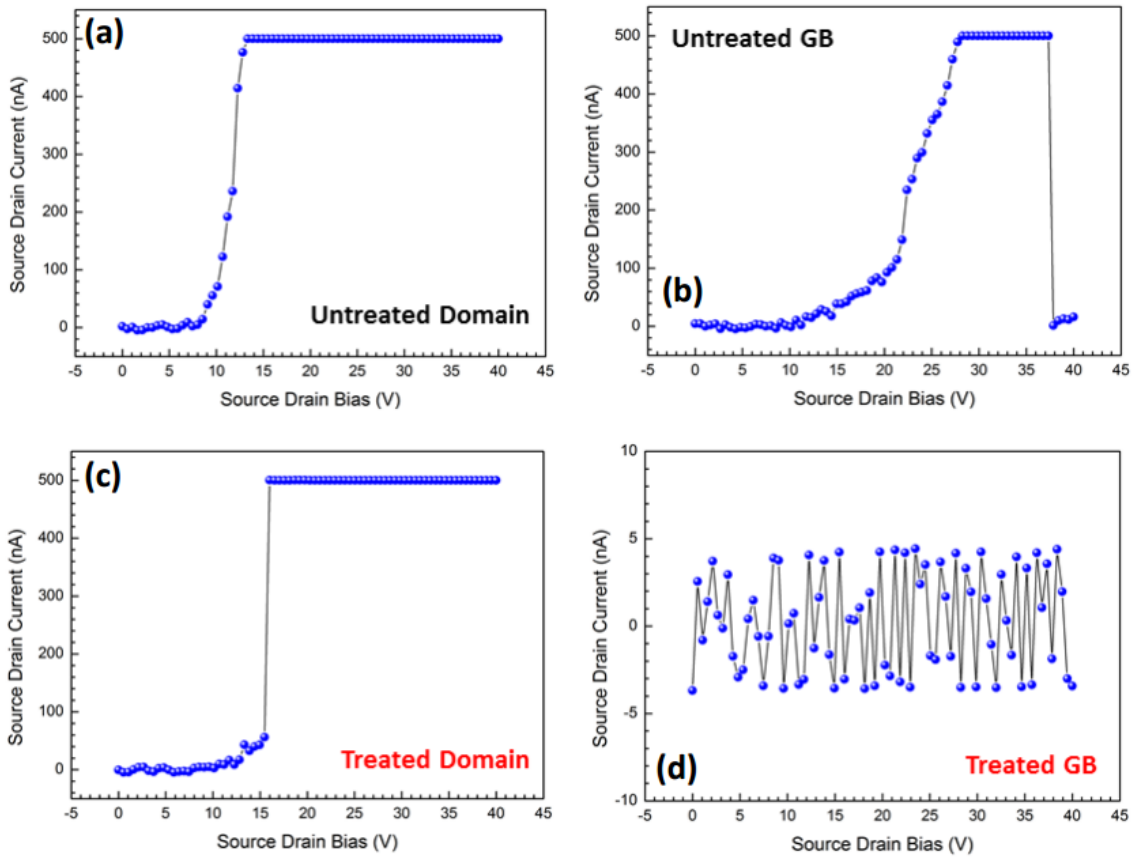

Figure 15. Additional example of IV source-drain electrical measurement conducted on untreated or treated WS_2 domains and GBs. (a) and (b) $I_{sd}V_{sd}$ output curve (0 to 40V) for an untreated WS_2 domain and a GB, respectively. (c) and (d) $I_{sd}V_{sd}$ output curve (0 to 40V) for a treated WS_2 domain and a GB, respectively.

These results show not only controlled heat treatment of WS_2 domains can lead to the GB becoming visible under the optical microscope through an oxidization process but also that applying a relatively large bias also causes the GB to become visible. During the biasing across a GB, current flows, causing heating that instigates an oxidization process in the more reactive area of the GB, similar to the heat-treatment process we developed. This is important when considering the operation of WS_2-based field effect transistors in air where similar effects might occur if current levels are high. If we limit current flow across the GB by implementing a severe compliance value (*i.e.,* 10nA) then this GB

degradation does not occur, indicating that it is related to some form of joule heating and not driven by the electric field alone. On the other hand, the increase of GB width in figure 14e results from heat localization in the W tip area rather than at the GB area. When current does not flow in between a GB, a leaking current through the SiO_2 substrate (large resistance) will generate heat to that WS_2 region, resulting in further oxidation of the WS_2 domain close to the GB.

5.3 Conclusion

The combination of diffraction mapping, optical imaging, Raman and PL mapping, and AFM has revealed that simply heating WS_2 domains in air at the right temperature for a short 20 minute burst causes the GBs to increased and observed using a standard optical microscope. This demonstrates that the grain boundary, which is known to contain defects, has lower oxidation reaction temperature than the bulk crystal. The process works for both domains and polycrystalline films, is high through-put and large-area, and does not require any fancy equipment of preparation. The ease of this approach should enable its uptake across the community for TMD 2D materials to provide a robust way of determining the degree of polycrystallinity of continuous large-area films and can be implemented on the centimetre scale. Knowing the grain size of TMD films will help correlations between electronic performance and structure, and should lead to the rapid improvement of continuous TMD films by CVD growth, which is critical to their further development in optoelectronics.

5.4 Reference

1. Li, X.; Cai, W.; An, J.; Kim, S.; Nah, J.; Yang, D.; Piner, R.; Velamakanni, A.; Jung, I.; Tutuc, E.; *et al.* Large-Area Synthesis of High-Quality and Uniform Graphene Films on Copper Foils. *Science* **2009***, 324*, 1312-1314.
2. Li, X.; Magnuson, C. W.; Venugopal, A.; Tromp, R. M.; Hannon, J. B.; Vogel, E. M.; Colombo, L.; Ruoff, R. S. Large-Area Graphene Single Crystals Grown by Low-Pressure Chemical Vapor Deposition of Methane on Copper. *J. Am. Chem. Soc.* **2011***, 133*, 2816-2819.
3. Bae, S.; Kim, H.; Lee, Y.; Xu, X.; Park, J.; Zheng, Y.; Balakrishnan, J.; Lei, T.; Kim, H. R.; Song, Y. I.; *et al.* Roll-to-roll Production of 30-inch Graphene Films for Transparent Electrodes. *Nat. Nanotechnol.* **2010***, 5*, 574-578.
4. Zhou, H.; Yu, W. J.; Liu, L.; Cheng, R.; Chen, Y.; Huang, X.; Liu, Y.; Wang, Y.; Huang, Y.; Duan, X. Chemical Vapour Deposition Growth of Large Single Crystals of Monolayer and Bilayer Graphene. *Nat.Commun.* **2013***, 4*, 2096.
5. Wu, Y. A.; Fan, Y.; Speller, S.; Creeth, G. L.; Sadowski, J. T.; He, K.; Robertson, A. W.; Allen, C. S.; Warner, J. H. Large Single Crystals of Graphene on Melted Copper Using Chemical Vapor Deposition. *ACS Nano* **2012***, 6*, 5010-5017.
6. Wu, Y. A.; Robertson, A. W.; Schaeffel, F.; Speller, S. C.; Warner, J. H. Aligned Rectangular Few-Layer Graphene Domains on Copper Surfaces. *Chem.Mater.* **2011***, 23*, 4543-4547.
7. Yu, Q.; Jauregui, L. A.; Wu, W.; Colby, R.; Tian, J.; Su, Z.; Cao, H.; Liu, Z.; Pandey, D.; Wei, D.; *et al.* Control and Characterization of Individual Grains and Grain Boundaries in Graphene Grown by Chemical Vapour Deposition. *Nat. Mater.* **2011***, 10*, 443-449.
8. van der Zande, A. M.; Huang, P. Y.; Chenet, D. A.; Berkelbach, T. C.; You, Y.; Lee, G.; Heinz, T. F.; Reichman, D. R.; Muller, D. A.; Hone, J. C. Grains and Grain Boundaries in Highly Crystalline Monolayer Molybdenum Disulphide. *Nat. Mater.* **2013***, 12*, 554-561.
9. Yazyev, O. V.; Louie, S. G. Electronic Transport in Polycrystalline Graphene. *Nat. Mater.* **2010***, 9*, 806-809.
10. Najmaei, S.; Amani, M.; Chin, M. L.; Liu, Z.; Birdwell, A. G.; O'Regan, T. P.; Ajayan, P. M.; Dubey, M.; Lou, J. Electrical Transport Properties of Polycrystalline Monolayer Molybdenum Disulfide. *ACS Nano* **2014***, 8*, 7930-7937.
11. Huang, P. Y.; Ruiz-Vargas, C. S.; van der Zande, A. M.; Whitney, W. S.; Levendorf, M. P.; Kevek, J. W.; Garg, S.; Alden, J. S.; Hustedt, C. J.; Zhu, Y.; *et al.* Grains and Grain Boundaries in Single-layer Graphene Atomic Patchwork Quilts. *Nature* **2011***, 469*, 389-392.
12. Kim, K.; Lee, Z.; Regan, W.; Kisielowski, C.; Crommie, M. F.; Zettl, A. Grain Boundary Mapping in Polycrystalline Graphene. *ACS Nano* **2011***, 5*, 2142-2146.
13. Rasool, H. I.; Song, E. B.; Allen, M. J.; Wassei, J. K.; Kaner, R. B.; Wang, K. L.; Weiller, B. H.; Gimzewski, J. K. Continuity of Graphene on Polycrystalline Copper. *Nano Lett.* **2011***, 11*, 251-256.
14. Gao, L.; Guest, J. R.; Guisinger, N. P. Epitaxial Graphene on Cu(111). *Nano Lett.* **2010***, 10*, 3512-3516.

15. Dinh Loc Duong; Han, G. H.; Lee, S. M.; Gunes, F.; Kim, E. S.; Kim, S. T.; Kim, H.; Quang Huy Ta; So, K. P.; Yoon, S. J.; *et al.* Probing Graphene Grain Boundaries with Optical Microscopy. *Nature* **2012***, 490*, 235-239.
16. Huang, J.; Pu, J.; Hsu, C.; Chiu, M.; Juang, Z.; Chang, Y.; Chang, W.; Iwasa, Y.; Takenobu, T.; Li, L. Large-Area Synthesis of Highly Crystalline WSe_2 Monolayers and Device Applications. *ACS Nano* **2014***, 8*, 923-930.
17. Rong, Y.; Fan, Y.; Koh, A. L.; Robertson, A. W.; He, K.; Wang, S.; Tan, H.; Sinclair, R.; Warner, J. H. Controlling Sulphur Precursor Addition for Large Single Crystal Domains of WS_2. *Nanoscale* **2014***, 6*, 12096-12103.
18. Wang, X.; Gong, Y.; Shi, G.; Chow, W. L.; Keyshar, K.; Ye, G.; Vajtai, R.; Lou, J.; Liu, Z.; Ringe, E.; *et al.* Chemical Vapor Deposition Growth of Crystalline Monolayer $MoSe_2$. *ACS Nano* **2014***, 8*, 5125-5131.
19. Zhang, J.; Yu, H.; Chen, W.; Tian, X.; Liu, D.; Cheng, M.; Xie, G.; Yang, W.; Yang, R.; Bai, X.; *et al.* Scalable Growth of High-Quality Polycrystalline MoS_2 Monolayers on SiO_2 with Tunable Grain Sizes. *ACS Nano* **2014***, 8*, 6024-6030.
20. Lee, Y.; Zhang, X.; Zhang, W.; Chang, M.; Lin, C.; Chang, K.; Yu, Y.; Wang, J. T.; Chang, C.; Li, L.; *et al.* Synthesis of Large-Area MoS_2 Atomic Layers with Chemical Vapor Deposition. *Adv.Mater.* **2012***, 24*, 2320-2325.
21. Chiu, M.; Li, M.; Zhang, W.; Hsu, W.; Chang, W.; Terrones, M.; Terrones, H.; Li, L. Spectroscopic Signatures for Interlayer Coupling in MoS_2-WSe_2 van der Waals Stacking. *ACS Nano* **2014***, 8*, 9649-9656.
22. Ramasubramaniam, A. Large Excitonic Effects in Monolayers of Molybdenum and Tungsten Dichalcogenides. *Phys. Rev. B* **2012***, 86*, 115409.
23. Gutierrez, H. R.; Perea-Lopez, N.; Elias, A. L.; Berkdemir, A.; Wang, B.; Lv, R.; Lopez-Urias, F.; Crespi, V. H.; Terrones, H.; Terrones, M. Extraordinary Room-Temperature Photoluminescence in Triangular WS_2 Monolayers. *Nano Lett.* **2013***, 13*, 3447-3454.
24. Tongay, S.; Fan, W.; Kang, J.; Park, J.; Koldemir, U.; Suh, J.; Narang, D. S.; Liu, K.; Ji, J.; Li, J.; *et al.* Tuning Interlayer Coupling in Large-Area Heterostructures with CVD-Grown MoS_2 and WS_2 Monolayers. *Nano Lett.* **2014***, 14*, 3185-3190.
25. Zhang, W.; Chuu, C.; Huang, J.; Chen, C.; Tsai, M.; Chang, Y.; Liang, C.; Chen, Y.; Chueh, Y.; He, J.; *et al.* Ultrahigh-Gain Photodetectors Based on Atomically Thin Graphene-MoS_2 Heterostructures. *Sci. Rep.* **2014***, 4*, 3826.
26. Zhang, W.; Chiu, M.; Chen, C.; Chen, W.; Li, L.; Wee, A. T. S. Role of Metal Contacts in High-Performance Phototransistors Based on WSe_2 Monolayers. *ACS Nano* **2014***, 8*, 8653-8661.
27. Chang, Y.; Zhang, W.; Zhu, Y.; Han, Y.; Pu, J.; Chang, J.; Hsu, W.; Huang, J.; Hsu, C.; Chiu, M.; *et al.* Monolayer $MoSe_2$ Grown by Chemical Vapor Deposition for Fast Photodetection. *ACS Nano* **2014***, 8*, 8582-8590.
28. Zhang, W.; Huang, J.; Chen, C.; Chang, Y.; Cheng, Y.; Li, L. High-Gain Phototransistors Based on a CVD MoS_2 Monolayer. *Adv. Mater.* **2013***, 25*, 3456-3461.

29. Zhang, Y.; Zhang, Y.; Ji, Q.; Ju, J.; Yuan, H.; Shi, J.; Gao, T.; Ma, D.; Liu, M.; Chen, Y.; *et al.* Controlled Growth of High-Quality Monolayer WS_2 Layers on Sapphire and Imaging Its Grain Boundary. *ACS Nano* **2013***, 7*, 8963-8971.
30. Ly, T. H.; Chiu, M.; Li, M.; Zhao, J.; Perello, D. J.; Cichocka, M. O.; Oh, H. M.; Chae, S. H.; Jeong, H. Y.; Yao, F.; *et al.* Observing Grain Boundaries in CVD-Grown Monolayer Transition Metal Dichalcogenides. *ACS Nano* **2014***, 8*, 11401-11408.
31. Ling, X.; Lee, Y.; Lin, Y.; Fang, W.; Yu, L.; Dresselhaus, M. S.; Kong, J. Role of the Seeding Promoter in MoS_2 Growth by Chemical Vapor Deposition. *Nano Lett.* **2014***, 14*, 464-472.
32. Najmaei, S.; Liu, Z.; Zhou, W.; Zou, X.; Shi, G.; Lei, S.; Yakobson, B. I.; Idrobo, J.; Ajayan, P. M.; Lou, J. Vapour Phase Growth and Grain Boundary Structure of Molybdenum Disulphide Atomic Layers. *Nat. Mater.* **2013***, 12*, 754-759.
33. Nan, H.; Wang, Z.; Wang, W.; Liang, Z.; Lu, Y.; Chen, Q.; He, D.; Tan, P.; Miao, F.; Wang, X.; *et al.* Strong Photoluminescence Enhancement of MoS_2 through Defect Engineering and Oxygen Bonding. *ACS Nano* **2014***, 8*, 5738-5745.
34. Tongay, S.; Zhou, J.; Ataca, C.; Liu, J.; Kang, J. S.; Matthews, T. S.; You, L.; Li, J.; Grossman, J. C.; Wu, J. Broad-Range Modulation of Light Emission in Two-Dimensional Semiconductors by Molecular Physisorption Gating. *Nano Lett.* **2013***, 13*, 2831-2836.
35. Peimyoo, N.; Shang, J.; Cong, C.; Shen, X.; Wu, X.; Yeow, E. K. L.; Yu, T. Nonblinking, Intense Two-Dimensional Light Emitter: Monolayer WS_2 Triangles. *ACS Nano* **2013***, 7*, 10985-10994.
36. Liu, Y.; Ghosh, R.; Wu, D.; Ismach, A.; Ruoff, R.; Lai, K. Mesoscale Imperfections in MoS_2 Atomic Layers Grown by a Vapor Transport Technique. *Nano Lett.* **2014***, 14*, 4682-4686.
37. Zhou, W.; Zou, X.; Najmaei, S.; Liu, Z.; Shi, Y.; Kong, J.; Lou, J.; Ajayan, P. M.; Yakobson, B. I.; Idrobo, J. Intrinsic Structural Defects in Monolayer Molybdenum Disulfide. *Nano Lett.* **2013***, 13*, 2615-2622.
38. Rong, Y.; He, K.; Pacios, M.; Robertson, A.; Bhaskaran, H.; Warner, J. Controlled Preferential Oxidation of Grain Boundaries in Monolayer Tungsten Disulphide for Direct Optical Imaging. *ACS Nano*, **2015**, 9(4), 3696-3703,

Chapter 6

Electroluminescence Dynamics across Grain Boundary Regions of Monolayer WS_2

6.1 Introduction

Monolayer (ML) two-dimensional (2D) transition metal dichalcogenides (TMDs) are often direct-band-gap semiconductors with unique optical properties that are absent in graphene and extend the functionality of 2D materials into the visible wavelength region.*(1-8)* Mechanically exfoliating thin flakes from layered bulk single crystals was one of the first approaches to obtaining monolayer TMDs and led to new investigations in optoelectronics*(9-13)* and valleytronics.*(14-16)* Two of the most explored types of 2D TMDs (*i.e.,* MX_2, M = Mo and W and X= S, Se, or Te) are MoS_2 and WS_2, with direct-bandgaps of ~1.8 *(3,4)* and ~2.0 eV,*(1,2)* respectively. Their electronic transport characteristics and sizable band gaps have been used to fabricate novel 2D photodetectors *(17-19)* and visible-range light-emitting devices.*(9,10)*

However, mechanical exfoliation is limited to small pieces of monolayer and is not industrially scalable for large area uniform wafer scale devices. In this regard, chemical vapour deposition (CVD) is a promising approach for the growth of inch-sized wafer-scale MoS_2 and WS_2 monolayers, much in the same way that has emerged for graphene CVD work.*(20,21)* Mechanically exfoliated materials rarely contain grain boundaries (GB), because it is typically single crystals that are mechanically detached from the bulk. In CVD-grown 2D materials, many individual domains nucleate at the same time across the substrate and grow in size until they merge together and if their crystal orientation is not

exact, then a GB forms.*(22)* For large nucleation density of domains, this causes excessive amounts of GBs across the sample that are detrimental to the electronic device quality due to scattering or trapping of charge carriers.*(23,24)* Therefore, intense efforts have been invested to increase the size of TMD single crystalline domains over large areas using CVD methods in order to minimize GBs.*(25,26)* CVD-grown ML-MoS_2 has also shown photosensitivity in devices comparable to exfoliated MoS_2.*(27,28)*

Electroluminescence (EL) can be generated in monolayer TMD nanoelectronic devices by applying source-drain bias and detecting the emission. In some cases the TMDs are sandwiched in the middle of a vertical stacked heterostructure,*(29,30)* but in several reported cases the TMD is horizontal with submicronmeter laterally spaced electrodes produced by electron beam lithography methods.*(9,10,31,32)* In prior work there has been no detailed study about how a GB within the device channel would influence the EL. We recently showed that applying high bias across a GB in ML-WS_2 caused preferential erosion at the GB region during current flow, most likely from Joule heating induced preferential oxidization.*(33)* This indicates that GBs can be unstable during biasing, which also has important implications for TMD-based EL devices that utilize such biasing to generate photon emission.

Here, we examine the time-dependent spatial variations of the electroluminescent signals in high biased CVD-grown ML-WS_2. Ultrafine tungsten (W) probe tips are used to directly contact the ML-WS_2 domains on SiO_2 (300 nm)/Si substrates without the need for any lithographic processing. High-quality contacts have been previously created in ML-MoS_2 transistors using Mo metal.*(34)* The large domain sizes of our CVD grown WS_2 samples (>100 μm) allows W probe tips to be placed either side of a known GB location.*(35)*

6.2 Results and Discussion

Large ML-WS_2 crystalline domains are directly fabricated on SiO_2/Si using our controlled CVD method (*i.e.,* monolayer thickness is confirmed in figure 1).*(25,33)* Due to the large crystal sizes, source-drain electrodes (W probes) are easily made with ML-WS_2 in an area of interest in the insulating SiO_2.*(35)* Figure 2a describes our experimental setup used for obtaining EL in ML-WS_2 when source-drain bias (V_{SD}) is applied. In our previous work we showed that GBs form mirror twin geometries within merged domains of WS_2 grown by our CVD conditions and this also allows us to place probe tips on either side of an expected GB, or within a single crystalline region, figure 2a and 2e.*(33)* In the same prior study, we showed that ML-WS_2 GBs degrade for increasing V_{SD} due to localized Joule heating, as indicated in figure 2c and 2g, a process we will define here as “e-burning”. Measurements were done at room temperature and in ambient conditions. When V_{SD} starts to ramp up, current flows through the WS_2 region and we observed strong red EL arcs across the two metal contacts, as shown in figure 2d. In many cases, the EL was strong enough that it could be observed while the entire sample was under white light illumination using a cheap simple CMOS camera. This enabled us to correlate the spatial position of the EL with the WS_2 structure and also observe how the WS_2 structure changes during biasing and its relation to the EL location. When the electrodes are connected across a single crystalline domain of ML-WS_2, figure 2f, under equivalent applied biasing conditions (figure 2g), we did not observe the strong arc shaped EL using the same imaging conditions (figure 2h).

Contacting ML-WS_2 with two W electrodes can establish Schottky barriers at the interfaces, as illustrated by the band diagram in figure 2i. Polycrystalline W metal has a theoretical work function (Φ_W) of ~4.55 eV,*(36)* however a W tip is generally coated with native oxide which can bring the value to ~4.8 eV.*(37,38)* Britnell *et al.* determined the work function of ML-WS_2 ($\Phi_{ML\text{-}WS2}$) to be approximately ~4.6 eV.*(18)* The ultrathin nature

of the WS_2 monolayer makes the creation of metal-induced gap states in the semiconductor likely, which would produce Fermi-level pinning and small Schottky barriers at the metal: semiconductor interfaces. Most mechanically-exfoliated and CVD-synthesized ML-WS_2 or MoS_2 are typically n-doped semiconductors.*(23,39-42)* The n-type doping behaviour of 2D TMDs is further enhanced when V_{SD} is applied across a GB. (43,44) The creation of two Schottky barriers at both electrodes gives rise to a metal-semiconductor-metal device structure, where current flow at room temperature is typically dictated by thermionic emission across the barriers. The degree of thermionic emission and hence current flow varies with increasing V_{SD}, due to the change in band bending and barrier width with increased bias. For low V_{SD}, minimal thermionic emission occurs and a low current flows through the device, with majority charge carrier being electrons (figure 2j). At high V_{SD}, minority hole injection from one electrode may also occur in conjunction with the majority carrier electron injection from the other electrode. The recombination of these two injected carriers could produce EL (figure 2k). An alternative mechanism for EL production is the interaction of majority carrier electrons with local p-type dopants, either defects or surface adsorbates. In 2D semiconducting TMDs, excitonic effects are widely known to be prominent due to reduced poor dielectric screening and 2D spatial confinement (*i.e.,* ML-WS_2 binding energy ~0.7 eV).*(45,46)*

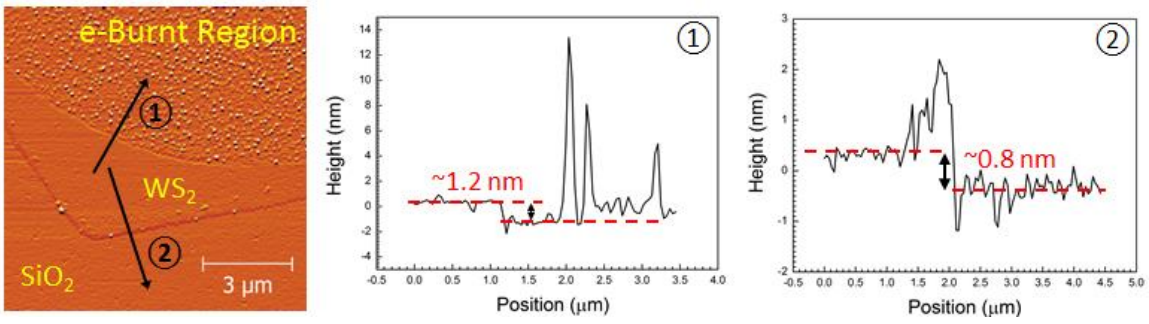

Figure 1. Characterization of an e-burnt ML-WS_2 region using atomic force microscopy (AFM).

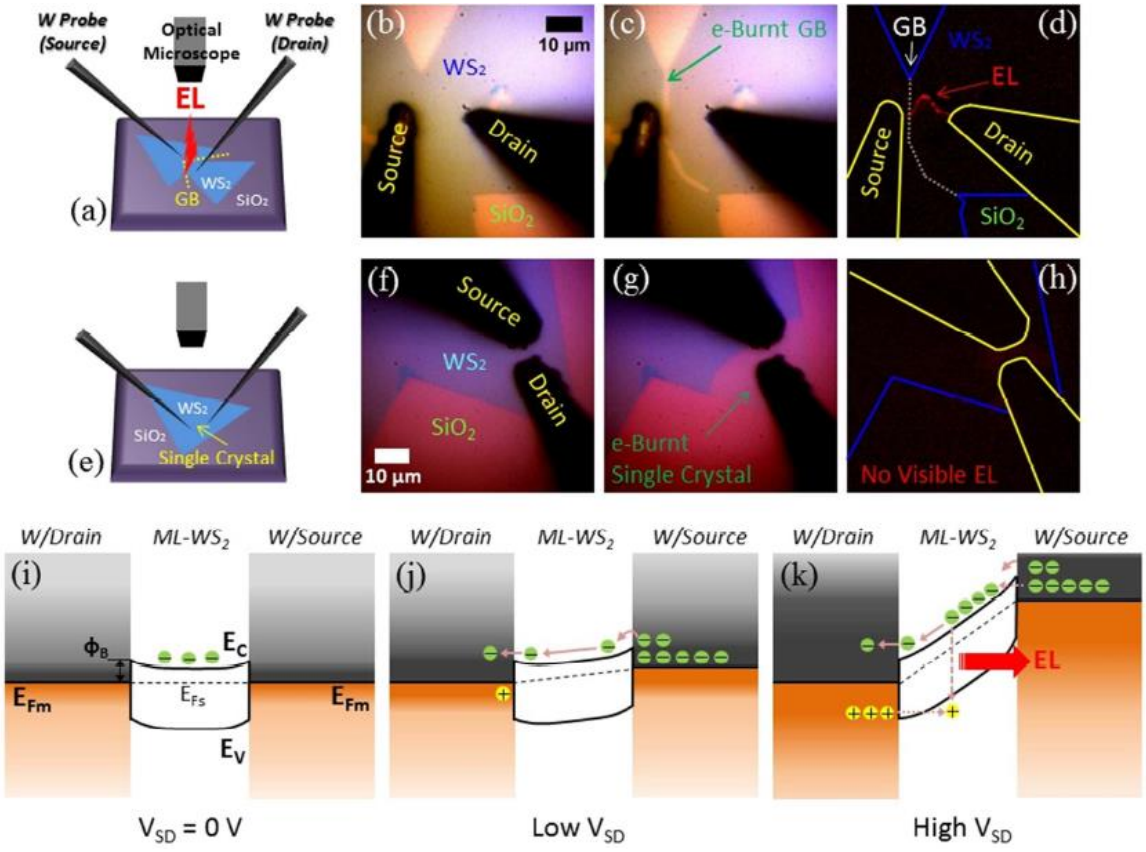

Figure 2. EL in a GB region of ML-WS_2 under applied source-drain bias, compared to that in a ML-WS_2 single crystal and illustration of light emitting mechanism of the electrical measurements. (a) A schematic illustration showing how the EL in a GB region of ML-WS_2 using W probes as source-drain electrodes is generated. (b) An optical image of W probes set in contact at two sides of a ML-WS_2 GB on a SiO_2/Si substrate. (c) After source-drain bias is applied, the GB erodes to be visible under an optical microscope. (d) A red-channel optical image taken to capture a visible-range (red) EL emission arc generated in the GB region shown in (c) (*i.e.,* the image was background subtracted and "Red" colour coded to show only EL). (e) A schematic illustration of source-drain bias applied to a ML-WS_2 single crystalline region (no internal GBs). (f) An optical image showing that W electrodes are placed in a single crystalline region of a ML-WS_2 domain. (g) The single crystalline region in (f) is eroded as result of the e-burning. (h) Through the CMOS camera (red-channel), no detectable EL is found in (g). (i) A schematic band diagram of ML-WS_2 forming Schottky barriers at W/ML-WS_2 interfaces when V_{SD} is not applied (equilibrium state). E_{Fm} is the Fermi level energy in metal contacts, E_{Fs} is the Fermi level in n-type ML-WS_2 semiconductor, E_C is the minimum conduction band energy, Φ_B is the Schottky barrier height and E_V is the

maximum valence band energy. (j) The band diagram at low V_{SD}, where there is no EL. (k) The band diagram at high V_{SD} activating near-bandgap photon emission.

Figure 3b shows an example of a V_{SD} ramping cycle starting from forward bias to reverse bias which was used for our EL generation at a ML-WS_2 GB in figure 3a (source-drain current (I_{SD}) compliance of 500 nA used). A symmetric $I_{SD}V_{SD}$ curve is expected since we have identical W/ML-WS_2 electrode interfaces. In figure 3b, before breakdown, the increase of I_{SD} at forward bias leads to the EL in figure 3c-f. When the ML-WS_2 GB is fully eroded, it separates the two domains, and no more current flows between the electrodes connected to each domain and concomitantly no EL is generated. Therefore, a current compliance (500 nA) was used to help control the e-burning at the GB. We were able to spatially resolve the EL dynamics while imaging the WS_2 GB erosion under biasing in figure 3g-k. We detected EL arcs between the source-drain electrodes at the start of forward biasing and then the EL eventually becomes localized at the defective GB region, figure 3k. Since EL requires the recombination of electron-hole pairs, the observation of EL arcs indicates that either current flows preferentially in these arc locations with increased electron-hole interactions, or there are hole donor dopants locally residing on the arc locations that result in radiative recombination of the majority electron charge carrier. Both mechanisms are likely the result of defects within the material.

According to the study of localized light-emission in single carbon nanotubes, defects can create pockets of trapped electrons in SiO_2 and forms locally p-doped segments that cause emission under biasing.*(47,48)* In the case of ML-WS_2, defects may be present close to the GB region, because this region has to reconstruct during growth in order to form the dominant mirror-twin GBs.*(33)* The presence of defects in this area might also lead to paths with different conductivity and result in arc-like current flow. The change in the geometry of the arc could be associated with migration of defects in the material

during biasing. This real-time tracking of EL arcs could potentially detect defect migration in single crystalline 2D-TMD semiconducting devices.*(48)*

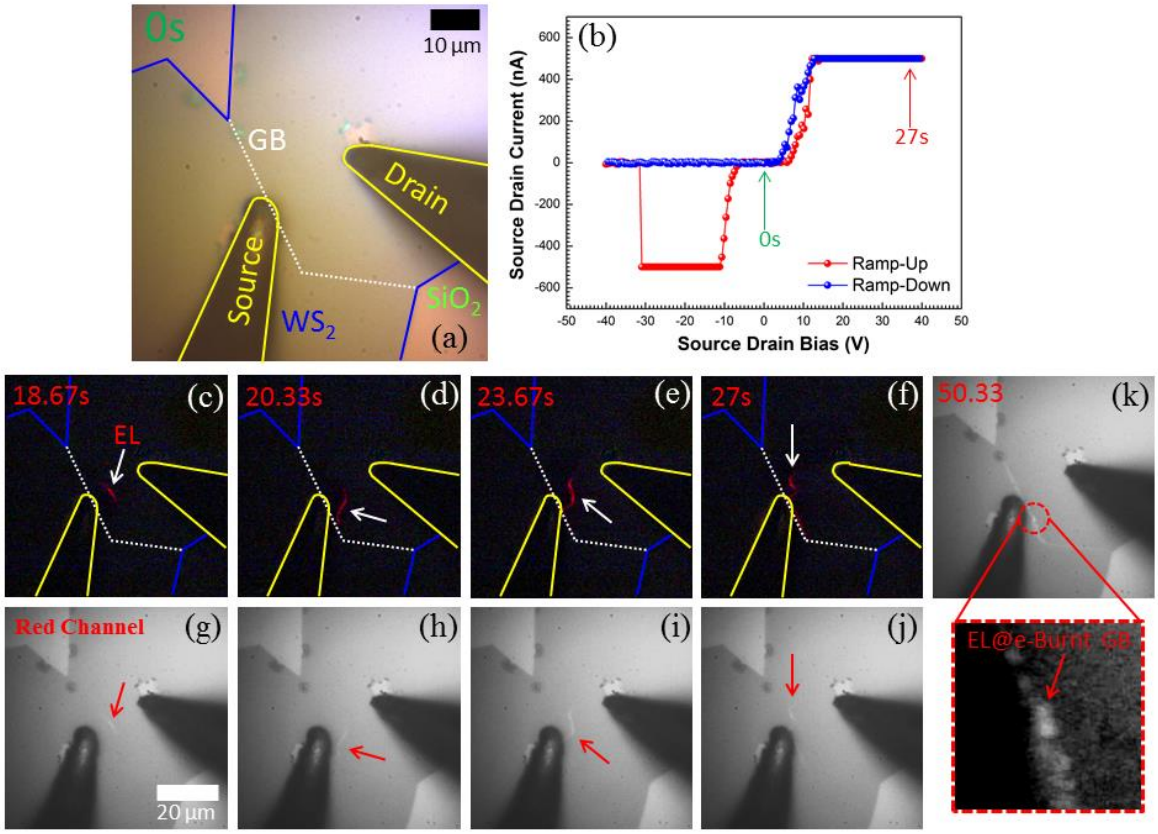

Figure 3. Spatially resolved EL in a ML-WS_2 GB region. (a) An optical image showing that a WS_2 GB area where two ML-WS_2 domains joined together is probed when no source-drain bias is applied. (b) A full ramping profile of $I_{SD}V_{SD}$ output in which the forward-bias ramp-up curve (0 to 40V) corresponds to the EL in (c) to (k). (c)-(f) A time-series of images showing EL dynamics in the ML-WS_2 GB region at forward bias. (g)-(j) Red-channel only optical images from the images in (c)-(f) respectively. (k) Red-channel only optical image showing EL localized within GB after migration, with a closer image of the EL spot within the e-burnt GB. EL images in (c) to (f) are obtained by subtracting the red-channel image of (a) from (g)-(j) to allow a more explicit observation. Source-drain bias ramping was at approximately 1.24 V/s.

In figure 4, we examine the dynamics of the EL arcing with higher spatial resolution than in figure 3. The EL arc intensity gradually builds-up within a very narrow time-window,

originating from the GB toward the W electrode, as shown in figure 4a-c. The as-established EL arc diminishes by disconnecting the anchor at GB and gradually vanishes in this particular region of WS_2 domain (figure 4d-f). Continuous ramping-up of V_{SD} caused a revival of the EL arc back to detectable intensity, reconnected between the electrode and GB at a completely new path (figure 4g-i). After figure 4i, the EL becomes localized within the GB.

The greatest difference of the e-burning process in ML-WS_2 single crystals as opposed to GBs is their starting position of degradation (figure 5). GBs in CVD-synthesized 2D crystalline domains or films have defective structures, offering low conductivity/high resistivity as compared to single crystalline regions.*(24,43,49)* The defect-induced high resistance gives rise to heat localization at GBs (resistive Joule heating) when biasing across them and initiates oxidization induced decomposition.*(33,50)* In our experiment, there was a sufficient amount of current flow at high bias before it breaks down (figure 3b). In single crystals, higher currents can be reached, but the large resistance is located at the metal-semiconductor interface causes heating induced decomposition. This is supported by the fact that e-burning decomposition in single crystals only occurs around the electrode which is highly biased (figure 5a-c).

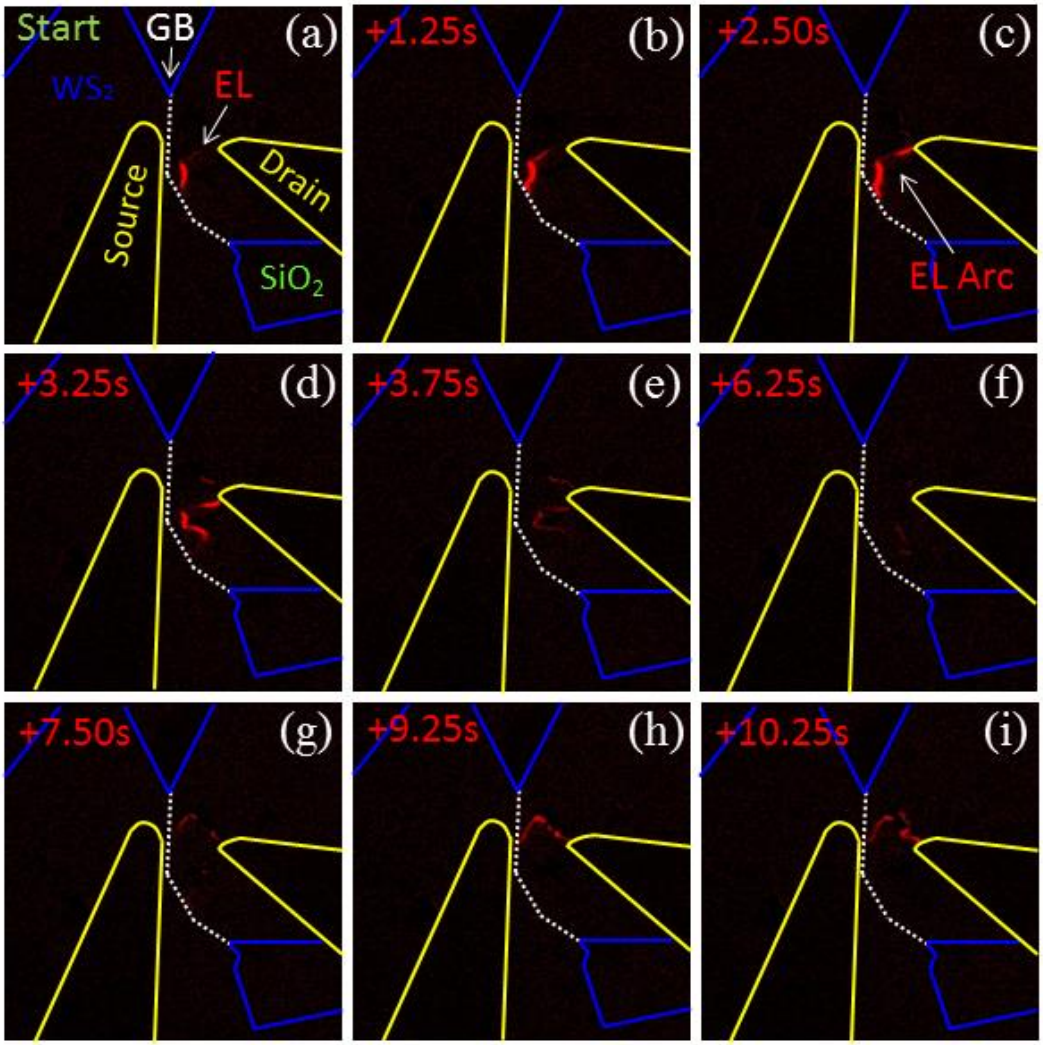

Figure 4. Time-dependence of EL arcing across a ML-WS_2 GB region at the start of increasing the source-drain bias. (a)-(c) EL arc grows from near the GB and progresses toward the W drain electrode. (d)-(f) EL arc breaks away from the GB and then fades in intensity. (g)-(i) EL arc reforms in a new location connecting the electrodes through a new path within the WS_2 domain.

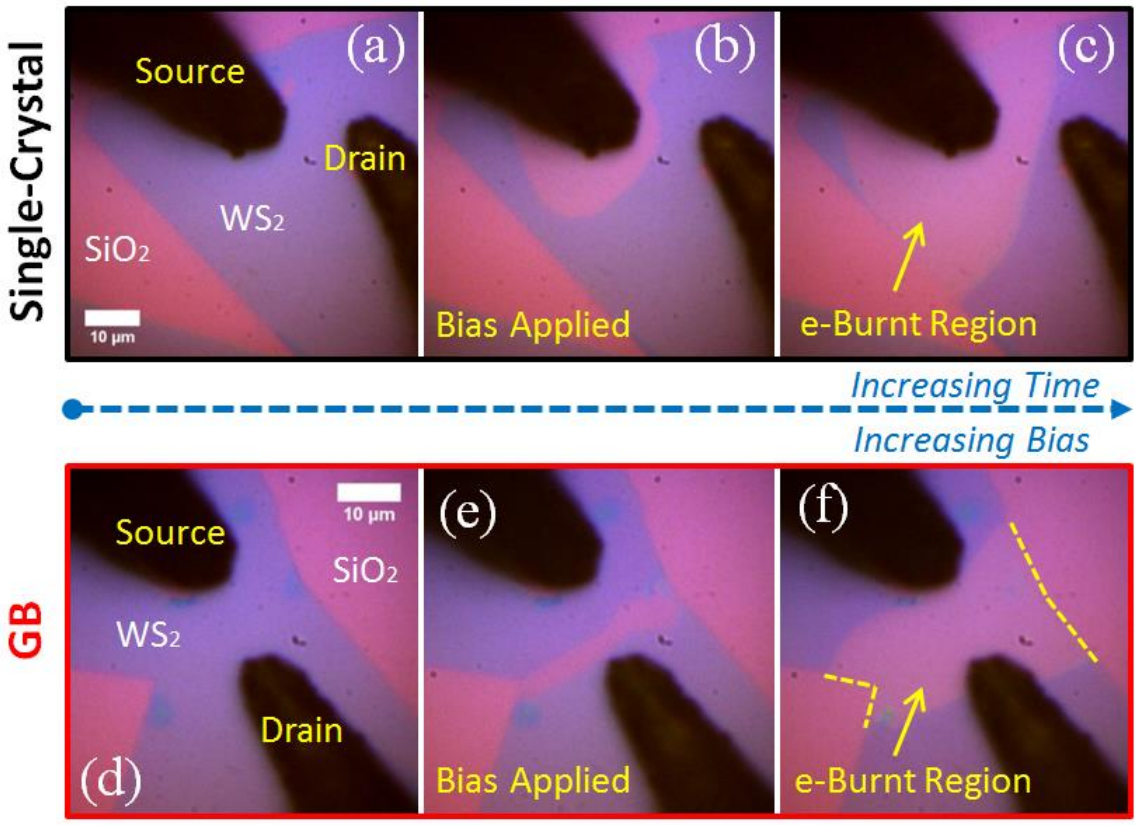

Figure 5. Evolution of e-burning in a ML-WS_2 single crystalline region (a)-(c) and a GB region (d)-(f), respectively, at increasing V_{SD}.

Figure 6a-c shows a pair of W electrodes positioned either side of a ML-WS_2 GB region and EL generated in the GB region (figure 6c). A time-series of images shows the EL at the GB in figure 6d, which corresponds to an applied forward biasing (I_{SD}/V_{SD}) profile shown separately in figure 6e and f. The current drop at 14 s (green) led to EL quenching but quickly revived for the ramp-up biasing. Once e-burning evokes erosion in the GB region, EL preferentially remains within the GB region over the whole course of the forward biasing. Optical images in figure 6d show the gradual increase of EL intensity with increasing V_{SD} (figure 6e) and then fading when ramping back down (figure 6f). There have been several reports of controlled Joule heating of graphene to burn away regions of high resistance and create nanogap electrodes.*(51-55)* Given that there is often spatial variations in the atomic structure of GBs, there might be sections of the GB with different

conductivity. This would result in sections of the GB starting to oxidize and decompose by Joule heating in air at different stages and give rise to ML-WS_2 constrictions (*i.e.,* narrow ribbons).

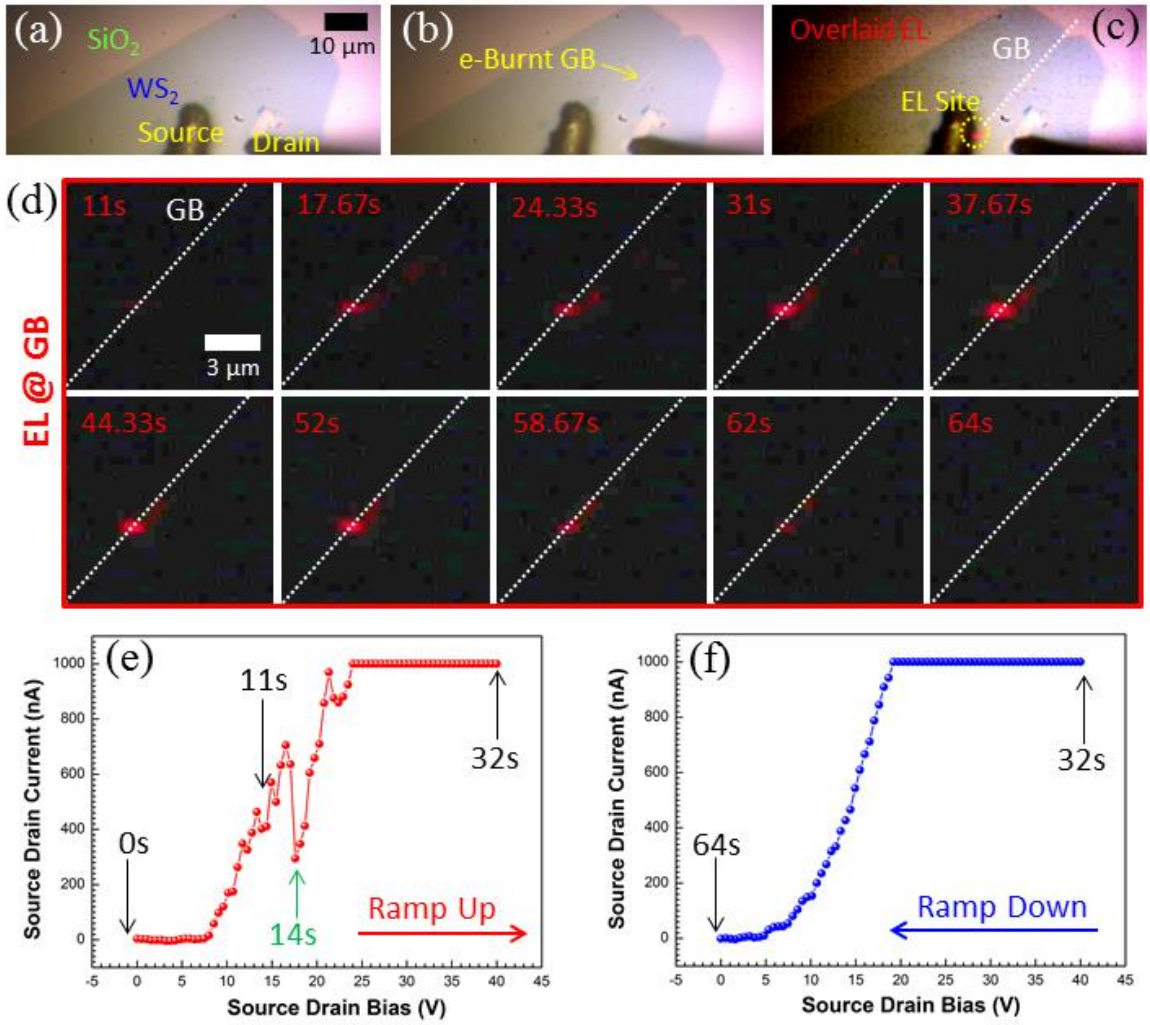

Figure 6. Evolution of EL localized within a ML-WS_2 GB for an applied forward bias. (a) An optical image showing the electrodes providing source-drain bias across a ML-WS_2 GB region. (b) The ML-WS_2 GB is eroded and visible under an optical microscope after e-burning. (c) Image formed by overlapping EL only image in (d) with the white light image of (b) to show the location of EL relative to the GB. (d) Time series of optical images showing EL at elevating and descending forward bias (with white light off), exhibiting the dynamics of the EL within the ML-WS_2 GB (*i.e.,* these images were taken when optical illumination was switched off in order to exclude the substrate background interference from the EL light colour.). (e) and (f) I_{SD}/V_{SD} output curves

correspond to respective EL at times in (d) (*i.e.,* the full ramping cycle is available in supporting figure S4). The source-drain bias for the EL process was ramped at approximately 1.26 V/s.

Scanning electron microscopy (SEM) was used to examine the microstructure of ML-WS_2 GBs after partial erosion and when there is still EL. This was achieved by e-burning the GB region until the EL is localized there, and then stopping the biasing immediately to avoid complete erosion. In figure 7a-d, we show that ML-WS_2 micro- and nanoribbons form within ML-WS_2 GBs, bridging between neighbouring domains. We have also optically and topologically characterized the e-burnt regions to make sure no other forms of WS_2 are involved in the GB region apart from the as-formed ML-WS_2 ribbons (figure 1 and 9). These narrow ribbons have the potential to go down to less than a hundred nanometres in width (figure 7d) as long as they remain anchored between two domains. The ribbons vary randomly in shape and width across the GB, as shown in figure 7a-d and 8. Restricting current to flow through the ribbons may increase the electron-hole interactions and lead to higher recombination rates, helping to explain why the EL becomes localized in these partially eroded GB regions. The mechanism of EL within a GB for applied biasing is schematically illustrated in figure 7e-g. In contrast, a biased ML-WS_2 single crystalline region will initially remain intact (figure 7i) when a GB region has already started to be e-burnt for the same V_{SD}. The domain will eventually decompose, originating at a source/drain probe and then propagate into a larger region (figure 7j).

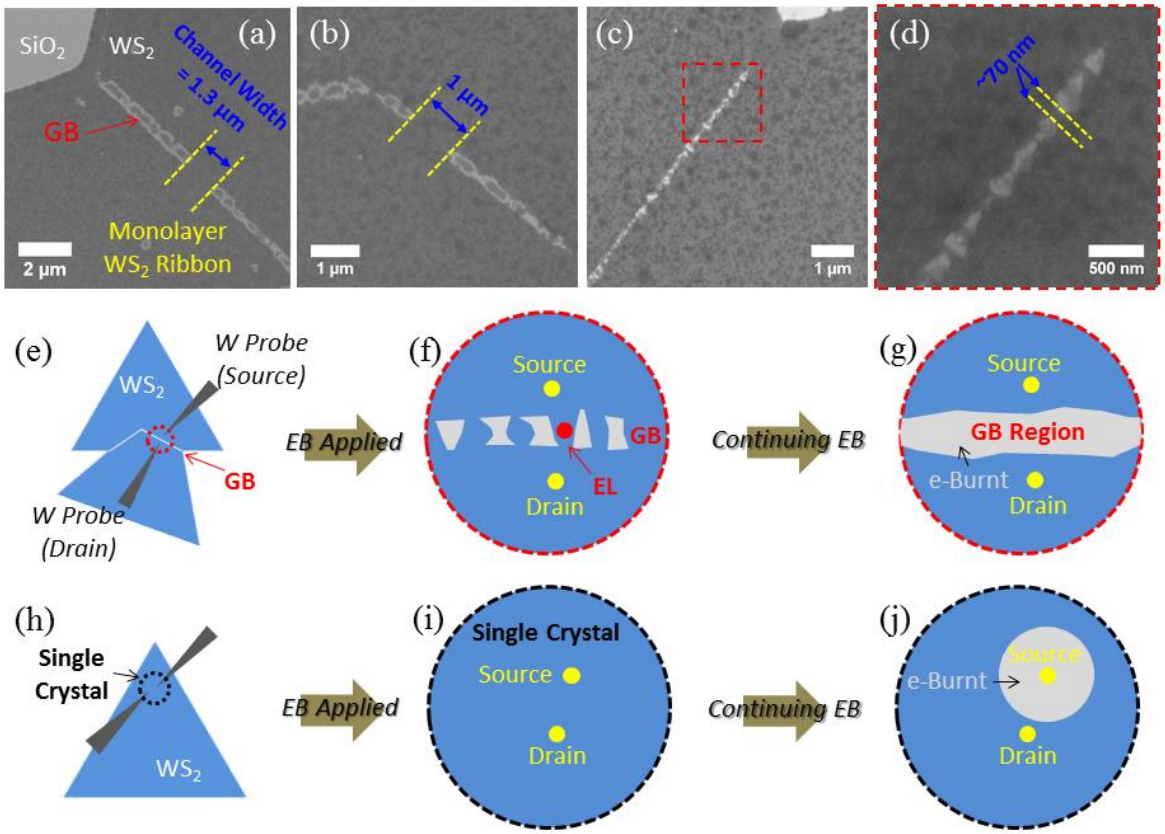

Figure 7. SEM observations and schematic illustrations of ML-WS_2 GB regions obtained at the time of EL, shown in comparison with those of a single crystalline region. (a)-(d) SEM images of ML-WS_2 micro/nanoribbons bridging at two source-drain ML-WS_2 domains formed at the time of EL. (e)-(g) A schematic demonstration of how e-burning (EB) can effectively transform crystalline configurations within a ML-WS_2 GB region, resulting in EL at the highlighted spot (red). (h)-(j) A schematic illustration of the e-burning (EB) in a ML-WS_2 single crystalline region, leading to no detectable localized EL.

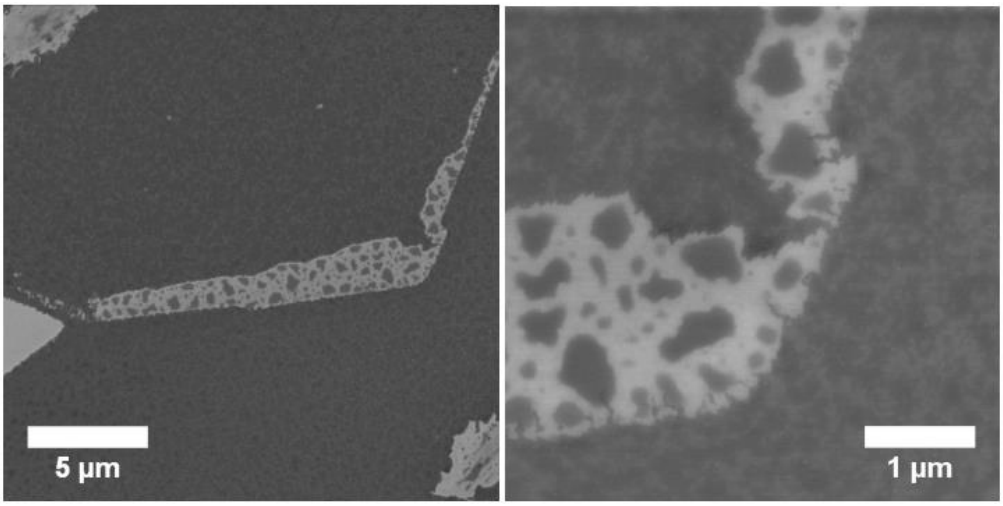

Figure 8. SEM images of a ML-WS_2 microribbon formed in an irregular structure.

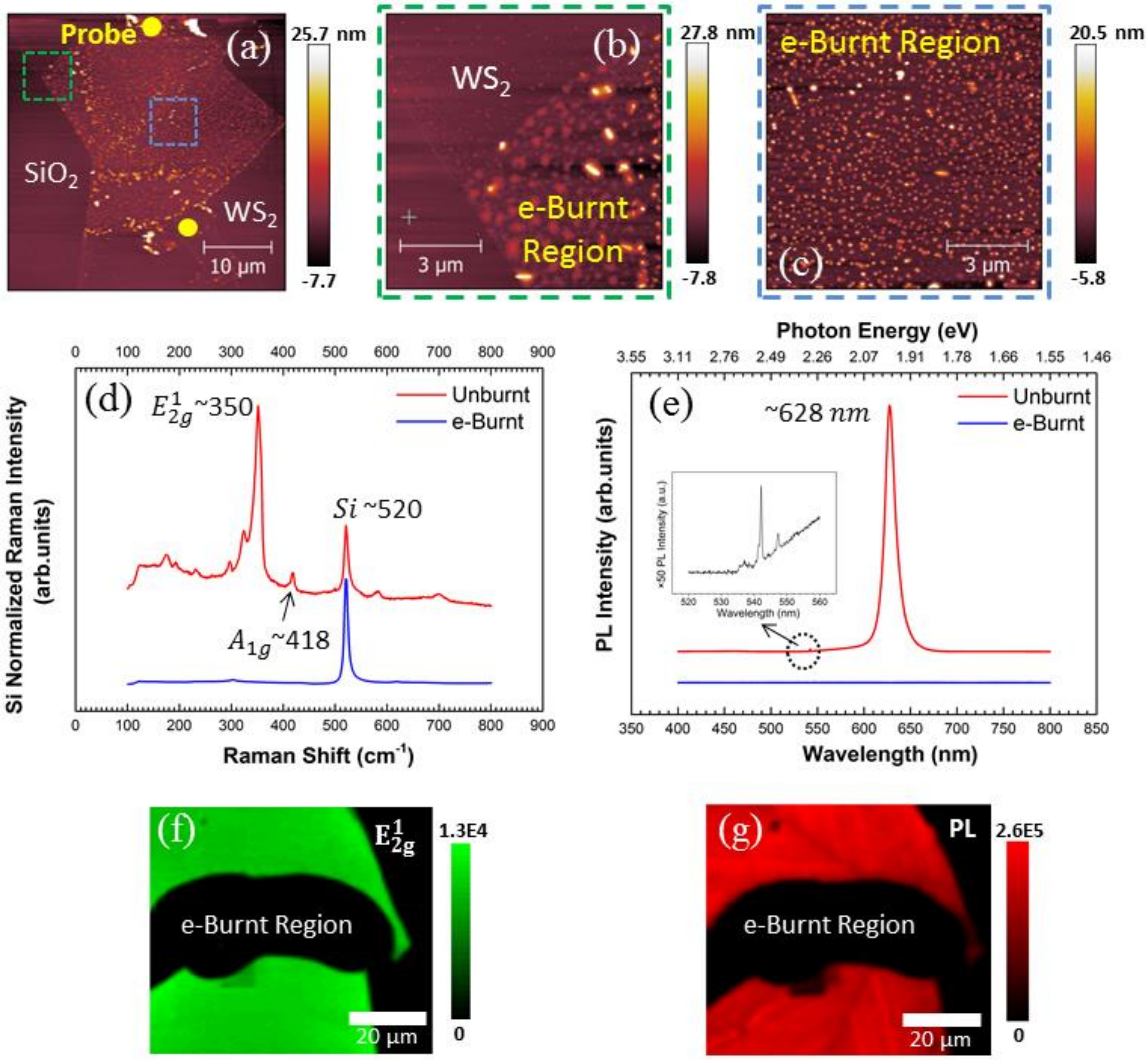

Figure 9. Optical, SEM, Raman, and PL characterization of e-burnt ML-WS_2 GB and single crystalline regions. (a)-(c) AFM images of an e-burnt GB region. (d) and (e) Raman and PL spectrum, respectively, obtained from unburnt and e-burnt ML-WS_2 regions. (f) and (g) Raman (integrated E_{2g}^1 peak 330 to 370 cm^{-1}) and PL (integrated PL peak 600 to 660 nm) mapping, respectively, conducted on an e-burnt ML-WS_2 GB region. Both Raman and PL were excited at 532 nm excitation wavelength.

To understand the mechanism of light generation by EL in the ML-WS_2, we measured the EL spectrum from a biased ML-WS_2 GB using a confocal microscope with an attached photoluminescence (PL) spectrometer. We also measured the PL spectrum from the WS_2 using a 532 nm laser before the biasing. Both the EL and PL are collected using the same microscope objective with an emission collection region of ~5 μm spot. The differences are that for the EL measurement no laser excitation is used and for the PL measurement no biasing is applied. In figure 10a, both the EL and PL spectra are plotted together (normalized to the EL intensity) showing very similar profiles. The similarity of the EL and PL spectra indicates that the EL originates from electron-hole (exciton) recombination across the direct band gap. Figure 10b shows that our EL is dominated by neutral A-exciton (X^0) emission at ~1.97 eV, with a spectral weight of 49%.*(56,57)* The PL spectrum shows similar fitting parameters to the EL spectrum (figure 10c). A second peak at longer wavelength may be related to trion emission (X^T). These samples are prone to impurity doping and lattice strain introduced by our atmospheric CVD growth of ML-WS_2 on SiO_2.*(56,58-60)*

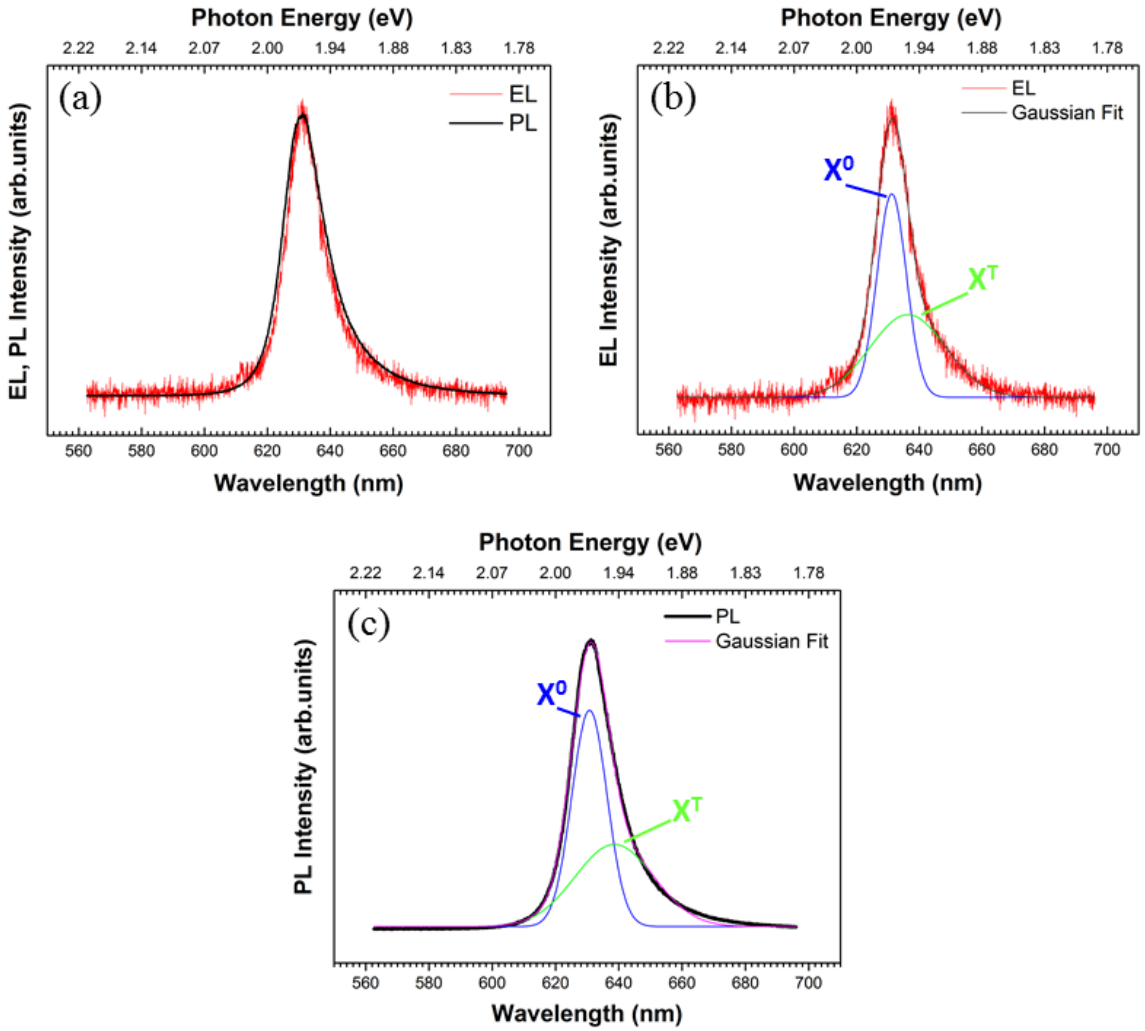

Figure 10. Optical spectroscopy of EL and PL from ML-WS_2 GBs and domains. (a) An EL spectrum is compared with a PL spectrum normalized to the EL intensity (*i.e.,* the PL is obtained at the EL domain region before source-drain bias is applied). (b) The EL spectrum in (a) with Gaussian-curve fittings revealing neutral A-exciton (X^0) and charged exciton (X^T) spectral contributions. (c) The PL spectrum in (a) which has been Gaussian-fitted to present X^0 and X^T subpeaks.

6.3 Conclusion

We show that lateral source-drain EL device structures in monolayer WS_2 are prone to degradation if GBs are present within the active region. Arcing of the EL is seen between

the two electrodes within the GB region of WS_2 before the GB degrades. The arc patterns change rapidly and most likely reflect changes in the internal structure of the WS_2 crystal, such as vacancy migration or dopant diffusion. The degradation of the GB results in the formation of micro/nanoconstrictions that localized the EL. The application of ML-WS_2 nanoribbons can be significantly versatile if they are developed in controllable manner. Hence, improvement could involve fabrication of these nanoribbons using feedback controlled electroburning *(51)* or reduced oxygen environment,(52) which can potentially lead to robust EL and molecular optoelectronic devices.*(61)*

This work is reprinted (adapted) with permission from ref.(62), © 2016 American Chemical Society.

6.4 Reference

1. Peimyoo, N.; Shang, J.; Cong, C.; Shen, X.; Wu, X.; Yeow, E. K. L.; Yu, T. Nonblinking, Intense Two-Dimensional Light Emitter: Monolayer WS_2 Triangles. *ACS Nano* **2013**, *7*, 10985-10994.
2. Gutierrez, H. R.; Perea-Lopez, N.; Elias, A. L.; Berkdemir, A.; Wang, B.; Lv, R.; Lopez-Urias, F.; Crespi, V. H.; Terrones, H.; Terrones, M. Extraordinary Room-Temperature Photoluminescence in Triangular WS_2 Monolayers. *Nano Lett.* **2013**, *13*, 3447-3454.
3. Mak, K. F.; Lee, C.; Hone, J.; Shan, J.; Heinz, T. F. Atomically Thin MoS_2: A New Direct-Gap Semiconductor. *Phys. Rev. Lett.* **2010**, *105*, 136805.
4. Splendiani, A.; Sun, L.; Zhang, Y.; Li, T.; Kim, J.; Chim, C.; Galli, G.; Wang, F. Emerging Photoluminescence in Monolayer MoS2. *Nano Lett.* **2010**, *10*, 1271-1275.
5. He, K.; Kumar, N.; Zhao, L.; Wang, Z.; Mak, K. F.; Zhao, H.; Shan, J. Tightly Bound Excitons in Monolayer WSe_2. *Phys. Rev. Lett.* **2014**, *113*, 026803.
6. Huang, C.; Wu, S.; Sanchez, A. M.; Peters, J. J. P.; Beanland, R.; Ross, J. S.; Rivera, P.; Yao, W.; Cobden, D. H.; Xu, X. Lateral Heterojunctions within Monolayer $MoSe_2$-WSe_2 Semiconductors. *Nat. Mater.* **2014**, *13*, 1096-1101.
7. Yang, J.; Lu, T.; Myint, Y. W.; Pei, J.; Macdonald, D.; Zheng, J.; Lu, Y. Robust Excitons and Trions in Monolayer $MoTe_2$. *ACS Nano* **2015**, *9*, 6603-6609.
8. Zhang, Y.; Chang, T.; Zhou, B.; Cui, Y.; Yan, H.; Liu, Z.; Schmitt, F.; Lee, J.; Moore, R.; Chen, Y.; *et al.* Direct Observation of the Transition from Indirect to Direct Bandgap in Atomically Thin Epitaxial $MoSe_2$. *Nat. Nanotechnol.* **2014**, *9*, 111-115.

9. Sundaram, R. S.; Engel, M.; Lombardo, A.; Krupke, R.; Ferrari, A. C.; Avouris, P.; Steiner, M. Electroluminescence in Single Layer MoS_2. *Nano Lett.* **2013***, 13*, 1416-1421.
10. Jo, S.; Ubrig, N.; Berger, H.; Kuzmenko, A. B.; Morpurgo, A. F. Mono- and Bilayer WS_2 Light-Emitting Transistors. *Nano Lett.* **2014***, 14*, 2019-2025.
11. Wang, Q. H.; Kalantar-Zadeh, K.; Kis, A.; Coleman, J. N.; Strano, M. S. Electronics and Optoelectronics of Two-Dimensional Transition Metal Dichalcogenides. *Nat. Nanotechnol.* **2012***, 7*, 699-712.
12. Pospischil, A.; Furchi, M. M.; Mueller, T. Solar-Energy Conversion and Light Emission in an Atomic Monolayer p-n Diode. *Nat. Nanotechnol.* **2014***, 9*, 257-261.
13. Ross, J. S.; Wu, S.; Yu, H.; Ghimire, N. J.; Jones, A. M.; Aivazian, G.; Yan, J.; Mandrus, D. G.; Xiao, D.; Yao, W.; *et al.* Electrical Control of Neutral and Charged Excitons in a Monolayer Semiconductor. *Nat.Commun.* **2013***, 4*, 1474.
14. Zeng, H.; Dai, J.; Yao, W.; Xiao, D.; Cui, X. Valley Polarization in MoS_2 Monolayers by Optical Pumping. *Nat. Nanotechnol.* **2012***, 7*, 490-493.
15. Jones, A. M.; Yu, H.; Ghimire, N. J.; Wu, S.; Aivazian, G.; Ross, J. S.; Zhao, B.; Yan, J.; Mandrus, D. G.; Xiao, D.; *et al.* Optical Generation of Excitonic Valley Coherence in Monolayer WSe_2. *Nat. Nanotechnol.* **2013***, 8*, 634-638.
16. Mak, K. F.; He, K.; Shan, J.; Heinz, T. F. Control of Valley Polarization in Monolayer MoS_2 by Optical Helicity. *Nat. Nanotechnol.* **2012***, 7*, 494-498.
17. Lopez-Sanchez, O.; Lembke, D.; Kayci, M.; Radenovic, A.; Kis, A. Ultrasensitive Photodetectors Based on Monolayer MoS_2. *Nat. Nanotechnol.* **2013***, 8*, 497-501.
18. Britnell, L.; Ribeiro, R. M.; Eckmann, A.; Jalil, R.; Belle, B. D.; Mishchenko, A.; Kim, Y. -.; Gorbachev, R. V.; Georgiou, T.; Morozov, S. V.; *et al.* Strong Light-Matter Interactions in Heterostructures of Atomically Thin Films. *Science* **2013***, 340*, 1311-1314.
19. Koppens, F. H. L.; Mueller, T.; Avouris, P.; Ferrari, A. C.; Vitiello, M. S.; Polini, M. Photodetectors Based on Graphene, Other Two-Dimensional Materials and Hybrid Systems. *Nat. Nanotechnol.* **2014***, 9*, 780-793.
20. Zhang, J.; Yu, H.; Chen, W.; Tian, X.; Liu, D.; Cheng, M.; Xie, G.; Yang, W.; Yang, R.; Bai, X.; *et al.* Scalable Growth of High-Quality Polycrystalline MoS_2 Monolayers on SiO_2 with Tunable Grain Sizes. *ACS Nano* **2014***, 8*, 6024-6030.
21. Kang, K.; Xie, S.; Huang, L.; Han, Y.; Huang, P. Y.; Mak, K. F.; Kim, C.; Muller, D.; Park, J. High-Mobility Three-Atom-Thick Semiconducting Films with Wafer-Scale Homogeneity. *Nature* **2015***, 520*, 656-660.
22. Wu, Y. A.; Fan, Y.; Speller, S.; Creeth, G. L.; Sadowski, J. T.; He, K.; Robertson, A. W.; Allen, C. S.; Warner, J. H. Large Single Crystals of Graphene on Melted Copper Using Chemical Vapor Deposition. *ACS Nano* **2012***, 6*, 5010-5017.
23. Zhu, W.; Low, T.; Lee, Y.; Wang, H.; Farmer, D. B.; Kong, J.; Xia, F.; Avouris, P. Electronic Transport and Device Prospects of Monolayer Molybdenum Disulphide Grown by Chemical Vapour Deposition. *Nat.Commun.* **2014***, 5*, 3087.

24. Yu, Q.; Jauregui, L. A.; Wu, W.; Colby, R.; Tian, J.; Su, Z.; Cao, H.; Liu, Z.; Pandey, D.; Wei, D.; *et al.* Control and Characterization of Individual Grains and Grain Boundaries in Graphene Grown by Chemical Vapour Deposition. *Nat. Mater.* **2011***, 10*, 443-449.
25. Rong, Y.; Fan, Y.; Koh, A. L.; Robertson, A. W.; He, K.; Wang, S.; Tan, H.; Sinclair, R.; Warner, J. H. Controlling Sulphur Precursor Addition for Large Single Crystal Domains of WS_2. *Nanoscale* **2014***, 6*, 12096-12103.
26. Wang, X.; Gong, Y.; Shi, G.; Chow, W. L.; Keyshar, K.; Ye, G.; Vajtai, R.; Lou, J.; Liu, Z.; Ringe, E.; *et al.* Chemical Vapor Deposition Growth of Crystalline Mono layer $MoSe_2$. *ACS Nano* **2014***, 8*, 5125-5131.
27. Perea-Lopez, N.; Lin, Z.; Pradhan, N. R.; Iniguez-Rabago, A.; Elias, A. L.; McCreary, A.; Lou, J.; Ajayan, P. M.; Terrones, H.; Balicas, L.; *et al.* CVD-grown Monolayered MoS_2 as an Effective Photosensor Operating at Low-Voltage. *2D Mater.* **2014***, 1*, 011004.
28. Zhang, W.; Huang, J.; Chen, C.; Chang, Y.; Cheng, Y.; Li, L. High-Gain Phototransistors Based on a CVD MoS_2 Monolayer. *Adv. Mater.* **2013***, 25*, 3456-3461.
29. Cheng, R.; Li, D.; Zhou, H.; Wang, C.; Yin, A.; Jiang, S.; Liu, Y.; Chen, Y.; Huang, Y.; Duan, X. Electroluminescence and Photocurrent Generation from Atomically Sharp WSe_2/MoS_2 Heterojunction p-n Diodes. *Nano Lett.* **2014***, 14*, 5590-5597.
30. Withers, F.; Del Pozo-Zamudio, O.; Mishchenko, A.; Rooney, A. P.; Gholinia, A.; Watanabe, K.; Taniguchi, T.; Haigh, S. J.; Geim, A. K.; Tartakovskii, A. I.; *et al.* Light-Emitting Diodes by Band-Structure Engineering in van der Waals Heterostructures. *Nat. Mater.* **2015***, 14*, 301-306.
31. Ross, J. S.; Klement, P.; Jones, A. M.; Ghimire, N. J.; Yan, J.; Mandrus, D. G.; Taniguchi, T.; Watanabe, K.; Kitamura, K.; Yao, W.; *et al.* Electrically Tunable Excitonic Light-Emitting Diodes Based on Monolayer WSe_2 p-n Junctions. *Nat. Nanotechnol.* **2014***, 9*, 268-272.
32. Zhang, Y. J.; Oka, T.; Suzuki, R.; Ye, J. T.; Iwasa, Y. Electrically Switchable Chiral Light-Emitting Transistor. *Science* **2014***, 344*, 725-728.
33. Rong, Y.; He, K.; Pacios, M.; Robertson, A. W.; Bhaskaran, H.; Warner, J. H. Controlled Preferential Oxidation of Grain Boundaries in Monolayer Tungsten Disulfide for Direct Optical Imaging. *ACS Nano* **2015***, 9*, 3695-3703.
34. Kang, J.; Liu, W.; Banerjee, K. High-Performance MoS_2 Transistors with Low-Resistance Molybdenum Contacts. *Appl. Phys. Lett.* **2014***, 104*, 093106.
35. He, Z.; Sheng, Y.; Rong, Y.; Lee, G.; Li, J.; Warner, J. H. Layer-Dependent Modulation of Tungsten Disulfide Photoluminescence by Lateral Electric Fields. *ACS Nano* **2015***, 9*, 2740-2748.
36. Michaelson, H. Work Function of Elements and its Periodicity. *J. Appl. Phys.* **1977***, 48*, 4729-4733.
37. Beleznai, C. S.; Vouagner, D.; Girardeau-Montaut, J. P. Work Function Variation during UV Laser-Induced Oxide Removal. *Appl. Surf. Sci.* **1999***, 138*, 6-11.

38. Tao, C.; Ruan, S.; Xie, G.; Kong, X.; Shen, L.; Meng, F.; Liu, C.; Zhang, X.; Dong, W.; Chen, W. Role of Tungsten Oxide in Inverted Polymer Solar Cells. *Appl. Phys. Lett.* **2009***, 94*, 043311.
39. Zhang, Y.; Zhang, Y.; Ji, Q.; Ju, J.; Yuan, H.; Shi, J.; Gao, T.; Ma, D.; Liu, M.; Chen, Y.; *et al.* Controlled Growth of High-Quality Monolayer WS_2 Layers on Sapphire and Imaging Its Grain Boundary. *ACS Nano* **2013***, 7*, 8963-8971.
40. Ovchinnikov, D.; Allain, A.; Huang, Y.; Dumcenco, D.; Kis, A. Electrical Transport Properties of Single-Layer WS_2. *ACS Nano* **2014***, 8*, 8174-8181.
41. Yun, S. J.; Chae, S. H.; Kim, H.; Park, J. C.; Park, J.; Han, G. H.; Lee, J. S.; Kim, S. M.; Oh, H. M.; Seok, J.; *et al.* Synthesis of Centimeter-Scale Monolayer Tungsten Disulfide Film on Gold Foils. *ACS Nano* **2015***, 9*, 5510-5519.
42. Dolui, K.; Rungger, I.; Sanvito, S. Origin of the n-Type and p-Type Conductivity of MoS_2 Monolayers on a SiO_2 Substrate. *Phys. Rev. B* **2013***, 87*, 165402.
43. van der Zande, A. M.; Huang, P. Y.; Chenet, D. A.; Berkelbach, T. C.; You, Y.; Lee, G.; Heinz, T. F.; Reichman, D. R.; Muller, D. A.; Hone, J. C. Grains and Grain Boundaries in Highly Crystalline Monolayer Molybdenum Disulphide. *Nat. Mater.* **2013***, 12*, 554-561.
44. Najmaei, S.; Amani, M.; Chin, M. L.; Liu, Z.; Birdwell, A. G.; O'Regan, T. P.; Ajayan, P. M.; Dubey, M.; Lou, J. Electrical Transport Properties of Polycrystalline Monolayer Molybdenum Disulfide. *ACS Nano* **2014***, 8*, 7930-7937.
45. Zhu, B.; Chen, X.; Cui, X. Exciton Binding Energy of Monolayer WS_2. *Sci. Rep.* **2015***, 5*, 9218.
46. Ramasubramaniam, A. Large Excitonic Effects in Monolayers of Molybdenum and Tungsten Dichalcogenides. *Phys. Rev. B* **2012***, 86*, 115409.
47. Freitag, M.; Tsang, J. C.; Kirtley, J.; Carlsen, A.; Chen, J.; Troeman, A.; Hilgenkamp, H.; Avouris, P. Electrically Excited, Localized Infrared Emission from Single Carbon Nanotubes. *Nano Lett.* **2006***, 6*, 1425-1433.
48. Avouris, P.; Freitag, M.; Perebeinos, V. Carbon-Nanotube Photonics and Optoelectronics. *Nat. Photonics* **2008***, 2*, 341-350.
49. Clark, K. W.; Zhang, X. -.; Vlassiouk, I. V.; He, G.; Feenstra, R. M.; Li, A. Spatially Resolved Mapping of Electrical Conductivity across Individual Domain (Grain) Boundaries in Graphene. *ACS Nano* **2013***, 7*, 7956-7966.
50. Grosse, K. L.; Dorgan, V. E.; Estrada, D.; Wood, J. D.; Vlassiouk, I.; Eres, G.; Lyding, J. W.; King, W. P.; Pop, E. Direct Observation of Resistive Heating at Graphene Wrinkles and Grain Boundaries. *Appl. Phys. Lett.* **2014***, 105*, 143109.
51. Prins, F.; Barreiro, A.; Ruitenberg, J. W.; Seldenthuis, J. S.; Aliaga-Alcalde, N.; Vandersypen, L. M. K.; van der Zant, H. S. J. Room-Temperature Gating of Molecular Junctions Using Few-Layer Graphene Nanogap Electrodes. *Nano Lett.* **2011***, 11*, 4607-4611.
52. Nef, C.; Posa, L.; Makk, P.; Fu, W.; Halbritter, A.; Schoenenberger, C.; Calame, M. High-Yield Fabrication of nm-Size Gaps in Monolayer CVD Graphene. *Nanoscale* **2014***, 6*, 7249-7254.

53. Shi, S.; Xu, X.; Ralph, D. C.; McEuen, P. L. Plasmon Resonance in Individual Nanogap Electrodes Studied Using Graphene Nanoconstrictions as Photodetectors. *Nano Lett.* **2011***, 11*, 1814-1818.
54. Standley, B.; Bao, W.; Zhang, H.; Bruck, J.; Lau, C. N.; Bockrath, M. Graphene-Based Atomic-Scale Switches. *Nano Lett.* **2008***, 8*, 3345-3349.
55. Lau, C. S.; Mol, J. A.; Warner, J. H.; Briggs, G. A. D. Nanoscale Control of Graphene Electrodes. *Phys. Chem. Chem. Phys.* **2014***, 16*, 20398-20401.
56. Chow, P. K.; Jacobs-Gedrim, R. B.; Gao, J.; Lu, T.; Yu, B.; Terrones, H.; Koratkar, N. Defect-Induced Photoluminescence in Monolayer Semiconducting Transition Metal Dichalcogenides. *ACS Nano* **2015***, 9*, 1520-1527.
57. Zhao, W.; Ghorannevis, Z.; Chu, L.; Toh, M.; Kloc, C.; Tan, P.; Eda, G. Evolution of Electronic Structure in Atomically Thin Sheets of WS_2 and WSe_2. *ACS Nano* **2013***, 7*, 791-797.
58. Conley, H. J.; Wang, B.; Ziegler, J. I.; Haglund, R. F.,Jr.; Pantelides, S. T.; Bolotin, K. I. Bandgap Engineering of Strained Monolayer and Bilayer MoS_2. *Nano Lett.* **2013***, 13*, 3626-3630.
59. Mak, K. F.; He, K.; Lee, C.; Lee, G. H.; Hone, J.; Heinz, T. F.; Shan, J. Tightly Bound Trions in Monolayer MoS_2. *Nat. Mater.* **2013***, 12*, 207-211.
60. Chernikov, A.; Berkelbach, T. C.; Hill, H. M.; Rigosi, A.; Li, Y.; Aslan, O. B.; Reichman, D. R.; Hybertsen, M. S.; Heinz, T. F. Exciton Binding Energy and Nonhydrogenic Rydberg Series in Monolayer WS_2. *Phys. Rev. Lett.* **2014***, 113*, 076802.
61. Marquardt, C. W.; Grunder, S.; Blaszczyk, A.; Dehm, S.; Hennrich, F.; v. Loehneysen, H.; Mayor, M.; Krupke, R. Electroluminescence from a Single Nanotube-Molecule-Nanotube Junction. *Nat. Nanotechnol.* **2010***, 5*, 863-867.
62. Rong, Y.; Sheng, Y.; Pacios, M.; Wang, X.; He, Z.; Bhaskaran, H.; Warner, J. Electroluminescence Dynamics across Grain Boundary Regions of Monolayer Tungsten Disulphide. *ACS Nano*, **2016**, 10, 1093-1100.

Chapter 7

Final Discussion, Conclusions and Future Outlook

7.1 Thesis Summary

The novel research in this thesis has been presented with regard to three major areas of current monolayer WS_2 research: material synthesis, structural characterisation and electrical characterisation. Each was given a dedicated focus for one chapter. *Chapter 4* introduced the techniques and procedures for synthesis of large area WS_2 monolayer domains by sulphur (precursor) controlled chemical vapour deposition (CVD); *Chapter 5* dived into the study of grain boundary (GB) structure of monolayer WS_2 *via* optical microscopy enabled by the controlled oxidation technique in air; *Chapter 6* investigated GBs from an electrical perspective where electroluminescence (EL) dynamics of monolayer WS_2 across GB regions was instigated by a strong source-drain bias.

7.2 Discussion and Conclusions

Subsequent to graphene, the incentive for improving synthesis and gaining characterisation of monolayer WS_2 should be accredited to 2D-TMD's paramount potential in optoelectronic applications. Inheriting mechanical exfoliation from graphene for the production of monolayer WS_2 is good enough for fundamental research but not adoptable for future industrial applications. CVD, the well-known technique for large-scale production of graphene, has once again proven its capability in scalable deployment of monolayer

TMDs. Monolayer WS_2 is generally developed on non-catalytic insulting substrates such as SiO_2/Si and sapphire. In this respect, synthesis of large-area CVD monolayer WS_2 is more challenging and requires delicate control of reaction parameters. The study here shows that the introduction timing of sulphur (S) vapour precursor to the reaction chamber (bulk WO_3 and SiO_2/Si) is a determining factor for the quality of monolayer WS_2 domain growth. By introducing the S vapour 10 min prior to the CVD reaction temperature, extra-large WS_2 monolayer domains (visible by naked eyes) are obtained, while capable of providing high-yield photoluminescence (PL). Further work also demonstrated that S and WO_3 precursor should be isolated such that the S vapour does not quench the bulk WO_3 precursor, which had led to growth of continuous monolayer WS_2 films.

The high-throughput ability of CVD synthesis provides the opportunity to prevalently obtain monolayer WS_2, but on the other hand, it introduces defect structure such as GB that often not encounters in mechanical exfoliation. GB is detrimental to the electronic device quality of monolayer WS_2; hence minimizing its amount (maximizing single crystal size) in large-area monolayer WS_2 thin films is a major goal in the implementation of monolayer WS_2 in commercial devices. In contrast to traditional GB characterisation techniques (*i.e.,* TEM and STM), this thesis demonstrates that by mildly oxidizing monolayer WS_2 domains or films in air the GBs are detectable under a standard optical microscopy. The process does not require any complicated equipment for preparation, and should be viable in all laboratory conditions and applicable for other 2D TMDs. Gaining access to probe GBs using optical microscope provokes an effective way of determining degree of polycrystallinity of continuous monolayer WS_2 films over centimetre scale. Furthermore, knowing the GB's spatial distribution helps relate electronic performance to specific GBs, which shall pave the way for improving future optoelectronic products.

Further work involving investigation of electronic performance of CVD monolayer WS_2 also led to the optical visualization of GBs, which however, was caused by strong biasing

across GBs. The defective nature of GBs (high resistance) gives rise to resistive Joule heating when biasing at high voltages. This electrically induced heat localization (electroburning) provokes monolayer WS_2 in GB regions to decompose in air (leading to zero conductance), similar in a way to the previous heat treatment process. This phenomenon implies that operation of electronic devices based on CVD monolayer WS_2 in air may be inhibited from the GBs if high biasing conditions are applied. Before GB decomposes fully, the study unveils that the GB region of monolayer WS_2 is prone to instigation of high-intensity EL at high bias, owing to direct bandgap recombination *via* minority hole injection. The EL process consists of two steps: initially, EL establishes between two electrodes as in arc shape before the GB degradation starts; then the EL becomes localized within the GB while the GB degradation occurs (*i.e.,* the EL vanishes when the GB is fully decomposed). The first step denotes that defects around a GB region are potentially trap states for injected carriers, triggering electron-hole recombination. The GB degradation process in the second step unfolds *via* formation of monolayer WS_2 micro/nanoribbons that localize the EL due to enhanced carrier density. As a result of this electrical characterisation, GBs in CVD-grown WS_2 monolayers are found to be opto-characteristic, which renders a new perspective regarding the role of GB in 2D electronic applications.

7.3 Future Outlook

The experiments conducted on one TMD are often cross-applicable for the rest of semiconducting TMD group. As to our CVD synthesis method, given the lateral size of monolayer WS_2 continuous film it is still far from industrial application. Further work should involve implementing vacuum instruments into the existing CVD system or substituting solid precursors and insulating substrates with liquid/gas precursors and catalytic gold substrates, respectively. This will facilitate much more uniform growth of monolayer WS_2

(as well as MoS_2, $MoSe_2$ and WSe_2) films over large areas. In addition, the optical GB imaging technique could be used for newly emergent types of monolayer TMD, as well as monolayer TMD deposited on new substrates such as gold. Enabling optical observation of GBs in different TMD types and on different TMD growth substrates is important for future industrial product quality control. Lastly, the fabrication of monolayer WS_2 micro/nanoribbons needs to be carried out in a controllable manner, for which the electroburning should be done either with a feedback controlled set-up or in a reduced oxygen environment. In this way, the as-developed narrow ribbons are potentially valuable to achieving constant robust EL and fabricating molecular optoelectronic devices.